Alma Mater Studiorum – Università di Bologna

Dipartimento di Fisica e Astronomia

Corso di Laurea Magistrale in Astrofisica e Cosmologia

Gravitational Waves as Dark Sirens: an Astrophysical and Cosmological Analysis

Relatore:
Dott. Michele Moresco

Candidato:
Matteo Schulz

Correlatori:
Prof. Andrea Cimatti
Dott. Michele Mancarella
Dott. Nicola Borghi

Anno Accademico 2021-2022

Abstract

Despite the success of the ΛCDM model in describing the Universe, a possible tension between early- and late-Universe cosmological measurements is calling for new independent cosmological probes. Amongst the most promising ones, gravitational waves (GWs) can provide a self-calibrated measurement of the luminosity distance. However, to obtain cosmological constraints, additional information is needed to break the degeneracy between parameters in the gravitational waveform.

In this thesis, we exploit the latest LIGO-Virgo-KAGRA Gravitational Wave Transient Catalog (GWTC-3) of GW sources to constrain the background cosmological parameters together with the astrophysical properties of Binary Black Holes (BBHs), using information from their mass distribution. We expand the public code `MGCosmoPop`, previously used for the application of this technique, by implementing a state-of-the-art model for the mass distribution, needed to account for the presence of non-trivial features, i.e. a truncated power law with two additional Gaussian peaks, referred to as `Multipeak`. We then analyse GWTC-3 comparing this model with simpler and more commonly adopted ones, both in the case of fixed and varying cosmology, and assess their goodness-of-fit with different model selection criteria, and their constraining power on the cosmological and population parameters. We also start to explore different sampling methods, namely Markov Chain Monte Carlo and Nested Sampling, comparing their performances and evaluating the advantages of both.

We find concurring evidence that the `Multipeak` model is favoured by the data, in line with previous results, and show that this conclusion is robust to the variation of the cosmological parameters. We find a constraint on the Hubble constant of $H_0 = 61.10^{+38.65}_{-22.43}$ km/s/Mpc (68% C.L.), which shows the potential of this method in providing independent constraints on cosmological parameters. The results obtained in this work have been included in [1].

Contents

Preface

Scientific Framework Driven by the discovery of the accelerated expansion of the Universe [2, 3], several cosmological probes have been thoroughly studied and improved in the last twenty years, such as the Cosmic Microwave Background (CMB) [4], the Supernovae Type Ia [5], and the Baryon Acoustic Oscillations (BAOs) [6], becoming standards in the landscape of modern cosmology. In particular, they recently reached percent and sub-percent accuracy in constraining cosmological parameters, highlighting a disagreement between early- and late-universe measurements in some cosmological parameters [7], such as the Hubble constant H_0 and the amplitude of matter perturbations smoothed over 8 Mpc/h σ_8. This former is commonly referred to as the Hubble tension. Breaking the Hubble tension by measuring with independent and accurate methods the value of the Hubble constant and determining the origin of the discrepancy between early- and late-time measurements is one of the main targets of modern cosmology. Given that the standard probes seem to have reached their potential, new complementary and independent probes are necessary to investigate this problem.

Gravitational wave (GW) events can be used as an alternative probe, since they can provide a measurement of the luminosity distance of the source directly from General Relativity first principles [8], requiring no other form of calibration, making them independent of the cosmic distance ladder.

$$d_L = c(1+z)\int_0^z \frac{dz'}{H_0 E(z')}. \tag{1}$$

In contrast, the measurement of H_0 from SNe [5] requires a distance ladder (parallaxes and Cepheids) calibration. In particular, compact binary coalescences (CBCs) are amongst the most favorable systems that are expected to produce well-detectable GW signals and can be therefore used as standard sirens, objects of a known "loudness" that can be used to constrain cosmology. The use of standard sirens would provide, through equation 1, an independent way to constrain the expansion history of the Universe, and in particular, its local value, the Hubble constant, contributing to a new and independent measurement that could give further evidence to solve the current tension between the early- and late-Universe measurements of H_0.

To obtain a measurement of the luminosity distance $d_L(z)$ from GW standard sirens, information on the redshift of the source is needed. However, z cannot be inferred by GW data alone, due to the existing degeneracy between redshift and binaries masses. In fact, the same signal can be produced by a more massive and more distant binary, and by a less massive but closer binary. Breaking this degeneracy is crucial to obtain information on both the cosmological parameters (including, e.g., H_0) and on the BBH population parameters (including, e.g., their mass distribution).

Method There are different methods to break the degeneracy between GW parameters [9], depending on the type of binaries involved in the process. For example, the detection of GW170817, the first binary neutron star merger, was characterised by the observation of its electromagnetic counterpart, a kilonova, that allowed to precisely measure the redshift of the GW host galaxy thanks to its observed spectrum, providing the first measurement of the Hubble constant based on GWs. If an electromagnetic counterpart is observed, the GW event is classified as *bright* standard siren. On the contrary, *dark* standard sirens, which are GWs without an electromagnetic counterpart from which the redshift can be obtained, require some statistical methods or prior knowledge of the source population to infer the missing information.

Among the different methods for dark sirens cosmology proposed, the one used in this work is based on the use of GW-only data without any other external source to provide for the missing redshift. In particular, this method requires some prior knowledge of the astrophysical properties of the GW emitters (mass distribution and rate evolution) to break the degeneracy between parameters.

In particular, in this Thesis, we use the latest LIGO-Virgo-KAGRA Gravitational Wave Transient Catalog (GWTC-3) to explore the constraints that can be obtained from GWs on astrophysical and cosmological parameters, what functional form of the Binary Black Hole (BBH) mass function is reproduced best by current data, and the dependence of the results on the assumed BBH mass function given different levels of degrees of freedom. For this reason, the work has been divided into three steps.

In the first part, we use the publicly available python software `MGCosmoPop` [10] to constrain and study the source population by developing the code further to include a new mass function currently not implemented, as suggested by [11]. Secondly, we use the newly updated code on the latest compilation of GWTC-3 data, in order to obtain the best parameters' values to describe the mass distribution of the selected events. This run was made thanks to a Markov Chain Monte Carlo (MCMC) analysis based on the available public code *emcee* [12], which for each of the four BBH mass functions explored the parameter space of the posterior distribution, in two different cases: (1) by assuming a fixed cosmology or (2) by leaving also two cosmological parameters free (H_0 and $\Omega_{0,m}$). We then explored how different posterior samplers can affect the parameters constraints, analyzing their advantages and drawbacks. Lastly, we analyze the results by comparing the different models thanks to the use of different implemented model selection methods, namely: the Deviance Information Criterion, and the Cumulative Distribution Function.

Scientific Objective The main objectives of this Thesis are the following:

1. Development and validation of a new module in `MGCosmoPop`, to include a BBH mass function model that extends and improves the currently included ones by adding a peak. This new feature has also been suggested in the latest LVK analysis [13];

2. Development of a new module to perform a statistical model comparison based on different robust estimators, and in particular: the Deviance Information Criterion, and the Cumulative Distribution Function. This analysis will allow us to assess which mass function is preferred by the current BBH GW data, and potentially which one is discarded.
3. Estimate the astrophysical and cosmological parameters from current GWTC-3 data, with particular attention to the Hubble constant, and its interpretation in the framework of the Hubble tension.

   As an additional point, we studied also the impact of a lower Signal-to-Noise Ratio (SNR) during the selection of the analyzed samples on the obtained results.

Outlook We summarize here the structure of the Thesis, with a brief description of the contents of each Chapter:

- In Chapter 1 the general cosmological framework of GWs is presented, together with a detailed description of how the GWs can be used as cosmological probes, as firstly suggested by [14]. Specifically, after a first introduction on the standard cosmological model, the physics of GW production and propagation will be discussed, followed by a brief description of the two main GW events: GW150914 and GW170817. Finally, the astrophysical properties that influence the BH population are presented, in particular by focusing on the star formation rate density (SFRD).
- In Chapter 2 a schematic description of the characteristics of the GW detectors (interferometers) will be given, followed by a more detailed presentation of the properties of the three main GW instruments to date: Advanced LIGO, Advanced Virgo and KAGRA. In this chapter, we also present the dataset used in our analysis.
- In Chapter 3 the approach for the data analysis is described. Specifically, after a first short description of the fundamental concepts of the hierarchical Bayesian formalism for the astrophysical inference of parameter (population function), a more complete picture of Bayesian inference is presented: likelihood, posterior and selection bias. Moreover, two different sampling methods, namely the affine invariant and nested sampling, are presented and their advantages and drawbacks are also analysed. Then the code used is described with all its main components, taking a more in-depth look into the classes directly involved in this work. Lastly, the developed extension will be introduced and discussed.
- In Chapter 4 we present the results of the dark sirens analysis by splitting them into two main sections: a first one in which the analysis is run only on the "astrophysical" parameters; a second analysis where two additional "cosmological" parameters are included in order to be constrained (H_0 and $\Omega_{0,m}$). Once the parameters are derived, a discussion regarding the constraining power on the

parameters defining the BBH mass population and on the cosmological parameters is presented. Finally, the results are analyzed and the different models are compared thanks to the use of different implemented model selection methods, namely: the Deviance Information Criterion, and the Cumulative Distribution Function.

- In Chapter 5 we summarize the results, draw the conclusions of this work and present possible future developments of this work.

Chapter 1

Gravitational Waves in the Cosmological Scenario

In this first chapter, the general cosmological framework of gravitational waves (GW) will be presented, together with a detailed description of how they can be used as cosmological probes, as first suggested by [14]. Specifically, the standard cosmological model will be introduced, and the physics of GW production discussed, together with the main mechanisms driving the generation of GW. Finally, the astrophysical properties of the various GW sources will be discussed, and the basics of how to use them as standard sirens will be presented.

1.1 Theoretical Framework

In this first section, a broad introduction to the cosmological and gravitational wave astronomical frameworks is given. The description of these topics will be provided following the structure provided in [15, 9, 14, 16].

1.1.1 Basic Equations

The basis of the entire modern cosmology is the *cosmological principle*: our Universe, on large enough scales ($\mathrm{R} \gtrsim 100\,\mathrm{Mpc}$), is homogeneous and isotropic, which means that in the Universe no preferential position nor preferential spatial direction exist. If this principle is assumed to be true, the space-time metric is described by the Friedmann-Lemaître-Robertson-Walker (FLRW) metric:

$$ds^2 = -c^2 dt^2 + a(t)^2 \left[\frac{dr^2}{1 - \kappa r^2} + r^2 \left(d\theta^2 + \sin^2 \theta d\phi^2 \right) \right] , \tag{1.1}$$

where $a(t)$ is the dimensional scale factor of the Universe, (r, θ, ϕ) are the three adimensional spherical coordinates of the metric, and κ is called curvature parameter and defines the geometry of the Universe depending on the value it has: if $\kappa = 0$ the Universe is flat

and therefore can be described with a Euclidean geometry; if $\kappa = -1$ the Universe is open and represented with a hyperbolic geometry; if $\kappa = 1$ the Universe is close and follows a spherical geometry.

The scale factor $a(t)$ describes the relative expansion of the Universe, in particular its definition is based on the relation between the proper distance between two objects at any time t and their distance a some referenced time t_0, thus:

$$d(t) = a(t)d_0 \ . \tag{1.2}$$

If the FRLW metric is assumed, a fundamental relation can be found linking the scale factor to the redshift z:

$$a(t) = \frac{1}{1+z} \ . \tag{1.3}$$

It is therefore clear that the expansion rate of the Universe is given by the time derivative of the scale factor with respect to the scale factor itself. Such parameter is crucial in cosmology and its evolution is described by the Hubble parameter:

$$H(t) := \frac{\dot{a}}{a}(t) \tag{1.4}$$

and from which the *Hubble constant* can be defined, which is the Hubble parameter at the current time:

$$H_0 := H(t = t_{now}) = \left[\frac{\dot{a}}{a}\right]_{t_{now}} \ . \tag{1.5}$$

It is also useful to introduce the normalized Hubble parameter, which is given by:

$$E(z) := \frac{H(z)}{H_0} \ . \tag{1.6}$$

Furthermore, starting from Einstein's field equations [17]:

$$R_{\mu\nu} - \frac{1}{2}g_{\mu\nu}R + \Lambda g_{\mu\nu} = \frac{8\pi G}{c^4}T_{\mu\nu} \ , \tag{1.7}$$

where $R_{\mu\nu}$ is the Ricci curvature tensor, R is the scalar curvature, $g_{\mu\nu}$ is the metric tensor, Λ is the cosmological constant, and $T_{\mu\nu}$ is the stress-energy tensor (the left-hand side of the equation describes the geometry of the Universe, while the right-hand represents the energy of the cosmos); it is possible to infer the evolution with time of the expansion rate of the Universe. In particular, these relations are expressed by the two Friedmann equations:

$$\left(\frac{\dot{a}}{a}\right)^2 = \frac{8\pi G\rho}{3} - \frac{\kappa}{a^2} + \frac{\Lambda}{3} \ , \tag{1.8}$$

$$\frac{\ddot{a}}{a} = -\frac{4\pi G}{3}(\rho + 3p) + \frac{\Lambda}{3} \ , \tag{1.9}$$

where ρ and p are the energy density and the pressure, respectively, and are bound by the adiabatic condition: $d(\rho c^2 a^3) = -p da^3$; while Λ is the cosmological constant.

In general, in order to quantify the contribution of the various constituents within the Universe, the density of the different components is considered, and typically, all the parameters are expressed with respect to the critical density $\rho_{crit} = \frac{3H^2}{8\pi G}$, or to the modern critical density:

$$\rho_{0,crit} = \frac{3H_0^2}{8\pi G} = 1.9\ 10^{-29}\ h^2\ g\ cm^{-3}. \tag{1.10}$$

Therefore, the total energy density of the Universe is given by the sum of the different components: matter, radiation and dark energy. So:

$$1 - \Omega_\kappa = \sum_i \Omega_i = \Omega_m + \Omega_r + \Omega_\Lambda\ , \tag{1.11}$$

where $\Omega_\kappa = \frac{\kappa}{H^2}$ is the energy density linked to the curvature of the Universe, and $\Omega_i = \frac{\rho_i}{\rho_{crit}}$. Thus, by assuming a flat universe ($\kappa = 0$ and $\Omega_\kappa = 0$), equation (1.11) becomes:

$$1 = \Omega_m + \Omega_r + \Omega_\Lambda\ , \tag{1.12}$$

which is the standard equation to express the density distribution in our Universe. Each component of the Universe has a different equation of state, expressed as a function of $w_i = \frac{p_i}{\rho_i}$, which is:

$$w = \begin{cases} 0 & \text{for matter;} \\ \frac{1}{3} & \text{for radiation;} \\ -1 & \text{for dark energy in } \Lambda\text{CDM model.} \end{cases} \tag{1.13}$$

It is possible to express the dependence of the density ρ with the redshift as:

$$\rho_i(z) = \rho_{i,0}(1+z)^{3(1+w_i)}\ . \tag{1.14}$$

So, by combining equations (1.5), (1.8), (1.9), and (1.10), we get an expression describing the evolution with redshift of the Hubble parameter:

$$H(z) = H_0 \left[\Omega_r(1+z)^4 + \Omega_m(1+z)^3 + \Omega_\kappa(1+z)^2 + \Omega_\Lambda(1+z)^{3(1+w)}\right]^{1/2}\ . \tag{1.15}$$

In particular, it is possible to evince more specific cases by assuming some particular values for the different parameters. For the aim of this work, we will focus on the flat ΛCDM model, where $w_\Lambda = -1$ and $\Omega_\kappa = 0$. Moreover, Ω_r has negligible contribution at $z \sim 0$, based on the current constraint on this parameter [18]: $\Omega_r \sim 2.47\ 10^{-5} h^{-2}$. For this reasons, equation (1.15) becomes:

$$H(z) = H_0 \left[\Omega_m(1+z)^3 + (1-\Omega_m)\right]^{1/2}\ . \tag{1.16}$$

Once all these equations have been defined, it is possible to introduce all the other physical quantities necessary to describe the variety of astrophysical phenomena. In particular, in the context of the flat ΛCDM model, the distance is given by:

$$d(z) = c\int_0^z \frac{dz'}{H(z')}\ , \tag{1.17}$$

from which two fundamental distance estimations can be inferred:

- **Luminosity distance** defined as:

$$d_L(z) := (1+z)d(z) = (1+z)c\int_0^z \frac{dz'}{H(z')} \; ; \tag{1.18}$$

- **Angular diameter distance** defined as:

$$d_A(z) := \frac{1}{(1+z)}d(z) = \frac{c}{(1+z)}\int_0^z \frac{dz'}{H(z')} \; . \tag{1.19}$$

1.1.2 Generation and Propagation of Gravitational Waves

Gravitational Waves (GWs) are "ripples" in the space-time and that can be derived from Einstein's field equations. In particular, if a region far from any gravitational source is considered, then it can be assumed to be flat, and if a GW perturbs this flat space, due to the far field hypothesis, the effects on the metric $g_{\mu\nu}$ can be approximated as a small perturbation:

$$g_{\mu\nu}(\mathbf{x}) = \eta_{\mu\nu} + h_{\mu\nu}(\mathbf{x}) \; , \tag{1.20}$$

where $\eta_{\mu\nu}$ is the Minkowski metric, given by:

$$\eta_{\mu\nu} = \begin{pmatrix} -1 & 0 & 0 & 0 \\ 0 & 1 & 0 & 0 \\ 0 & 0 & 1 & 0 \\ 0 & 0 & 0 & 1 \end{pmatrix} \; , \tag{1.21}$$

which describes the flat Cartesian metric; and $|h_{\mu\nu}| \ll 1$. In these conditions (far and weak field) it is possible to consider gravity as linearized, resulting in much simpler field equations:

$$\Box h_{\mu\nu}(\mathbf{x}) = -16\pi G\mathcal{S}_{\mu\nu}, \tag{1.22}$$

where $\mathcal{S}_{\mu\nu} = T_{\mu\nu} - \frac{1}{2}g_{\mu\nu}T^{\lambda}_{\lambda}$ represents the source term of gravitational perturbation and $\Box := -\frac{1}{c^2}\frac{\partial^2}{\partial t^2} + \nabla^2$ is the D'Alembert operator.

Generation

The formation of GW can be derived by finding the solution of equation (1.22). To simplify the calculations, some assumptions are typically made:

1. the time-dependent part of $\mathcal{S}_{\mu\nu}$ is a sinusoidal oscillation with frequency ω, i.e. it is the *real* part of $\mathcal{S}_{\mu\nu} = \mathrm{S}_{\mu\nu}e^{-i\omega t}$. This condition in astrophysics is typically verified, thanks to the fact that the main GW sources are periodic: pulsars and binary systems.

2. the region of space in which $\mathrm{S}_{\mu\nu} \neq 0$ is small compared to $\lambda_{GW} = 2\pi/\omega$, which is called slow-motion assumption. This hypothesis implies that: $\mathrm{R}\cdot\omega \ll 2\pi \sim 1$, where R represent the scale of the system and ω the typical velocities within it.

If we revise equation (1.22) considering the first assumption and assume the following *ansatz* as solution $h_{\mu\nu} = B_{\mu\nu}(x^i)e^{-i\omega t}$, we obtain:

$$(\nabla^2 + \omega^2)B_{\mu\nu} = -16\pi \mathrm{S}_{\mu\nu} \ . \tag{1.23}$$

By assuming r the radial spherical coordinate taken from the centre of the source, the solution of such an equation is:

$$B_{\mu\nu} = \frac{A_{\mu\nu}}{r}e^{i\omega t} + \frac{Z_{\mu\nu}}{r}e^{-i\omega t} \ , \tag{1.24}$$

but due to the fact that waves are only emitted by the source and are not ingoing into the source, it is possible to set $\mathrm{Z}_{\mu\nu} = 0$. Furthermore, by making the slow-motion assumption, it is found that $A_{\mu\nu} = 4J_{\mu\nu}$, where $J_{\mu\nu} = \int \mathrm{S}_{\mu\nu} d^3x$.

Therefore, the solution is:

$$h_{\mu\nu} = 4J_{\mu\nu}\frac{e^{i\omega(r-t)}}{r} \ , \tag{1.25}$$

in which it is evident that the amplitude of the GW declines as $\propto r^{-1}$, meaning that the further the source is, the harder it will be to measure the space-time deformation due to the GW crossing.

Furthermore, by considering that the components of $\mathrm{h}_{\mu\nu}$ are not uncorrelated functions, it is possible to simplify equation (1.25) even further. In particular, by observing that:

$$J_{\mu\nu}e^{-i\omega t} = \int \mathcal{S}_{\mu\nu} d^3x \tag{1.26}$$

and by applying Gauss' theorem and the slow-motion approximation we get:

$$h_{\alpha\beta} = -2\omega^2 D_{\alpha\beta}\frac{e^{i\omega(r-t)}}{r}, \tag{1.27}$$

where $D_{\alpha\beta} = I_{\alpha\beta}e^{-i\omega t}$, in which $I_{\alpha\beta} := \int \mathcal{S}_{00} x_\alpha x_\beta d^3x$ is the quadrupole moment tensor of the mass distribution, where, for slow motion sources, it can be proven that $\mathcal{S}_{00} \approx \rho$, with ρ being the "classical" Newtonian mass density. It is therefore clear how an accelerating or an asymmetric self-rotating object emits GW mainly through the quadrupole moment of the source, hence the detectors have to be sensitive to such emission in order to detect GWs sources.

Propagation

Now that the production of GW has been discussed, we can focus on the propagation of the emitted gravitational radiation through the Universe. In order to study the propagation of the GW, it is necessary to rewrite equation (1.22) under the assumption of being in vacuum, hence the source term goes to zero ($\mathcal{S}_{\mu\nu} = 0$), leaving us with the homogeneous wave equation:

$$\Box h_{\mu\nu}(\mathbf{x}) = 0. \tag{1.28}$$

Being a wave equation, equation (1.28) has wavelike solutions, the *gravitational wave*, which can be written as:

$$h_{\mu\nu}(\mathbf{x}) = A_{\mu\nu} \exp\left[i(\omega t + \mathbf{k}\cdot\mathbf{x})\right], \tag{1.29}$$

where $A_{\mu\nu}$ is the 4×4 matrix which defines the amplitude of the GW, and $\omega = k^0 = ct$ is the frequency of the wave. If we now choose the z-axis as the direction of motion of the wave, so that $\mathbf{k}^\mu = (\omega,\ 0,\ 0,\ \omega)$ and then impose the gauge condition and the additional transverse-traceless gauge, we get:

$$h_{\mu\nu}(\mathbf{x}) = \begin{pmatrix} 0 & 0 & 0 & 0 \\ 0 & h_+ & h_\times & 0 \\ 0 & h_\times & -h_+ & 0 \\ 0 & 0 & 0 & 0 \end{pmatrix} \exp\left[i(kz - \omega t)\right] \tag{1.30}$$

where h_+ and $h_\times$ can be physically interpreted as two different polarization of the GW. So, by recalling the Minkowsky metric, it is possible to study the effects of the crossing of GW on space-time, in particular by considering:

$$\begin{aligned} ds^2 &= g_{\mu\nu}dx^\mu dx^\nu = (\eta_{\mu\nu} + h_{\mu\nu})dx^\mu dx^\nu = \cdots = \\ &= -dt^2 + \left[1 + h_+ e^{i(kz-\omega t)}\right] dx^2 + \left[1 - h_+ e^{i(kz-\omega t)}\right] dy^2 + 2h_\times e^{i(kz-\omega t)} dxdy + dz^2 \end{aligned} \tag{1.31}$$

where it can be clearly seen how the polarization h_+ deforms the space-time along the x and the y axis, while the $h_\times$ perturbs the mixed component, and thus the deformation is rotated by an angle of $\frac{\pi}{4}$. A visual representation of the perturbation due to GWs is presented in Figure 1.1.

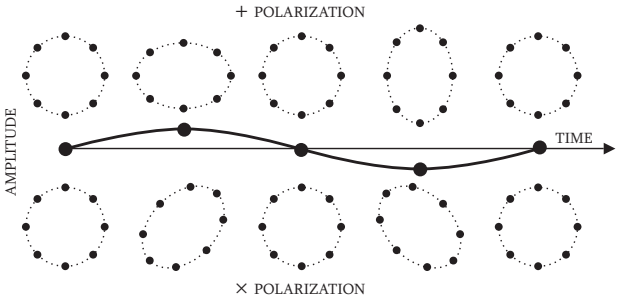

Figure 1.1: Illustration of the effects of a GW crossing on a ring. Image taken from [19].

1.2 Gravitational Waves as Standard Sirens

The existence of GWs was predicted by Einstein in 1916 [20] as a consequence of General Relativity (GR), since accelerating masses will perturb space-time by creating ripples which propagate through it at the speed of light. Nevertheless, the first evidence for the existence

of GWs, despite being an indirect one, came only in the 1980s thanks to the orbital decay of binary pulsars [21]. The first direct observation occurred in 2015 [22], when a signal from a coalescing binary black hole system approximately 440 Mpc away was observed by the LIGO (Laser Interferometer Gravitational-wave Observatory) detectors.

One of the main reasons why GWs are interesting in astrophysics and cosmology is the fact that the luminosity distance of the source can be directly measured from the GW signal, without needing additional calibration[1], hence providing an independent measurement of its distance from the observer. Since their "loudness" can be measured from GR, they have been defined as standard sirens [8].

As previously stated, GWs perturb the space-time they travel through and in particular they produce a distortion perpendicular to the direction of the propagation. Such perturbation can be detected as a relative change in length $\Delta L/\mathrm{L}$ of the laser path within an L-shaped interferometer, and is called strain h. This strain depends on both the intrinsic properties of the emitting system and on its orientation relative to the observer. Typically, if a binary system made of a primary mass m_1 and a secondary mass m_2 is assumed to be the GW source, h is order of 10^{-21} and is measured at a characteristic frequency ν, which is twice the orbital frequency of the emitting binary system. This has the result that the frequency of the signal evolves over time as the two orbiting objects move closer and closer.

As electromagnetic radiation, and as obtained in Section 1.1.2, the GW signal can be polarized and written as a sum of two different components: a plus-polarized component, h_+, and a cross-polarized component, $h_\times$. Following [23] and assuming natural units $\mathrm{c} = \mathrm{G} = 1$, the two components are given by equation (1.32) and equation (1.33), respectively, where it can be clearly seen how the strain is inversely proportional to the distance travelled by the signal, i.e. to the luminosity distance of the source:

$$h_+(t) \equiv \frac{2\mathcal{M}_z}{d_L}\left[1+\cos^2(\iota)\right](\pi\mathcal{M}_z\nu)^{2/3}\cos(\Phi+\Psi_c) \tag{1.32}$$

$$h_\times(t) \equiv \frac{4\mathcal{M}_z}{d_L}\cos^2(\iota)(\pi\mathcal{M}_z\nu)^{2/3}\sin(\Phi+\Psi_c) \tag{1.33}$$

where:

- d_L is the luminosity distance of the source;
- $\mathcal{M}_z = (1+z)\frac{(m_1 m_2)^{3/5}}{(m_1+m_2)^{1/5}}$ is the redshifted chirp mass of the binary system, with components m_1 as primary mass and m_2 as secondary mass;
- ι is the inclination angle with respect to the observer;
- ν is the frequency of the observed signal, which is time-dependent;
- Ψ_c is the phase of the signal at the time of coalescence T;

[1] On the contrary, SN Ia distance measurements require a distance ladder, e.g. parallax and Cepheids from [5]

- $\Phi = -2\left[\frac{T-t}{5\mathcal{M}_z}\right]^{5/8}$ describes the time evolution of the phase of the signal.

In fact, the observed signal is given by a combination of the two components depending on the response of the detector (F_+, $F_\times$) based on their relative position with respect to the sky position of the emitting system. It results that:

$$h(t) = F_+ h_+ + F_\times h_\times \tag{1.34}$$

One of the most established techniques in standard sirens cosmology is to measure the cosmological parameters using the distance-redshift relation (equation (1.18)), which can be rewritten by substituting equation (1.6):

$$d_L = c(1+z)\int_0^z \frac{dz'}{H_0 E(z')}. \tag{1.35}$$

At sufficiently low redshift ($z \lesssim 0.01$) the dependence on the other cosmological parameters is low, hence one can directly estimate H_0 via the relation:

$$d_L = \frac{cz}{H_0} + \mathcal{O}(z^2). \tag{1.36}$$

Therefore, by combining equation (1.34) with equation (1.35), it is possible to obtain an estimate of the Hubble constant by measuring the luminosity distance from the GW strain. In equation (1.35) it is evident that by knowing both d_L and z it is possible to infer some cosmological parameters as H_0 and $\Omega_{0,m}$, which is encoded within $E(z')$. However, the redshift could not be obtained by GW-only data, due to the degeneracy with the chirp mass $\mathcal{M}_z$ of the event, as visible from the definition. Therefore, to extract the valuable cosmological information some external redshift measurement is needed, in order to break the degeneracy, thus enabling the measurement of the cosmological parameters thanks to equation (1.35).

The first time that GWs were proposed to be used as standard sirens for cosmology was by [8], where two different methods for the use of binary neutron star (BNS) mergers were presented: *with* and *without* an electromagnetic counterpart. In the following sections, these two cases will be presented more extensively.

With an electromagnetic counterpart (bright sirens)

This case is based on obtaining multi-messenger observations of compact binary coalescences, i.e. by observing a GW and its associated electromagnetic counterpart, which could be either a short gamma-ray burst or a kilonovae, which would provide a direct redshift measurement, especially when it is possible to localize and identify the host galaxy [24]. The redshift of the host galaxy can then be used in combination with the distance estimate from the BNS to measure H_0. The best example of this method is the observation of GW170817 [25, 26], where it was obtained that $H_0 = 70^{+12}_{-8}$ km/s/Mpc. In this case, we referred to this type of GW event as bright (standard) siren.

Without an electromagnetic counterpart (dark sirens)

In this second case, the GW events are referred to as dark (standard) sirens and several different methods can be used to infer the redshift of the source. First, in most of the GW events observed with current detectors the signal is too poorly localized on the sky ($\Delta\Omega \sim 100 - 1000 deg^2$ for most of the LVK-GWTC3 sources [13]) to allow a similar method like in the "with electromagnetic counterpart" [27], due to the fact that more than one plausible host galaxy can be identified in the sky region of the emitting GW. Nevertheless, if an external and sufficiently complete galaxy catalogue is available, it is possible to consider all the galaxies within the sky volume of the GW event as possible host candidates. The true host would be the one which has the redshift that, in combination with the distance luminosity of the event, produces the "real" H_0 value. This method needs several GWs detections, over time the "true" H_0 will stand out as a result of the stacking of different results, while the contributions from non-host galaxies would statistically average out [28].

A second method consists in calculating the redshift of an event by matching the spatial clustering of GW (if localized enough: $\Delta\theta^2 \lesssim 16z^2$, $\Delta \ln(d_L) \lesssim 0.07z$) as a function of distance to the clustering of the galaxies as a function of redshift [29, 30, 31, 32].

Another application is based on a statistical method, in which prior knowledge of the merger redshift distribution, given by external measurements of the star formation rate and time delay distribution of binary mergers, is compared against the observed GW distance distribution [33, 34, 35].

Finally, the method studied in this work is based on the use of GW-only data without any external dataset to provide information on the missing redshift. In particular, this method relies on the knowledge of some relevant features in the source population (mass distribution, spin distribution, and rate evolution), to directly extract the redshift **and** the luminosity distance from the same GW event alone. The presence of such features in the source-frame mass distribution can be used to infer some information about the source-frame GW frequency, from which a redshift estimate can be derived.

As it will be discussed further in Chapter 3, the astrophysical knowledge about the source population is still a matter of discussion, except the steep drop-off in the BH mass distribution, observed at $\sim$40–65 $M_\odot$, interpreted as the imprint of the pair-instability mechanism, which gives rise to a pile-up of BH immediately below the gap at $\gtrsim 35 M_\odot$ [36]. Therefore, by observing a set of GW the redshifted mass distribution as a function of luminosity distance can be extracted, from which the location of the pair-instability feature can be jointly inferred together with the redshift-distance relation. Thus it is possible to break the degeneracy which prevents the cosmological parameters estimate.

In the current situation, this method is not able to produce a competitive measurement of the Hubble constant ($H_0 = 62^{+87}_{-41}$ km/s/Mpc [37]), but, as the number of available data increase and the BH population models improve, such features in the BH mass distribution can be theoretically calibrated and reach their potential as robust cosmological probes [9].

1.3 Observational Framework

In general, every massive object that undergoes rapid acceleration generates GW that can potentially be detected by sensitive enough instruments. Some of the most notable objects are for example: binary neutron stars systems, binary black holes systems, binary systems formed by a stellar to supermassive black hole and a neutron star, binary supermassive black hole systems or massive stars blowing up into a supernova (SN). As for light, different sources have different emission ranges, therefore a variety of detectors are needed to cover the entire frequency range. Figure 1.2 shows the frequency range predicted for such systems as well as their potential detectors.

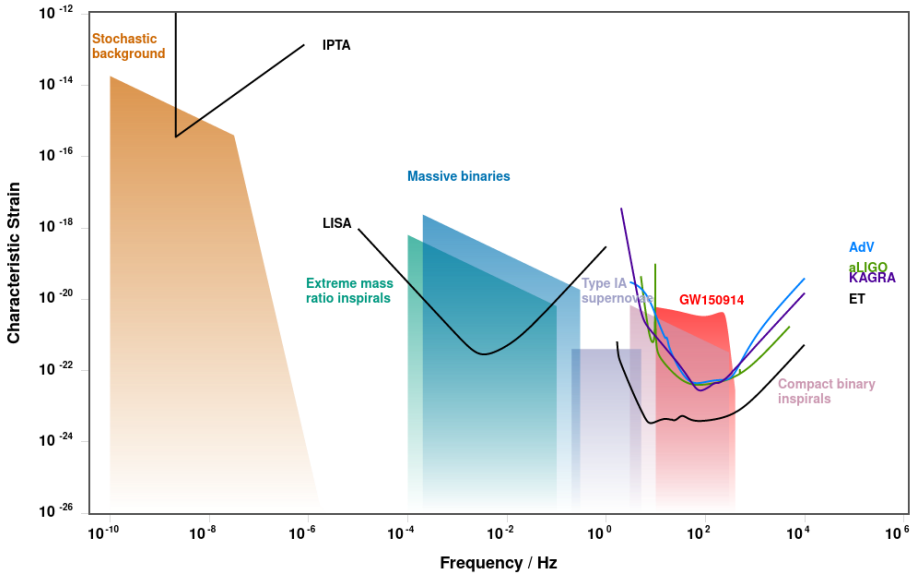

Figure 1.2: Schematic representation of the GW spectrum with the emitting sources and the corresponding instrument for the possible detection. Image from [38].

1.3.1 Astrophysical Sources of Gravitational Waves

It is possible to identify four different GW classes, based on their properties and possible emission sources [39]:

1. **Burst:** short-lived and with a difficult-to-predict waveform. This type of GW signal is typically associated with SN explosions;

2. **Compact Binary Coalescences:** short-lived and with a well-defined waveform. Typically this kind of GW is emitted by an inspiraling binary system;

3. **Continuous-Wave:** long-lived and with a well-defined waveform, which in most cases is emitted by spinning neutron stars;

4. **Stochastic Background:** long-lived and random, the most remarkable example of such an emission is the primordial GWs from the Big Bang.

Examples of such GW categories are given in Figure 1.3.

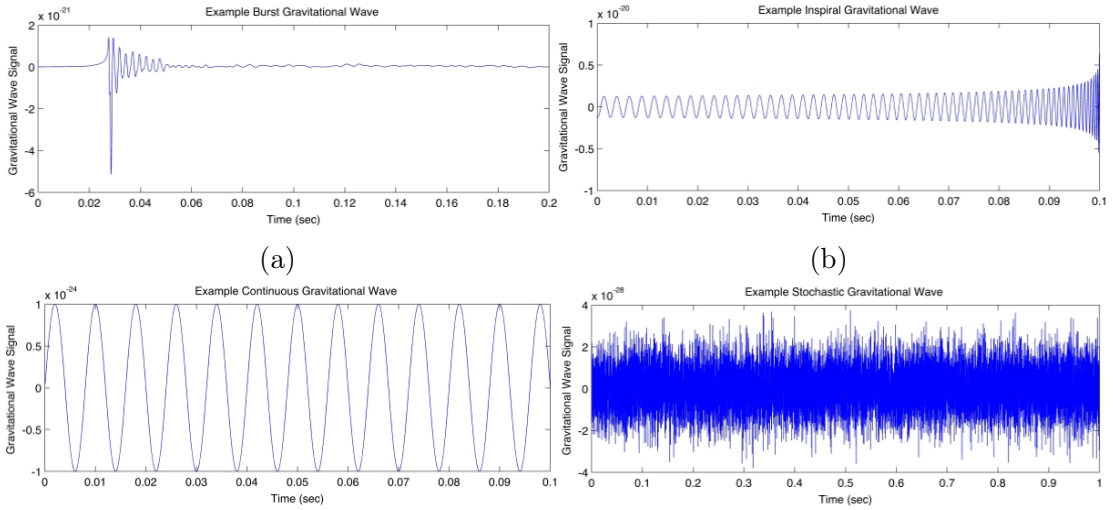

Figure 1.3: Examples of the different GW strain signals: (a) GW burst using data from [40]; (b) Compact Binary Coalescence GW; (c) Continuous GW; (d) Stochastic GW. Image from A. Stuver/LIGO.

Burst

GW bursts indicates short-duration (from $\sim 1\,\mathrm{ms}$ to $\sim 1\,\mathrm{s}$) unknown or unanticipated sources. The nature of such events makes the observation extremely difficult because no characteristic signature can be expected or predicted. There are hypotheses that some systems such as supernovae or gamma-ray bursts may produce burst gravitational waves, but too little is known about the details of these systems to precisely predict the form these waves will have. Due to these difficulties, it is clear why this type of GWs has to be detected yet. Despite not knowing if the prediction is correct, an example of a potential waveform of a GW burst can be calculated and is given in Figure 1.3a.

Another potential transient source which can give rise to the production of a short waveform with an unpredictable shape is the emission of a superflare from a magnetized neutron star (magnetar) [16]. The actual process for the GW emission is still unclear but it is proposed that the energy released into the neutral crustal vibrations could be comparable to the electromagnetically released one [41], giving, therefore, rise to a not negligible GW event from those vibrations.

It is possible to estimate the general energy released by a GW burst, given the source

distance and the detectable strain amplitude [42], the obtained relation states:

$$E \sim 3 \times 10^{-3} M_{\odot} c^2 \left(\frac{h}{10^{-21}}\right)^2 \left(\frac{T}{1ms}\right) \left(\frac{\nu}{1kHz}\right) \left(\frac{r}{10Mpc}\right)^2 \tag{1.37}$$

Thus, the energy required for its waves to be detectable increases as the square of the distance between the source and the observer.

CBC

Compact Binary Coalescences (CBC) waves are produced during the end-of-life stage of a binary system, where the two objects combining the system are inspiraling towards one another until they merge together. Typically, these systems are made of two NSs, two BHs, or a NS and a BH, and as their orbital distance decrease their speed increase, resulting in a steady boost of the GW frequency until the merger is completed. The pattern created by the merger is unique depending on the objects of which the binary system is composed. An example of a typical waveform of an inspiral GW is given in Figure 1.3b.

The evolution of a binary system of two compact objects into a single one can be divided into three parts, which have a characteristic signature in the detected waveform [43]:

1. *Inspiral* is the longest[2] of the three phases, during which the loss of energy to gravitational radiation causes the orbit to become narrower and narrower with the passing of time. As the objects move closer the frequency and amplitude increase, allowing the detection of the emitted signal from GW interferometers during the last stages of this phase.

2. *Merger* is the phase in which the two objects fuse together. The orbital speed of the objects grows to values $\sim c$, until the two bodies merge together into a final BH, making it impossible to distinguish the two initial compact bodies. During this phase the maxima of the frequency and of the amplitude of the signal are reached, thus the merger stage is the most "detectable" of the three.

3. *Ringdown* is the phase during which the newly formed BH emits all its excess energy in the form of quasi-normal mode oscillations, and by doing so it reaches its fundamental state.

An illustrative representation of these stages is given in Figure 1.4.

It has been calculated [44] that the rates at which these events could happen, change based on the type of binary system. In a galaxy like the Milky Way, or equivalent, it results:

- **NS-NS coalescence:** the most probable value is $\mathrm{R} \approx 10^4\,\mathrm{years}^{-1}$, within a plausible range of $10^3 - 10^6\,\mathrm{years}^{-1}$;

[2]The inspiral phase can last up to hundreds-millions of years after the formation of the compact binary system.

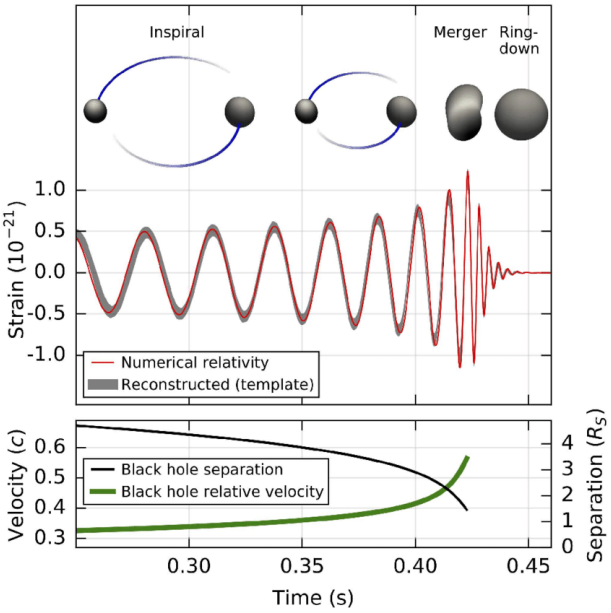

Figure 1.4: Representation of the three stages of a CBC GW emission. Image from [22].

- **NS-BH coalescence:** the most realistic value is $\mathrm{R} \approx 3 \cdot 10^5\,\mathrm{years}^{-1}$, within a plausible range of $10^4 - 2 \cdot 10^6\,\mathrm{years}^{-1}$;

- **BH-BH coalescence:** the corresponding rate is $\mathrm{R} \approx 2.5 \cdot 10^6\,\mathrm{years}^{-1}$, within a plausible range of $3 \cdot 10^3 - 10^8\,\mathrm{years}^{-1}$;

From [45, 16], it is possible to infer some of the most important features of a GW event emitted by a compact binary system. In particular, the characteristic frequency of an event is given by:

$$\nu_{GW}(t) = 1.9\mathrm{Hz} \left(\frac{1.4\mathrm{M}_\odot}{\mathrm{M}}\right)^{\frac{5}{8}} \left(\frac{1\ \mathrm{day}}{\tau}\right)^{\frac{3}{8}} \tag{1.38}$$

while the strain amplitude is given by:

$$h_0(t) = 1.7 \times 10^{-23} \left(\frac{15\mathrm{Mpc}}{r}\right) \left(\frac{\mathrm{M}}{1.4\mathrm{M}_\odot}\right)^{\frac{5}{4}} \left(\frac{1\ \mathrm{day}}{\tau}\right)^{\frac{1}{4}} \tag{1.39}$$

where τ is the time until coalescence detection and r is the distance between the inspiraling objects.

A more detailed discussion of some of the most crucial CBC GW signals ever detected, namely: GW150914 the first ever detected GW event, and GW170817 the first confirmed NS-NS coalescence, will be provided in the section 1.3.2 and section 1.3.3.

Continuous

Continuous GWs are long-lasting and almost with a single constant frequency, i.e. monochromatic. It is thought that this type of GW is emitted by a single spinning massive object like a neutron star. In particular, in order to emit GWs, such an object has to depart from the spherical symmetry, on the contrary, no emission is possible due to the lack of a monopole term in mass current. Therefore, based on the grade of deformity, thanks to the high-speed rotation of the object (which can reach $\mathrm{T} \sim 10^{-3}\,\mathrm{s}$) it is possible to generate GWs with increasing amplitude, while if the spherical symmetry if perfect no GW will be emitted. Due to the fact that the neutron star is constantly spinning the emission will be *continuous* and always at the same frequency and amplitude.

Different mechanisms have been proposed to explain the formation of a deformity. One of the possibilities is that the non-axisymmetry is due to a residual crustal deformation, which can be a consequence of the cooling and resulting in the cracking of the crust [46]. Another mechanism could be based on the presence of a non-axisymmetry distribution of magnetic field energy trapped within the NS crust [47]. Another possible process could be linked to a non-isotropic accretion of external matter by the NS [48].

As before, an estimate of the key parameters of a GW can be obtained [16]. In particular, the emission frequency is given by:

$$\nu_{GW} = 2\nu_{rot} \tag{1.40}$$

While the strain amplitude is:

$$h_0 = 1.1 \times 10^{-24} \left(\frac{I_{zz}}{I_0}\right) \left(\frac{\nu_{GW}}{1\ \mathrm{kHz}}\right)^2 \left(\frac{1\ \mathrm{kpc}}{r}\right) \left(\frac{\epsilon}{10^{-6}}\right) \tag{1.41}$$

where I_{zz} is the z-component of the quadrupole moment, $I_0 = 10^{38}\,\mathrm{kg\ m^2}$ is a nominal quadrupole moment of a neutron star and $\epsilon = \frac{I_{xx} - I_{yy}}{I_{zz}}$ is the ellipticity of the NS, which parametrize the quadrupole of the object.

Such a GW has yet to be detected, but a visual representation of what a continuous GW would look like is shown in Figure 1.3c.

A special case of magnetically asymmetric NSs are pulsars, which, due to their strong magnetic field, are able to produce periodic light flashes. Until now, no GW event from such astrophysical objects has been detected, which could be proof of the fact that NSs are perfectly spherical.

Stochastic

Stochastic GWs are supposed to be formed by the mixing of incoherent events coming from unresolved sources scattered isotropically in the entire Universe [49]. The combination of all these events will probably form a stochastic GW background of astrophysical origin.

In addition to this, a cosmological background of primordial GWs can be created in the first moments after the Big Bang [50]. This primordial background is predicted by

most cosmological models, but its magnitude changes depending on the model chosen and is typically measured as [51]:

$$\Omega_{GW}(\nu) = \frac{1}{\rho_{0,crit}} \frac{d\rho_{GW}(\nu)}{d\ln(\nu)} \tag{1.42}$$

where $\rho_{0,crit} = \frac{3H_0^2c^2}{8\pi G} = 1.9 \cdot 10^{-29} h^2 \,\mathrm{g\,cm^{-3}}$ is the present-day critical energy density, where $h = \mathrm{H_0}/100\,(\mathrm{km/s/Mpc})^{-1}$. It is also important to note that, as the CMB, the primordial GW background would be redshifted by the expansion of the Universe, but, due to the eventually much earlier decoupling time, the effects would much greater.

While on the estimate of the characteristic frequency of primordial GW there is an enormous disagreement, a formulation of the amplitude can be given as [52]:

$$h(\nu) = 5.6 \times 10^{-22} h (\Omega_{GW}(\nu))^{\frac{1}{2}} \left(\frac{100\ \mathrm{Hz}}{\nu}\right)^{\frac{3}{2}} \mathrm{Hz}^{\frac{-1}{2}} \tag{1.43}$$

As for the other GW signal types, an example of what a stochastic GW would look like is provided in Figure 1.3d.

Now that all the GW categories have been described, it is possible to focus on two of the most significant observed events. It is important to note that these and all the other GW events detected until now are CBC GWs.

1.3.2 GW150914

The first detection of a GW came on September 14, 2015 thanks to the two detectors of the LIGO Observatory, located at Hanford and Livingston (USA) [22]. As expected from a CBC event, the signal started to be detected at $\nu_{GW} \approx 30\,\mathrm{Hz}$, followed by eight inspiral phase cycles, which were characterized by a steady increase in frequency and amplitude. The GW signal reached its maximum amplitude at $\nu_{GW} \approx 144\,\mathrm{Hz}$ at which the merger took place (followed by the ringdown phase).

After a complete statistical analysis it was possible to infer that this event, only afterwards classified as GW150914, was produced by two BHs with initial masses of $\sim 36\,\mathrm{M_\odot}$ and $\sim 29\,\mathrm{M_\odot}$ which merged into a $62\,\mathrm{M_\odot}$ BH at a luminosity distance of $d_L \sim 440\,\mathrm{Mpc}$ (corresponding to a redshift $z \approx 0.09$, assuming the cosmology from [4]).

The properties obtained from the analysis of this event give us the opportunity to study in further detail the features of compact binary coalescences, and in particular of BBH systems, of which GW150914 is one of. This is especially important because before the observation of GW150914 no BBH system had ever been detected, given that it is not expected to produce an electromagnetic counterpart.

One of the main pieces of information regarding the BH-BH binaries population obtained from GW150914, was the first observation of two BHs with masses of $\sim 30\,\mathrm{M_\odot}$ and the birth of a BH with mass $\gtrsim 60\,\mathrm{M_\odot}$. The novelty of this result is linked to the fact that until that point the only stellar-mass BHs that had been observed had masses mostly in

the range $(5 - 10)\,M_\odot$, with some exceptions but always with masses smaller than $20\,M_\odot$. In particular, due to the need of observing an electromagnetic emission, these observations were all of X-ray binaries. Therefore, it is clear how the detection of GW150914 greatly widened the mass range of stellar-mass BHs.

The observation of GW150914 provided proof that binary BH systems form and can merge within the time scale of the Universe at a detectable rate. The observation of such an event was not obvious, because a BH-BH could also not form at all, due to some processes that could effectively suppress the two main formation mechanisms:

1. The BBH is formed by the evolution of an isolated binary system. In this case, the suppression mechanism is linked to the interaction between a first BH and a companion star, which undergoes massive expansion during its post main-sequence phases. In particular, due to the extended envelope of the star, the binary system enters a phase of common-envelope evolution, in which the BH moves through the envelope of its companion. This motion within the envelope produces some friction, which will bring to the merger of the two objects before the formation of the second BH, and therefore blocking the possibility of the formation of a BBH system.

2. The BBH is formed thanks to dynamical interaction between pre-existing isolated BHs in a dense star cluster. In this case, the main suppression mechanism is due to the dynamical ejection of central objects as a result of three-body interactions.

1.3.3 GW170817

Another fundamental GW observation was made by the LIGO and Virgo interferometers on August 17, 2017 [26], when a NS-NS merger was detected for the first time. In addition to this a short γ-ray burst (GRB) was observed independently by Fermi-GBM and was later associated to the same merger event. The signal entered the detectors at a frequency of $\nu_{GW} \approx 30\,\mathrm{Hz}$, and in $\approx 100\,\mathrm{s}$ it reached its maximum amplitude at $\nu_{GW} \approx 400\,\mathrm{Hz}$.

After a complete statistical analysis, it was possible to infer the astrophysical properties of the compact objects which were responsible for the emission. In particular, it resulted that: the masses of the two objects composing the binary system were $m_1 \approx 1.48\,M_\odot$ and $m_2 \approx 1.27\,M_\odot$, respectively; while the luminosity distance was of $d_L \approx 40\,\mathrm{Mpc}$, corresponding to a redshift $z \approx 0.008$.

The obtained masses, which are much smaller than the ones of GW150914, were the first proof of the fact that this event was involving two NS and not a NS-BH binary system nor a BH-BH merger. Furthermore, the detection of this electromagnetic counterpart was additional proof of the fact that GW170817 was a binary neutron stars (BNSs) merger.

Electromagnetic Counterpart

The detection of GW170817 was made by all three interferometers (both aLIGO detectors and adVirgo), which enabled the localization of the event within a region of

$\approx 28\,\mathrm{deg}^2$. Soon after this observation, the Fermi-GBM telescope detected a short γ-ray burst (GRB170817A) coming from the same region identified for GW170817. The discrepancy between the GW detection and the GRB observation was obtained to be [43]:

$$\Delta t = 1.734 \pm 0.054\mathrm{s} \tag{1.44}$$

which is in accordance with the theoretical time difference expected for such events. In fact, the most accredited theory believe that GRBs are produced by internal processes, such as shocks or magnetic reconnection, in an ultra-relativistic and highly collimated jet [43], which just follow from the merger of the compact objects.

Moreover, the Fermi-GBM observation, combined with other optical/IR observations, identified the GRB 170917A at a location on the sky with right ascension $\alpha(\mathrm{J2000}) = 13^h09^m48^s.085 \pm 0.018$ and declination $\delta(\mathrm{J2000}) = -23°22'53''.343 \pm 0.218$ from the centre of the galaxy NGC 4993. Thanks to the observation by MUSE/VLT it was possible to measure the redshift of the galaxy: $z = 0.009783$, corresponding to a luminosity distance $d_L = 40.4 \pm 3.4\,\mathrm{Mpc}$ [53], which is consistent with the GW estimate, therefore confirming that GW170817 occurred in NGC 4993.

So, the detection of a short GRB spatially and temporally associated with GW170817 gave us the first proof that GRBs can be produced during a BNSs merger event.

Furthermore, thanks to the independent measurement of the redshift it was possible to infer cosmological parameters without the assumption of the cosmic distance ladder. In particular, the Hubble constant was inferred to be $\mathrm{H}_0 = 70^{+12}_{-8}\,\mathrm{km/s/Mpc}$ [54].

The precise localization of the event allowed to do some follow-up observations in the entire electromagnetic spectrum with several different telescopes:

- Radio (VLA, ATCA, GMRT & ALMA): no detection was made until September 2, when two different emissions at two different frequencies (e.g. [55, 56]).
- IR-Optical-UV: observations were possible just after the GW event and the obtained spectrum was characterized by a peak of emission that with time shifted from the UV band toward the IR, and by the presence of some features of r-processes. These two elements are consistent with the kilonova scenario (e.g. [57]).
- X-ray (*Swift*, NuSTAR, *XMM-Newton* & *Chandra*): no counterpart emission was observed until 9 days after the GW detection (e.g. [58, 59]).
- γ-ray: no further bursts have been detected, thus excluding all persistent emission models (e.g. [60]).

1.4 Astrophysical Framework

As described in Section 1.2 the additional knowledge of the astrophysical population of the GW sources can enable the usage of GW as cosmological probes. Before introducing the involved astrophysical parameters, it is worth describing the different formation channels for BHs in general and the subsequent generation of compact binary systems.

1.4.1 Black Holes Formation

It is commonly known that BHs form as remnants of stars with a total mass of $\gtrsim 25\,M_\odot$, but given that the main processes which ultimately yield their formation (e.g., stellar winds and SNe) are not fully understood, this topic is still a matter of discussion. For example, one of the main processes that a star undergoes during most of its life is the emission of stellar winds, i.e. gas outflows from the atmosphere of the star, which lead to mass loss. Determining how relevant this process is in the evolution of a star is crucial since its total and core masses directly impact the following evolution of the SNe [61, 62].

A first step in the formation of a BH is a core-collapse (CC) SN of a star. The process is schematically summarized in the following steps, as presented in [63, 64]:

1. as the star approaches the end of its life, it develops an inactive Fe-Ni core surrounded by several stratified shells where the nuclear fusion of different elements is taking place. The innermost shell is made of Si that burns into Fe, which is then deposited onto the core. Once the combustion of the entire Si is concluded, the star has ended its nuclear fusion fuel and therefore, as the gravitational force has lost its antagonist, the core begins to contract.

2. As the contraction goes on, the density of the core and the degeneracy of the electrons within the core continue to increase, until the URCA process[3] [65, 66] becomes relevant, which causes an even more rapid core contraction.

3. The collapse continues until the critical density of $\rho_c = 2.4 \cdot 10^{14}\,\mathrm{g/cm^3}$ is reached, at which the repulsive strong nuclear force comes into play: the collapsing core bounce off against the innermost and most dense part of the core and begins to propagate outwards; by doing so it collides with the infalling outer layers of the star, thus producing a shock wave that, if the SNe is successful, moves outwards.

4. As the shock is rapidly damped, it is crucial that the shock front expansion, in order to have a successful SNe, is sustained by the flux of neutrinos, which, after the collapse, are finally allowed to escape the dense core and therefore able to push the shock outward, until the stellar matter is ejected into the Inter-Stellar Medium (ISM).

Two possible paths are possible depending on the success of the CC-SN:

- if the explosion succeeds, the star is probably turned into a NS or a light BH as part of the ejected matter falls back onto the core. This typically happens for stars with mass $11\,M_\odot \lesssim M_\star \lesssim 40\,M_\odot$;

[3] The URCA process is a self-sustained process based on two different physical mechanisms: (1) the photo-disintegration ($Fe^{56} + \gamma \rightarrow 13He^4 + 4n$ and $He^4 + \gamma \rightarrow 2p^+ + 2n$); and (2) the electron capture ($p^+ + e^- \rightarrow n + \nu$). The general effect in stars is of lowering the electron density while increasing the neutrino density, which again lowers the degeneracy of the electrons in the core of the star and prevents heating, as the neutrinos "steal" energy from the system. Both the high degeneracy and the high temperature oppose the collapse of the star, thus reducing them leads to an enhancement of the contraction.

- if the explosion fails, the star becomes a "massive" stellar BH ($M_\bullet \gtrsim 20\,M_\odot$) [63], due to the fact that most of its mass directly collapses into a BH. The direct BH creation happens for stars with $M_\star \gtrsim 40\,M_\odot$.

However, the mechanisms governing the SNe and all their dependencies from the physical quantities of stars (e.g.: mass, metallicity, spin) are highly uncertain, which makes it impossible to construct a complete model for the description of BH formation.

Pair Instability and Remnant Mass

Stars with a core with $M_c \gtrsim 30\,M_\odot$ can reach at the end of their carbon burning cycle temperatures of up to $T \gtrsim 7 \cdot 10^8$ K at which the electron-positron pair production process[4] becomes relevant. This process is able to effectively reduce the photon pressure within stars, which leads to a sudden contraction of the carbon-oxygen core, before the formation of an iron core [67, 68, 69, 70]. Again, depending on the mass of the helium core the fate of the star is different:

- if $M_c \gtrsim 135\,M_\odot$ the collapse cannot be stopped and the star becomes directly a BH;
- if $64\,M_\odot \lesssim M_c \lesssim 135\,M_\odot$ the collapse triggers an explosive combustion of heavier elements, which causes the complete destruction of the star, thus leaving no remnant. This process is referred to as Pair Instability SN (PISN);
- if $32\,M_\odot \lesssim M_c \lesssim 64\,M_\odot$ the mass is too little to trigger a complete explosion of the star, however, the pair instability induces a series of pulsation of the core, which causes an increase in the mass loss of the star until an equilibrium state is found. After that, the star continues its "normal" evolution until it explodes into a SN and leaves a remnant behind, which is however less massive than expected if the pulsation mass losses have not occurred.

The main consequence of the pair instability is to create a gap in the BH mass distribution in the mass range of $\sim 80\,M_\odot - 120\,M_\odot$ [71, 72], as shown in Figure 1.5.

Given the big uncertainties in the comprehension of the processes linked to the creation of BHs, it is evident how determining the mass of compact remnants is a critical task. One example of this can be observed in Figure 1.5, where the impact of metallicity on the final mass is displayed as a function of the Zero Age Main Sequence (ZAMS) mass of stars.

1.4.2 Binary Systems

One of the main channels through which BBH systems form is the isolated binary formation scenario: merging BHs form from the evolution of stellar binary systems which are not perturbed by other stars or compact objects, the so-called isolated binaries.

A schematic representation of the evolution of an isolated binary star into a BBH merger is given in Figure 1.6 and its main steps are briefly summarized as follows [63, 73]:

[4] $(Z+)\,\gamma \rightarrow e^- + e^+$.

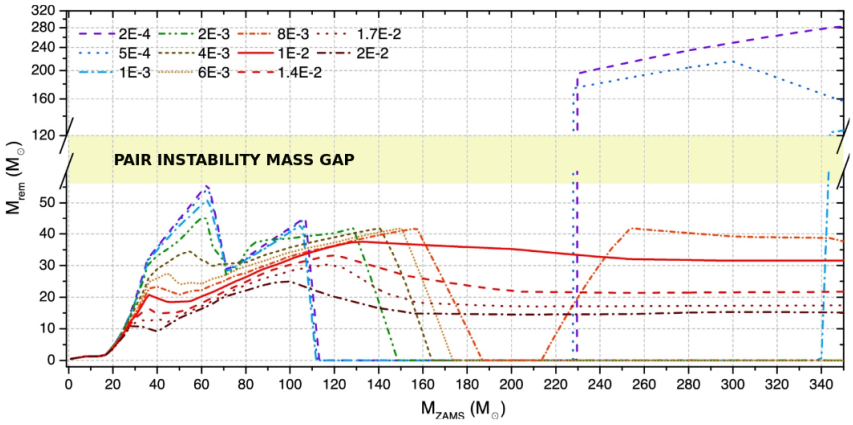

Figure 1.5: Mass of the compact remnants (m_{res}) as a function of the ZAMS mass of the star (m_{ZAMS}), where pulsation pair-instability and pair-instability SNe are taken into account. The dashed/dotted lines represent the different mass distributions depending on the metallicity of the star. Figure from [63].

1. Two stars, which are gravitationally bound since their formation, begin to evolve along their main sequence (MS).

2. The more massive (primary) star is the first one to leave the MS, and thus it expands into a giant star. If its radius becomes larger or equal to the dimensions of its Roche lobe[5], a stable mass-transfer starts from the primary to the secondary (less massive) star.

3. Once the entire mass exceeding the Roche lobe is transferred to the companion or lost by the primary star, it continues its evolution "normally" until collapsing, if possible, into a BH.

4. Once the secondary star reaches the end of its MS, it also expands into a giant star, which makes the system enter a common envelope phase, i.e.: two objects are embedded in the same non-corotating envelope and start spiralling in as an effect of gas drag produced by the envelope. Part of the orbital energy is lost into heating due to the drag of the envelope, thus resulting in a less gravitationally bound system. Depending on the magnitude of this effect, the binary system has two different possible fates:

   a) if the envelope is not ejected by the system, the BH merges with the core of the secondary star leaving a single BH;

   b) if the envelope is ejected, a new binary system forms made of a BH and a "naked" star, and a much smaller orbital radius with respect to the initial binary system.

[5]If we describe a binary system in a non-inertial frame of reference that rotates along with the objects, it is possible to define the gravitational equipotential surface, which delimits the radius of influence of each component of the binary system.

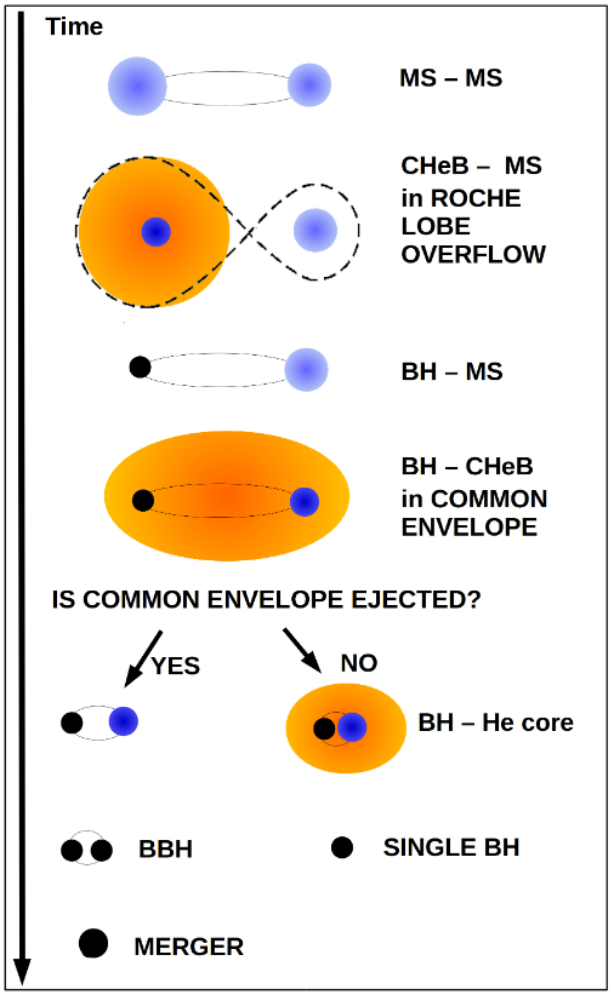

Figure 1.6: Binary Evolution. Figure from [63].

5. Assuming case (b), if the binary system is not disrupted, the secondary star evolves further until evolving into a BH, thus giving birth to a BBH system, which could then eventually merge leading to a GW emission.

As pointed out in Section 1.3.2, another possible channel for BBH formation is thanks to the dynamical interaction between pre-existing isolated BHs in a dense star cluster.

1.4.3 Rate Evolution of Compact Binary Coalescence Systems

One of the most important parameters to be accounted for is the cosmic star formation rate (SFR) density ($\rho_{\rm SFR}$), which describes the average star formation of the Universe per unit comoving volume at a given cosmic time. Since the first result by [74], it is commonly accepted that the SFR density has the form presented in Figure 1.7, with a characteristic maximum at $z \sim 2$.

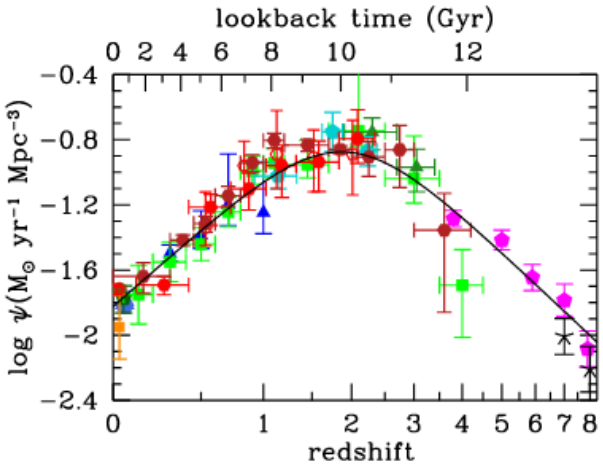

Figure 1.7: Cosmic star formation rate as a function of redshift. Image from [74].

In order to measure the ρ_{SFR}, it is first necessary to infer the luminosity function from galaxy observation, from which it is then possible to obtain the total luminosity density ρ_L, thanks to:

$$\rho_L(z) = \int_0^\infty L\Phi(L,z)dL. \tag{1.45}$$

Once obtained, the SFR density can be inferred thanks to the relation between the SFR and the luminosity density:

$$\rho_{\mathrm{SFR}} = C\rho_L, \tag{1.46}$$

where C is a conversion factor to be determined under a number of assumption [75, 74], which can be inferred from some luminosity indicators that could track the abundance of young type O and type B stars in the galaxy of interest. Typically, the most used indicator is linked to the Hα luminosity, which is emitted by the interaction of the UV light of type O and B stars and the $\mathrm{H_{II}}$ molecular cloud where the stars mainly are formed. It is also possible to define luminosity indicators in other ranges of the electromagnetic spectrum by evaluating the luminosity of a strictly related mechanism, e.g.: in the IR range it is possible to infer an indicator from the luminosity emitted at $\lambda \approx 8-1000\,\mu$m by the dust grains surrounding OB stars, which is heated up to $\mathrm{T} \approx 20$–$60\,\mathrm{K}$ by the absorption of UV radiation; in the X range the indicator can be calculated by observing the emission at $\approx 2-10\,\mathrm{keV}$ due to the matter accretion in X-ray binaries, where the companion star is a young massive star of type OB.

Due to the nature of this parameter, which describes the number of new stars formed at a given time, it greatly influences also the formation rate of compact objects, which has a crucial role in the formation of binary systems, which are necessary for the emission of GW. So, as a result of the close relationship between the star formation rate and the compact binary coalescence rate, it can be assumed that the two rates follow the same evolution over cosmic time [76].

In general, it has been proven [77] that the mass distribution of all binary compact objects, massive enough to produce detectable a GW signal (BNS, BHNS, BBH), depend only mildly on the merger redshift. From LVC data it was possible to obtain some measurements on the rates of the different binary types [78, 79, 80], as displayed in Table 1.1.

CBC Class	Rates ($\mathrm{Gpc^{-3}yr^{-1}}$)
BBH	24–140
BHNS	< 610
BNS	250–2810

Table 1.1: Cosmic merger rates for the different CBC categories obtained by LVC [78, 79, 80].

Nevertheless, it is important to describe the evolution rate of the population of merging compact objects as a function of the redshift, for then evaluating the probability to originate an astrophysical signal for the different categories of binary sources, focusing in particular on CBC sources due to their predisposition on being observed by the modern detectors.

At the current moment, the mass distribution to best described the population of merging objects is the *Power Law + two Gaussian peaks* model [11]. In particular, one of the aims of this work will be to develop the analysis further and to discuss the goodness-of-fit of the model. Additional information regarding all the parameters that influence the mass distributions of compact objects will be presented in Chapter 3, followed, in Section 4, by the evaluation of the different mass functions and their goodness-of-fit.

Chapter 2

Detection and Observation of Gravitational Waves

In order to have a wider understanding of this work a brief description of the detectors used for the observations is given, followed by a summary of the current available observations from the LIGO-Virgo Collaboration (LVC). Finally, the GW dataset studied in this work is described.

2.1 Gravitational Waves Interferometers

In the field of gravitational-wave observations, a network of different interferometers is used for the observation of GW events. In particular, the necessity of multiple detectors is due to the fact that the combination of the observations enables the detection of GW from the noise, the sky localization of the emitting system, and the measurement of the polarization of the GW. The modern GW detectors are modified Michelson interferometers that measure the GW strain by evaluating the magnitude of the difference in the length of its arms. A visual representation of the structure of an interferometer is displayed in Figure 2.1.

Typically, each interferometer is made of two arms, each one delimited by two mirrors set $\sim 4\,\mathrm{km}$ apart. As GWs produce a deformation of space-time due to its crossing, they also perturb the arm lengths of the interferometer, which can be measured and is proportional to the GW strain h, as expressed in equation (2.1).

$$\Delta L(t) = \delta L_{arm_1} - \delta L_{arm_2} = h(t)L \tag{2.1}$$

where $L = L_{arm_1} = L_{arm_2}$. The length change can be measured thanks to the use of a laser source that emits two beams into the interferometer's arms and are then recollected in a photodetector positioned at the end of the two different light paths. The variation of the arm length generates a dis-alignment of the phase of the two beams, which is measured by the photodetector and is proportional to the arm length deformation, hence proportional

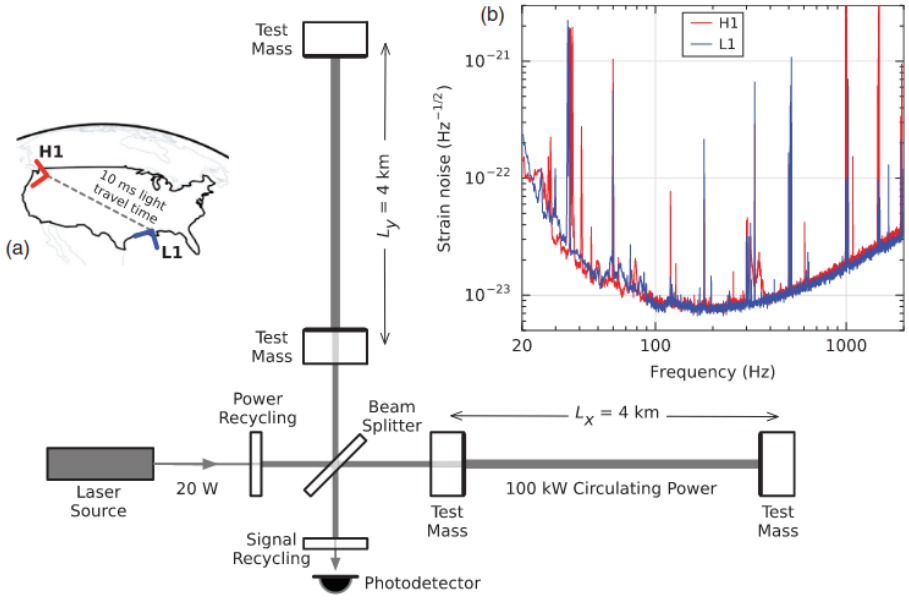

Figure 2.1: Schematic representation of a LIGO detector. (a) Location and orientation of the LIGO detectors at Hanford (H1) and Livingston (L1); (b) the instrumental noise at the two sites at the time of the first detection. Figure is taken from [22].

to the GW strain. An example of the observation of the strain is given in Figure 2.2 (provided by [22]), in which the first ever observed GW signal is shown.

As stated before, GW detectors are *modified* Michelson interferometers. These modifications were needed to hugely improve the sensitivity of each detector, because otherwise the strain would have been covered by the noise, thus not permitting any GW detection. The main adjustments made, which can also be seen in Figure 2.1, are:

1. **Resonant optical cavity** for both arms of the detector, which are formed by its two test mass mirrors and are needed to magnify the light phase distortion due to the GW crossing by a factor of 300 [82];

2. **Input power-recycling mirror** works as an additional resonant cavity [83], allowing a general power increase of the laser from 20 W to 700 W and then up to 100 kW in each arm cavity;

3. **Output power-recycling mirror** widens the bandwidth of the cavities, thus enabling the improvement of the GW signal extraction [84, 85].

Despite the fact that the type of laser used for the phase distortion measurement varies depending on the interferometer studied, all the beams, in order to reduce even more the instrumental noise, are stabilized in amplitude, frequency and geometry [86, 87, 88, 89]. The characteristics of the main GW detectors are reported in Table 2.1.

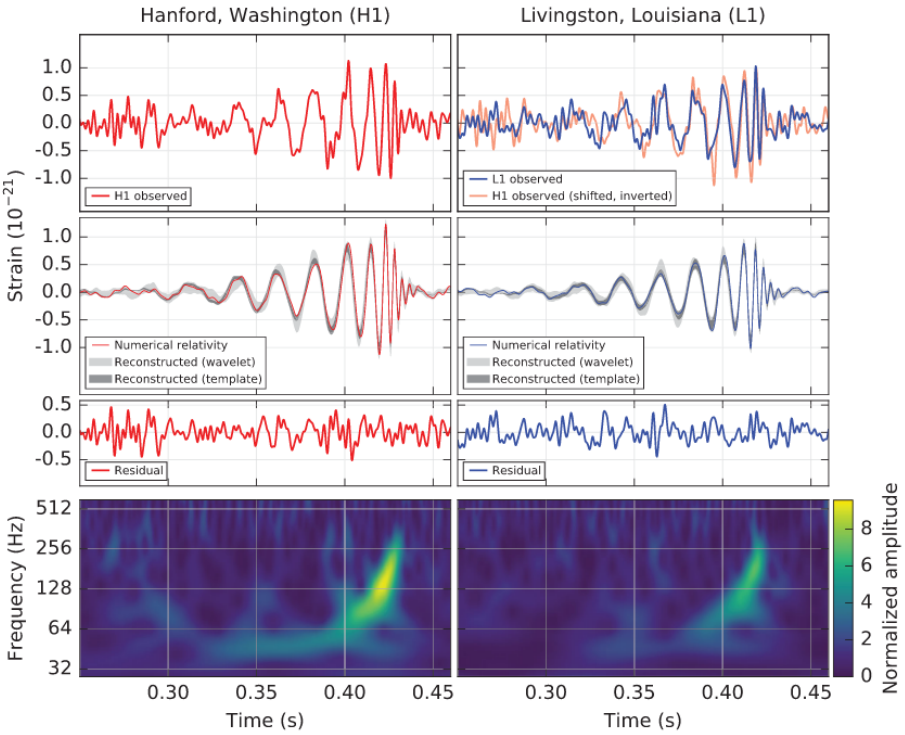

Figure 2.2: The gravitational-wave event GW150914 observed by the LIGO Hanford (H1, left column panels) and Livingston (L1, right column panels) detectors on September 14, 2015, at 09:50:45 UTC. *Top row*: left: H1 strain. Top row, right: L1 strain. *Second row*: Gravitational-wave strain projected onto each detector in the 35–350 Hz band. *Third row*: Residuals after subtracting the filtered numerical relativity waveform from the filtered detector time series. *Bottom row*: A time-frequency representation [81] of the strain data, showing the signal frequency increasing over time.

The entirety of these tweaks is needed to reduce, in the best way instrumentally possible, the noise affecting all detectors. An example of the total noise affecting an interferometer is presented in Figure 2.1(b). The total noise disturbing the detections has different components, which dominate one over another based on the frequency regime [22]:

1. in the *high frequency* regime the photon shot noise, i.e. the Poisson noise that occurs in photon counting, dominates;

2. in the *intermediate frequency regime* the thermal noise, i.e. the noise due to the thermal agitation of components of the detector, dominates;

3. in the *low frequency* regime the displacement noise, i.e. the noise generated by the motion of some components of the detector due to ground activity, dominates;

In particular, the corresponding adjustments are:

1. the signal-to-noise ratio due to photon shot noise is proportional to the square root of the observed counts ($\mathrm{SNR} \propto \sqrt{N}$). Therefore, the optimization of the strain-signal conversion provided by the several power recycling systems is effective in the reduction of the effects of photon shot noise on the detection of GWs signals;

2. the thermal noise is reduced by using low-mechanical-loss materials in the test masses and their suspensions: the mirrors used as test masses depend on the detector: fused silica substrates with low-loss dielectric optical coatings for aLIGO and adVirgo [90, 88] and sapphire for KAGRA [89];

3. thanks to the usage of a pendulum system [91, 88, 89] as suspension for each test mass mirror combined with an active seismic isolation platform [92, 88, 89] the displacement noise is reduced even more.

In order to reduce eventual other noise sources vibration isolation stages are deployed in the entire interferometer, except for the laser source, and kept in an ultra-high vacuum regime with pressure retained at values below $1\,\mu$Pa.

In general, each interferometer, in order to keep track of environmental disturbances and their impact on the detectors, is equipped with an array of sensors: seismometers, accelerometers, microphones, magnetometers, radio receivers, weather sensors, ac-power line monitors, and a cosmic-ray detector [93, 88, 89]. Data collection is synchronized to Global Positioning System (GPS) time, thanks to the use of an atomic clock and a secondary GPS receiver in every detector location.

Lastly, several methods are used to check if the response of the detectors is calibrated, which means achieving an uncertainty of less than 10% in amplitude and 10 degrees in phase. For example, continuous monitoring of the calibration is achieved thanks to laser excitations at selected frequencies. Furthermore, two alternative methods are used to validate the absolute calibration, one referenced to the main laser wavelength and the other to a radio-frequency oscillator [94]. Moreover, the detector response to GWs is tested by injecting simulated waveforms with the calibration laser, a more in-depth analysis is presented in Section 2.3.

It is also important to evaluate the sensitivity of each interferometer. In fact, the sensitivity of a detector network is typically estimated by evaluating the BNS inspiral range, which quantifies the average distance at which a fiducial $1.4\,\mathrm{M}_\odot + 1.4\,\mathrm{M}_\odot$ BNS could be detected with a signal-to-noise ratio (SNR) of 8 [23, 95, 96].

2.1.1 Advanced LIGO, Advanced Virgo & KAGRA

Advanced LIGO [90], Advanced Virgo [88] and KAGRA [97, 98] are laser interferometers, which together form an advanced detector network, that is able to detect, localize, and characterize the coalescence of compact binary mergers, continuous gravitational waves, and burst gravitational waves with frequencies of $\sim$20–2000 Hz. The main characteristics of these two instruments are displayed in Table 2.1.

Parameter	LIGO	Virgo	KAGRA
Arm cavity length	3994.5 m	3000 m	3000 m
Arm cavity finesse	450	440	1530
Laser type and wavelength	Nd:YAG	Nd:YVO4	Nd:YAG
Laser wavelength	1064 nm	1064 nm	1064 nm
Input power, at PRM	up to 125 W	200 W	78 W
Test mass material	Fused silica	Fused silica	Sapphire
Test mass size	34 cm ⌀ x 20 cm	35 cm ⌀ x 20 cm	22∼25 cm ⌀ x 15 cm
Test mass mass	40 kg	42 kg	22.8∼30kg
Beam radius, ITM / ETM	5.3 cm / 6.2 cm	4.87 cm / 5.8 cm	3.5 m / 4.0 m
Radius of curvature, ITM / ETM	1934 m / 2245 m	1420 m / 1683 m	1680 m / 1870 m
Input mode cleaner length & finesse	32.9 m, 500	143.424 m, 1200	53.3 m, 540
Recycling cavity lengths, PRC / SRC	57.6 m / 56.0 m	≈ 12 m	66.591 m / 66.591 m

Table 2.1: Main parameters of the Advanced LIGO, Advanced Virgo and KAGRA interferometers [90, 88, 97, 98, 89]. ITM: input test mass; ETM: end test mass; PRC: power recycling cavity; SRC: signal recycling cavity.

The first observation with these interferometers was possible when the detectors were able to reach and maintain a good enough sensitivity for a long period of time, thus enabling a stable observation of GWs. After observing run 1 (O1) and observing run 2 (O2), which had a lower sensitivity [99], all the detectors underwent an upgrade to reach an even higher level of sensitivity. The advanced "generation" of these interferometers started working at different times: aLIGO in 2015, adVirgo in 2017, and KAGRA in 2019. Thanks to the improvement of the sensitivity of the detector network it was possible to greatly increase the number of GW candidates during the following observing run 3 (O3).

2.2 Observing Phases

An overview of the various observing runs is presented in Table 2.2 and Figure 2.3, in which also the different times at which the interferometer started working are reported. In the following section, the diverse observing runs will be presented with an indication of the detectors that collected the data.

2.2.1 O1: aLIGO

The first observing run O1 lasted from 12 September 2015 to 12 January 2016 [100]. In addition to this period, the data collected during the engineering periods[1] were good enough to be considered valuable data, therefore the actual observing period was from 12

[1]Observing runs aimed to understand how the detector works during a scientific observation. This type of run does not necessarily provide astrophysical results, but it is not excluded.

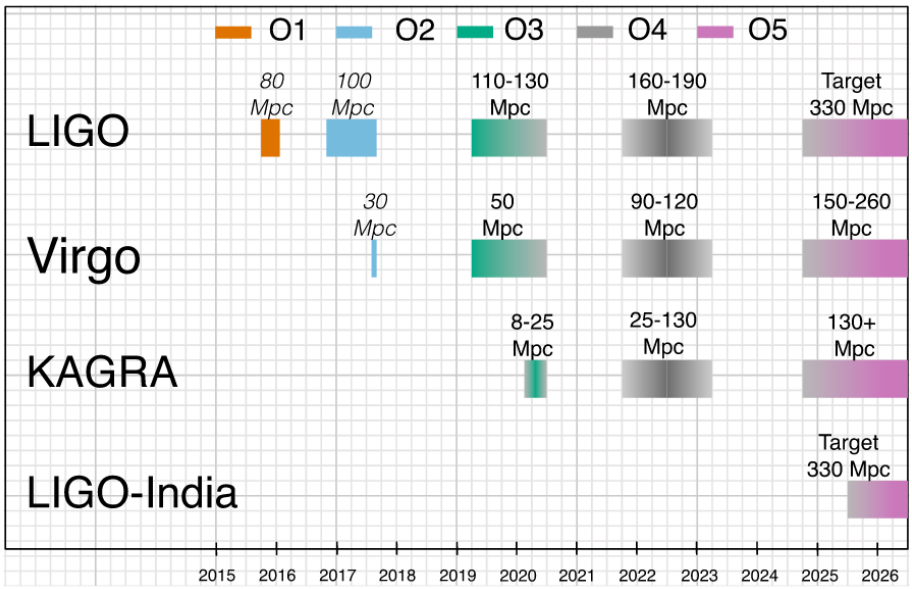

Figure 2.3: The planned observing runs timetable for aLIGO, adVirgo and KAGRA, with the corresponding expected sensibilities. [27]. For a more precise look at the sensibilities, they are presented in Figure 2.4 and Table 2.2.

	O1 [Mpc]	O2 [Mpc]	O3 [Mpc]
aLIGO	80	100	110–130
adVirgo	–	30	50
KAGRA	–	–	8–25

Table 2.2: Achieved sensibilities, expressed in Mpc, of each detector during the different observing runs. Taken from [27].

September 2015 to 19 January 2016. This observing run was made by LIGO alone with a duty factor of $\sim 60\%$, which was able to achieve a sensitivity of 80 Mpc [27].

During the observation it was possible to detect three events:

1. GW150914 [22]: is a BBH merger observed on September 14, 2015, at 09:50:45 UTC with a significance greater than $5\,\sigma$;

2. GW151226 [101]: is a BBH merger observed on December 26, 2015, at 03:38:53 UTC with a significance greater than $5\,\sigma$;

3. LVT151012: is a marginal BBH merger observed on October 12, 2015, at 09:54:43 UTC with a significance of $\lesssim 2\,\sigma$.

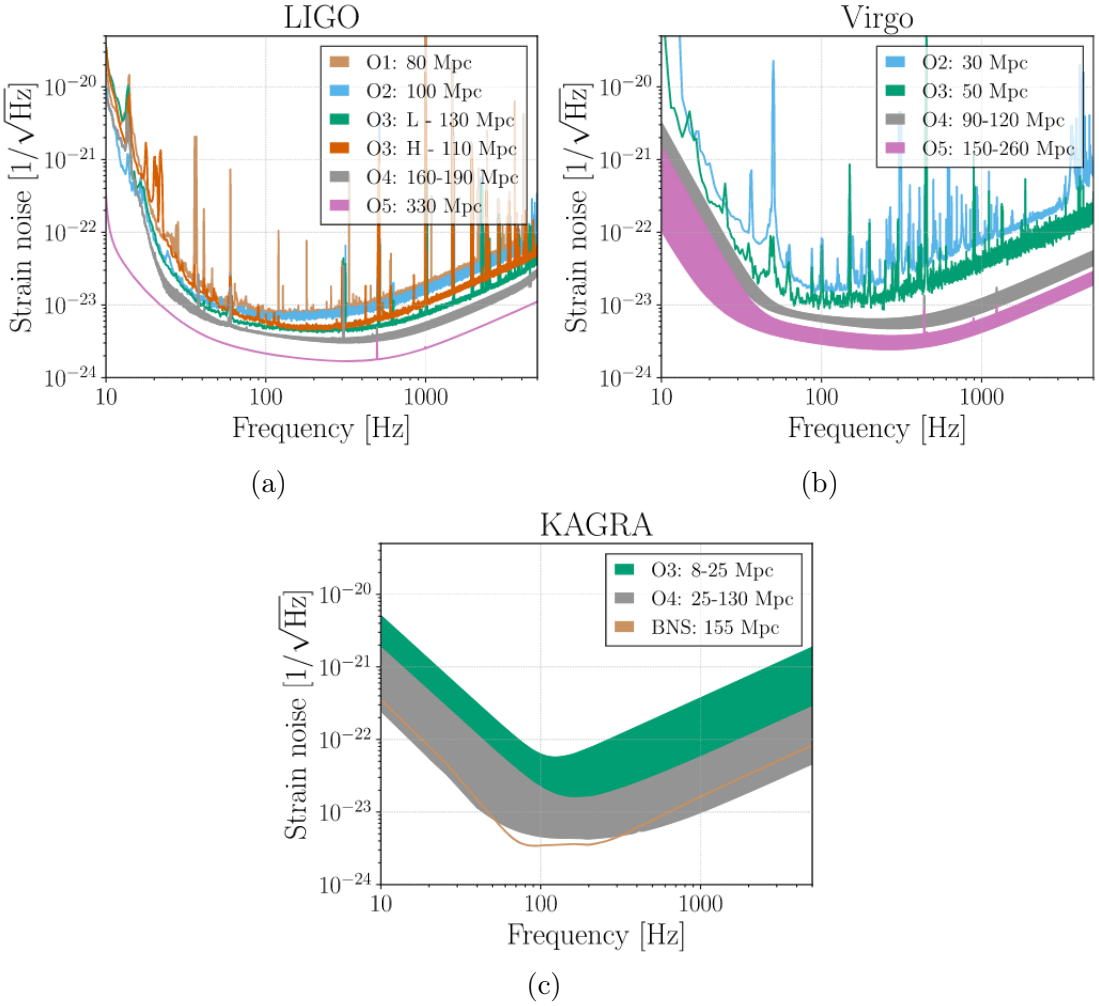

Figure 2.4: aLIGO (top left), AdV (top right) and KAGRA (bottom) target strain sensitivities as a function of frequency. Where bands can be seen, they represent the expected sensitivity ranges with the respective uncertainties, due to future upgrades. Taken from [27].

2.2.2 O2: aLIGO & adVirgo

The second observing run was made by both aLIGO and adVirgo [27]. The aLIGO was observing from 30 November 2016 to 25 August 2017 with a sensitivity ranging between 80 and 100 Mpc [78] and a duty factor of $\gtrsim 62\%$. While, adVirgo started observing on 1 August 2017 until 25 August 2017 with a sensitivity of 30 Mpc. Despite beginning the observations only on the last month, its duty factor was $\sim 85\%$. It resulted that in 34%–42% of the time the three detectors were running simultaneously, and in 78%–84% of the time at least two of the interferometers were working at the same time.

During the observation, eight new GW events were detected, among which, the one also observed by adVirgo, could be localized in a much better way with respect to the events observed only by aLIGO. Between these events, two GW signals stand out:

1. GW170817 [26]: is the first confirmed detection of a BNS merger;

2. GW170818 [78]: was the best localized BBH detection to that date[2].

2.2.3 O3: aLIGO & adVirgo + KAGRA

The last observing run lasted from 1 April 2019 to 27 March 2020. During this run, the median BNS inspiral range, i.e. the sensitivity [13], for aLIGO Livingston was 133 Mpc, for aLIGO Hanford was 115 Mpc, for adVirgo was 51 Mpc, and 8–25 Mpc for KAGRA [27].

The duty cycles for the three interferometers were: 79% (115.7 days) for LIGO Hanford, 79% (115.5 days) for LIGO Livingston and 76% (111.3 days) for Virgo. Furthermore, for 96.6% of the time (142.0 days) at least one interferometer was observing, while for 85.3% (125.5 days) at least two detectors were observing. While KAGRA joined only for the final part of the run by completing a two-week observation [102] run combined with GEO 600 [103].

In addition to the 3 events from observing run 1 (O1) [22, 100], 11 from the GWTC-1 [78], i.e. corresponding to the second observing run (O2), during the O3 a total of 90 new GW events were observed [13]. In particular, among these 90 signals, 55 are from GWTC-2.1 [104], i.e. released after the first part of O3 (O3a), while the remaining 35 candidates were observed during O3b, which is the second and last part of O3, and released as GWTC-3 [37]. A more complete presentation of these events will be presented in Section 2.5.

2.3 Injections of Gravitational Waves Events

As mentioned previously, it is possible to evaluate the uncertainties of a detector thanks to the use of, the so-called, (hardware) injections, which are a GW signal simulated in order to study the response of the interferometer.

The method used to produce such injections is based on the physical displacement of the test masses of the detectors, which mimics a GW signal. Therefore, the interferometer is able to measure the produced differential displacement of the test masses and produce a response. Despite not being exactly equal to a response generated by a real GW event [105, 106], the difference is well understood, thus it is possible to account for those deviations. So, the comparison of the injected signal with the obtained response gives an additional check of the detectors' calibration.

For each interferometer, there are different methods designed for the hardware injections:

- Electrostatic drive systems [107]: used by aLIGO [108] only until 2015, i.e. the first observing run.

[2]With the release of GWTC-3, it was outdone by GW200203-130117 [37]

- Photon (radiation pressure) calibrator [109, 110]: used by all three interferometers (aLIGO [108], adVirgo [111], KAGRA [89]);
- Newtonian calibrators [112]: used by the adVirgo [111];

Due to the fact that interferometers are sensitive to a variety of GW event types, of which each one has different signal characteristics and properties, at least one injection for each type is needed: BBH/NS mergers [100] have a rapidly changing frequency from low to high as the compact objects inspiral closer together, stochastic GW background [113] is the superposition of several events that give rise to a low-level broadband non-deterministic signal, and spinning NSs [114] have an almost constant frequency which is Doppler shifted by Earth's motion.

2.4 Detection and Selection Methods

Once the data are collected from the interferometers, an analysis is necessary in order to find and extract the GW events. The type of analysis made depends on the kind of objects and events that is searched for. Given the purpose of this work, we will present only the methods relevant for the search of compact binary coalescences (CBCs), which includes BNS, NSBH and BBH systems [100].

The detection pipelines are *workflows* that inspect the available data for signal-like features, thanks to the comparison of a set of waveform templates, that model the expected signal, to the observed data. When a trigger is found in a candidate, it is flagged and the corresponding data set is assigned a detection statistic (p_{astro}) that quantifies the level of similarity between the candidate and the template, i.e. it expresses the level of likelihood of the data being an astrophysical GW signal. This level of similarity is found by comparing the data to the estimated detector noise background[3] in order to determine the probability that detector noise would give rise to one or more equally significant event. Therefore, the larger the probability, the less likely the found event is an astrophysical GW signal.

In particular, this method is based on the evaluation of the matched-filter SNR $\rho(\mathrm{t})$ for each template waveform and each dataset from the detectors as described in [95, 117]:

$$\rho^2(t) \equiv \langle s|h_c\rangle^2(t) + \langle s|h_s\rangle^2(t), \tag{2.2}$$

where $\langle s|h\rangle$ represents the correlation between the signal s and h_c and h_s, which are the normalized[4] orthogonal sine and cosine parts of the template, respectively. The analysis searches for every time that the SNR is found to be a local maximum, and classified these as triggers. To be sure that the found value corresponds to a real GW signal, the analysis makes additional tests to evaluate the agreement between the data and the template. Despite the fact that the type of these tests depends on the method used for the analysis,

[3]Given the difficulty of constructing a valid background distribution based on theoretical assumption only, the noise distribution is estimated from the data [115, 116].

[4]i.e. such that $\langle s|h_{c,s}\rangle^2(t)$ is stationary.

typically the different methods try to select trigger pairs that occur within a 15-ms window and come from the same template. Therefore, a detection statistic for each event is given by the combination of the information obtained from the SNR test, the value of the signal consistency tests, and details of the template.

The significance of a candidate event is given by the comparison of the event with the background, from which it is possible to obtain the rate at which the noise of the detectors is able to produce an event with a detection statistic value equal or higher to the event itself. Such a rate is called the False Alarm Rate (FAR). The estimation of this parameter is extremely difficult, due to different causes:

- the non-gaussianity of the noise makes it impossible to determine the noise properties theoretically, thus it must be calculated empirically;
- the detectors have no method to shield GW in order to measure the noise separately, thus some subtraction method is needed to measure the background.

Therefore, the analysis gives as results two different lists of candidate events: one based on the p_{astro}, and one based on the FAR. If a candidate event has a low FAR, it is identified as a possible GW event and is then investigated further in order to extract the parameter values.

Before moving on to the description of the studied events, an important observation has to be made regarding the connection between the FAR and the SNR of an event. In general, signals are considered to be GW events if they have $\mathrm{SNR} > 12$. This is due to the fact that if also lower SNR events are considered, inevitably the number of signals with higher FAR will be included in the analysis resulting in an incorrect (and biased) outcome [10]. Consequently, the analysis made in this work will make use of $\mathrm{SNR} > 12$ events only. Nevertheless, a complete analysis considering all the events with $\mathrm{SNR} > 8$ is presented in Appendix A.

2.5 Sample Selection

The third Gravitational-wave Transient Catalog (GWTC-3) [13] describes signals detected with Advanced LIGO and Advanced Virgo up to the end of their third observing run. Updating the previous GWTC-2 [118] and GWTC-2.1 [104], it contains candidate gravitational waves from CBCs during the second half of the third observing run (O3b) between 1 November 2019, 15:00 UTC and 27 March 2020, 17:00 UTC.

There were 35 compact binary coalescence candidates, which were identified by at least one of the available search algorithms with a probability of astrophysical origin $p_{astro} > 0.5$, of which, 18 were previously reported as low-latency public alerts, and 17 were reported for the first time. Based upon LVC's estimates for the component masses, the O3b candidates with $p_{astro} > 0.5$ are consistent with gravitational-wave signals from BBH or NSBH, and none from BNS. The range of inferred component masses is similar to that found with previous catalogues, but the O3b candidates include the first confident observations of neutron star–black hole binaries.

Once the signals were observed and confirmed to be GW events, data analysis was made to infer the properties of each source based on the amplitude and form of the corresponding GW event. In particular, under the assumption of Gaussian, stationary and uncorrelated noise, by fitting different model waveform templates to the observed signals it is possible to calculate the posterior probabilities of the various parameters defining a GW emitting binary system [119, 120].

In particular, the GWTC-3 catalogue contains the sample on which the entire analysis of this work is based, and a summary of the properties of all GWTC-3 events with SNR > 12 is given in Table 2.3.

As described in Section 1.3, the events could be produced by different types of sources: BBH, BNS, and BHNS systems, but in this work, only the events produced by BBH will be analysed. This choice is due to two main reasons. First, BNS and NSBH have lower detection rates than BBH and have therefore lower statistics, which does not allow making the same analysis and inferring the properties of the emitting systems. Moreover, since the different types of CBC follow different formation channels, the inferred parameters do not necessarily have the same physical meaning and therefore they cannot be simply combined.

In particular, from Table 2.3 the main properties of the selected events can be evinced:

- **SNR**: the mean value for SNR is 15.38, which could be evidence of the fact that the selected events are without any doubt real GW events. In particular, the maximum value is SNR $= 26.8$ for GW200129_065458.

- **Luminosity distance** d_L: on average the events are at a distance of $d_L = 1445.7\,\mathrm{Mpc}$, with a maximal value of $d_L = 4420\,\mathrm{Mpc}$, corresponding to the event classified as GW90706_222641.

- **Redshift** z: the average redshift is $z = 0.27$, given by assuming the flat ΛCDM cosmological model. The maximum value is found to be $z = 0.71$, again corresponding to the event GW90706_222641.

- **Primary mass** M_1: on average is obtained to be $\mathrm{M}_1 = 34.2\,\mathrm{M}_\odot$, with a maximum value of $\mathrm{M}_1 = 95.3\,\mathrm{M}_\odot$ for event GW190521.

- **Secondary mass** M_2: its average value is $\mathrm{M}_2 = 24.0\,\mathrm{M}_\odot$, with a maximum value of $\mathrm{M}_1 = 69.0\,\mathrm{M}_\odot$ for event GW190521.

- **Chirp mass** $\mathcal{M}_{chirp}$: describes the phase evolution during the inspiral [121, 122] and is given by $\mathcal{M}_{chirp} = \frac{(M_1 M_2)^{3/5}}{(M_1+M_2)^{1/5}}$. Its average value is $\mathcal{M}_{chirp} = 24.5\,\mathrm{M}_\odot$, with a maximal value $\mathcal{M}_{chirp} = 69.2\,\mathrm{M}_\odot$ for event GW190521. These values point to a stellar origin for all the selected BBH events.

- **Effective inspiral spin** χ_{eff}: is the effective inspiral spin given by the combination of the two separated spins of the objects χ_1 and χ_2 [123, 124]. In particular, $\chi_{eff} = \frac{(M_1\chi_1 + M_2\chi_2)\cdot \hat{L_N}}{\mathcal{M}_{chirp}}$, where $\chi_i = \frac{c\vec{S_i}}{GM_i^2}$ and $\vec{S_i}$ is the spin angular momentum, which

Name	SNR	d_L [Mpc]	z	M_{chirp} [$M_\odot$]	M_1 [$M_\odot$]	M_2 [$M_\odot$]	χ_{eff}	FAR
GW150914	24.4	440^{+150}_{-170}	$0.09^{+0.03}_{-0.03}$	$28.60^{+1.70}_{-1.50}$	$35.60^{+4.70}_{-3.10}$	$30.60^{+3.00}_{-4.40}$	$-0.01^{+0.12}_{-0.13}$	10^{-7}
GW151226	13.1	450^{+180}_{-190}	$0.09^{+0.04}_{-0.04}$	$8.90^{+0.30}_{-0.30}$	$13.70^{+8.80}_{-3.20}$	$7.70^{+2.20}_{-2.50}$	$0.18^{+0.20}_{-0.12}$	10^{-7}
GW170104	13.0	990^{+440}_{-430}	$0.20^{+0.08}_{-0.08}$	$21.40^{+2.20}_{-1.80}$	$30.80^{+7.30}_{-5.60}$	$20.00^{+4.90}_{-4.60}$	$-0.04^{+0.17}_{-0.21}$	10^{-7}
GW170608	14.9	320^{+120}_{-110}	$0.07^{+0.02}_{-0.02}$	$7.90^{+0.20}_{-0.20}$	$11.00^{+5.50}_{-1.70}$	$7.60^{+1.40}_{-2.20}$	$0.03^{+0.19}_{-0.07}$	10^{-7}
GW170809	12.4	1030^{+320}_{-390}	$0.20^{+0.05}_{-0.07}$	$24.90^{+2.10}_{-1.70}$	$35.00^{+8.30}_{-5.90}$	$23.80^{+5.10}_{-5.20}$	$0.08^{+0.17}_{-0.17}$	10^{-7}
GW170814	15.9	600^{+150}_{-220}	$0.12^{+0.03}_{-0.04}$	$24.10^{+1.40}_{-1.10}$	$30.60^{+5.60}_{-3.00}$	$25.20^{+2.80}_{-4.00}$	$0.07^{+0.12}_{-0.12}$	10^{-7}
GW190408_181802	14.7	1550^{+400}_{-600}	$0.29^{+0.06}_{-0.10}$	$18.30^{+1.90}_{-1.20}$	$24.60^{+5.10}_{-3.40}$	$18.40^{+3.30}_{-3.60}$	$-0.03^{+0.14}_{-0.19}$	10^{-5}
GW190412	18.9	740^{+140}_{-170}	$0.15^{+0.03}_{-0.03}$	$13.30^{+0.40}_{-0.30}$	$30.10^{+4.70}_{-5.10}$	$8.30^{+1.60}_{-0.90}$	$0.25^{+0.08}_{-0.11}$	10^{-5}
GW190503_185404	12.1	1450^{+690}_{-630}	$0.27^{+0.11}_{-0.11}$	$30.20^{+4.20}_{-4.20}$	$43.30^{+9.20}_{-8.10}$	$28.40^{+7.70}_{-8.00}$	$-0.03^{+0.20}_{-0.26}$	10^{-5}
GW190512_180714	12.3	1430^{+550}_{-550}	$0.27^{+0.09}_{-0.10}$	$14.60^{+1.30}_{-1.00}$	$23.30^{+5.30}_{-5.80}$	$12.60^{+3.60}_{-2.50}$	$0.03^{+0.12}_{-0.13}$	10^{-5}
GW190513_205428	12.3	2060^{+880}_{-800}	$0.37^{+0.13}_{-0.13}$	$21.60^{+3.80}_{-1.90}$	$35.70^{+9.50}_{-9.20}$	$18.00^{+7.70}_{-4.10}$	$0.11^{+0.28}_{-0.17}$	10^{-5}
GW190519_153544	12.1	2530^{+1830}_{-920}	$0.44^{+0.25}_{-0.14}$	$44.50^{+6.40}_{-7.10}$	$66.00^{+10.70}_{-12.00}$	$40.50^{+11.00}_{-11.10}$	$0.31^{+0.20}_{-0.22}$	10^{-5}
GW190521	14.4	3920^{+2190}_{-1950}	$0.64^{+0.28}_{-0.28}$	$69.20^{+17.00}_{-10.60}$	$95.30^{+28.70}_{-18.90}$	$69.00^{+22.70}_{-23.10}$	$0.03^{+0.32}_{-0.39}$	$2.0 \cdot 10^{-4}$
GW190521_074359	24.4	1240^{+400}_{-570}	$0.24^{+0.07}_{-0.10}$	$32.10^{+3.20}_{-2.50}$	$42.20^{+5.90}_{-4.80}$	$32.80^{+5.40}_{-6.40}$	$0.09^{+0.10}_{-0.13}$	10^{-5}
GW190602_175927	12.1	2690^{+1790}_{-1120}	$0.47^{+0.25}_{-0.17}$	$49.10^{+9.10}_{-8.50}$	$69.10^{+15.70}_{-13.00}$	$47.80^{+14.30}_{-17.40}$	$0.07^{+0.25}_{-0.24}$	$1.1 \cdot 10^{-5}$
GW190630_185205	15.6	890^{+560}_{-370}	$0.18^{+0.10}_{-0.07}$	$24.90^{+2.10}_{-2.10}$	$35.10^{+6.90}_{-5.60}$	$23.70^{+5.20}_{-5.10}$	$0.10^{+0.12}_{-0.13}$	10^{-5}
GW190706_222641	12.3	4420^{+2590}_{-1930}	$0.71^{+0.32}_{-0.27}$	$42.70^{+10.00}_{-7.00}$	$67.00^{+14.60}_{-16.20}$	$38.20^{+14.60}_{-13.30}$	$0.28^{+0.26}_{-0.29}$	10^{-5}
GW190707_093326	13.0	770^{+380}_{-370}	$0.16^{+0.07}_{-0.07}$	$8.50^{+0.60}_{-0.50}$	$11.60^{+3.30}_{-1.70}$	$8.40^{+1.40}_{-1.70}$	$-0.05^{+0.10}_{-0.08}$	10^{-5}
GW190708_232457	13.1	880^{+330}_{-390}	$0.18^{+0.06}_{-0.07}$	$13.20^{+0.90}_{-0.60}$	$17.60^{+4.70}_{-2.30}$	$13.20^{+2.00}_{-2.70}$	$0.02^{+0.10}_{-0.08}$	$2.8 \cdot 10^{-5}$
GW190727_060333	12.3	3300^{+1540}_{-1500}	$0.55^{+0.21}_{-0.22}$	$28.60^{+5.30}_{-3.70}$	$38.00^{+9.50}_{-6.20}$	$29.40^{+7.10}_{-8.40}$	$0.11^{+0.26}_{-0.25}$	10^{-5}
GW190728_064510	13.6	870^{+260}_{-370}	$0.18^{+0.05}_{-0.07}$	$8.60^{+0.50}_{-0.30}$	$12.30^{+7.20}_{-2.20}$	$8.10^{+1.70}_{-2.60}$	$0.12^{+0.20}_{-0.07}$	10^{-5}
GW190828_063405	16.0	2130^{+660}_{-930}	$0.38^{+0.10}_{-0.15}$	$25.00^{+3.40}_{-2.10}$	$32.10^{+5.80}_{-4.00}$	$26.20^{+4.60}_{-4.80}$	$0.19^{+0.15}_{-0.16}$	10^{-5}
GW190910_112807	13.4	1460^{+1030}_{-580}	$0.28^{+0.16}_{-0.10}$	$34.30^{+4.10}_{-4.10}$	$43.90^{+7.60}_{-6.10}$	$35.60^{+6.30}_{-7.20}$	$0.02^{+0.18}_{-0.18}$	$1.9 \cdot 10^{-5}$
GW190915_235702	13.1	1620^{+710}_{-610}	$0.30^{+0.11}_{-0.10}$	$25.30^{+3.20}_{-2.70}$	$35.30^{+9.50}_{-6.40}$	$24.40^{+5.60}_{-6.10}$	$0.02^{+0.20}_{-0.25}$	10^{-5}
GW190924_021846	13.2	570^{+220}_{-220}	$0.12^{+0.04}_{-0.04}$	$5.80^{+0.20}_{-0.20}$	$8.90^{+7.00}_{-2.00}$	$5.00^{+1.40}_{-1.90}$	$0.03^{+0.30}_{-0.09}$	10^{-5}
GW191109_010717	$17.3^{+0.5}_{-0.5}$	1290^{+1130}_{-650}	$0.25^{+0.18}_{-0.12}$	$47.50^{+9.60}_{-7.50}$	$65.00^{+11.00}_{-11.00}$	$47.00^{+15.00}_{-13.00}$	$-0.29^{+0.42}_{-0.31}$	$1.8 \cdot 10^{-4}$
GW191129_134029	$13.1^{+0.2}_{-0.3}$	790^{+260}_{-330}	$0.16^{+0.05}_{-0.06}$	$7.31^{+0.43}_{-0.28}$	$10.70^{+4.10}_{-2.10}$	$6.70^{+1.50}_{-1.70}$	$0.06^{+0.16}_{-0.08}$	10^{-5}
GW191204_171526	$17.5^{+0.2}_{-0.2}$	650^{+190}_{-250}	$0.13^{+0.04}_{-0.05}$	$8.55^{+0.38}_{-0.27}$	$11.90^{+3.30}_{-1.80}$	$8.20^{+1.40}_{-1.60}$	$0.16^{+0.08}_{-0.05}$	10^{-5}
GW191216_213338	$18.6^{+0.2}_{-0.2}$	340^{+120}_{-130}	$0.07^{+0.02}_{-0.03}$	$8.33^{+0.22}_{-0.19}$	$12.10^{+4.60}_{-2.30}$	$7.70^{+1.60}_{-1.90}$	$0.11^{+0.13}_{-0.06}$	10^{-5}
GW191222_033537	$12.5^{+0.2}_{-0.3}$	3000^{+1700}_{-1700}	$0.51^{+0.23}_{-0.26}$	$33.80^{+7.10}_{-5.00}$	$45.10^{+10.90}_{-8.00}$	$34.70^{+9.30}_{-10.50}$	$-0.04^{+0.20}_{-0.25}$	10^{-5}
GW200112_155838	$19.8^{+0.1}_{-0.2}$	1250^{+430}_{-460}	$0.24^{+0.07}_{-0.08}$	$27.40^{+2.60}_{-2.10}$	$35.60^{+6.70}_{-4.50}$	$28.30^{+4.40}_{-5.90}$	$0.06^{+0.15}_{-0.15}$	10^{-5}
GW200129_065458	$26.8^{+0.2}_{-0.2}$	900^{+290}_{-380}	$0.18^{+0.05}_{-0.07}$	$27.20^{+2.10}_{-2.30}$	$34.50^{+9.90}_{-3.20}$	$28.90^{+3.40}_{-9.30}$	$0.11^{+0.11}_{-0.16}$	10^{-5}
GW200224_222234	$20.0^{+0.2}_{-0.2}$	1710^{+490}_{-640}	$0.32^{+0.08}_{-0.11}$	$31.10^{+3.20}_{-2.60}$	$40.00^{+6.90}_{-4.50}$	$32.50^{+5.00}_{-7.20}$	$0.10^{+0.15}_{-0.15}$	10^{-5}
GW200225_060421	$12.5^{+0.3}_{-0.4}$	1150^{+510}_{-530}	$0.22^{+0.09}_{-0.10}$	$14.20^{+1.50}_{-1.40}$	$19.30^{+5.00}_{-3.00}$	$14.00^{+2.80}_{-3.50}$	$-0.12^{+0.17}_{-0.28}$	$1.1 \cdot 10^{-5}$
GW200311_115853	$17.8^{+0.2}_{-0.2}$	1170^{+280}_{-400}	$0.23^{+0.05}_{-0.07}$	$26.60^{+2.40}_{-2.00}$	$34.20^{+6.40}_{-3.80}$	$27.70^{+4.10}_{-5.90}$	$-0.02^{+0.16}_{-0.20}$	10^{-5}

Table 2.3: BBH events from the GWTC-3 catalog [13] with SNR > 12 and the associated median value of the different parameters with the 90% symmetric credible intervals. The redshift is calculated from d_L under the assumption of a Flat ΛCDM cosmology given in [4]. The events are listed at `https://www.gw-openscience.org/eventapi/html/GWTC/`.

can theoretically range in magnitude from 0 (non-spinning) to 1 (Kerr limit) for BHs, and $\hat{L_N}$ is the unit vector in the direction of the Newtonian orbital angular momentum. On average $\chi_{eff} = 0.06$, which could be an indication of the low spinning rate of the binary systems. Its maximum value is $\chi_{eff} = 0.31$, corresponding to the event GW190519_153544.

- **FAR**: the average FAR value is $1.95 \cdot 10^{-5}$, thus proving the fact that the selected events are real GW signals. The maximum value is found to be $\mathrm{FAR} = 2.0 \cdot 10^{-4}$ for event GW190521.

Chapter 3

Statistical Analysis

In this chapter the approach followed for the data analysis will be described. In particular, after a first short description of the hierarchical Bayesian formalism, the code used and its extension will be presented, supported by some validation runs on the LVK data.

3.1 Hierarchical Bayesian Framework

In this section, the hierarchical Bayesian framework necessary for inferring astrophysical and cosmological quantities from multiple GW signals will be presented. It finds a particularly useful application in the field of GW astronomy. As pointed out in Section 1.2, to infer some information regarding the models governing the physics of compact objects it is necessary to process the data through the use of hierarchical Bayesian inference [125, 126, 127, 128].

In order to completely understand how hierarchical Bayesian inference works, we first state the main problem [126]: we have a population of events, each described by a set of parameters θ that represent the characteristics of individual events, i.e. the parameters appearing in equation (1.32) and equation (1.33): masses ($\mathcal{M}_z$), spins, inclination angle (ι) and distances of the sources (d_L), etc.; so the distribution of the events in the population, i.e. the number of sources depending on the parameters Λ, is such that:

$$\frac{dN}{d\theta}(\Lambda) = N p_{pop}(\theta|\Lambda), \tag{3.1}$$

where Λ contains the properties of the population which could be for example the slope of the mass function, or the shape of the spin distribution, and $p_{pop}(\theta|\Lambda)$ is the distribution of the properties of the individual event called population function and it is usually modelled analytically, as presented in Section 3.4. For each event in the population, we make a noisy measurement of θ_i, represented by a likelihood function, which links the measured data (d_i) with the parameters of the event θ: $\mathcal{L}(d_i|\theta_i)$ [126]. From the observed data ($\mathcal{L}(d_i|\theta_i)$) we want to reconstruct the general properties of the population (Λ) thanks to the use of Bayesian inference, which means inferring the posterior probability density for the different parameters given the observed data.

The unknown parameters Λ, which are the ones that define the model of the population, can actually be divided into two different categories:

1) Λ_{cosmo} are the cosmological parameters, for example: H_0 and $\Omega_{0,M}$;

2) Λ_{astro} are the parameters that define the astrophysical population of emitting GW, i.e. defines the properties of the BBH population, for example, the primary m_1 and the secondary m_2 masses of the binary system;

thus: $\Lambda = \{\Lambda_{cosmo}, \Lambda_{astro}\}$. The definition of both classes is crucial in order to make a correct inference since both categories have a great impact on the model that is obtained.

It can be obtained from [125, 126] that the likelihood observing all the $\mathcal{D} = \{d_i\}$ GW events given the Λ parameters is:

$$\mathcal{L}(\mathcal{D}|\Lambda) \propto e^{-N_{exp}(\Lambda)} \prod_{i=1}^{N_{obs}} \int d\theta_i \mathcal{L}(d_i|\theta_i) \frac{dN}{d\theta_i}(\Lambda). \tag{3.2}$$

Therefore, the parameters Λ can be estimated by jointly inferring the likelihood thanks to the use of a MCMC code.

In equation (3.2) three components can be identified. The first component on which to focus is $\frac{dN}{d\theta_i}(\Lambda)$, i.e. the part that describes the number of events as a function of the parameters. Thanks to equation (3.1) it is clear that this building block describes the population of the events. It is also evident that the modelling of the population function is a key part in the description of GW events [36], because, as described in equation (3.2), the entire Bayesian analysis is based on it. The distribution is given as a function of redshift and source masses [37]:

$$\begin{aligned} \frac{dN}{d\theta_i}(\Lambda) &= \frac{dN}{dm_{1,i} dm_{2,i} d(d_{L,i})}(\Lambda_{astro}, \Lambda_{cosmo}) = \\ &= \frac{1}{(1+z)^2 \frac{d(d_{L,i})}{dz_i}(\Lambda_{cosmo})} \cdot \frac{dN}{dm_{1,i} dm_{2,i} dz_i}(\Lambda_{astro}), \end{aligned} \tag{3.3}$$

where two different parts can be identified: $\frac{1}{(1+z)^2 \frac{d(d_{L,i})}{dz_i}(\Lambda_{cosmo})}$ is the part which describes the dependency of the population model on cosmological parameters; while $\frac{dN}{dm_{1,i} dm_{2,i} dz_i}(\Lambda_{astro})$ represent the mass-redshift distribution of the BBH population and is given by [79]:

$$\frac{dN}{dm_{1,i} dm_{2,i} dz_i}(\Lambda_{astro}) = \left[\frac{dV_c}{dz}(z_i)\right] \frac{T_{obs}}{1+z_i} R(z_i|\Lambda_z) p(m_{1,i}, p_{2,i}|\Lambda_m), \tag{3.4}$$

where T_{obs} is the total observation time, $\frac{dV_c}{dz}$ is the differential comoving volume per unit redshift [129], and Λ_{astro} is assumed to be $\Lambda_{astro} = \{\Lambda_z, \Lambda_m\}$, in which Λ_z and Λ_m are the parameters defining the merger rate density distribution $R(z_i|\Lambda_z)$ and the BBH mass distribution $p(m_{1,i}, m_{2,i}|\Lambda_m)$, respectively. It is worth noting that the spin distribution has

been completely neglected, and will not be considered in the following analysis. All the other terms will be presented in more detail in Section 3.4.

It is therefore clear the fundamental role that $p(m_1, m_2|\Lambda_m)$ plays in the definition of the entire population function of the BBH merger. So, defining it in the best phenomenological way, to reproduce the true BBH mass distribution is crucial: $\mathcal{L}(\mathcal{D}|\Lambda)$ depends on it through the population function $\frac{dN}{dm_{1,i}dm_{2,i}dz_i}$.

Furthermore, by looking at equation (3.3) it is evident how to correctly evaluate the BBH population distribution it is necessary to perform a global fit inferring both the astrophysical properties and cosmological properties together, as they are the two components of the distribution.

A physically informed model of the source–frame mass distribution is precisely the additional piece of information that can be used to break the degeneracy between mass and redshift in the GW waveform, and is given by:

$$m_{z,i} = (1 + z)m_i. \tag{3.5}$$

This can be done by obtaining some independent information on a mass scale encoded within the BH mass distribution, which would allow to determine z and reconstruct m_i [36]. In the case of BBH, the main mass scale feature is the drop in the merger rate for masses larger than $\sim 45\,\mathrm{M}_\odot$ [130, 78]. Such a feature may be explained thanks to the pair-instability supernova (PISN) mechanism [67]. This process happens in cores of massive stars ($\sim$30–133 $\mathrm{M}_\odot$) [70] when the core temperature reaches a critical temperature at which the production of electron-positron pairs from photons becomes relevant, resulting in a reduction of the radiation pressure of the core, which leads to a collapse of the star, eventually stopped by the nuclear burning [131]. Therefore, the ending scenario can be two: the unleashed energy destroys the star from within, leaving no remnant at all, or trigger a mass-loss pulsation process until the temperature is not high enough to sustain the PISN mechanism, thus leaving a $\lesssim 45\,\mathrm{M}_\odot$ remnant. The presence of such a feature can be used to break the degeneracy between source frame masses and redshifts, thanks to the fact that the feature can be used as a "cosmological indicator", i.e. the source must have a redshift z such that the measured (detector-frame) mass to be "converted" in a source-frame mass compatible with the theoretical BBH mass distribution. By doing so, it thereby provides independent statistical information on the redshift, which is again needed to infer the value of the Hubble constant in from the measurement of the luminosity distance:

$$d_L = \frac{c(1 + z)}{H_0} \int_0^z \frac{dz'}{E(z')}, \tag{3.6}$$

where $E(z) = \frac{H(z)}{H_0} = \sqrt{\Omega_{0,\mathrm{m}}(1 + z)^3 + \Omega_{0,\mathrm{K}}(1 + z)^2 + \Omega_{0,\Lambda}}$ contains all the cosmological information about the chosen universe model.

Moving on to the other components of equation (3.2):

- $e^{-N_{exp}(\Lambda)}$, where N_{exp} is the number of expected detection. This term works as factor correcting for the selection bias, which makes sure that the integral of $\mathcal{L}(d_i|\theta_i)$ over all

available data is normalized. A more complete description of this term is presented in Section 3.2.1.

- $\mathcal{L}(d_i|\theta_i)$ is the likelihood of the single event and it is typically provided by the LIGO-Virgo-KAGRA Collaboration in its data releases. In the context of this work, the single event likelihoods are taken from the GWTC-3 catalogue.

  A broader discussion regarding the Bayesian framework is given in Section 3.2.

3.2 Likelihood, Priors, and Posteriors

Our main aim is to determine the population properties Λ given a set of observations obtained from the GW detectors. Therefore, we try to construct, thanks to the Bayes theorem, a posterior distribution on Λ as:

$$p(\Lambda|\mathcal{D}) = \frac{\mathcal{L}(\mathcal{D}|\Lambda)\pi(\Lambda)}{\mathcal{E}}, \tag{3.7}$$

where $\mathcal{D} = \{d_i\}$ is a set of N_{obs} observations of binary coalescences from the GW detectors, $\mathcal{L}(\{D_{GW}\}|\Lambda)$ is the likelihood of the data given the parameters, $\pi(\Lambda)$ is the prior distribution for the parameters, and $\mathcal{E}$ is the evidence and works as a normalization factor, so:

$$\mathcal{E} := \int d\Lambda \mathcal{L}(\mathcal{D}|\Lambda)\pi(\Lambda). \tag{3.8}$$

The evidence, in addition to normalization, can be also used as a model selector, i.e. finding the statistical best-fit model given the available data [132]. In particular, the ratio of the evidence for two different models is called the Bayes factor and is often reported in its logarithmic form:

$$\ln \mathrm{BF} = \ln(\mathcal{M}_0) - \ln(\mathcal{M}_1), \tag{3.9}$$

thus, large absolute values of lnBF indicate that one model is disfavored over the other, where the threshold is set to be at $|\ln \mathrm{BF}| = 8$ to determine if the evidence is strong enough in favour of one hypothesis over another.

The prior is a chosen function, which contains all the previous knowledge about the set of parameters before the execution of the measurement itself. In some cases, the choice is obvious and dictated by the starting assumption of an experiment, while in some other cases the available knowledge is too little to construct a valid prior for constraining the parameters, in such situations a uniform or log-uniform distribution is chosen as a prior.

The total likelihood is a description of the measurement and can be recognized as the one defined in equation (3.2).

Thus, once all terms are calculated the posterior can be inferred thanks to equation (3.7).

One interesting feature of posterior distributions is the ability to marginalize, i.e. integrate, over a given parameter that we are interested in to obtain the so-called marginalized posterior, which incorporates the best guess for a parameter given the uncertainty in the

variables over which we are marginalizing. Therefore, it gives the possibility to study the covariance between the different parameters defining a given model.

3.2.1 Selection Effects

Selection effects arise from the fact that some events are easier to detect than others depending on some of their physical properties. In fact, GW events result easier to detect if they are closer, have higher mass, and with a face–on/off inclination angles. Hence, it is a crucial task to understand if a given event is detectable or not, based on its intrinsic properties Λ. For this reason, it was necessary to calculate the probability that an event is detectable, thus calculating the last missing piece of equation (3.2): N_{exp}.

We assume that a GW event has been detected with a Signal-to-Noise Ratio (SNR) above some fixed threshold r_{thr}, in particular, $\mathrm{r}_{thr} = 12$ for the detector network. Then the number of the expected events can be written as [125, 126]:

$$N_{exp}(\Lambda) = \int_{f(\mathcal{D})>r_{thr}} d\mathcal{D}d\theta\mathcal{L}(\mathcal{D}|\theta)\frac{dN}{d\theta}(\Lambda), \tag{3.10}$$

where we can define the $p_{det}(\theta)$ as the probability of a signal being detected, i.e. exceeding the detection threshold, and is typically written as [100, 126]:

$$p_{det}(\theta) = p(r > r_{thr}, \theta) = \int_{f(\mathcal{D})>r_{thr}} d\mathcal{D}\mathcal{L}(\mathcal{D}|\theta), \tag{3.11}$$

thus, equation (3.10) becomes:

$$N_{exp}(\Lambda) = \int d\theta p_{det}(\theta)\frac{dN}{d\theta}(\Lambda). \tag{3.12}$$

From equation (3.12) it is evident that defining and describing the BBH population in the best way possible is fundamental also in the evaluation of the bias effect. So, if the population is not correctly defined the entire inference will be systematically biased.

3.3 Sampling Methods

In many cases, the integrals for the likelihood and posterior evaluation are too demanding in terms of CPU time to perform due to the high dimension of the parameter space. So, instead of estimating them "brute-force" on a grid, it is possible to sample the posterior distribution with statistical methods that explore the parameter space in optimal ways that significantly reduce the computation time without losing accuracy in the estimate of parameters. These methods, commonly known as Monte Carlo Markov Chains (MCMC) sample the parameter space with random steps. There are different implementations that have been developed to sample the parameter space, in this work we focus on affine invariant sampling and on nested sampling. Their algorithms are presented schematically in Figure 3.1a and in Figure 3.1b, respectively.

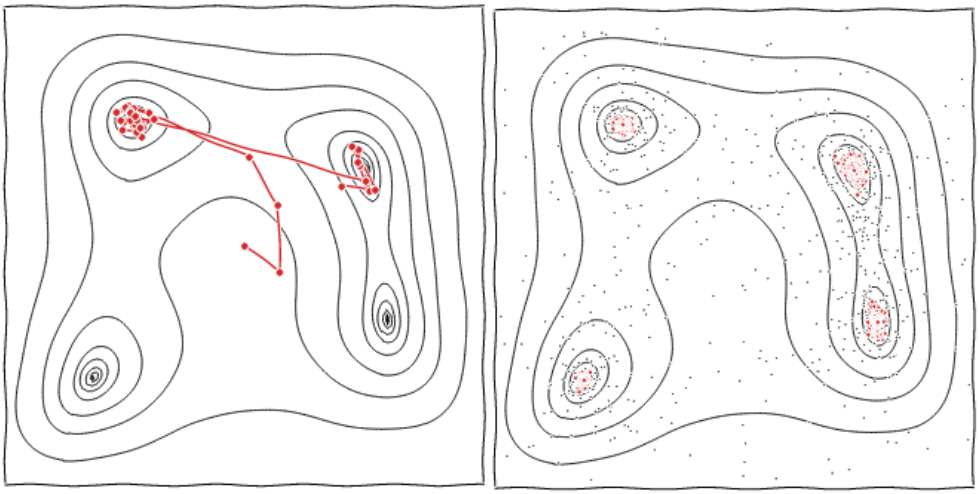

(a) (b)

Figure 3.1: Schematic representation of the different working algorithms of (a) affine invariant sampling and (b) nested sampling. Taken from `https://indico.cern.ch/event/1191458/contributions/5033394/attachments/2504951/4304391/will_handley_corfu_2022%20(1).pdf` [133].

3.3.1 Affine Invariant Sampling

The affine invariant sampling [134] is a variation to the basic Metropolis-Hasting algorithm [135] for MCMC, in which the sampler has the property of being invariant under affine transformations[1]. Assuming an affine invariant method, if a variable x has probability density $p(x)$ then $y = \mathrm{A}x + \mathrm{b}$ has density given by: $p(y) = p(Ax+b) \propto p(x)$. Therefore, a sampler is affine invariant if the MCMC transition probability density $p(x'|x)$ transforms in the same way, so:

$$p(y'|y) = Cp(x'|x), \tag{3.13}$$

where y' = Ax' + b and C is a normalization factor.

The main steps of the affine invariant sampling algorithm are summarized as follows:

1. A set of n_{walk} walkers (x_1, ..., x_{walk}) are drawn from the posterior parameter distribution, where $x_k \in \mathbb{R}^N$.

2. Each walker is moved, independently, further by one step, i.e. $x_k(\mathrm{t}) \rightarrow x_k(\mathrm{t}+1)$. The walkers are updated one at a time by using the current positions of all of the other walkers in the ensemble, called complementary ensemble. So, as the walker x_k is updated, its complementary ensemble is given by:

$$E_k(t) = \{x_1(t+1), \ldots, x_{k-1}(t+1), x_{k+1}(t), \ldots, x_{n_{walk}}(t)\} \tag{3.14}$$

[1] An affine transformation is an invertible mapping $\mathbb{R}^N \mapsto \mathbb{R}^N$ with the form $\vec{\psi} = A\vec{\theta} + b$ where A is a non-singular matrix.

The crucial point in this method is to define the move made to update the set of walkers. In this case, the walker x_k is updated by using one random complementary walker $x_{j\neq k}$:

$$x_k(t) \rightarrow y = x_j + Z(x_k(t) - x_j), \tag{3.15}$$

where Z is a random variable with density g(z), given by:

$$g(z) = \begin{cases} \frac{1}{C\sqrt{z}} & \text{if z} \in \left[\frac{1}{a}, a\right], \\ 0 & \text{otherwise,} \end{cases} \tag{3.16}$$

where a is the stretch factor parameter and $C = \frac{1}{2}\left(\sqrt{a} - \frac{1}{\sqrt{a}}\right)$. The move presented in equation (3.15) has the property of being affine invariant. A schematic representation of an affine invariant step is presented in Figure 3.2.

3. The move has the probability $\min\left\{1, Z^{N-1}\frac{\pi(y)}{\pi(x_k(t))}\right\}$ of being accepted. If so the walker is updated, thus $x_k(t+1) = y$.
4. If the move is rejected, the walker remains unchanged, thus: $x_k(t+1) = x_k(t)$.
5. Points from 2 to 4 are repeated until a stopping criterion is satisfied.

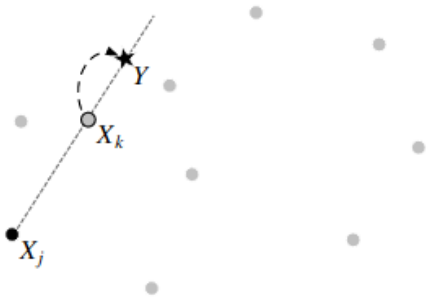

Figure 3.2: Schematic representation of a stretch move, where the light dots are the complementary walkers not taking part in the move, while the stretch takes place along the $x_j - x_k$ line.

3.3.2 Nested Sampling

The nested sampling [136] is a Monte Carlo integration technique used mainly for the calculation of Bayesian evidence $\mathcal{E}$, as the evidence can be considered the expectation value of a non-negative random variable. This method is based on the decomposition of the integration space into volume elements and then summing over them [137], thus:

$$\mathcal{E} = \int d\Lambda \mathcal{L}(\mathcal{D}|\Lambda)\pi(\Lambda) = \lim_{\delta\Lambda\rightarrow 0}\sum \mathcal{L}(\mathcal{D}|\Lambda)\pi(\Lambda)\delta\Lambda. \tag{3.17}$$

It is then possible to combine all the volume cells in which the integrand $(\mathcal{L}(\mathcal{D}|\Lambda)\pi(\Lambda))$ is almost constant, so:

$$\mathcal{E} = \int \mathcal{L}(X)dX = \sum \mathcal{L}(X)\delta X, \tag{3.18}$$

where δX is the volume of the elements with similar integrand and X is the volume variable

$$X(\mathcal{L}^\star) = \int_{\mathcal{L}>\mathcal{L}^\star} \pi(\Lambda)d\Lambda, \tag{3.19}$$

enclosed by the contour $\mathcal{L}^\star$. Given the difficulty of calculating equation (3.19) analytically in high dimension, nested sampling is used.

A schematic representation of the nested sampling algorithm is given in Figure 3.3 and it is summarized in the following steps:

1. A set of n_{live} random points are drawn from the prior $\pi(\Lambda)$, each of which has its likelihood $\mathcal{L}(\Lambda)$.

2. All the drawn points are then sorted in ascending order, such that: $\mathcal{L}(\Lambda_1) < \mathcal{L}(\Lambda_2) < \ldots < \mathcal{L}(\Lambda_{n_{live}})$.

3. The point with the smallest likelihood, denoted by $\mathcal{L}^\star$, is then discarded, thus the remaining points are now distributed on a smaller volume. This operation is called compression and the factor by which the volume shrinks is called t.

4. A new point is drawn from a new prior subject to $\mathcal{L} > \mathcal{L}^\star$:

$$\pi^\star(\Lambda) \propto \begin{cases} \pi(\Lambda) & \text{if } \mathcal{L}(\Lambda) > \mathcal{L}^\star; \\ 0 & \text{otherwise.} \end{cases} \tag{3.20}$$

   Thus giving a new sample of n_{live} on the compressed parameter space volume $\mathrm{X}_1 = t_1 X_0$, where X_0 is the original volume.

5. Points from 2 to 4 are repeated until a stopping criterion is satisfied.

6. The evidence can be calculated thanks to equation (3.18):

$$\mathcal{E} = \sum_{i=1}^{n_iter} \mathcal{L}^\star(X_i)\delta X, \tag{3.21}$$

   where $\delta X = \frac{1}{2}(X_{i-1} - X_{i+1})$. Furthermore, the posterior distribution could be constructed thanks to the Bayes theorem as $p_i = \frac{\mathcal{L}^\star(X_i)\delta X_i}{\mathcal{E}}$.

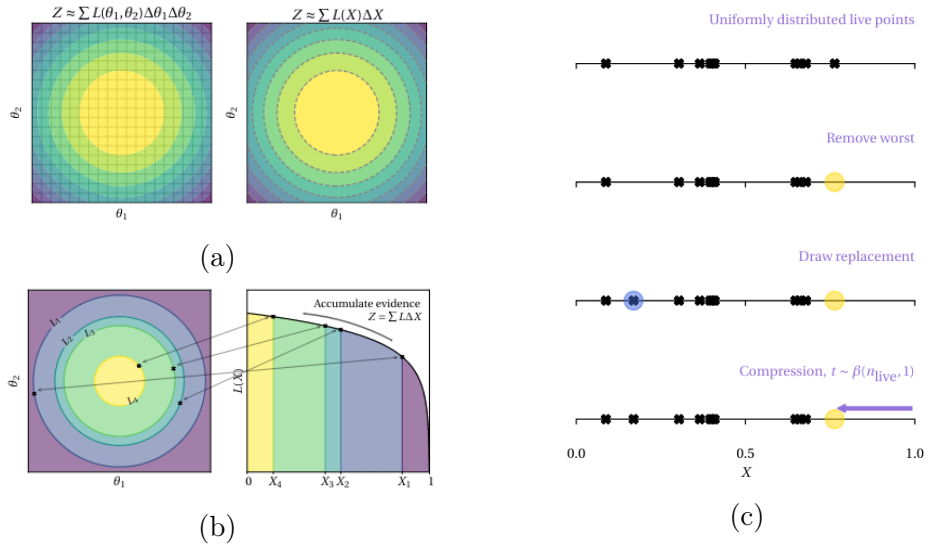

Figure 3.3: Illustration of the nested sampling algorithm, taken from [137]: (a) the colours represent contours of a two-dimensional likelihood function. Rather than summing over little cubes (left), in the nested sampling algorithm the cubes of similar likelihood are combined together and summed over them (right); (b) nested sampling on a two-dimensional problem: on the left the dead points and their iso-likelihood contours are shown, while on the right the corresponding contributions to the evidence integral are displayed; (c) compression in one iteration of nested sampling.

3.4 The MGCosmoPop Code

`MGCosmoPop` is a public software that implements a hierarchical Bayesian framework for constraining the standard cosmological parameters (Hubble constant and Dark Matter density) and modified Gravitational Wave propagation parameters together with the Binary Black Hole (BBH) population parameters (mass function, merger rate density and spin distribution) [10]. A schematic representation of the global structure of the code is given in Figure 3.4.

The code is divided into components containing:

- *cosmology:* a class implementing cosmology-related functions;
- *dataStructures:* one abstract class for data and classes for reading and using mock data and data from the O1-O2 and O3a observing runs. Classes for reading and using injections to compute selection effects are also there;
- *mock:* tools to generate mock datasets and injections;
- *population:* classes for implementing the population function as defined in equation (3.3);
- *posteriors:* classes implementing likelihood, posterior, and selection effects;

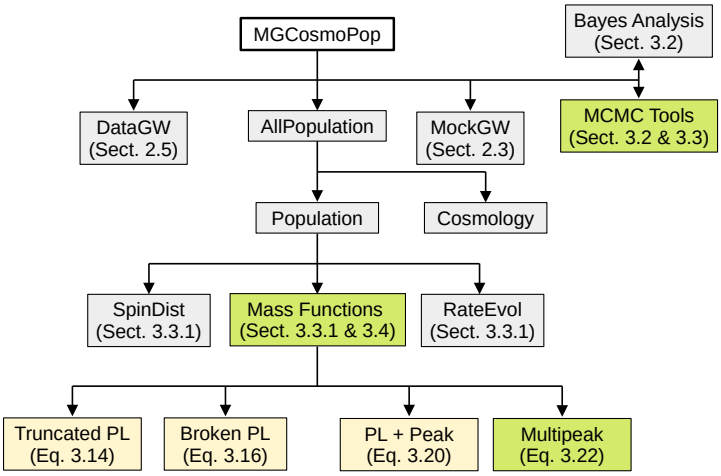

Figure 3.4: Schematic representation of structure of code `MGCosmoPop`. The different colours represent: in green the parts of the code, which were added and modified; in yellow the parts of the code which were tested and run within the context of this work; while in grey the parts which were not touched.

- *sample:* MCMC tools.

The most important module for the population function definition is "population", which is again divided in:

- *ABSpopulation.py:* abstract Base Classes for describing a population. Contains three ABCs (*Population*, *RateEvolution*, *BBHdistfunction*);

- *allPopulation.py:* collects the differential rates from all populations, adds the volume element Jacobian, the Jacobian between source and detector frame variables, observation time, and yields the full population function $\frac{dN}{d\theta}$ where $\theta = \{\mathrm{m}_1^{det}, \mathrm{m}_2^{det}, d_L, \chi_1, \chi_2, \dots\}$, which enters equation (3.1).

- *astro:* population of astrophysical black holes, which again contains *astroPopulation.py* which constructs, thanks to the other classes within *astro*, the astrophysical part of p_{pop}, *astroMassDistribution.py* which contains the definitions of the different $p(m_1, m_2|\Lambda_m)$, *astroSpinDistribution.py* which describes the neglected spin distribution, and *rateEvolution.py* contains the definitions of $R(z|\Lambda_z)$.

3.4.1 Astrophysical and Cosmological Parameters

Before describing the astrophysical models, relevant to this work, we introduce the parameters necessary to describe the cosmological part of equation (3.3). The cosmological parameters are always the same for all the mass functions that will be described. For this reason, I will present their physical meaning only once:

- H_0 is the Hubble constant, i.e. the parameter describing the speed of the expansion of the Universe and, despite the modern tension surrounding its value, in this work the results will be confronted with the value obtained by Planck: $H_0 = 67.4\,\mathrm{km/s/Mpc}$;
- $\Omega_{0,M}$ is the mass density parameter, i.e. the parameter describing the amount of matter (both dark and baryonic) within the Universe. The reference value is given by the ΛCDM model and confirmed by Planck: $\Omega_{0,M} \approx 0.3$.

On the contrary, the astrophysical BBH population (*astro* part of equation (3.3)) is defined by different distributions which will be presented below.

In particular, as it can be seen in [37], it is crucial to test different mass function models to fit the BBH mass distribution with the aim of reproducing the events in the best way possible. In fact, apart from the already discussed PISN feature, no real other theoretical property is known of the mass distribution, so, thanks to the increasing number of data it is possible to recognise more and more experimental sub-structures in the BH primary mass spectrum [37, 76]. Therefore, fitting the observed events with more and more complex mass functions is necessary to try to find all the most important features that define the BBH mass distribution.

Merger Rate Evolution

Two models were implemented to describe the merger rate of BBH systems:

- Power law profile: $\mathrm{R(z|\Lambda_z) = R_0(1+z)^{\lambda}}$;
- Madau-Dickinson rate [74, 138]: $\mathrm{R(z|\Lambda_z) = R_0\ [1 + (1+z_p)^{-\gamma-k}]\frac{(1+z)^{\gamma}}{1+\left(\frac{1+z}{1+z_p}\right)^{\gamma+k}}}$;

where $\Lambda_z = (R_0, \gamma, \kappa, z_p)$, of which $\mathrm{R_0}$ is a normalization constant, γ is a constant describing the slope of the R(z) behavior for redshift below $\mathrm{z_p}$: $\mathrm{R(z) \propto (1+z)^{\gamma}}$, and κ is a constant describing the slope of the R(z) behavior for redshift $\mathrm{z \gg z_p}$: $\mathrm{R(z) \propto (1+z)^{-\kappa}}$.

Mass Functions

Even though several mass functions were already defined in the code, only three of them will be presented, because, according to [37], they are the main candidates for the description of the real BH population and thus relevant to the work.

1) Truncated Power Law

The first and simplest mass function used in the analysis is a truncated power law with a sharp cut-off at the lower and upper end, as shown in Figure 3.5 and described by equation (3.22).

$$p(m_1|\alpha) \propto \begin{cases} m_1^{-\alpha} & \text{if } m_l < m_1 < m_h \\ 0 & \text{otherwise,} \end{cases} \tag{3.22}$$

where:

- α is the spectral index for the power law of the primary mass distribution;
- m_l is the minimum mass of the power law component of the primary mass distribution;
- m_h is the maximum mass of the power law component of the primary mass distribution.

A last additional parameter is needed to completely define the truncated power law: β, i.e. is the spectral index for the power law of the mass ratio distribution, which is necessary to construct the distribution for the secondary mass of the BBH system. Thus the `truncated` mass function is given by the following equation:

$$p(m_1, m_2|\Lambda_m) = p(m_1|\alpha, m_l, m_h) \cdot p(m_2|\beta, m_1, m_l), \tag{3.23}$$

where $\mathrm{m}_1 > \mathrm{m}_2$ and $p(m_2|\beta, m_1, m_l) = m_2^{\beta}$ is the secondary mass distribution.

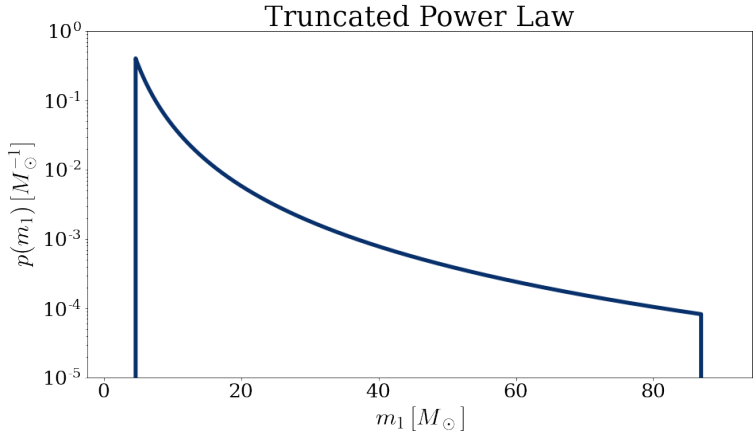

Figure 3.5: Truncated power law.

Therefore, by combining all the building blocks together, the BBH population created based on the truncated power law is defined by a total of ten parameters:

1) $\Lambda_{cosmo} = \{\ \mathrm{H}_0,\ \Omega_{0,\mathrm{M}}\ \}$;
2) $\Lambda_{astro} = \{\ \mathrm{R}_0,\ \gamma,\ \kappa,\ \mathrm{z}_p,\ \alpha,\ \beta,\ \mathrm{m}_l,\ \mathrm{m}_h\ \}$.

2) Broken Power Law

The second mass function used in the analysis is an extension of the truncated power law, which tries to take into account the presence of a scale in the mass distribution ($\approx 45\,\mathrm{M}_\odot$) due to the PISN mass gap without introducing a sharp cut-off at the lower

edge. An example of this kind of mass function is shown in Figure 3.6 and described by equation (3.24).

$$p(m_1|\alpha_1,\alpha_2,m_l,m_h) \propto \begin{cases} m_1^{-\alpha_1} S(m_1|m_l,\delta_m) & \text{if } m_l \leq m_1 < m_{break} \\ m_1^{-\alpha_2} S(m_1|m_l,\delta_m) & \text{if } m_{break} \leq m_1 \leq m_h \\ 0 & \text{otherwise,} \end{cases} \tag{3.24}$$

where $\mathrm{m_{break}} = \mathrm{m}_l + \mathrm{b}\,(\mathrm{m}_h - \mathrm{m}_l)$ and $S(m|m_l,\delta_m)$[2] is a smoothing function that removes the sharp cut-off at the lower end of the mass distribution ($\approx 5\,\mathrm{M}_\odot$) present in the truncated power law model. The other parameters are:

- α_1 is the power law slope of the primary mass distribution for masses below $\mathrm{m_{break}}$;
- α_2 is the power law slope of the primary mass distribution for masses above $\mathrm{m_{break}}$;
- β is the spectral index for the power law of the mass ratio distribution;
- δ_m is the range of mass tapering on the lower end of the mass distribution;
- m_l is the minimum mass of the power law component of the primary mass distribution;
- m_h is the maximum mass of the primary mass distribution;
- b is the parameter defining $\mathrm{m_{break}}$, i.e. the scale at which the power law changes steepness, thanks to the relation: $\mathrm{m_{break}} = \mathrm{m}_l + \mathrm{b}\,(\mathrm{m}_h - \mathrm{m}_l)$;

Thus the `broken` mass function is given by the following equation:

$$p(m_1,m_2|\Lambda_m) = p(m_1|\alpha_1,\alpha_2,\delta_m,m_l,m_h,b)\cdot p(q|\beta,m_1,m_l,\delta_m), \tag{3.27}$$

where $\mathrm{q} = \frac{m_2}{m_1}$ is the mass fraction with $\mathrm{m}_1 > \mathrm{m}_2$, and $p(q|\beta,m_1,m_l,\delta_m) \propto q^\beta S(qm_1|m_l,\delta_m)$, where $S(qm_1|m_l,\delta_m)$ is given by equation (3.25).

Therefore, by combining all the building blocks together, the BBH population created based on the broken power law is defined by a total of thirteen parameters:

- $\Lambda_{cosmo} = \{\ \mathrm{H}_0,\ \Omega_{0,\mathrm{m}}\ \}$;
- $\Lambda_{astro} = \{\ \mathrm{R}_0,\ \gamma,\ \mathrm{k},\ \mathrm{z}_p,\ \alpha_1,\ \alpha_2,\ \beta,\ \delta_m,\ \mathrm{m}_l,\ \mathrm{m}_h,\ \mathrm{b}\ \}$.

[2]
$$S(m|m_l,\delta_m) = \begin{cases} 0 & \text{if } m < m_l \\ [f(m-m_l,\delta_m)+1]^{-1} & \text{if } m_l \leq m < m_l+\delta_m \\ 1 & \text{if } m \geq m_l+\delta_m \end{cases} \tag{3.25}$$

with

$$f(m,\delta_m) = \exp\left(\frac{\delta_m}{m} + \frac{\delta_m}{m-\delta_m}\right). \tag{3.26}$$

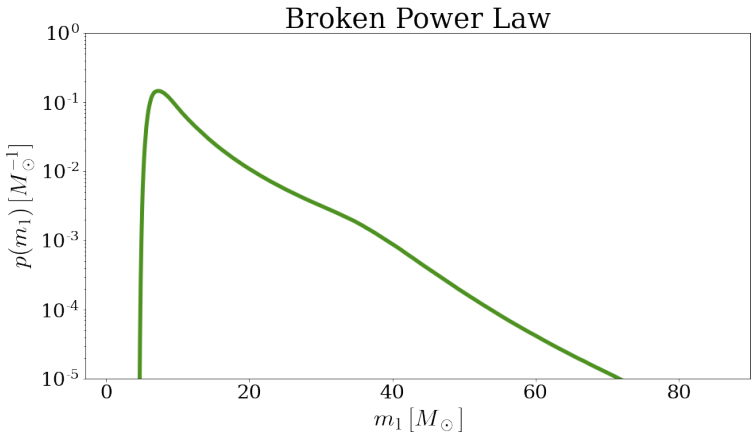

Figure 3.6: Broken power law.

3) Power Law + Gaussian Peak

The third mass function used in the analysis is a second extension of the truncated power law, which tries to take into account the presence of an empirical concentration around $\approx 35\,\mathrm{M}_\odot$ in the mass distribution by adding a Gaussian peak at the concentration scale. In the further development of this work, the Power Law + Gaussian Peak model will be referred to as `PowerLawPeak`. An example of this kind of mass function is displayed in Figure 3.7 and defined by an equation like equation (3.28).

$$p(m|\lambda_p, \alpha, m_l, m_h, \delta_m, \mu_g, \sigma_g) = \\ = [(1-\lambda_p)\mathfrak{T}(m|-\alpha, m_h) + \lambda_p \mathcal{G}(m|\mu_g, \sigma_g)]\, S(m_1|m_l, \delta_m), \quad (3.28)$$

Where $\mathfrak{T}$ is a normalized truncated power law distribution like in equation (3.22), while $\mathcal{G}$ is a normalized Gaussian distribution with mean μ_g and width σ_g and $S(m_1|m_l, \delta_m)$ is a smoothing function similar to equation (3.25). The other parameters are:

- α is the spectral index for the power law of the primary mass distribution;
- β is the spectral index for the power law of the mass ratio distribution;
- δ_m is the range of mass tapering at the lower end of the mass distribution;
- m_l is the minimum mass of the power law component of the primary mass distribution;
- m_h is the maximum mass of the power law component of the primary mass distribution;
- λ_p is a mixing fraction determining the relative prevalence of mergers in $\mathfrak{T}$ and $\mathcal{G}$, or in other words the fraction of BBH systems in the Gaussian component. By definition its value is included between 0 and 1;

- μ_g is the mean of the Gaussian component in the primary mass distribution;
- σ_g is the width of the Gaussian component in the primary mass distribution.

Thus the `PowerLawPeak` mass function is given by the following equation:

$$p(m_1, m_2|\Lambda_m) = p(m_1|\alpha, \delta_m, m_l, m_h, \lambda_p, \mu_g, \sigma_g) \cdot p(q|\beta, m_1, m_l), \tag{3.29}$$

where $\mathrm{q} = \frac{m_2}{m_1}$ is the mass fraction with $\mathrm{m}_1 > \mathrm{m}_2$, and $p(q|\beta, m_1, m_l, \delta_m) \propto q^\beta S(qm_1|m_l, \delta_m)$, where $S(qm_1|m_l, \delta_m)$ is given by equation (3.25).

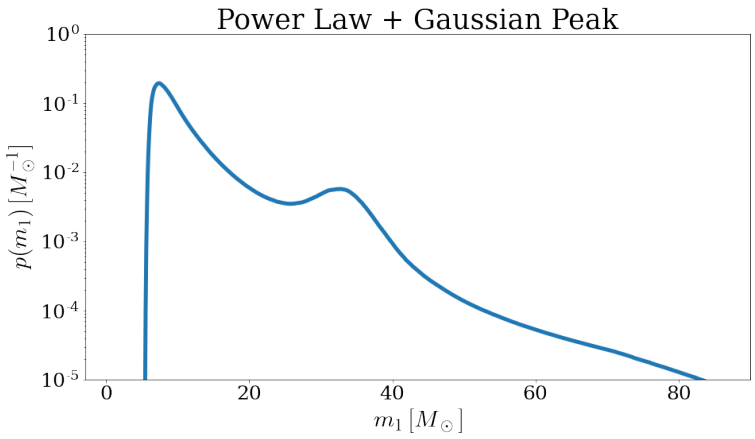

Figure 3.7: Power law + Gaussian peak.

Therefore, by combining all the building blocks together, the BBH population created based on the broken power law is defined by a total of fifteen parameters:

- $\Lambda_{cosmo} = \{\ \mathrm{H}_0,\ \Omega_{0,\mathrm{m}}\ \}$;
- $\Lambda_{astro} = \{\ \mathrm{R}_0,\ \gamma,\ \mathrm{k},\ \mathrm{z}_p,\ \alpha,\ \beta,\ \delta_m,\ \mathrm{m}_l,\ \mathrm{m}_h,\ \lambda_p,\ \mu_g,\ \sigma_g\ \}$.

3.5 Extending the Binary Black Holes Mass Function Models

One of the main aims of this work was to extend the MGCosmoPop code with a new mass function: the `Multipeak` mass function, which is defined as a truncated power law with two Gaussian peaks. The introduction of this new mass function, which is more complex than the Power Law + Gaussian Peak model, is needed to expand the already existing mass function in order to fit the new features discovered thanks to the increasing number of data. In particular, this new mass function attempts to take into account the presence of a second empirical concentration around $\approx 10\,\mathrm{M}_\odot$ [37, 76] in the mass distribution by

adding a second Gaussian peak at that scale. An example of this kind of mass function is shown in Figure 3.8 and is described by equation (3.30).

$$\begin{aligned} &p(m_1|\lambda_p, \lambda_1, \alpha, m_l, m_h, \delta_m, \mu_1, \sigma_1, \mu_2, \sigma_2) = \\ &\quad = [(1-\lambda_p)\mathfrak{T}(m_1|-\alpha, m_h) + \lambda_p\lambda_1\mathcal{G}(m_1|\mu_1, \sigma_1)\lambda_p(1-\lambda_1)\mathcal{G}(m_1|\mu_2, \sigma_2)]\, S(m_1|m_l, \delta_m), \end{aligned} \tag{3.30}$$

where $\mathfrak{T}$ is a normalized truncated power law distribution like in equation (3.22), while $\mathcal{G}$ are the two normalized Gaussian distributions with means μ_1 and μ_2 and widths σ_1 and σ_2 and $S(m_1|m_l, \delta_m)$ is a smoothing function similar to equation (3.25). The other parameters are:

- α is the spectral index for the power law of the primary mass distribution;
- β is the spectral index for the power law of the mass ratio distribution;
- δ_m is the range of mass tapering at the lower end of the mass distribution;
- m_l is the minimum mass of the power law component of the primary mass distribution;
- m_h is the maximum mass of the power law component of the primary mass distribution;
- λ_p is a mixing fraction determining the relative prevalence of mergers in $\mathfrak{T}$ and the two $\mathcal{G}$;
- λ_1 is a mixing fraction determining the relative prevalence of mergers in $\mathcal{G}(\mu_1, \sigma_1)$ and $\mathcal{G}(\mu_2, \sigma_2)$;
- μ_1 is the mean of the first Gaussian component in the primary mass distribution;
- σ_1 is the width of the first Gaussian component in the primary mass distribution;
- μ_2 is the mean of the second Gaussian component in the primary mass distribution;
- σ_2 is the width of the second Gaussian component in the primary mass distribution.

Thus the `Multipeak` mass function is given by the following equation:

$$p(m_1, m_2|\Lambda_m) = p(m_1|\lambda_p, \lambda_1, \alpha, m_l, m_h, \delta_m, \mu_1, \sigma_1, \mu_2, \sigma_2) \cdot p(q|\beta, m_1, m_l), \tag{3.31}$$

where $\mathrm{q} = \frac{m_2}{m_1}$ is the mass fraction with $\mathrm{m}_1 > \mathrm{m}_2$, and $p(q|\beta, m_1, m_l, \delta_m) \propto q^\beta S(qm_1|m_l, \delta_m)$, where $S(qm_1|m_l, \delta_m)$ is given by equation (3.25).

Therefore, by combining all the building blocks together, the BBH population created based on the Power Law + Gaussian Peak is defined by a total of seventeen parameters:

- $\Lambda_{cosmo} = \{\ \mathrm{H}_0,\ \Omega_{0,\mathrm{m}}\ \}$;

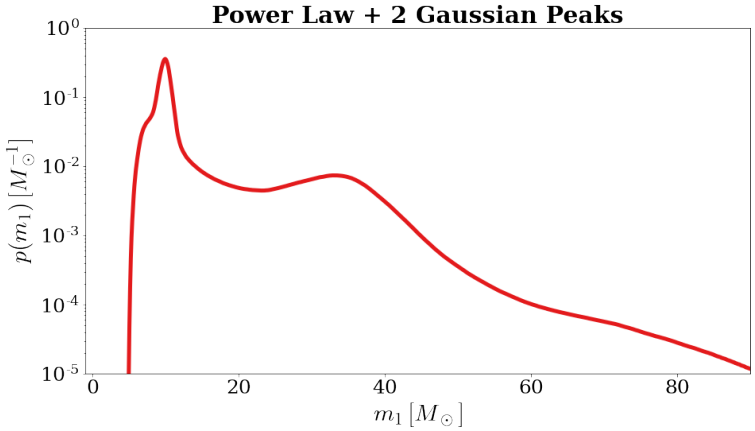

Figure 3.8: Power law + two Gaussian peaks.

- $\Lambda_{astro} = \{$ R_0, γ, k, z_p, α, β, δ_m, m_l, m_h, λ_p, λ_1, μ_1, σ_1, μ_2, σ_2 $\}$.

In order to evaluate if the newly implemented mass function was defined correctly some tests on the `MGCosmoPop` tutorial were run, consisting in checking the distribution normalization, estimating and displaying the joint and marginal mass distribution, and, given some "testing" data, computing the corresponding population function. In particular, the normalization was almost perfect, since the integral of the constructed mass function was equal to 0.99959, and some examples of possible $p(m_1|\Lambda_m)$ and $p(m_1, m_2|\Lambda_m)$ mass distribution are presented in Figure 3.9 and Figure 3.10, respectively.

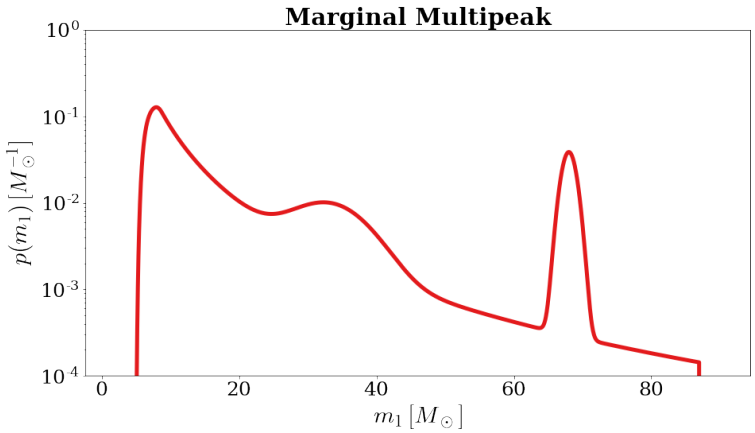

Figure 3.9: Validation results for the implemented mass function `Multipeak`: marginal mass distribution $p(m_1|\Lambda_m)$.

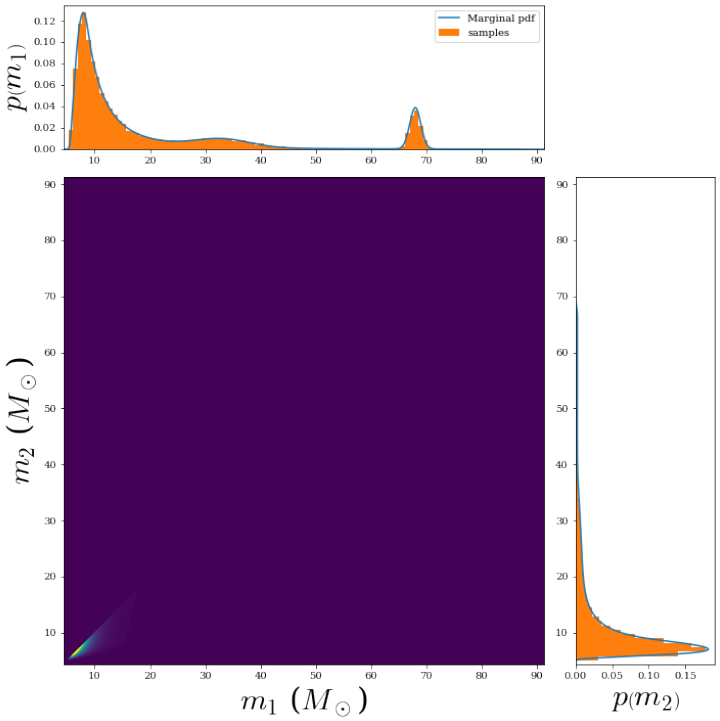

Figure 3.10: Validation results for the implemented mass function `Multipeak`: joint mass distribution $p(m_1, m_2|\Lambda_m)$.

3.6 Extending MGCosmoPop to Run a Nested Sampling MCMC

Based on the description of Section 3.3 we implemented a code, based on the public code `bilby`[3] [139], to perform MCMC with different samplers, namely an affine invariant sampler based on the `emcee` package [12] and a nested sampler based on the `dynesty` package [140, 141]. This code represents a step forward with respect to the previous version, where the MCMC was performed only through the `emcee` package since it introduces the possibility to use alternative samplers, which will allow us to calculate the Bayes factors of the different models considered, calculate their evidence, and sample the posterior distributions of the various parameters.

In particular, to run the code a new likelihood class has been developed specifically to run within the `bilby` code. This class builds the likelihood from the mass function classes of `MGCosmoPop`, and, after taking the selection effects correctly into account, formats them properly to be ingested by the code.

The main advantage is that with the new code it is possible to run MCMC from `bilby`,

[3] `Bilby` is a python code that has been developed within the LIGO/Virgo Collaboration to perform accurate and reliable GW parameter estimation on data and to do population studies using hierarchical Bayesian modelling.

with the possibility to switch between different samplers and to use the `bilby` optimization in terms of computing parallelization.

To test the code, we decided to perform a run with the two samplers considered, `emcee` and `bilby`, and to compare the results. To optimize the computing time, we decide to consider our best mass function model (`MultiPeak`, see Section 4.2.5) with all parameters fixed to their best fit values (Figure 4.9), except for the Hubble constant H_0, in order to see if the results are reasonable.

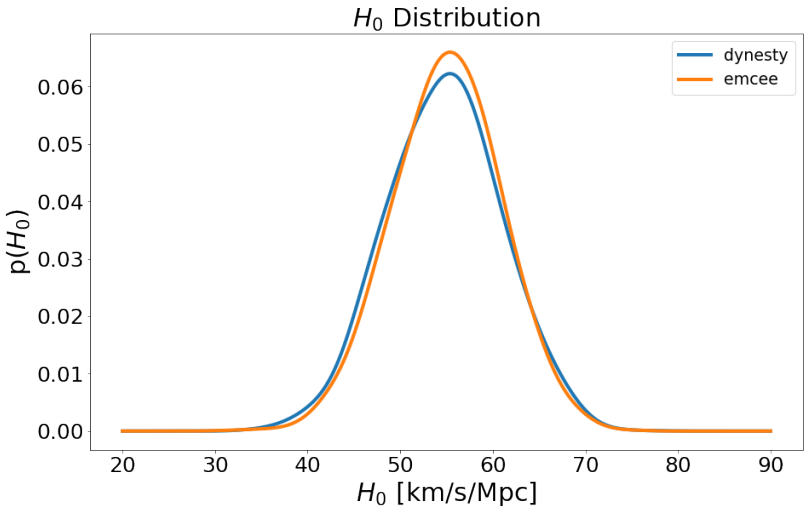

Figure 3.11: H_0 distributions obtained for the two different samplers.

It is therefore important to underline that in this run we are not interested in obtaining the absolute value of H_0, since fixing all the other parameters may induce a bias in the derived H_0 value. In fact, we are interested in comparing the relative results obtained with the new code on the two different runs: with `emcee` and with `dynesty`.

The results are shown in Figure 3.11. We find that the H_0 estimated with the two samplers are in very good agreement, with an absolute value slightly lower ($H_0^{emcee} = 55.15^{+5.61}_{-5.98}$ km/s/Mpc and $H_0^{dynesty} = 54.86^{+6.06}_{-6.39}$ km/s/Mpc) than the value obtained in the run when all the parameters are free (see Section 4.2.6 and Table 4.15), probably due to the fact that all the other parameters have been fixed.

The code, therefore, appears to perform correctly, and we plan in the near future to run it on a cluster exploring all the models studied in Chapter 4. This would allow us to derive, with `dynesty`, the bias factors and obtain an additional model selection indicator for the evaluation of the best model.

Chapter 4

Analysis of the GWTC-3 Binary Black Holes Population

In this chapter, the constraining power on the parameters defining the BBH population and on the cosmological parameters will be investigated, thanks to the code described in Section 3.4 and its extension (Section 3.5). In this analysis the already presented and implemented mass functions will be used to study the selected sample from O3 with SNR > 12 (Section 2.4).

First, the results obtained by constraining only the population parameters (Λ_{astro}), described in Section 3.4.1, of the different implemented mass functions will be presented. Then, the results will be extended by jointly fitting the astrophysical and some cosmological parameters, with a particular interest in the Hubble constant H_0 as a free parameter. Lastly, the results of the various model selection methods will be described, which were implemented in order to find the best fit model for the analysed data set.

4.1 Astrophysical Constraints at Fixed Cosmology

In this first section, the results found by only fitting the astrophysical population parameters will be described, which in practice means to evaluate equation (3.3), by considering Λ_{astro} free to vary within the parameter space and keeping Λ_{cosmo} fixed to their ΛCDM values.

The presented results are found by only considering the 35 events with SNR > 12 from O3, due to the fact that, as described in Section 2.4, they represent the most robust sample for being CBC systems. Despite that, in the interest of completeness, the analysis has also been made for a wider sample of 80 events, corresponding to evaluating all the events with SNR > 8. The related results are presented in Appendix A.

The analysis was made by running a Markov Chain Monte Carlo [142] (MCMC) thanks to the use of the available public code *emcee* [12], which enabled the drawing of a number of samples from the posterior distribution (given the prior distribution and the likelihood function) to explore the parameters space and find their best values according to the

data. The following analysis was made for all the four mass function models presented in Chapter 3 by assuming the flat priors displayed in Table 4.1.

Parameter	R_0	λ_z	α_z	β_z	z_p
Range	$\mathcal{U}$(0, 100)	$\mathcal{U}$(-15, 15)	$\mathcal{U}$(0, 12)	$\mathcal{U}$(0, 6)	$\mathcal{U}$(0, 4)

Parameter	α	β	m_l	s_l	m_h	s_l
Range	$\mathcal{U}$(1.5, 12)	$\mathcal{U}$(-4, 12)	$\mathcal{U}$(2, 50)	$\mathcal{U}$(0.01 , 1)	$\mathcal{U}$(50, 200)	(0.01 , 1)

Parameter	α_1	α_2	δ_m	b	μ_{eff}	χ_{eff}
Range	$\mathcal{U}$(1.5, 12)	$\mathcal{U}$(1.5, 12)	$\mathcal{U}$(0, 10)	$\mathcal{U}$(0, 1)	$\mathcal{U}$(-1, 1)	$\mathcal{U}$(0.01, 1)

Parameter	μ_p	σ_p	λ_p	μ_g	σ_g
Range	$\mathcal{U}$(0.01, 1)	$\mathcal{U}$(0.01, 1)	$\mathcal{U}$(0, 1)	$\mathcal{U}$(20, 50)	$\mathcal{U}$(0.4, 10)

Parameter	λ_1	μ_1	σ_1	μ_2	σ_2
Range	$\mathcal{U}$(0, 1)	$\mathcal{U}$(20, 50)	$\mathcal{U}$(0.4, 10)	$\mathcal{U}$(7, 15)	$\mathcal{U}$(0.4, 5)

Table 4.1: Prior choice for the entire fixed cosmology analysis. The parameters follow the definitions presented in Section 3.4 and Section 3.5.

Before moving on to the description of the analysis, a brief digression on the parameters that have been evaluated is necessary, and to do so we focus on the corner plot of `Multipeak` displayed in Figure 4.1. For clarity and conciseness, we will present the corner plot only for the Multipeak mass function case, while the others will be presented in Appendix B.

From a closer look at Figure 4.1, some first observations on the parameters can be inferred. First, the constraining power on the parameters is not the same for all of them. In fact, despite finding a best-fit value for all parameters, as shown on top of each square, some of them are loosely (z_p and δ_m) or not constrained (κ) at all. This is proven by the fact that the corresponding corner plots are respectively almost and completely flat. Therefore, in the following analysis, the results for these parameters will be omitted.

Moreover, even though the corner plots show a good constraining power, the analysis for parameters α and β will also be neglected due to the fact that these parameters are not common to all the implemented mass functions, and therefore not interesting for a proper model comparison.

Lastly, instead of evaluating and then comparing m_l and m_h, the 5% and 95% percentile will be studied, respectively. The reason why this choice was made is the fact that m_l and m_h do not always represent the same physical quantity for all mass functions, thus not making them the best parameters for a results comparison of the different mass functions.

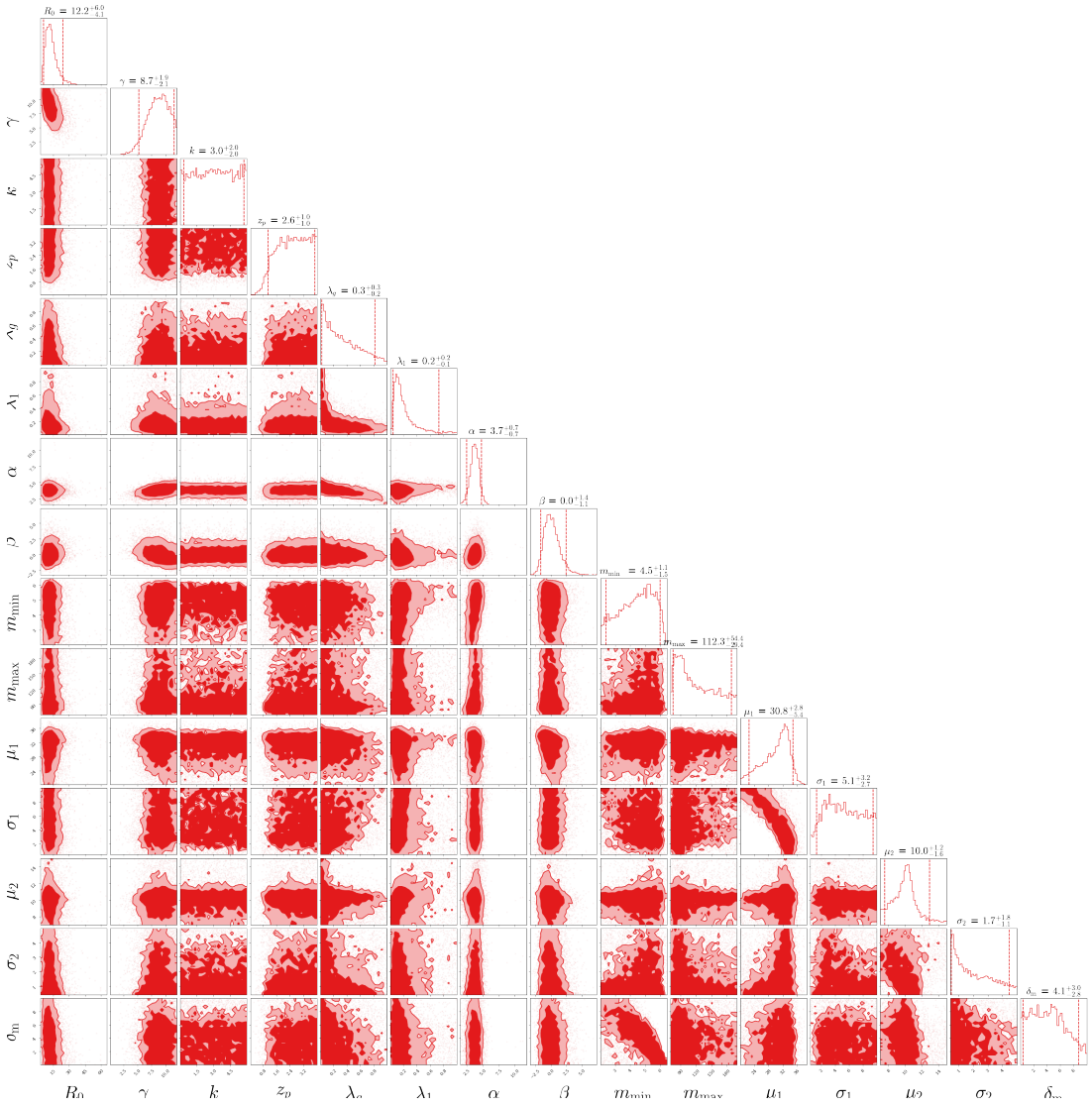

Figure 4.1: Corner plot of the parameters for the power law + two peaks mass function obtained from the Bayesian analysis by using BBH events with SNR > 12.

In addition to this, it is also crucial to evaluate the mass "concentration" for each implemented distribution, and, while m_h is not a good indicator of it, the percentile distribution is an optimal tool to assess this quantity. Therefore, the entire analysis described in this section will be concentrating on the evaluation of the following parameters: $\Lambda = \{ R_0, \gamma, m_{5\%}, m_{95\%} \}$, with a smaller focus also on λ_g and λ_1, when present.

The percentile is defined as the score at or below which a given percentage falls, which means that, for example, the 95^{th} percentile is the score at or below which 95% of the scores in the distribution are found. In particular, in the context of this work, the percentiles were calculated as the n-th percentage of the Cumulative Distribution Function (CDF).

4.1.1 Analysis of the Truncated Power Law Model

The first mass function to be presented is the truncated power law. The obtained values are displayed in Figure B.5 and summarized in Table 4.2 with median, 68%, and 90% confidence intervals (C.I.).

C.I.	R_0 [1/Gpc^3/yr]	γ	κ	z_p
68%	$21.46^{+8.33}_{-6.38}$	$7.63^{+1.94}_{-2.18}$	$2.93^{+2.05}_{-2.02}$	$2.47^{+1.04}_{-1.14}$
90%	$21.46^{+16.01}_{-9.67}$	$7.63^{+3.14}_{-3.56}$	$2.93^{+2.72}_{-2.65}$	$2.47^{+1.38}_{-1.69}$

C.I.	α	β	m_l [$M_\odot$]	m_h [$M_\odot$]
68%	$3.57^{+0.48}_{-0.48}$	$0.52^{+1.56}_{-1.33}$	$6.17^{+0.18}_{-0.30}$	$79.58^{+17.93}_{-6.88}$
90%	$3.57^{+0.76}_{-0.78}$	$0.52^{+2.51}_{-2.09}$	$6.17^{+0.25}_{-0.60}$	$79.58^{+61.32}_{-8.86}$

Table 4.2: Astrophysical parameters obtained for the truncated power law model obtained from the Bayesian analysis by using events with SNR > 12.

The mass function obtained with values from Table 4.2 is shown in Figure 4.2.

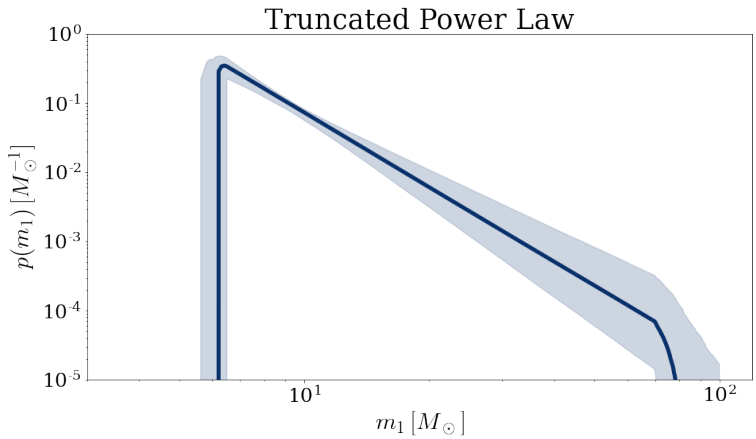

Figure 4.2: Truncated power law obtained from the Bayesian analysis by using BBH events with SNR > 12. The solid line represents the median values, while the shaded area shows the 90% confidence intervals.

4.1.2 Analysis of the Broken Power Law Model

The next studied mass function is the broken power law. The resulting values are shown in the corner plot in Figure B.6 and then summarized in Table 4.3 with median, 68% and 90% confidence intervals (C.I.).

C.I.	R_0 [1/Gpc^3/yr]	γ	κ	z_p	α_1
68%	$11.33^{+5.85}_{-3.78}$	$9.27^{+1.66}_{-2.06}$	$2.97^{+2.08}_{-2.02}$	$2.56^{+0.99}_{-1.02}$	$2.98^{+0.56}_{-0.58}$
90%	$11.33^{+11.38}_{-5.47}$	$9.27^{+2.37}_{-3.57}$	$2.97^{+2.74}_{-2.68}$	$2.56^{+1.29}_{-1.43}$	$2.98^{+0.93}_{-0.92}$

C.I.	α_2	β	δ_m	m_l [$M_\odot$]	m_h [$M_\odot$]	b
68%	$7.90^{+1.87}_{-1.48}$	$0.49^{+1.46}_{-1.13}$	$4.82^{+2.87}_{-3.06}$	$4.29^{+1.17}_{-1.32}$	$118.03^{+50.53}_{-33.16}$	$0.29^{+0.13}_{-0.09}$
90%	$7.90^{+3.10}_{-2.43}$	$0.49^{+2.55}_{-1.75}$	$4.82^{+4.12}_{-4.27}$	$4.29^{+1.67}_{-1.94}$	$118.03^{+71.37}_{-41.76}$	$0.29^{+0.22}_{-0.13}$

Table 4.3: Astrophysical parameters obtained for the broken power law model obtained from the Bayesian analysis by using events with SNR > 12.

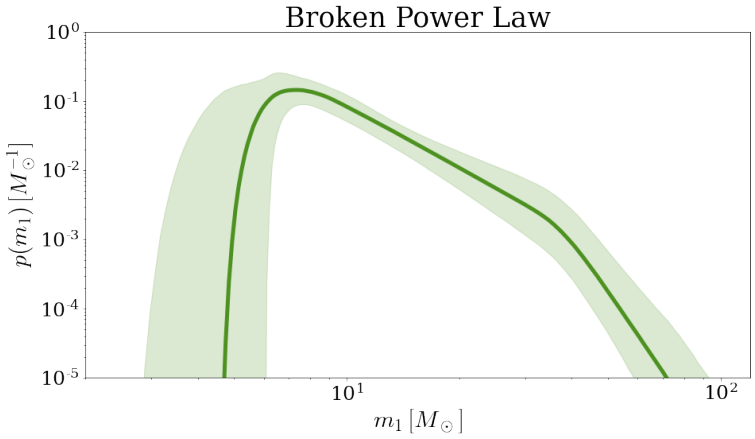

Figure 4.3: Broken power law obtained from the Bayesian analysis by using BBH events with SNR > 12. The solid line represents the median values, while the shaded area shows the 90% confidence intervals.

Despite not being defined by all the same parameters as the truncated mass function, a first comparison can be made between some parameters. For example, γ, which is the same physical quantity in both cases, has been found to be larger in the latter case, thus

indicating a steeper slope for the merger rate evolution. Moreover, it is also possible to compare α and α_1, thanks to the fact that the two mass functions have the same physical meaning at masses lower than mass break. In fact, in `Broken` the second slope (after the mass break) was only introduced with the aim of improving the data fitting at the high end of the distribution. For this reason, it is not surprising that the obtained values for α and α_1 are not so unsimilar and have consistent estimates: $3.57^{+0.48}_{-0.48}$ vs. $2.98^{+0.56}_{-0.58}$.

The mass function obtained with such values is shown in Figure 4.3.

4.1.3 Analysis of the Power Law + Gaussian Peak Model

The third mass function to be presented is the power law + Gaussian peak. The resulting values are shown in the corner plot in Figure B.7 and then summarized in Table 4.4 with median, 68%, and 90% confidence intervals (C.I.).

C.I.	R_0 [1/Gpc^3/yr]	γ	κ	z_p	α	β
68%	$12.12^{+5.90}_{-4.08}$	$8.51^{+1.98}_{-2.08}$	$2.98^{+2.13}_{-2.01}$	$2.51^{+1.00}_{-1.03}$	$4.16^{+0.54}_{-0.56}$	$-0.05^{+1.41}_{-1.09}$
90%	$12.12^{+11.29}_{-6.03}$	$8.51^{+2.92}_{-3.51}$	$2.98^{+2.74}_{-2.71}$	$2.51^{+1.32}_{-1.46}$	$4.16^{+0.95}_{-0.90}$	$-0.05^{+2.56}_{-1.70}$

C.I.	δ_m	m_l [$M_\odot$]	m_h [$M_\odot$]	λ_p	μ_g [$M_\odot$]	σ_g [$M_\odot$]
68%	$3.99^{+2.68}_{-2.62}$	$5.14^{+0.70}_{-0.98}$	$116.01^{+54.32}_{-31.24}$	$0.02^{+0.04}_{-0.02}$	$31.83^{+2.22}_{-4.00}$	$4.04^{+3.39}_{-2.10}$
90%	$3.99^{+4.30}_{-3.53}$	$5.14^{+0.96}_{-1.70}$	$116.01^{+75.04}_{-39.46}$	$0.02^{+0.08}_{-0.02}$	$31.83^{+3.49}_{-7.92}$	$4.04^{+5.12}_{-2.99}$

Table 4.4: Astrophysical parameters obtained for the power law + peak model obtained from the Bayesian analysis by using BBH events with SNR > 12.

Again, we can draw some connections between the results found for `PowerLawPeak` and the previously found ones. As before, the α can be compared, thanks to the fact that this power law is actually a truncated power at which a Gaussian peak was added. This parameter is again consistent with the value found for the truncated mass function ($4.16^{+0.54}_{-0.56}$ vs. $3.57^{+0.48}_{-0.48}$), but, it is not with the one found for the broken power law ($4.16^{+0.54}_{-0.56}$ vs. $2.98^{+0.56}_{-0.58}$). In contrast, the merger rate normalization R_0 resulted similar to the value obtained for `Broken`: $12.12^{+5.90}_{-4.08}$ vs. $11.33^{+5.85}_{-3.78}$; and much more different from the one found for `Truncated`: $12.12^{+5.90}_{-4.08}$ vs. $21.46^{+8.33}_{-6.38}$. These results could be a first indication of the different "behaviour" that each mass function follows in order to optimize the fitting, which could be a hint to the fact that the different models describe different physical processes at work. A last crucial parameter to study is λ_p, which defines the importance of the Gaussian

peak with respect to the power law. In this case, it was obtained: $\lambda_p = 0.02$, meaning that the Gaussian prevails only by just a 2%.

The mass function obtained with such values is shown in Figure 4.4.

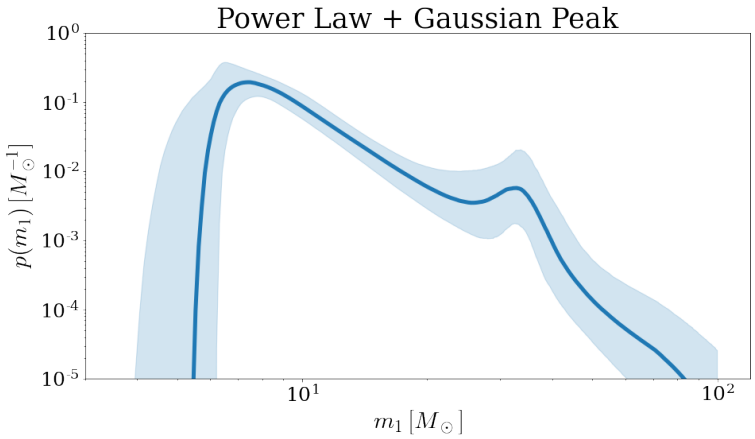

Figure 4.4: Power law + Gaussian peak obtained from the Bayesian analysis by using BBH events with SNR > 12. The solid line represents the median values, while the shaded area shows the 90% confidence intervals.

4.1.4 Analysis of the Power Law + Two Gaussian Peaks Model

The last mass function to be presented is the power law + two Gaussian peaks. The resulting values are shown in the corner plot in Figure 4.1 and then summarized in Table 4.5 with median, 68% and 90% symmetric confidence intervals (C.I.).

Due to the big differences between this new mass function and the three previous ones no real comparison can be made between them, except for the one between μ_g and μ_1, and σ_g and σ_1, of the "high mass" Gaussian peaks of the power law + peak model and the multipeak one. In particular, the found mass scale is very similar to the power law + peak model having a little bit larger value of $31.83\,\mathrm{M}_\odot$ against the $30.85\,\mathrm{M}_\odot$ of the multipeak mass function. It seems as if the small "disagreement" in the mass scale estimate is compensated by the width of the peak. In fact, for the multipeak, which has a smaller mass value, a larger width value is found ($\sigma_g = 5.11\,\mathrm{M}_\odot$) in respect to the one obtained for the single peak mass function ($\sigma_1 = 4.04\,\mathrm{M}_\odot$), which has a larger mass scale value. Lastly, it worth noticing that the "low mass" peak is obtained to be $\mu_2 = 9.99^{+1.21}_{-1.60}\,\mathrm{M}_\odot$ in accordance with the value predicted by [11]: $\mu \approx 10\,\mathrm{M}_\odot$.

The mass function obtained with such values is shown in Figure 4.5.

Before moving on with a more complete model comparison, it is worth, in order to get a better overview of the mass functions and of the differences between them discussed in this section, to present a summarizing figure of the obtained model. Such an image is shown in Figure 4.6, where it is important to note that the x-axis is a *linear* scale in contrast with the *logarithmic* scale of the previous mass distribution plot of this Section.

C.I.	R_0 [1/Gpc^3/yr]	γ	κ	z_p	α
68%	$12.17^{+6.00}_{-4.14}$	$8.73^{+1.94}_{-2.11}$	$3.04^{+2.04}_{-2.04}$	$2.57^{+0.98}_{-1.04}$	$3.73^{+0.67}_{-0.69}$
90%	$12.17^{+12.00}_{-6.07}$	$8.73^{+2.75}_{-3.51}$	$3.04^{+2.68}_{-2.75}$	$2.57^{+1.29}_{-1.49}$	$3.73^{+1.08}_{-1.20}$

C.I.	β	δ_m	m_l [$M_\odot$]	m_h [$M_\odot$]	λ_p
68%	$0.00^{+1.36}_{-1.08}$	$4.15^{+2.96}_{-2.77}$	$4.52^{+1.09}_{-1.45}$	$112.34^{+54.39}_{-29.36}$	$0.27^{+0.35}_{-0.21}$
90%	$0.00^{+2.50}_{-1.67}$	$4.15^{+4.62}_{-3.73}$	$4.52^{+1.49}_{-2.14}$	$112.34^{+77.29}_{-36.79}$	$0.27^{+0.55}_{-0.25}$

C.I.	λ_1	μ_1 [$M_\odot$]	σ_1 [$M_\odot$]	μ_2 [$M_\odot$]	σ_2 [$M_\odot$]
68%	$0.16^{+0.24}_{-0.08}$	$30.85^{+2.76}_{-5.37}$	$5.11^{+3.24}_{-2.72}$	$9.99^{+1.21}_{-1.60}$	$1.73^{+1.84}_{-1.06}$
90%	$0.16^{+0.57}_{-0.12}$	$30.85^{+4.08}_{-8.39}$	$5.11^{+4.37}_{-3.80}$	$9.99^{+2.93}_{-2.48}$	$1.73^{+2.74}_{-1.25}$

Table 4.5: Astrophysical parameters obtained for the power law + 2 peaks model obtained from the Bayesian analysis by using BBH events with SNR > 12.

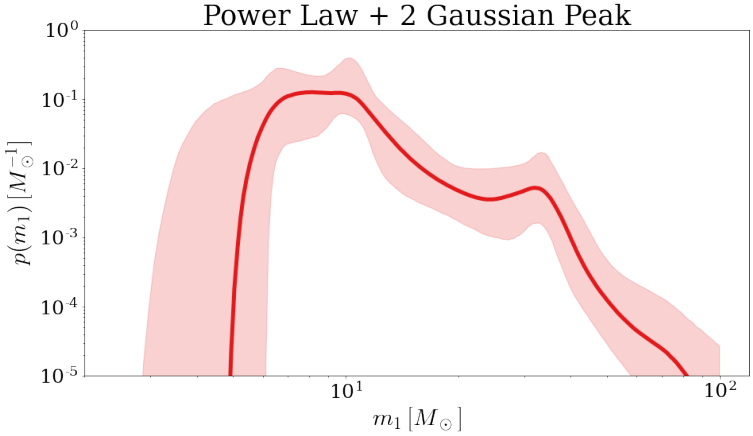

Figure 4.5: Power law + two Gaussian peaks obtained from the Bayesian analysis by using BBH events with SNR > 12. The solid line represents the median values, while the shaded area shows the 90% confidence intervals.

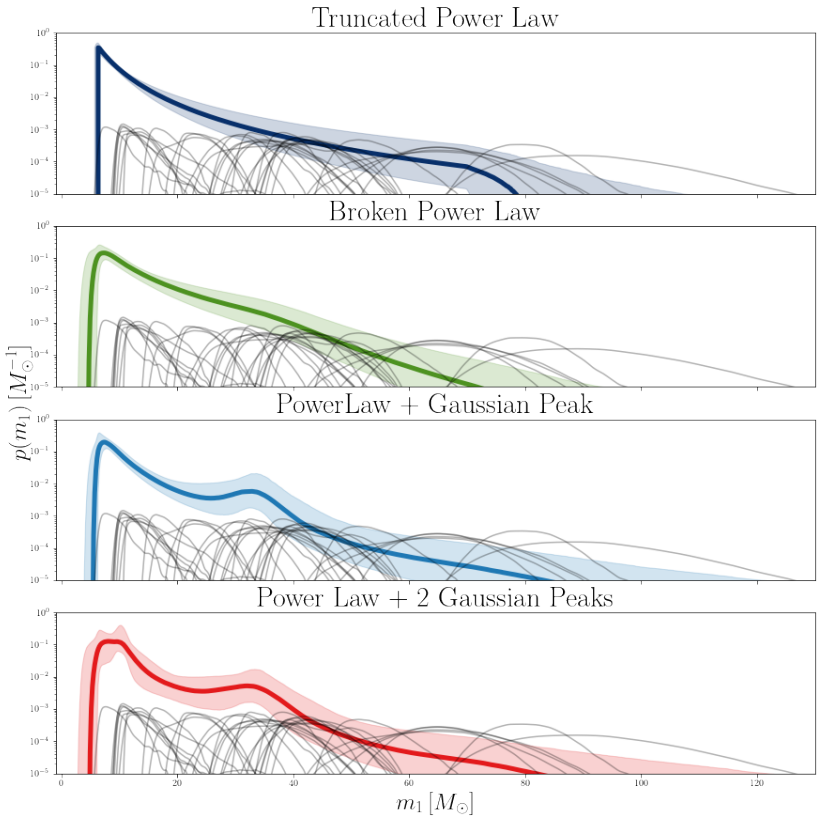

Figure 4.6: Mass Functions obtained with parameters presented in this section using SNR > 12 BBH events: single mass function (coloured) with considered events (grey).

4.1.5 Model Comparison

Now that all the mass distributions have been presented, it is possible to compare in a more complete and systematic way the obtained results by looking at the common and most important parameters, reported in Table 4.6 with the corresponding corner plot in Figure 4.7a. In addition to this, a superimposition of the mass functions with all the events considered is presented in Figure 4.8.

Furthermore, in order to make the result evaluation more complete and more quantitative, a detailed model selection will be presented in Section 4.4, in which the preferred model by the data will be determined.

To simplify the discussion regarding the constraining power of the different models, we assume the errors of each parameter as a "Gaussianized" error, i.e. the mean between the

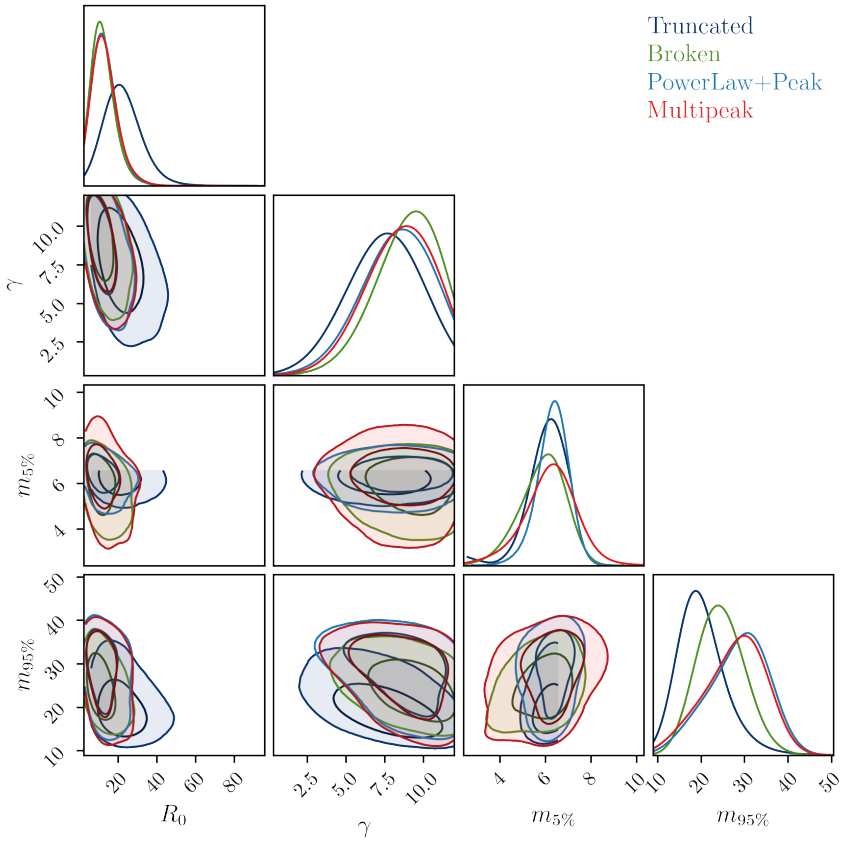

(a)

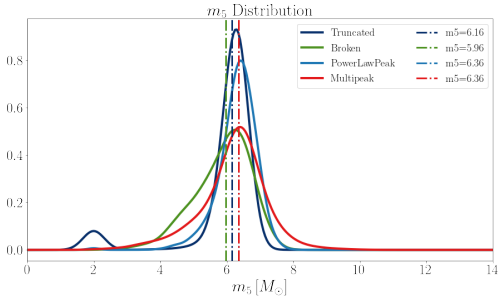

(b)

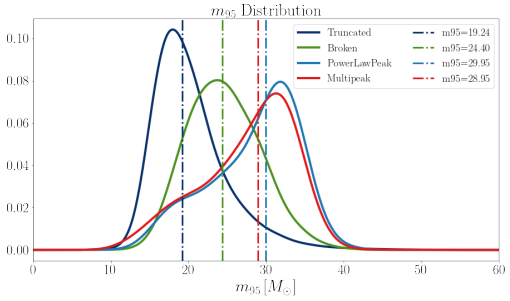

(c)

Figure 4.7: (a) Corner plot for the common parameters for the different mass functions obtained by using SNR >12 BBH events. A zoomed view of $m_{5\%}$ and $m_{95\%}$ distributions is presented in (b) and (c) respectively.

upper and lower errors of a given parameter[1]. In order to evaluate the constraining power

[1]

$$\epsilon_g = \frac{\epsilon_u + \epsilon_l}{2}$$

SNR > 12	R_0 $[1/Gpc^3/yr]$	γ	m_l $[M_\odot]$	m_h $[M_\odot]$	$m_{5\%}$ $[M_\odot]$	$m_{95\%}$ $[M_\odot]$
`Truncated`	$21.46^{+8.33}_{-6.38}$	$7.63^{+1.94}_{-2.18}$	$6.17^{+0.18}_{-0.30}$	$79.58^{+17.93}_{-6.88}$	$6.16^{+0.20}_{-0.20}$	$19.24^{+5.15}_{-3.16}$
`Broken`	$11.33^{+5.85}_{-3.78}$	$9.27^{+1.66}_{-2.06}$	$4.29^{+1.17}_{-1.32}$	$118.03^{+50.53}_{-33.16}$	$5.96^{+0.79}_{-0.99}$	$24.40^{+4.95}_{-4.36}$
`PowerLawPeak`	$12.12^{+5.90}_{-4.08}$	$8.51^{+1.98}_{-2.08}$	$5.14^{+0.70}_{-0.98}$	$116.01^{+54.32}_{-31.24}$	$6.36^{+0.40}_{-0.59}$	$29.95^{+3.96}_{-8.13}$
`Multipeak`	$12.17^{+6.00}_{-4.14}$	$8.73^{+1.94}_{-2.11}$	$4.52^{+1.09}_{-1.45}$	$112.34^{+54.39}_{-29.36}$	$6.36^{+0.59}_{-0.99}$	$28.95^{+4.36}_{-8.13}$

Table 4.6: Common astrophysical parameters obtained in the fixed cosmology analysis for SNR > 12.

on each parameter, it is necessary to compare the corresponding percentage errors: the smaller the error the most constrained the parameter is. Therefore, to get a better insight in Table 4.7 the obtained "Gaussianized" percentage errors of each parameter are reported.

SNR > 12	ΔR_0	$\Delta\gamma$	Δm_l	Δm_h	$\Delta m_{5\%}$	$\Delta m_{95\%}$
`Truncated`	0.34	0.27	0.04	0.16	0.03	0.22
`Broken`	0.42	0.20	0.29	0.35	0.15	0.19
`PowerLawPeak`	0.44	0.24	0.16	0.37	0.08	0.20
`Multipeak`	0.42	0.23	0.28	0.37	0.12	0.22

Table 4.7: Percentage errors of the parameters obtained in the population analysis for SNR > 12.

By focusing on Table 4.7, it can be observed that the broken power law seems to be the most constraining model based on the fact that it has the smallest error in two cases (γ and $m_{95\%}$), the second smallest on R_0, and the largest only once: $m_{5\%}$. This model is just followed by the truncated mass function, which is the most constraining in two cases (R_0 and $m_{5\%}$), but the worst one in regards to γ and $m_{95\%}$. In contrast, `PowerLawPeak` and `Multipeak` appear to be similarly bad in relation to their constraining power.

Such a result is not surprising at all once the number of parameters of each model is taken into account. As described in Section 3, the truncated power law and the broken power law have the least number of parameters: 10 and 13, respectively, thus corresponding to the least number of degrees of freedom. As a result of this, the degeneracy between the different parameters is lower, thus leading to smaller errors. Following the same logic, it becomes clear why the `Multipeak` and the single peak models appear to be less constraining: the single peak has 15 parameters, while the double peak has 17 parameters. Therefore, from this observation, it can be inferred that the truncated power law will probably not

be the best model to describe the observed events, due to the fact that even though it has fewer free parameters it is not able to constrain them in a stronger manner. Even if the `Multipeak` seems to be more constraining than `PowerLawPeak`, a similar strong conclusion cannot be drawn, because the difference in constraining power is too little, at most 4% for $m_{5\%}$, with respect to the corresponding number of parameters. Nevertheless, the similarity of these two models and the need for the additional peak will be investigated further in Section 4.4 thanks to a complete model selection analysis. So, by temporarily passing over the small differences between the double and the single peak models and by discarding the truncated mass function, the ranking of the constraining power follows the number of degrees of freedom.

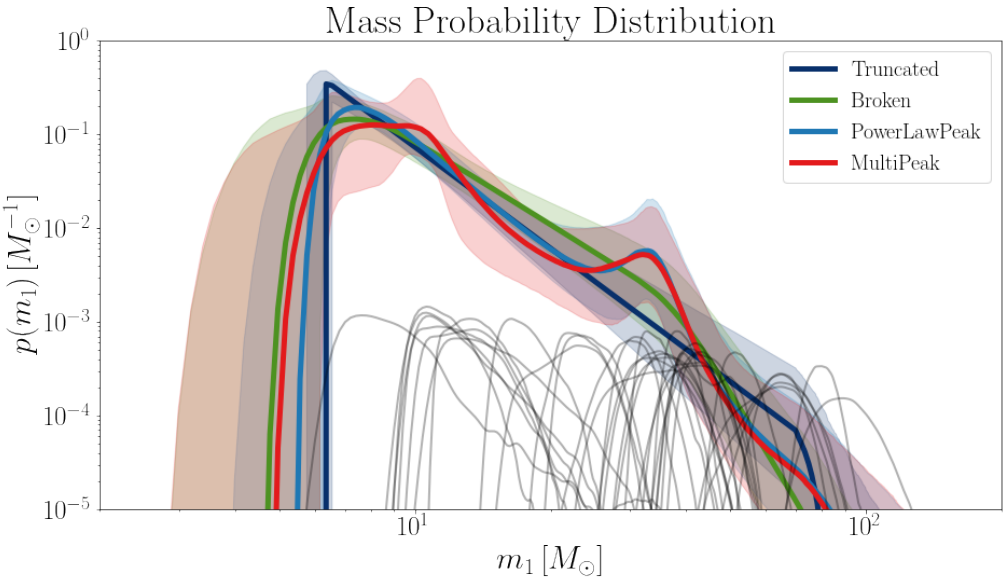

Figure 4.8: Superimposition of the mass functions obtained with parameters presented in this section using SNR >12 BBH events. The different colors represent the different models as described in the legend, with the solid line indicating the median, the shaded area the 95% confidence interval, and in grey the selected GW events.

At last, we focus on Figure 4.8, which displays a superimposition of the mass functions obtained by fitting the 35 BBH events with SNR >12. It can be observed how the distributions fit the data differently at different mass scales. In particular, by concentrating on the high end of the mass function, it stands out how the introduction of some feature to better fit the data with respect to simple truncated power law is necessary. In fact, the truncation at $\sim 80\,M_\odot$ is not able to describe the higher mass events. Similarly, it appears that the introduction of a second slope within the first truncated power law, i.e. defining the broken power law, is not enough to increase the goodness-of-fit of the high-end mass scale. On the contrary, both the power law + peak and the multipeak models, thanks to a Gaussian peak at $M\sim 30\,M_\odot$, are able to reproduce the high-end event distribution, thus

giving a first indication of which mass functions will be the favoured ones.

Moreover, two additional features of the event distribution, that have to be fitted, are the concentrations at two different mass scales: $\sim 10\,M_\odot$ and $\sim 30\,M_\odot$ [116]. Clearly, the truncated power law lacks the ability to reproduce such features, and this is the reason why the second slope was first introduced. Despite the fact that a higher value around the $30\,M_\odot$ mass scale with respect to the truncated mass function is reached, at the low mass scale no significant difference can be observed, making this model again not the perfect fit for the data. The same behaviour can be spotted also for the single peak model, even though the $30\,M_\odot$ mass scale is fitted better thanks to the implementation of the Gaussian peak. Therefore, the power law + peak model will probably be favoured as a mass function candidate. It is now evident why it was necessary to implement the second Gaussian peak and construct the multipeak mass function. In fact, it is the best model to reproduce both event concentrations, especially the peak at $\sim 10\,M_\odot$.

Nevertheless, these conclusions are only qualitative ones, hence it is crucial to strengthen this evidence in a more quantitative way: this is provided thanks to the model selection described in Section 4.4.

4.2 Exploring the Cosmological Constraints

Now that the population analysis is complete, we move on by adding new degrees of freedom into our system, in particular by taking also the Hubble constant H_0 and the mass density parameter $\Omega_{0,m}$ into the equation as free parameters. In particular, in this section, the results found by doing the same analysis as before will be described, with the difference that in this case, the parameters to be constrained are $\Lambda \equiv \{\Lambda_{astro}, \Lambda_{cosmo}\}$ where $\Lambda_{cosmo} = \{H_0,\, \Omega_{0,m}\}$.

As in the previous section, the results will be only presented for the 35 events with $SNR > 12$, while a broader analysis of the 80 BBH events with $SNR > 8$ is reported in Appendix A. Moreover, the analysis was again made for all the four mass function models presented in Chapter 3 by assuming the flat priors displayed in Table 4.8.

As previously, the corner plot will be discussed only in this first case, in order to make some first evaluations about the potential constraining power of the studied parameters. For the other mass distributions, the plots will be presented in Appendix B. Therefore, by looking at 4.9 it stands out that, again, κ, z_p, and δ_m can be neglected during the analysis, as their distributions are almost flat. In addition to this also $\Omega_{0,m}$ will be omitted as a result of the unconstrained distribution obtained.

Moreover, by following the same logic described in the previous section the analysis for parameters α and β will be neglected and, instead of evaluating m_l and m_h, the 5% and 95% percentile will be studied, respectively. Therefore, the entire analysis described in this section will be concentrating on the evaluation of the following parameters: $\Lambda = \{\, H_0, R_0, \gamma, m_{5\%}, m_{95\%} \,\}$, with eventually a smaller focus on λ_g and λ_1, when analysing `PowerLawPeak` and `Multipeak`.

Parameter	H_0	$\Omega_{0,m}$	R_0	λ_z	α_z	β_z	z_p
Range	$\mathcal{U}(10, 200)$	$\mathcal{U}(0.05, 1)$	$\mathcal{U}(0, 100)$	$\mathcal{U}(-15, 15)$	$\mathcal{U}(0, 12)$	$\mathcal{U}(0, 6)$	$\mathcal{U}(0, 4)$

Parameter	α	β	m_l	s_l	m_h	s_l
Range	$\mathcal{U}(1.5, 12)$	$\mathcal{U}(-4, 12)$	$\mathcal{U}(2, 50)$	$\mathcal{U}(0.01 , 1)$	$\mathcal{U}(50, 200)$	$\mathcal{U}(0.01 , 1)$

Parameter	α_1	α_2	δ_m	b	μ_{eff}	χ_{eff}
Range	$\mathcal{U}(1.5, 12)$	$\mathcal{U}(1.5, 12)$	$\mathcal{U}(0, 10)$	$\mathcal{U}(0, 1)$	$\mathcal{U}(-1, 1)$	$\mathcal{U}(0.01, 1)$

Parameter	μ_p	σ_p	λ_p	μ_g	σ_g
Range	$\mathcal{U}(0.01, 1)$	$\mathcal{U}(0.01, 1)$	$\mathcal{U}(0, 1)$	$\mathcal{U}(20, 50)$	$\mathcal{U}(0.4, 10)$

Parameter	λ_1	μ_1	σ_1	μ_2	σ_2
Range	$\mathcal{U}(0, 1)$	$\mathcal{U}(20, 50)$	$\mathcal{U}(0.4, 10)$	$\mathcal{U}(7, 15)$	$\mathcal{U}(0.4, 5)$

Table 4.8: Prior choice for the entire free cosmology analysis. The parameters follow the definitions presented in Section 3.4 and Section 3.5.

4.2.1 Analysis of the Truncated Power Law Model

Following the same order as before, the truncated power law is the first mass function to be presented. The obtained values are displayed in Figure B.13 and summarized in Table 4.9 with median, 68%, and 90% confidence intervals (C.I.).

Table 4.9 provide a first value for $H_0 = 90.56^{+52.05}_{-44.32}$ km/s/Mpc. Despite being much larger with respect to the accepted Planck value of 67.4 km/s/Mpc, the estimate obtained for `Truncated` is consistent with it.

The mass function obtained with those values is shown in Figure 4.10.

4.2.2 Analysis of the Broken Power Law Model

The next studied mass function is the broken power law. The resulting values are shown in the corner plot in Figure B.14 and then summarized in Table 4.10 with median, 68% and 90% confidence intervals (C.I.).

By comparing these two mass functions some first observations can be made. For example, by comparing the parameters defining the merger rate evolution, it stands out that the normalization R_0 is much larger in the truncated model than in `Broken`, while the slope γ is found to have an opposite behaviour: larger in the broken power law and smaller in `Truncated`. Thus, eventually suggesting that in the broken mass function the larger slope tends to compensate for the smaller normalization. As in the population case, the parameters defining the mass slopes (α an α_1) have comparable and consistent values

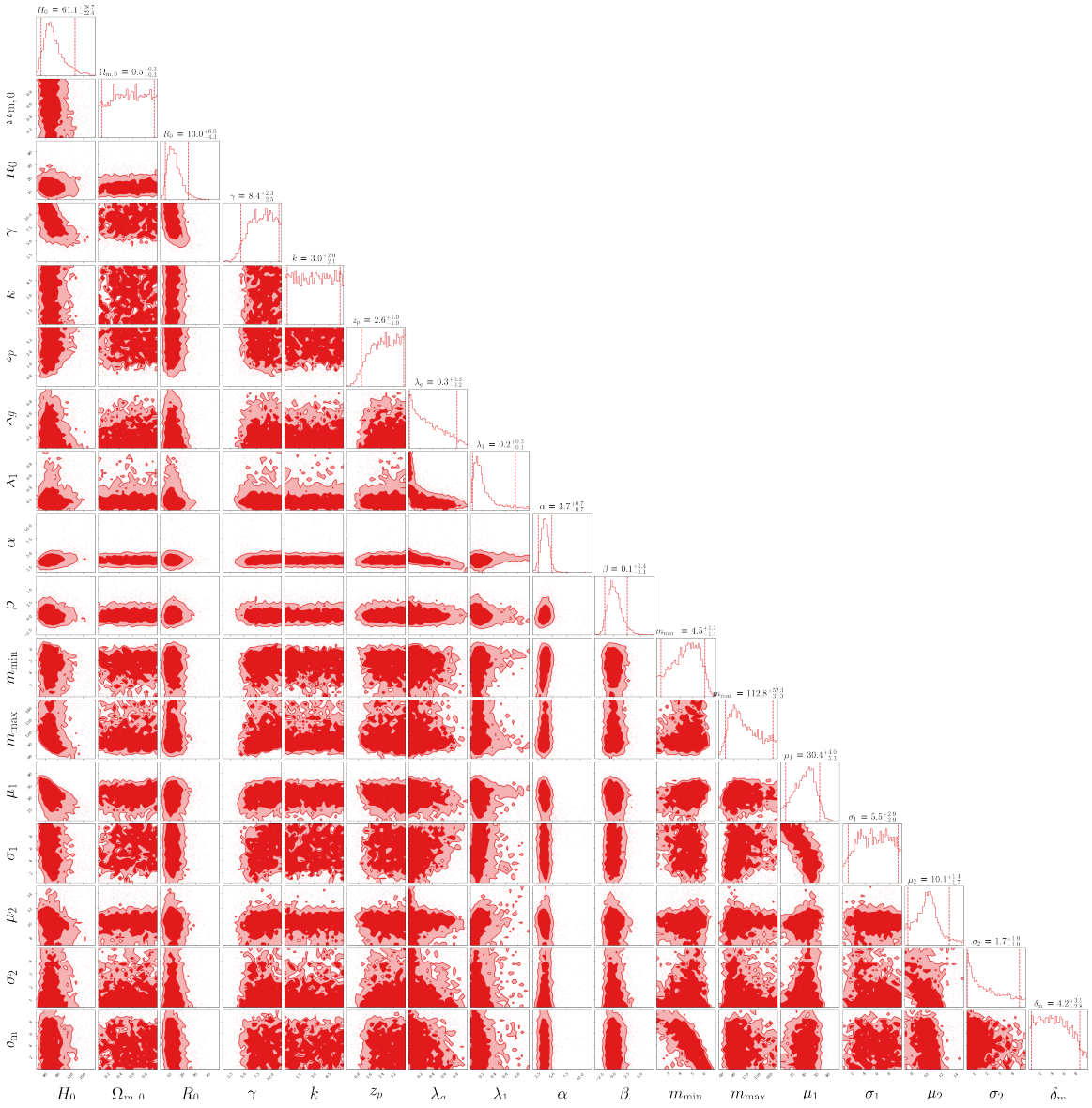

Figure 4.9: Corner plot for the `Multipeak` parameters obtained from the Bayesian analysis by using BBH events with SNR > 12.

$(3.47^{+0.48}_{-0.49}$ vs. $2.86^{+0.59}_{-0.59})$, as expected due to the similar nature of those two parameters.

At last, the Hubble constant can be considered. In this case, the obtained value is $H_0 = 74.48^{+52.00}_{-31.73}$ km/s/Mpc, which is a much smaller value compared to the value obtained for the truncated power law, thus more similar to the expected value, but due to the big error linked to both results it is not possible to infer which of the two cases is the better estimate.

The mass function obtained with such values is shown in Figure 4.11.

C.I.	H_0 [km/s/Mpc]	$\Omega_{0,m}$
68%	$90.56^{+52.05}_{-44.32}$	$0.53^{+0.31}_{-0.32}$
90%	$90.56^{+83.81}_{-63.52}$	$0.53^{+0.42}_{-0.42}$

C.I.	R_0 [1/Gpc^3/yr]	γ	κ	z_p
68%	$23.71^{+11.30}_{-7.70}$	$6.23^{+2.45}_{-1.88}$	$2.91^{+2.12}_{-2.02}$	$2.56^{+0.99}_{-1.13}$
90%	$23.71^{+21.68}_{-11.54}$	$6.23^{+4.33}_{-2.96}$	$2.91^{+2.79}_{-2.62}$	$2.56^{+1.30}_{-1.74}$

C.I.	α	β	m_l [$M_\odot$]	m_h [$M_\odot$]
68%	$3.47^{+0.48}_{-0.49}$	$0.67^{+1.57}_{-1.37}$	$5.94^{+0.42}_{-0.43}$	$71.06^{+35.45}_{-15.33}$
90%	$3.47^{+0.80}_{-0.81}$	$0.67^{+2.63}_{-2.10}$	$5.94^{+0.67}_{-1.00}$	$71.06^{+82.41}_{-19.32}$

Table 4.9: Cosmological and astrophysical parameters obtained for the truncated power law model from the Bayesian analysis by using BBH events with SNR > 12.

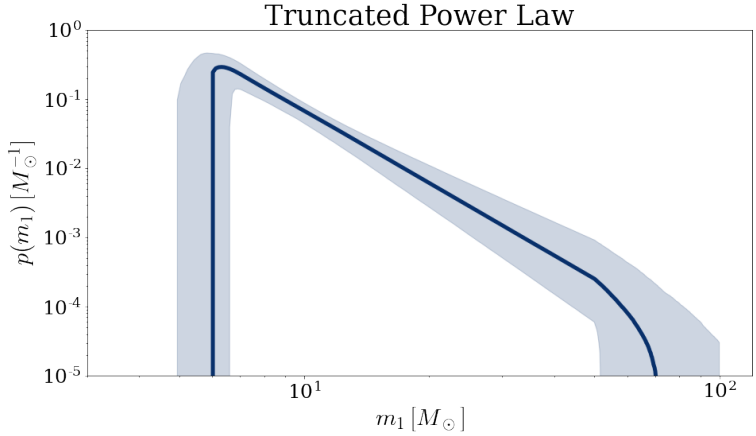

Figure 4.10: Truncated power law obtained from the Bayesian analysis by using BBH events with SNR > 12. The solid line represents the median values, while the shaded area shows the 90% confidence intervals.

C.I.	H_0 [km/s/Mpc]	$\Omega_{0,m}$
68%	$74.48^{+52.00}_{-31.73}$	$0.56^{+0.30}_{-0.32}$
90%	$74.48^{+91.23}_{-45.11}$	$0.56^{+0.39}_{-0.44}$

C.I.	R_0 [1/Gpc^3/yr]	γ	κ	z_p	α_1
68%	$14.07^{+8.31}_{-5.05}$	$7.74^{+2.74}_{-2.38}$	$3.04^{+1.94}_{-2.01}$	$2.74^{+0.88}_{-1.06}$	$2.86^{+0.59}_{-0.59}$
90%	$14.07^{+16.47}_{-7.36}$	$7.74^{+3.78}_{-3.67}$	$3.04^{+2.66}_{-2.70}$	$2.74^{+1.15}_{-1.63}$	$2.86^{+1.00}_{-0.94}$

C.I.	α_2	β	δ_m	m_l [$M_\odot$]	m_h [$M_\odot$]	b
68%	$7.83^{+2.22}_{-1.74}$	$0.54^{+1.48}_{-1.18}$	$4.65^{+2.88}_{-3.01}$	$4.16^{+1.21}_{-1.34}$	$116.17^{+51.00}_{-36.67}$	$0.30^{+0.15}_{-0.10}$
90%	$7.83^{+3.45}_{-2.79}$	$0.54^{+2.42}_{-1.83}$	$4.65^{+4.31}_{-4.07}$	$4.16^{+1.73}_{-1.87}$	$116.17^{+72.84}_{-52.37}$	$0.30^{+0.29}_{-0.13}$

Table 4.10: Cosmological and astrophysical parameters obtained for the broken power law model from the Bayesian analysis by using BBH events with SNR > 12.

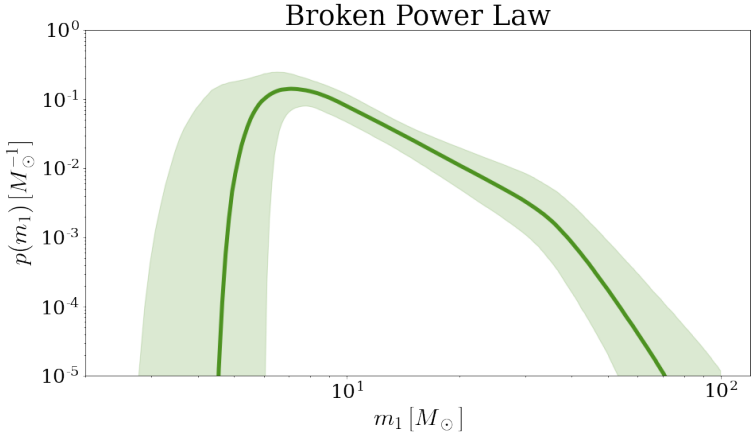

Figure 4.11: Broken power law obtained from the Bayesian analysis by using BBH events with SNR > 12. The solid line represents the median values, while the shaded area shows the 90% confidence intervals.

4.2.3 Analysis of the Power Law + Gaussian Peak Model

Moving on, the next mass function to be studied is the power law + Gaussian peak. The resulting values are shown in the corner plot in Figure B.15 and then summarized in Table 4.4 with median, 68%, and 90% confidence intervals (C.I.).

C.I.	H_0 [km/s/Mpc]	$\Omega_{0,m}$
68%	$62.83^{+43.08}_{-26.01}$	$0.53^{+0.32}_{-0.32}$
90%	$62.83^{+82.76}_{-37.31}$	$0.53^{+0.43}_{-0.43}$

C.I.	R_0 [1/Gpc^3/yr]	γ	κ	z_p	α	β
68%	$14.72^{+8.55}_{-5.20}$	$7.68^{+2.89}_{-2.58}$	$3.01^{+2.08}_{-2.07}$	$2.59^{+0.96}_{-1.08}$	$4.05^{+0.59}_{-0.55}$	$0.04^{+1.40}_{-1.07}$
90%	$14.72^{+15.58}_{-7.62}$	$7.68^{+3.87}_{-3.97}$	$3.01^{+2.72}_{-2.70}$	$2.59^{+1.27}_{-1.65}$	$4.05^{+1.08}_{-0.88}$	$0.04^{+2.50}_{-1.70}$

C.I.	δ_m	m_l [$M_\odot$]	m_h [$M_\odot$]	λ_p	μ_g [$M_\odot$]	σ_g [$M_\odot$]
68%	$3.99^{+2.69}_{-2.64}$	$5.10^{+0.78}_{-0.99}$	$121.19^{+50.44}_{-35.75}$	$0.03^{+0.04}_{-0.02}$	$31.42^{+3.73}_{-4.91}$	$4.56^{3.13}_{2.33}$
90%	$3.99^{+4.38}_{-3.56}$	$5.10^{+1.13}_{-1.72}$	$121.19^{+69.33}_{-50.50}$	$0.03^{+0.08}_{-0.02}$	$31.42^{+5.92}_{-8.49}$	$4.56^{4.59}_{3.44}$

Table 4.11: Cosmological and astrophysical parameters obtained for the power law + peak model obtained from the Bayesian analysis by using BBH events with SNR > 12.

As always, it is possible to draw some observations from the obtained values. First, we compare the values obtained for α: the result obtained for the power law + peak model is larger than both results from the previous mass functions, in particular, it is consistent with the one found for the truncated power law, while it is not consistent with the one from the broken model. This is probably due to the fact that `PowerLawPeak` starts to be too different from the broken mass function, while the `Truncated` is still comparable probably thanks to the fact that the single peak model is just defined as "the same" model with an additional Gaussian peak. In contrast to this, the values obtained for the merger rate (R_0 and γ) are much more similar to values found for `Broken` than to the ones for the truncated model. Moreover, it is obtained $\lambda_p = 0.03$, which means that the Gaussian peak prevails on the basic truncated power law by only 3%.

Lastly, the H_0 obtained is even smaller than the value found for the broken mass function, but the deviation from the Planck value is only of ~ 4.91 km/s/Mpc. Nevertheless,

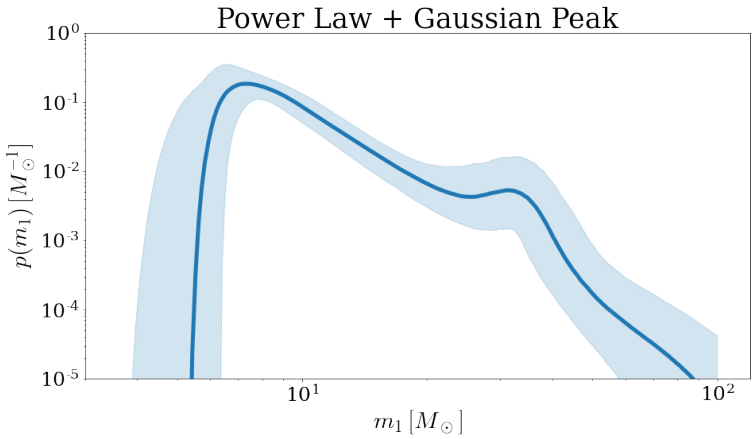

Figure 4.12: Power law + Gaussian peak obtained from the Bayesian analysis by using BBH events with SNR > 12. The solid line represents the median values, while the shaded area shows the 90% confidence intervals.

due to the wide error range, it is not possible to conclude any assumption on the goodness-of-estimate of this model with respect to the other ones.

The mass function obtained with such values is shown in Figure 4.4.

4.2.4 Analysis of the Power Law + Two Gaussian Peaks Model

The last mass function to be presented is the power law + two Gaussian peaks. The resulting values are shown in the corner plot in Figure 4.9 and then summarized in Table 4.12 with median, 68% and 90% confidence intervals (C.I.).

Surprisingly, despite the big differences between this multipeak model and the other presented mass functions, the value obtained for $\alpha = 3.67^{+1.30}_{-1.15}$ is consistent with all other corresponding found values. Furthermore, it is possible to compare the parameters defining the "high mass" Gaussian peak. In particular, the same behaviour as in the population analysis is found: the multipeak has a lower mass scale ($30.36^{+3.98}_{-5.27}\,\mathrm{M}_\odot$) but with a larger peak ($5.50^{+2.88}_{-2.86}\,\mathrm{M}_\odot$), while `PowerLawPeak` has a higher mass scale ($31.42^{+3.73}_{-4.91}\,\mathrm{M}_\odot$) but with a narrower peak ($4.56^{3.13}_{2.33}\,\mathrm{M}_\odot$). So, the lower mass scale is compensated by the larger peak width. Moreover, it worth noticing that the "low mass" peak is obtained to be $\mu_2 = 10.07^{+1.37}_{-1.67}\,\mathrm{M}_\odot$ in accordance with the value obtained for the substructure found by [11]: $\mu \sim 10\,\mathrm{M}_\odot$.

At last, the value obtained for the Hubble constant is the lowest of all four estimates: $\mathrm{H}_0 = 61.10^{+38.65}_{-22.43}\,\mathrm{km/s/Mpc}$. The value found is quite similar to the one obtained for the single peak model, thus it suggests a similar behaviour in parameter space for the two models, thus a similar "goodness-of-fit". In addition to this, it can be observed that the deviation of the multipeak model from the Planck value is comparable to the deviation of the broken power law: ~ 6.64 and ~ 6.74, respectively.

The mass function obtained with such values is shown in Figure 4.13.

C.I.	H_0 [km/s/Mpc]	$\Omega_{0,m}$
68%	$61.10^{+38.65}_{-22.43}$	$0.55^{+0.31}_{-0.31}$
90%	$61.10^{+73.92}_{-34.67}$	$0.55^{+0.41}_{-0.44}$

C.I.	R_0 [1/Gpc^3/yr]	γ	κ	z_p	α
68%	$12.95^{+6.03}_{-4.33}$	$8.41^{+2.32}_{-2.52}$	$3.03^{+2.01}_{-2.12}$	$2.61^{+0.96}_{-1.04}$	$3.67^{+0.73}_{-0.69}$
90%	$12.95^{+11.67}_{-6.25}$	$8.41^{+3.17}_{-3.92}$	$3.03^{+2.66}_{-2.74}$	$2.61^{+1.26}_{-1.54}$	$3.67^{+1.30}_{-1.15}$

C.I.	β	δ_m	m_l [$M_\odot$]	m_h [$M_\odot$]	λ_p
68%	$0.09^{+1.39}_{-1.10}$	$4.20^{+3.09}_{-2.76}$	$4.52^{+1.06}_{-1.41}$	$112.84^{+52.29}_{-31.35}$	$0.29^{+0.35}_{-0.22}$
90%	$0.09^{+2.53}_{-1.70}$	$4.20^{+4.47}_{-3.71}$	$4.52^{+1.52}_{-2.13}$	$112.84^{+75.66}_{-44.03}$	$0.29^{+0.53}_{-0.27}$

C.I.	λ_1	μ_1 [$M_\odot$]	σ_1 [$M_\odot$]	μ_2 [$M_\odot$]	σ_2 [$M_\odot$]
68%	$0.18^{+0.25}_{-0.10}$	$30.36^{+3.98}_{-5.27}$	$5.50^{+2.88}_{-2.86}$	$10.07^{+1.37}_{-1.67}$	$1.71^{+1.92}_{-1.04}$
90%	$0.18^{+0.58}_{-0.13}$	$30.36^{+6.11}_{-8.13}$	$5.50^{+3.91}_{-4.16}$	$10.07^{+2.99}_{-2.58}$	$1.71^{+2.81}_{-1.23}$

Table 4.12: Cosmological and astrophysical parameters obtained for the power law + 2 peaks model obtained from the Bayesian analysis by using BBH events with SNR > 12.

To conclude this section, before moving on with a more complete model comparison, an overview of the different mass functions discussed in this section is given in Figure 4.6.

4.2.5 Model Comparison

Now that all the mass distributions are defined, it is possible to move on to the comparison of that models with the aim of finding which one is the best to describe the real BBH distribution given by the data. In order to do that a summary of the common parameters is reported in Table 4.13 with the corresponding corner plot in Figure 4.15a. To complete the overview, a superimposition of the mass functions with all the events considered is

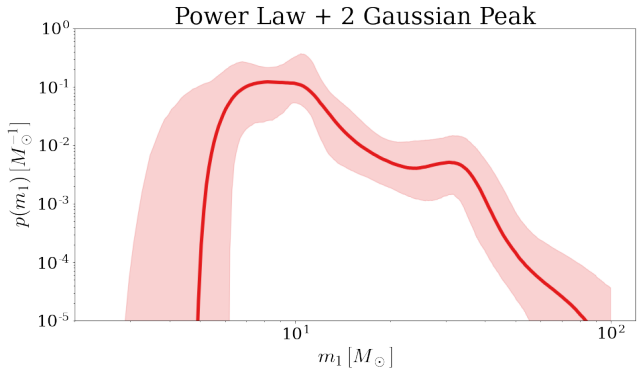

Figure 4.13: Power law + two Gaussian peaks obtained from the Bayesian analysis by using events with SNR > 12. The solid line represents the median values, while the shaded area shows the 90% confidence intervals.

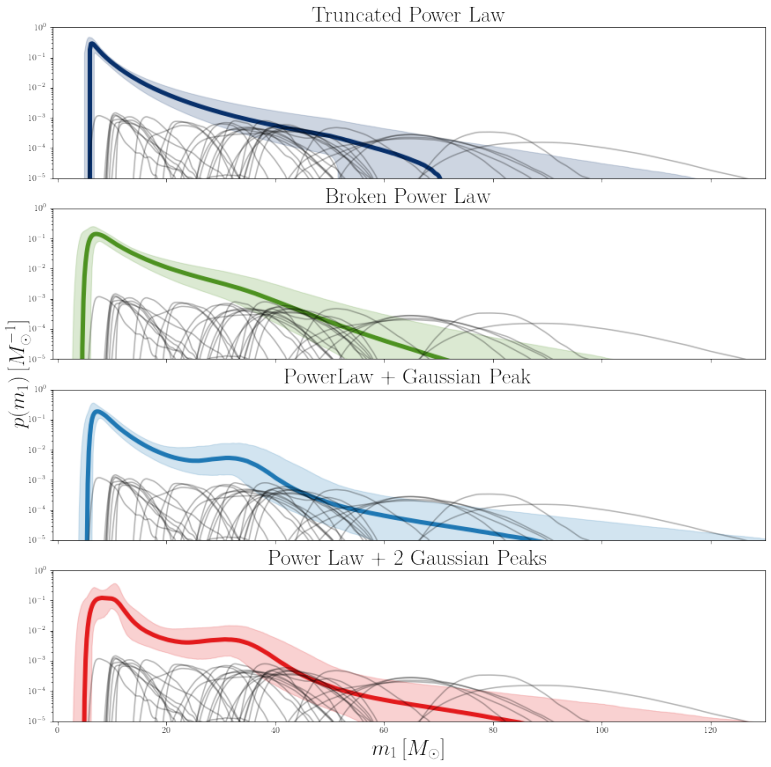

Figure 4.14: Mass Functions obtained with parameters presented in this section using SNR > 12 BBH events: single mass function (coloured) with considered events (grey).

presented in Figure 4.16.

As before, an exhaustive model selection will be presented in Section 4.4, in which, assuming the additional two free cosmological parameters, the preferred model by the data will be determined.

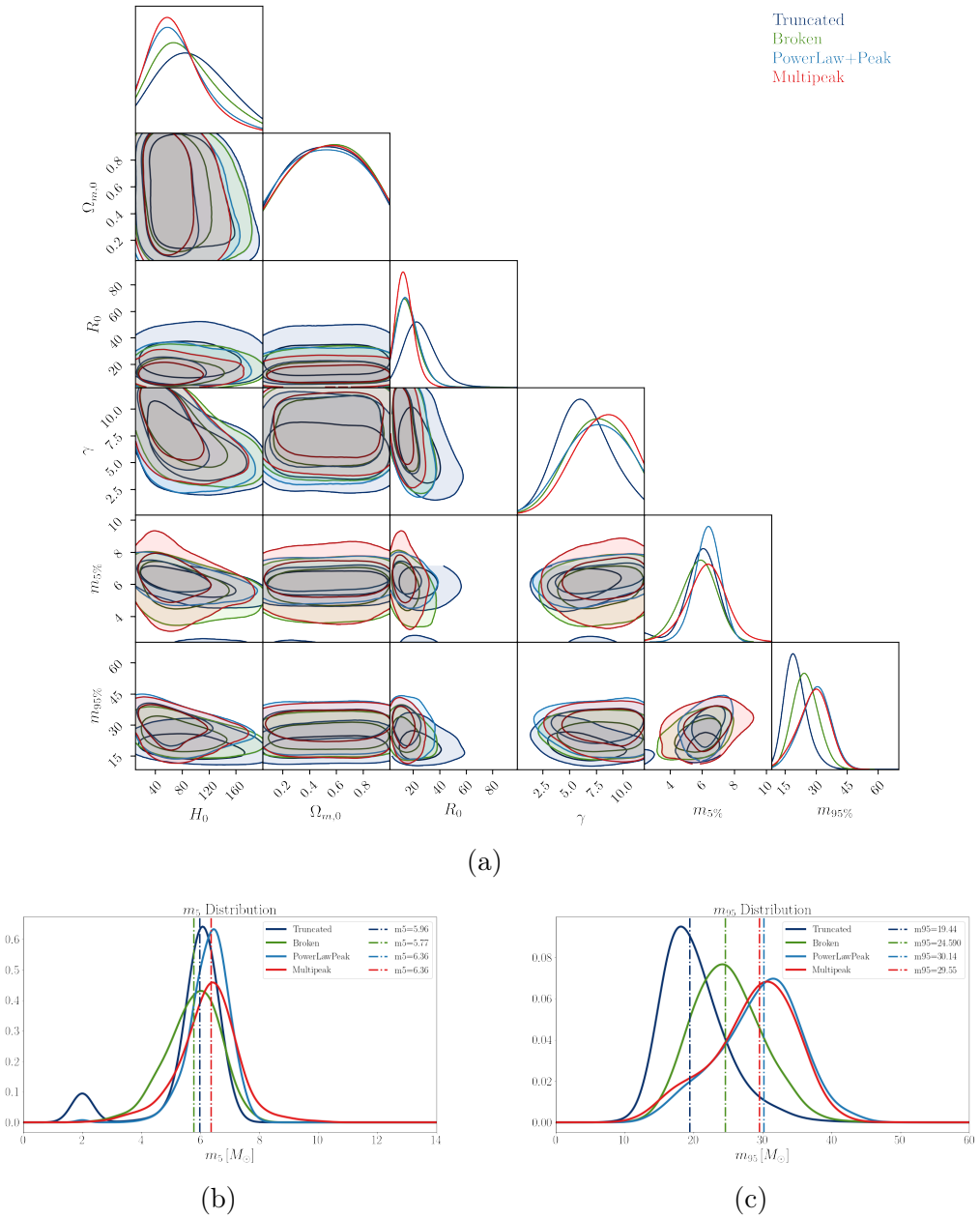

(a)

(b) (c)

Figure 4.15: (a) Corner plot for the common parameters for the different mass functions obtained by using SNR > 12 BBH events. A zoomed look of $m_{5\%}$ and $m_{95\%}$ distributions is presented in (b) and (c) respectively.

As done in Section 4.1.5, in order to evaluate the constraining power on each parameter,

SNR > 12	H_0 [km/s/Mpc]	R_0 [1/Gpc^3/yr]	γ	m_l [$M_\odot$]	m_h [$M_\odot$]	$m_{5\%}$ [$M_\odot$]	$m_{95\%}$ [$M_\odot$]
`Truncated`	$90.56^{+52.05}_{-44.32}$	$27.31^{+11.30}_{-7.70}$	$6.23^{+2.45}_{-1.88}$	$5.94^{+0.42}_{-0.43}$	$71.06^{+35.45}_{-15.33}$	$5.96^{+0.59}_{-0.59}$	$19.44^{+5.15}_{-3.37}$
`Broken`	$74.48^{+52.00}_{-31.73}$	$14.07^{+8.31}_{-5.05}$	$7.74^{+2.74}_{-2.38}$	$4.16^{+1.21}_{-1.34}$	$116.17^{+51.00}_{-36.67}$	$5.77^{+0.79}_{-0.99}$	$24.59^{+5.35}_{-4.56}$
`PowerLawPeak`	$62.83^{+43.08}_{-26.01}$	$14.72^{+8.55}_{-5.20}$	$7.68^{+2.89}_{-2.58}$	$5.10^{+0.78}_{-0.99}$	$121.19^{+50.44}_{-35.75}$	$6.36^{+0.59}_{-0.59}$	$30.14^{+4.95}_{-6.94}$
`Multipeak`	$61.10^{+38.65}_{-22.43}$	$12.95^{+6.03}_{-4.33}$	$8.41^{+2.32}_{-2.52}$	$4.52^{+1.06}_{-1.41}$	$112.84^{+52.29}_{-31.35}$	$6.36^{+0.79}_{-0.99}$	$29.55^{+4.95}_{-7.53}$

Table 4.13: Common cosmological and astrophysical parameters for SNR > 12 obtained by freeing the H_0 parameter.

the corresponding "Gaussianized" percentage errors will be compared. Therefore, to get a better insight in Table 4.14 the obtained percentage errors of each parameter are reported.

SNR > 12	ΔH_0	ΔR_0	$\Delta\gamma$	Δm_l	Δm_h	$\Delta m_{5\%}$	$\Delta m_{95\%}$
`Truncated`	0.53	0.35	0.35	0.07	0.36	0.10	0.22
`Broken`	0.56	0.47	0.33	0.31	0.38	0.15	0.20
`PowerLawPeak`	0.55	0.47	0.36	0.17	0.36	0.09	0.20
`Multipeak`	0.50	0.40	0.29	0.27	0.37	0.14	0.21

Table 4.14: Percentage errors of the parameters obtained in the free cosmology analysis for SNR > 12.

By focusing on Table 4.14, it is possible to infer that the largest constraining power of the different model is of the multipeak mass function based on the fact that it has the smallest error twice (H_0 and γ), the second best once (R_0), and the third smallest twice ($m_{5\%}$ and $m_{95\%}$). Regarding the constraining power, the second best model appears to be the power law + peak model, which has the most constraining parameter two times ($m_{5\%}$ and $m_{95\%}$), the third best two times (H_0 and R_0), and the worst one only one time (γ). In general, the difference between these two models is almost negligible as the percentage error is at maximum 7%, hence it is not possible to exclude `PowerLawPeak` from the analysis. Nevertheless, the `Multipeak` has more parameters than the single peak model, and thus it is probably a better fit model for the data. The other two mass functions (`Truncated` and `Broken`) appear to be similarly bad in regard to their constraining power and, due to their smaller number of parameters, they are probably disfavoured as candidate best-fit models, especially the truncated model that has only 10 parameters.

This result is extremely different from the one obtained in the population analysis. It appears that the addition of the two cosmological parameters, H_0 and $\Omega_{0,m}$, tends to reward the more complex mass functions with better constraining power, hence suggesting that eventually, those models are the best ones to reproduce the events.

A more complete evaluation of the results obtained for the H_0 parameter is presented

in Section 4.2.6.

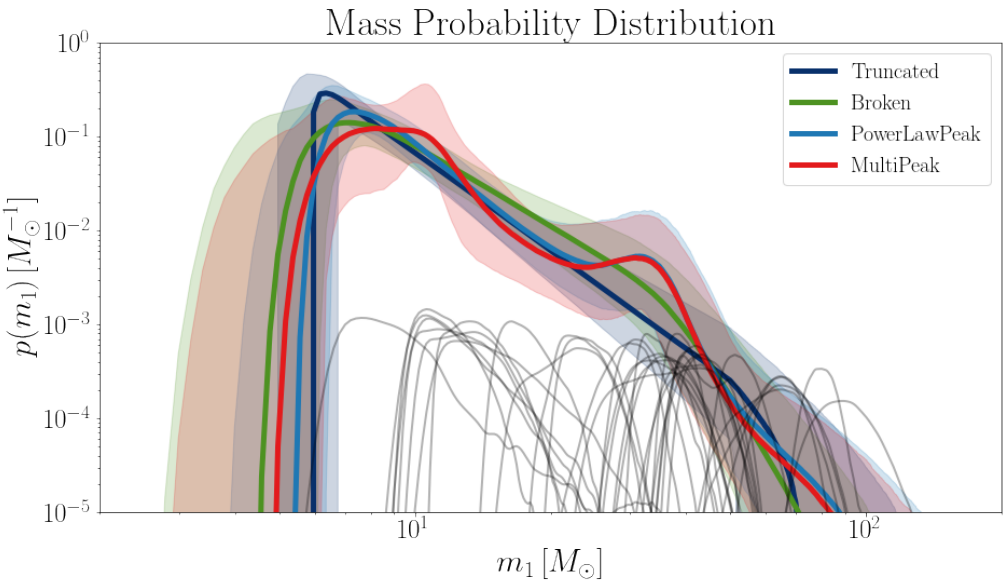

Figure 4.16: Superimposition of the mass functions obtained with parameters presented in this section using SNR >12 BBH events. The different colours represent the different models as described in the legend, with the solid line indicating the median, the shaded area the 95% confidence interval, and in grey the GW events.

At last, we focus on Figure 4.16, which displays a superimposition of the mass functions obtained by fitting the 35 events with SNR >12. It can be observed how the distributions fit the data differently at different mass scales in a similar way to the population analysis, thus it is possible to infer the same conclusion:

- **Truncated power law:** is not able to reproduce the $\sim 10\,M_\odot$ mass scale and not to fit the high mass events;
- **Broken power law:** the second power law is not enough to increase the goodness-of-fit of the high-end mass scale and at the lower mass scale the distribution does not implement any feature to fit the $\sim 10\,M_\odot$ scale structure;
- **Power law + peak:** fits the high-end event distribution, while at the lower end the model is similar to the broken power law;
- **Multipeak:** fits both mass structures thanks to the implementation of two Gaussian peaks at $\sim 10\,M_\odot$ and $\sim 30\,M_\odot$.

Therefore, as in the population analysis, the power law + two Gaussian peaks model will probably be favoured as mass function candidate.

Nevertheless, it is crucial to strengthen this evidence in a more quantitative way: the model selection described in Section 4.4 will provide the necessary proof.

4.2.6 Estimating the Hubble Constant with Dark Sirens

In this section, the main results regarding the H_0 distribution will be presented. First, it is worth taking a closer look at the values obtained for the Hubble constant, as reported in Table 4.15.

SNR > 12	H_0 [km/s/Mpc]	ϵ_g [km/s/Mpc]	$\epsilon_{\%}$
`Truncated`	$90.56^{+52.05}_{-44.32}$	± 48.19	0.53
`Broken`	$74.48^{+52.00}_{-31.73}$	± 41.87	0.56
`PowerLawPeak`	$62.83^{+43.08}_{-26.01}$	± 34.55	0.55
`Multipeak`	$61.10^{+38.65}_{-22.43}$	± 30.54	0.50

Table 4.15: H_0 values obtained from the free cosmology analysis with the corresponding "absolute Gaussianized" errors and the percentage errors.

It stands out that the multipeak model, despite not having the nearest value to the one obtained by Planck [4], represents the most constraining value of the four different models. However, as the percentage error describes, the difference in precision of the method is not more than 6%, thus it does not provide a strong enough evidence for a new constraint on the Hubble constant.

At last, we can focus on Figure 4.17 that displays the H_0 obtained distribution. The broadness of the different distributions follows, as expected, the trend of the "absolute" error presented in Table 4.15: the truncated mass function has the largest width corresponding to the largest error; while `Multipeak` is the narrowest model with the smallest error. Therefore, it seems that `Multipeak` is the best model to produce a H_0 distribution, thanks to its narrowness and hence making it also the model which potentially could be the best to break the Hubble tension. Nevertheless, due to a lack of precision in the estimates, which is linked to the small number of GW events observed available, no model can at the moment be excluded from the analysis, because all the models produce a predicted value consistent with both the Planck [4] and the SH0ES [5] values for H_0. A more complete and concrete analysis of the goodness-of-fit of each model for the H_0 case will be presented in Section 4.4.

4.3 Comparison of the Results between Fixed and Free Cosmology

We can now move on to the model comparison between mass distributions obtained from the fixed cosmology analysis and the free cosmology analysis by confronting the results

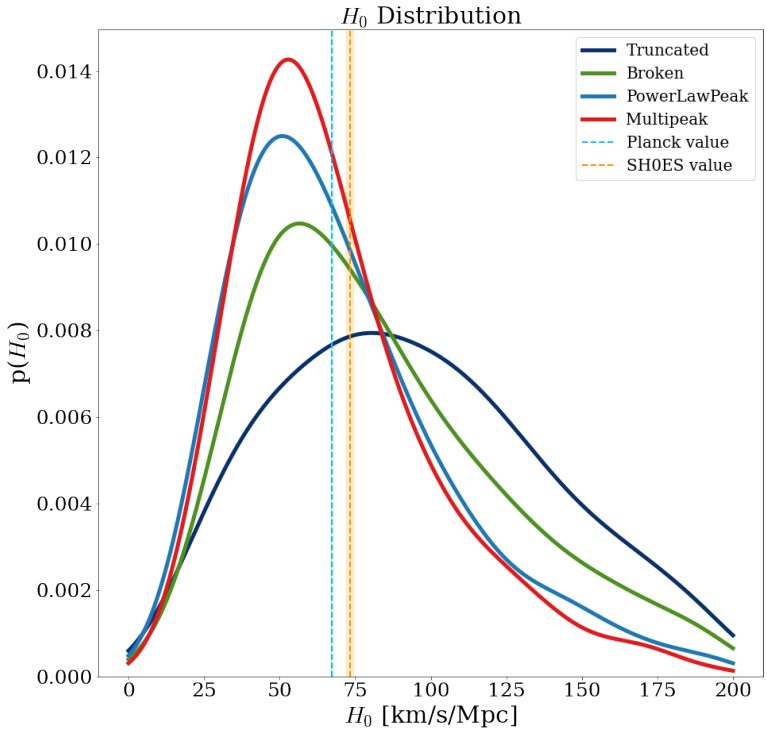

Figure 4.17: H_0 distribution obtained by using SNR > 12 BBH events.

obtained until now for SNR > 12, i.e. comparing the mass functions represented in the figures from the two previous sections (Figure 4.8 and Figure 4.16) and the parameters' estimates of Table 4.6 and Table 4.13 with the corresponding errors. This kind of analysis allows us to study the impact of the additional cosmological parameters H_0 an $\Omega_{0,m}$ on the model construction.

Despite the strong similarities, some differences can be spotted in the figures:

- the width of the 95% confidence intervals in the cosmology models is wider;
- in the `Multipeak` cosmology mass function both Gaussian peaks are not as recognizable as in the corresponding population mass function.

The fact that the obtained mass functions are so similar is not surprising, given how small the differences between the different estimates of the parameters are (see Table 4.6 and Table 4.13): for example, the obtained values for $m_{5\%}$ differs at most of $\sim 0.2\,M_\odot$, while $m_{95\%}$ at maximum of $\sim 0.6\,M_\odot$.

On the contrary, it appears, by looking at Table 4.7 and Table 4.14, that the extension to a variable cosmology affects the errors of the estimates a little bit more. In particular,

the general percentage error increase is of $\sim 4\%$, but in some cases the error growth is much larger, reaching a maximum of 13 % percentage error in the γ estimate.

These differences can be explained by recalling that the additional cosmological parameters give some extra degrees of freedom to the system, thus making the parameter degeneracy larger resulting in a more uncertain model construction.

4.4 Model Selection

After a qualitative discussion about the different types of models and a first consideration of the fit quality of each model, we can move on to a more quantitative way to determine which mass function is the best to represent the real mass distribution of a BH in a coalescent binary system. In order to do that various model selection methods were implemented: Deviance Information Criterion (DIC), and Posterior Predictive Distribution (PPD) check. They are displayed respectively in Table 4.16, and Figures 4.18 to 4.19.

4.4.1 Approximate Information Criteria

In certain cases, instead of employing complete model selection methods which are often too complex, the same results can be achieved by using methods that aim for an approximated model selection. These methods work by assigning, under some basic assumptions, a fixed penalty to models with higher complexity, thus succeeding in finding the best model. Despite this appealing feature, some caution is needed in the evaluation of the results, because the validity of the starting assumptions is not always met in astrophysical and cosmological contexts.

Keeping this in mind, in this work some different approximate model selectors were implemented:

- **Akaike Information Criterion (AIC)** is similar to a frequentist criterion which sets the penalty term equal to twice the number of free parameters in the model (k):

$$\mathrm{AIC} \equiv -2\ln(\mathcal{L}_{\max}) + 2k \tag{4.1}$$

  where $\mathcal{L}_{\max}$ is the maximum likelihood value of the evaluated model;

- **Bayesian Information Criterion (BIC)** is a Gaussian approximation of the Bayesian evidence in the large sample limit and given by:

$$\mathrm{BIC} \equiv -2\ln(\mathcal{L}_{\max}) + klnN \tag{4.2}$$

  where N is the number of data points;

- **Deviance Information Criterion (DIC)** is a generalization of the Akaike Information Criterion, so:

$$\mathrm{DIC} \equiv -2\left[\overline{\ln(\mathcal{L})} - \sigma^2(\ln(\mathcal{L}))\right] \tag{4.3}$$

where $\overline{\ln(\mathcal{L})}$ and $\sigma^2(\ln(\mathcal{L}))$ are the mean and the variance of the log-likelihood respectively.

Once defined, the various criteria were used to evaluate the goodness-of-fit of the different mass functions for both fixed and free cosmology analysis, and in both SNR regimes. Again, the SNR > 8 case in reported and discussed in Appendix A.4.

The AIC and the BIC criteria, due to the nature of their assumptions (the evaluation of Gaussian distributed parameters and the negligence of the choice of the priors and their informative power) were not appropriate for the model selection of our mass functions. On the other hand, the DIC does not suffer from the same problem, thus making it a valuable method for model selection. The obtained results are displayed in Table 4.16.

SNR > 12	Fixed Cosmology	Free Cosmology
`Truncated`	-14.96	-18.29
`Broken`	-4.28	-7.66
`PowerLawPeak`	-0.33	-3.59
`Multipeak`	0.00	0.00

Table 4.16: Model selection results: DIC, for SNR > 12 BBH events for both analysis cases: fixed and free cosmological parameters.

It can be seen that `Multipeak` is the preferred one, with all values being zero. Furthermore, as already observed in Sections 4.1.5 and 4.2.5, `Truncated` is disfavoured, which is proven by DIC $\gtrsim 15$, indicating that such distribution cannot be the correct one to describe the BBH population. Other relevant comments can be made depending on the parameter choice (Population or Cosmology), for example:

- `PowerLawPeak` is practically as good as `Multipeak` in the population case, while in the other case the model results to be more disfavoured, despite not being ruled out;
- `Broken` is always disfavoured with respect to `Multipeak`, but the level of disagreement is variable: for the population analysis the mass function is less disfavoured with respect to the cosmology case: DIC ~ 4 and DIC ~ 8, which again can be a proof of the fact that the fewer number of degrees of freedom enables a more precise estimate, thus it permits to construct a more valid model.

4.4.2 Posterior Predictive Check

The last model selection method is based on the Posterior Predictive Distribution. In particular, the posterior predictive check compares simulated (expected) data using a draw from a posterior distribution to the observed data. Therefore, if the observed data are too different from the expected ones the mass function is rejected as the best-fit candidate.

As before this analysis was made for all implemented distributions and both SNR values. Results are shown in Figures 4.18 and Figure 4.19 for SNR >12, while the results obtained for SNR >8 are presented in Appendix A.4 in Figures A.9 and Figure A.10.

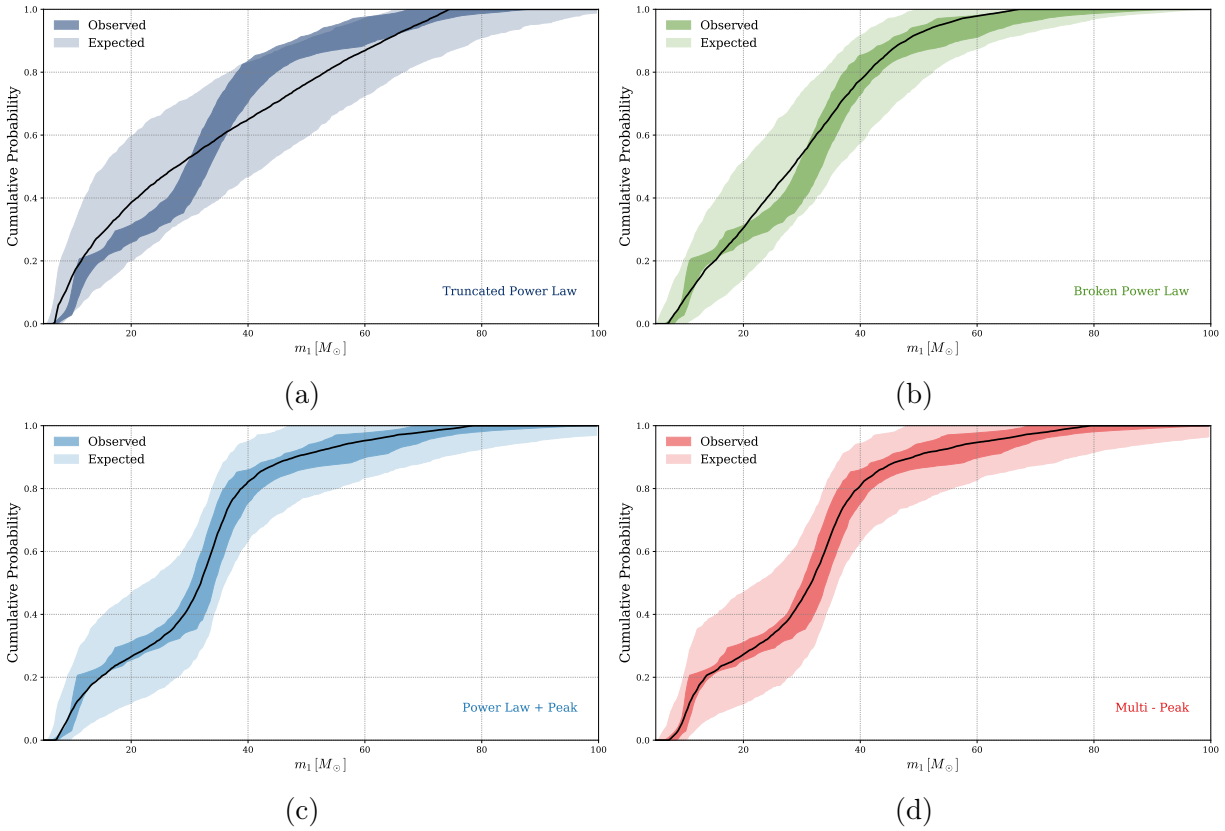

Figure 4.18: PPD check in the SNR >12 population analysis, with the different implemented mass functions: (a) Truncated Power Law; (b) Broken Power Law; (c) Power Law + Peak; (d) Multipeak Power Law. In each plot, the solid line represents the median of the expected cumulative distribution function.

- **Truncated Power Law:** the observed data do not follow the general median trend and cross the borders of the expected distribution at $M \gtrsim 40\,M_\odot$;
- **Broken Power Law:** even though the observed data do not follow the median trend, they can fit the median in a better way than the truncated model, as a confirmation that this model does not cross the limit of the expected distribution;
- **Power Law + Peak and Multipeak:** the observed data follow in a good way the median trend of the expected cumulative distribution function without crossing its borders.

Therefore, it appears that the already established ranking of the different models in the population analysis, based on the goodness-of-fit, is confirmed by its PPD test: `Multipeak`

is the best one, just followed by `PowerLawPeak` which in comparison is not as good as `Multipeak` in fitting the low mass end of the PPD; the third mass function is `Broken`, which despite being clearly disfavoured cannot be ruled out completely; and the worst model is `Truncated`, which due to the exceeding at $M \gtrsim 40\,M_\odot$, can be discarded as a valuable model.

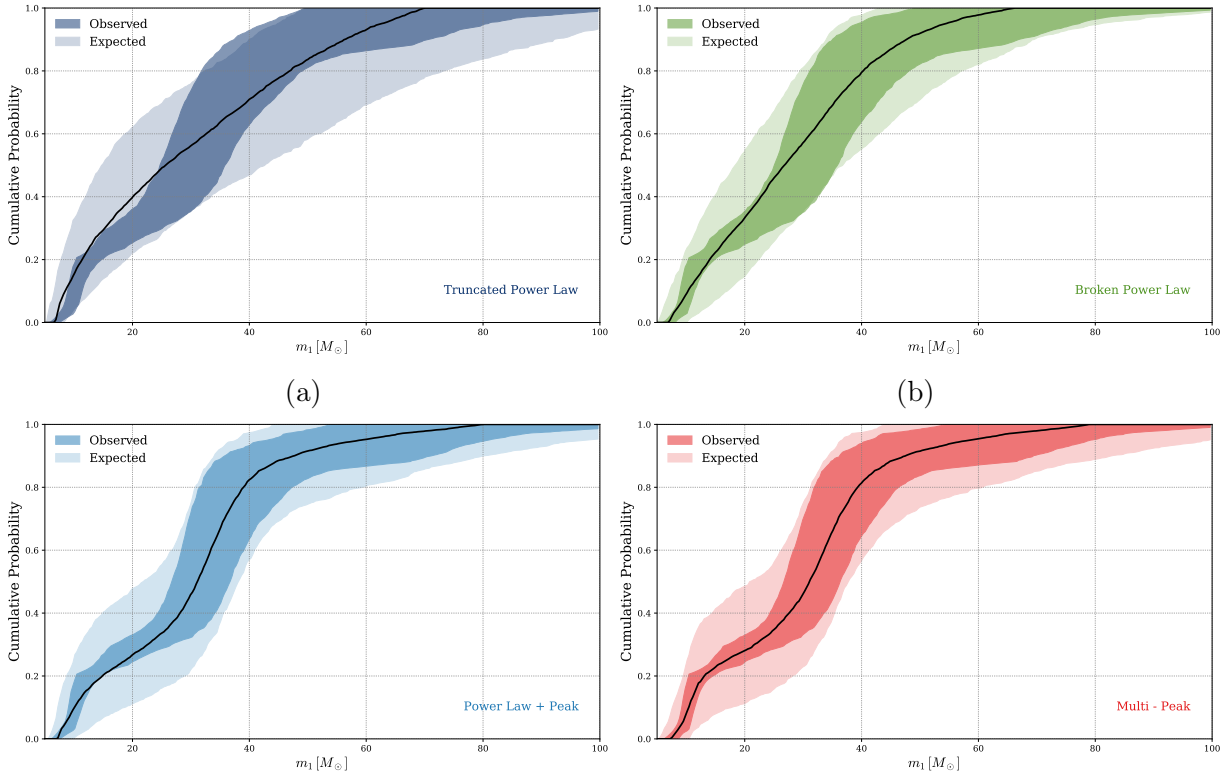

Figure 4.19: PPD check in the SNR > 12 cosmological parameters analysis, with the different implemented mass functions: (a) Truncated Power Law; (b) Broken Power Law; (c) Power Law + Peak; (d) Multipeak Power Law. In each plot, the solid line represents the median of the expected cumulative distribution function.

It is possible to do a similar discussion also for the free cosmology analysis of Figure 4.19:

- **Truncated Power Law:** the observed data do not follow the general median trend and cross the borders of the expected distribution at $M \gtrsim 35\,M_\odot$;

- **Broken Power Law:** even though the observed data do not follow the median trend, they completely include it within their range. In contrast to the population case, due to the broadening of the distribution, the model does slightly cross the limit of the expected distribution;

- **Power Law + Peak and Multipeak:** despite the general broadening of the distributions, the observed data follow in a good way the median trend of the expected cumulative distribution function without crossing the borders.

Therefore, also in this second free cosmology case, the already established ranking of the different models is confirmed by the PPD test: `Multipeak` is the best one, which is followed by `PowerLawPeak` which in comparison is not as good as the `Multipeak` in fitting the PPD at $M \sim 10\,M_\odot$; the third mass function is `Broken`, which despite being clearly disfavoured due to its border crossing cannot be ruled out completely, based on the small dimensions of the excess; and the worst model is `Truncated`, which again exceeds the expected distribution at $M \gtrsim 35\,M_\odot$, and can therefore be discarded as a valuable model.

By comparing these figures it is possible to evaluate the impact of the different parameter choices on the global goodness-of-fit of each model. The addition of the cosmological parameters broadens the different distributions without modifying their form. Therefore, it is still possible to observe that `PowerLawPeak` and `Multipeak` follow the median trend, while `Truncated` and `Broken` do not present such a behaviour. Moreover, due to the general broadening of the distributions resulting from the addition of degrees of freedom, whenever one of the observed distributions is over the boundaries of the expected distribution, the excess is more evident, thus discarding even stronger the exceeding models. This result agrees with the obtained DIC values of Table 4.16, as the excess increases with the number of degrees of freedom, so the level of disagreement with the best-fit model (multipeak mass function) grows by moving from the population to the cosmology analysis.

4.5 Summary and Discussion

Now that all the results have been presented, we could take a step back and summarize and discuss our findings.

In this Thesis, we analyzed 35 BBH events extracted from the GWTC-3 with SNR > 12, following the cut proposed by [76]. The first result we obtain is that in both the analysis performed at fixed and free cosmology, the `Multipeak` mass function model finds two overdensities in the BBH mass distribution, around $\sim 10\,M_\odot$ and $\sim 30\,M_\odot$, respectively. Therefore, this double peak, not accounted for in previous mass function models, appears to be a stable feature of the mass function distribution, and not dependent on cosmology.

To quantify the constraining power of the various mass function models, we estimated the "Gaussianized" relative error of each parameter, and compared those between the different models. We obtained that at fixed cosmology the models providing the smallest error are the simplest ones (`Truncated` and `Broken`), with a relative error on parameters smaller than more complex models by $\sim 5\%$. The situation changes, instead, when the cosmological parameters are let free in the fit, as in this case the `PowerLawPeak` and `Multipeak` model perform better than the other one. In general, given the estimated errors, we do not find a model that outperforms the others in terms of relative errors, and therefore we proceeded to compare them on a more statistical basis.

The analyses of the DIC and the Posterior Predictive Check indicate that the best mass function model is the newly implemented one, the `Multipeak`, despite being the most complex. We find a small preference with respect to the `PowerLawPeak` model, with a $|\Delta DIC| \lesssim 0.3$, while a significant improvement for the other models. This result provides a significant indication that oversimplistic models are not able to reproduce the observed features in the mass distribution of BBHs, which are becoming relevant with the increasing statistics of O3, and will be fundamental to be modelled during O4 and in future GW experiments. It is worth noticing that all model selection methods are independent and complementary, therefore the fact that the results are in agreement further strengthens the validity of the analysis. Nevertheless, some differences between the results obtained for the two analysis cases can be identified. Most notably, for all mass distributions the level at which the other models are disfavored with respect to `Multipeak` one increases when also the cosmological parameters are set free.

Thus, all collected evidence points to the same result: among the models tested in this work to fit the distribution of the primary BBH source–frame mass, `Multipeak` is favoured by the data, followed by `PowerLawPeak`, which is only weakly disfavored and providing a statistically comparable result, whereas the `Broken` model is significantly disfavored with respect to the first two, and the `Truncated` is always rejected as a possible BBH population model. This analysis confirms the results obtained by [11] while probing in addition that those are also robust to a variation of the cosmological parameters. For a similar conclusion, see [143].

Finally, in Section 4.2.6 we conclude by analyzing the Hubble constant distribution obtained in the various analyses performed, which allowed us to infer a measurement for the Hubble constant as reported in Table 4.15. We find that assuming a `MultiPeak` mass function model, we obtain a value $\mathrm{H_0} = 61.10^{+38.65}_{-22.43}\,\mathrm{km/s/Mpc}$, compatible with both the estimates obtained in the early-Universe ($\mathrm{H_0} = 67.4 \pm 0.5\,\mathrm{km/s/Mpc}$ [4]) and in the late-Universe ($\mathrm{H_0} = 74.0 \pm 1.4\,\mathrm{km/s/Mpc}$ [5]).

Despite the fact that also for the Hubble constant the `Multipeak` model provides the most stringent relative errors, we notice that they are still significantly larger ($\sim 50\%$) than the errors obtained by the other probes ($\sim 1\%$), as shown in Figure 4.20. To get a more valid result for the dark sirens method used in this work, much more GW events are needed in order to constrain the different mass functions in a much stronger way thanks to the larger number of data available [143, 146]. From this point of view, the future looks bright as more accurate and deeper observing runs for the GW detector network of LIGO, Virgo and KAGRA are already planned and are expected to detect hundreds of events annually, and in the future third-generation GW observatories will allow increasing the statistics by a factor of 1000 [147].

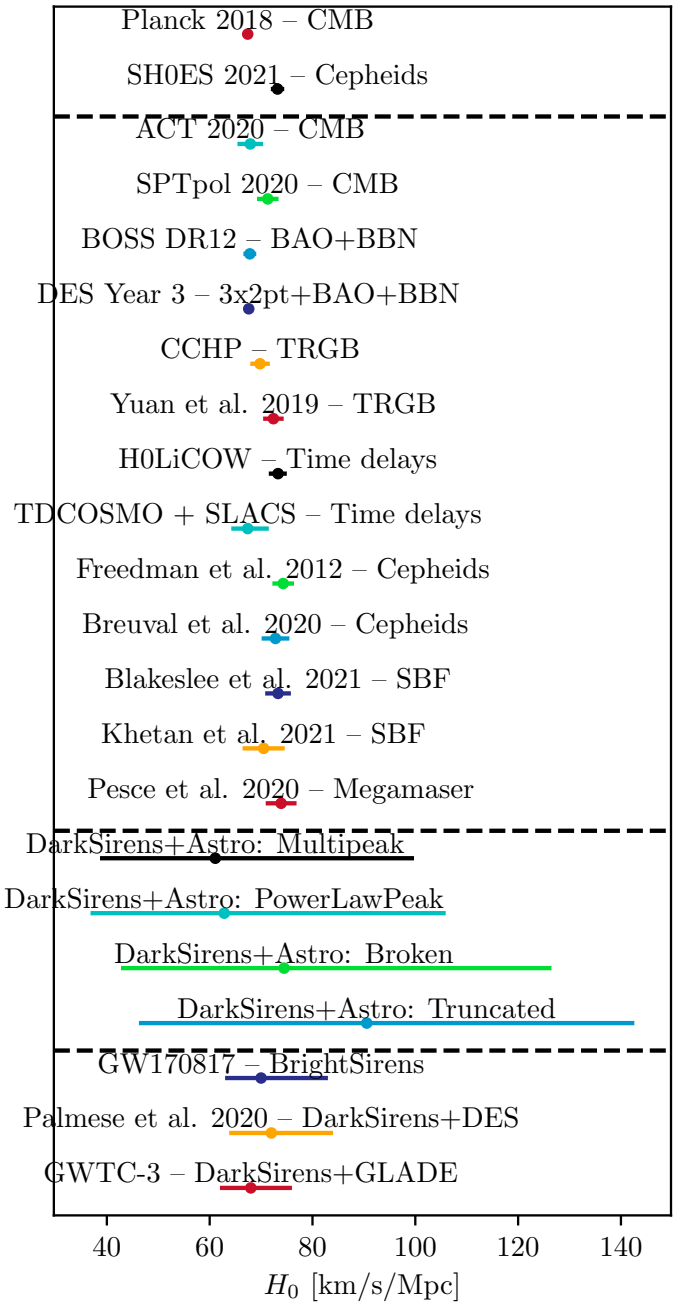

Figure 4.20: Some measurements of the Hubble constant H_0. In the top section the two main results for the early- [4] and late-time [5] measurements; in the second section all the other measurements from literature are presented; in the third section the results found in this work are displayed; while in the bottom panel some H_0 measurements from GW events are shown [144, 145, 37].

Chapter 5

Conclusions and Future Perspective

Since the first evidence of the expansion of the Universe by Hubble in 1929 [148], one of the main questions of modern cosmology has been to measure the speed at which the Universe expands, which, in its local value, is commonly referred to as the Hubble constant H_0. Over the years, as new and more data came in, some tension on the measured value of H_0 started to emerge between the so-called early-universe measurements, based on cosmological observations of the early Universe (e.g., CMB), and late-universe measurements, obtained at much lower redshifts (typically $z \lesssim 2$). In particular, the most notable disagreement is between the value of the Hubble constant inferred from Planck observation of the CMB [4] ($H_0 = 67.4 \pm 0.5\,\mathrm{km/s/Mpc}$) and the value obtained by the SH0ES collaboration [5] ($H_0 = 74.0 \pm 1.4\,\mathrm{km/s/Mpc}$) based on a distance ladder of SNe and Cepheids. However, it is not clear what the cause of this discrepancy between the two types of measurements is: it could be either some unaccounted systematics within one or both the probes, and/or some unexpected new physics. In any case, in order to understand which scenario is the correct one, some independent measurement from complementary probes is needed, which would also allow us to solve the Hubble tension. Therefore, the search for some new observations is needed to obtain some incontrovertible evidence on the Hubble constant.

In this context, GW could bring the last piece of evidence to solve the Hubble tension. In fact, GW events can be used as an alternative probe thanks to their unique property of providing a direct measurement of the luminosity distance of the emitting object, requiring no other form of calibration, making them independent of the cosmic distance ladder. However, as it can be evinced from equation (1.35), in order to use GWs as standard sirens some other information is necessary to break the degeneracy between GW parameters, e.g. the redshift and the chirp mass of the emitting CBC ($\mathcal{M}_z$). To address this issue, several methods have been developed depending on the characteristics of the GW signal.

Among the different methods for dark sirens cosmology proposed in [9], the one used in this work, is based on the use of only GW without any other external information on the redshift. In particular, this method requires some prior knowledge on the astrophysical properties of the GW emitters to break the degeneracy between parameters.

In order to constrain and study the mass source population, the public MGCosmoPop

code [10] was used and developed further to include a new mass function previously not implemented, as suggested by [11]. Then, the newly implemented code has been run on the latest compilation of GWTC-3 data, in order to obtain the best parameters' values to describe the event distribution for each of the mass distributions available: `Truncated`, `Broken`, `PowerLawPeak`, and `Multipeak`. To find the parameters' values a MCMC code was run, which explored the parameter space of the posterior distribution of all BBH mass functions, in two different cases: by assuming a fixed cosmology or by leaving also two cosmological parameters free. Lastly, the results were analyzed and the different models were compared thanks to the use of different implemented model selection methods, namely: the Deviance Information Criterion and the Cumulative Distribution Function calculated with code presented in [149].

5.1 Main Results

In this section, the main results obtained within this work will be summarized, some of which have been included in [1].

1. Binary Black Holes mass function implementation and validation

- The first step in the analysis was to implement the new `Multipeak` mass function in the `MGCosmoPop` code. In this way, four different mass function models are available: `Truncated`, `Broken`, `PowerLawPeak`, and `Multipeak`. Once the mass functions were all implemented, it was possible to run some tests to check if the different distributions were correctly normalized, if the mass model reproduced the expected trend, and if, given some testing data, it was possible to compute the corresponding population function.

- To derive constraints for the population parameters, a MCMC code was run for each mass function on the latest compilation of GWTC-3 data. In particular only the 35 BBH events with a SNR > 12 were selected for the analysis. The most representative parameters are summarized in Table 5.1, which suggests that the `Multipeak` model is the best mass function to reproduce the data. This tendency is also strengthened by Figure 5.1 since the `Multipeak` is the only distribution able to reproduce the two substructures in the event distribution. This analysis provides independent constraints of the results obtained by [76, 150].

- In order to analyze the results in a more quantitative way, the different models were compared considering two implemented model selection methods: the Deviance Information Criterion and the Cumulative Distribution Function calculated with code presented in [149]. Despite the fact that the different evaluations did not always give consistent results, it was possible, by combining the different indicators, to obtain the following mass function ranking: 1) `Multipeak`, which had the lowest DIC and the CDF was found to follow precisely the median CDF distribution; 2)

SNR >12	R_0 $[1/Gpc^3/yr]$	γ	m_l $[M_\odot]$	m_h $[M_\odot]$	$m_{5\%}$ $[M_\odot]$	$m_{95\%}$ $[M_\odot]$
`Truncated`	$21.46^{+8.33}_{-6.38}$	$7.63^{+1.94}_{-2.18}$	$6.17^{+0.18}_{-0.30}$	$79.58^{+17.93}_{-6.88}$	$6.16^{+0.20}_{-0.20}$	$19.24^{+5.15}_{-3.16}$
`Broken`	$11.33^{+5.85}_{-3.78}$	$9.27^{+1.66}_{-2.06}$	$4.29^{+1.17}_{-1.32}$	$118.03^{+50.53}_{-33.16}$	$5.96^{+0.79}_{-0.99}$	$24.40^{+4.95}_{-4.36}$
`PowerLawPeak`	$12.12^{+5.90}_{-4.08}$	$8.51^{+1.98}_{-2.08}$	$5.14^{+0.70}_{-0.98}$	$116.01^{+54.32}_{-31.24}$	$6.36^{+0.40}_{-0.59}$	$29.95^{+3.96}_{-8.13}$
`Multipeak`	$12.17^{+6.00}_{-4.14}$	$8.73^{+1.94}_{-2.11}$	$4.52^{+1.09}_{-1.45}$	$112.34^{+54.39}_{-29.36}$	$6.36^{+0.59}_{-0.99}$	$28.95^{+4.36}_{-8.13}$

Table 5.1: Astrophysical parameters derived in the population analysis for GWTC-3 BBH events selected with SNR >12.

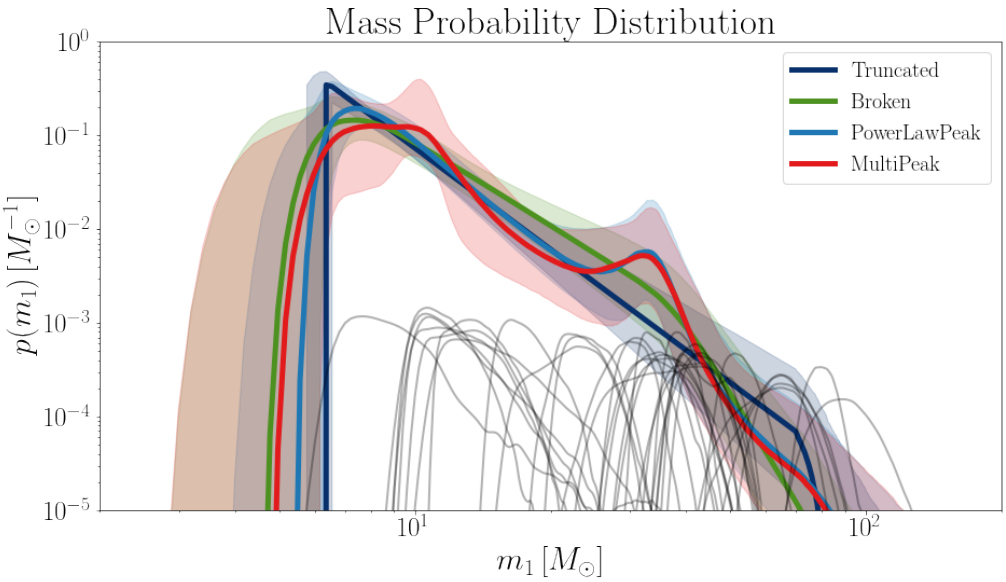

Figure 5.1: Superimposition of the mass functions obtained using SNR >12 BBH events. The different colours represent the different models as described in the legend, with the solid line indicating the median, the shaded area the 95% confidence interval, and in grey the selected GW events.

`PowerLawPeak`, just following with $|\Delta\text{DIC}| \approx 0.33$ and a CDF only slightly different; 3) `Broken`, which is disfavoured by its $|\Delta\text{DIC}| \approx 4.28$ and by its CDF that struggles in following the median trend; and 4) `Truncated`, which is ruled out as a mass distribution candidate due to $|\Delta\text{DIC}| \approx 14.96$ and to a CDF that crosses the allowed borders of the distribution.

- We explored different posterior sampling methods, namely the affine invariant sampling (based on `emcee`) and nested sampling (based on `dynesty`). A new code has

been developed that allows us to easily choose between the different samplers, thus extending the current version with the possibility of directly estimating the Bayes factors for the various models explored. The new code has been tested to work correctly by comparing the results obtained in a given model (`Multipeak`), providing constraints in perfect agreement with each other. Even if successful, it was not possible to adopt this code for the full analysis yet, since the nested sampler is significantly more demanding in terms of computing time. The plan for the next future is to take advantage of this new code and repeat the full analysis obtaining the Bayes factors for all models, thus providing a new model selection indicator.

2. Estimating the constraining power in different models

- Analyzing the previously presented results, it has been possible to infer also the different constraining power under the assumption of the four different mass function models. The constraining power has been quantified as the "Gaussianized" relative error of each parameter estimate. Results are reported in Table 4.7. As expected, it was obtained that the two simplest models (`Truncated` and `Broken`) were the most constraining, due to their on average smaller relative errors ($\epsilon_{\%} \approx 0.22$) in comparison to the more complex ones (`PowerLawPeak` and `Multipeak`), which had on average bigger errors ($\epsilon_{\%} \approx 0.25$). This result is in agreement with what was expected, because the two simpler models have the least number of parameters (`Truncated` has 10 and `Broken` has 13), resulting in a smaller degeneracy between them, and thus in a higher constraining power.

- To study the impact of not fixing the cosmological model, the analysis has been repeated also in a flat ΛCDM model where $\Omega_{0,\mathrm{m}}$ and H_0 were free to vary. This allowed us both to quantify how dependent the results (and their errors) are on fixing the cosmological model, and which cosmological constraints can be obtained with this method.

  In contrast to the previous analysis, it was obtained that the additional cosmological parameters tend to prefer even more the more complex models. In fact, the `Multipeak` has the lowest average error ($\epsilon_{\%} \approx 0.31$) despite being the model with the most parameters, thus with the most degeneracy between the parameters. This result is confirmed even more by analyzing the obtained DIC values: `Multipeak` has again the lowest value, and the difference with the other model is higher than in the previous case, thus indicating that the other mass functions are more disfavoured than before. In particular: `PowerLawPeak` has $|\Delta\mathrm{DIC}| \approx 3.59$ and is the second best model, followed by the `Broken`, which has a $|\Delta\mathrm{DIC}| \approx 7.66$, while the `Truncated` has $|\Delta\mathrm{DIC}| \approx 18.29$, indicating that it can be ruled out again.

- As the analysis has been repeated twice (once by constraining only the astrophysical parameters of the BBH population, and once by letting also H_0 and $\Omega_{0,\mathrm{m}}$ vary) it was possible to compare the obtained mass functions. It was found that the addition of the

cosmology parameters into the analysis did not impact significantly the estimate of the mass distribution, as it could be inferred by looking at Figure 4.8 and Figure 4.16 where all mass function looks similar, and by looking at Table 4.7 and Table 4.14 where on average errors increases at most of $\approx 10\%$.

- Lastly, from Figure 4.17, some further comparison between the different models could be inferred by analyzing their H_0 distribution. In particular, it is evident that the previously mentioned ranking is confirmed by the obtained distributions, as `Multipeak` and `PowerLawPeak` are the narrowest, followed by `Broken`, while the `Truncated` has an extremely broad distribution, proving its inadequacy in the description of the mass distribution of the BBH population.

3. Constraints on the Hubble constant and the Hubble tension

- Lastly, we focused on analyzing the constraints obtained on H_0, to quantify the precision of the current method and its dependence on the assumed mass function. In particular, for each mass function, a distribution of the Hubble constant was obtained, providing also a best estimate value, presented in Table 4.15.

  As `Multipeak` is the preferred model, it is possible to describe the obtained H_0 values of the different mass distribution as a function of it. The obtained value for `Multipeak` is $H_0 = 61.10^{+38.65}_{-22.43}\,\mathrm{km/s/Mpc}$, corresponding to a percentage error of 50 %, which also correspond to most precise estimate found, as `PowerLawPeak` gave $H_0 = 62.83^{+43.08}_{-26.01}\,\mathrm{km/s/Mpc}$, corresponding to a percentage error of 55 %, for `Broken` was found $H_0 = 74.48^{+52.00}_{-31.73}\,\mathrm{km/s/Mpc}$, corresponding to a percentage error of 56 %, `Truncated` gave $H_0 = 90.56^{+52.05}_{-44.32}\,\mathrm{km/s/Mpc}$, corresponding to a percentage error of 53 %.

- By considering the Planck value $H_0 = 67.4 \pm 0.5\,\mathrm{km/s/Mpc}$ [4] and the SH0ES value $H_0 = 74.0 \pm 1.4\,\mathrm{km/s/Mpc}$ [5] as the reference H_0 values for early- and late-universe estimates, respectively, a comparison with the values obtained in this work can be made. In particular, from Figure 4.20 it is evident that all models are consistent with the theoretical values, but are not able with the current statistics to constrain the Hubble constant in a strong enough way to solve the Hubble tension.

The results of this analysis have been included in [1].

5.2 Future Perspectives

Given all the results obtained, it is finally possible to discuss some of the possible future developments of this work.

First at all, it might be interesting to implement an internal method for the evaluation of the Bayes factor as a model selection technique, as described in Section 3.2. The first step in this direction was done in this work since a method based on nested sampling

within the Bayesian inference framework has already been implemented and tested (see Section 3.6). However, some additional work is necessary in order to build a fully working method for the evaluation of the evidence and the Bayes Factor.

Furthermore, the entire analysis in this work was made by first considering all the cosmological parameters as fixed, and then by additionally freeing the Hubble constant and the density parameter. For now, the use of GW data only limits the precision of the estimates. To increase the precision of the presented method it may be possible to integrate the missing information with some redshift estimate of the sources, which could be obtained through cross-correlation with some galaxy catalogues. So, the analysis could be expanded by doing a combined analysis where both the astrophysical and the cosmological parameters are free, resulting in values that are free from any starting assumption other than the prior choice, eventually avoiding systematic bias.

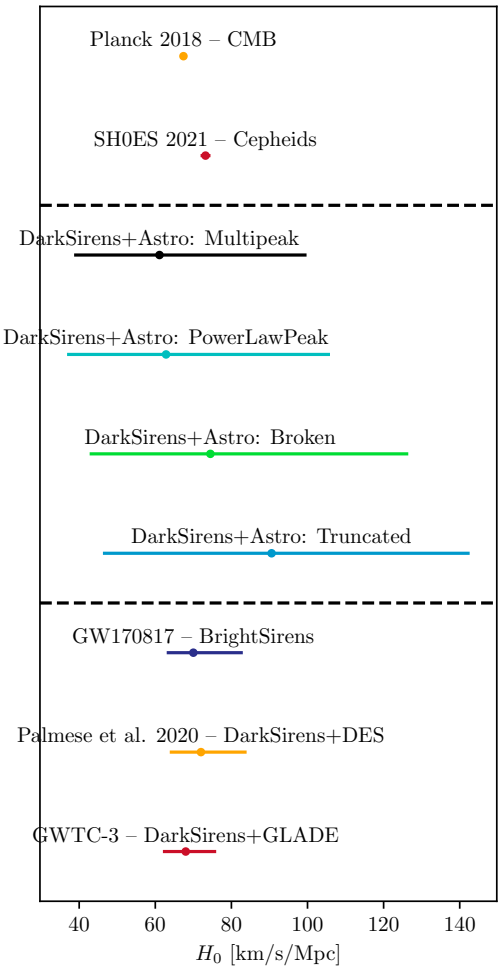

Figure 5.2: Comparison of the H_0 measurements obtained in the context of this work with the results found with other GW methods.

Nevertheless, in the context of a GW-only analysis, which uses features in the source mass distribution to fit cosmological parameters together with the source population, further progress from a theoretical point of view is needed, in order to describe the mass functions in a good enough way to produce robust cosmological constraints (also in comparison with other GW methods), as it can be evinced from Figure 5.2. A valuable approach to increase the knowledge about the astrophysical population could be to follow an approach as suggested in [150]: trying to fit the GW events with a non-parametric mass function, thus allowing for more freedom to reproduce the features of the observed event distribution.

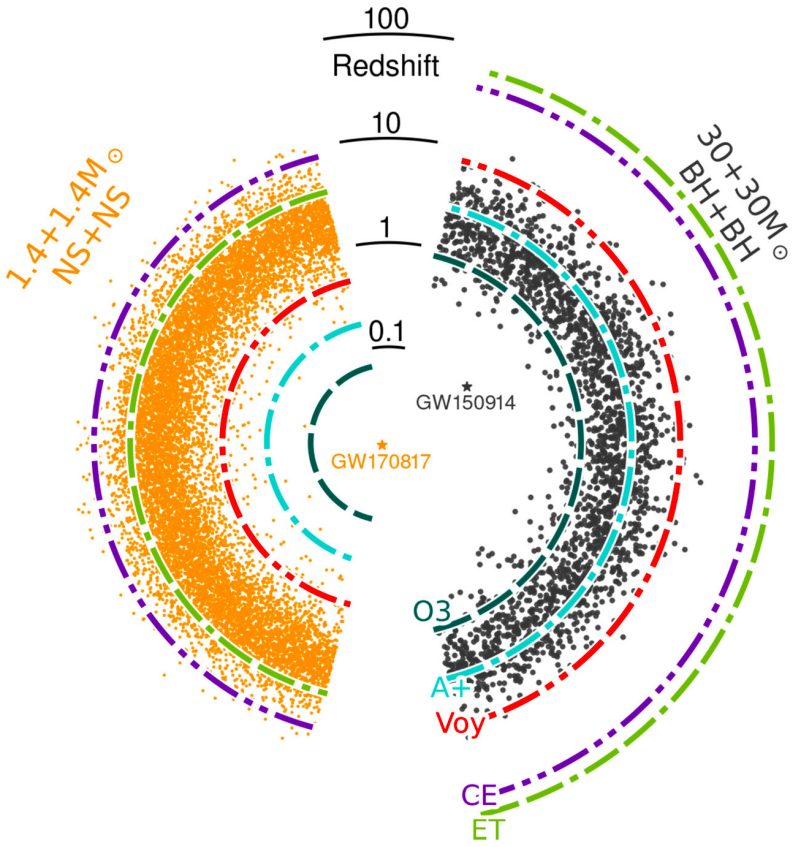

Figure 5.3: The conceptual reach of next-generation, ground-based detectors. The different ranges of the current ground-based detectors and future planned detectors Einstein Telescope (ET) and Cosmic Explorer (CE) are presented as a function of redshift: (left) ranges to detect BNS mergers, (right) ranges to detect BBH mergers. Figure from [151].

Moreover, by considering GW dark sirens more in general, their future looks bright. In fact, the era of GW astrophysics and cosmology has just started. As presented in Figure 2.3 future more accurate and deeper observing run for the GW detector network of LIGO, Virgo and KAGRA are already planned and are expected to detect hundreds to thousands of events annually. In addition to this, in the near future, the space-based Laser Interferometer Space Antenna (LISA) for GW detection will be launched, the ground-

based GW detectors Cosmic Explorer (CE) [152] and the Einstein Telescope (ET) [153] will become reality, which will enable even deeper and even more sensitive observations (as displayed in Figure 5.3), leading to an enormous growth of the available dataset. The widening of the GW catalogue will allow us to understand and develop further the models for the GW source population, eventually resulting in more robust predictions from the dark sirens method used in this work. At the same time as the advancements in the GW detectors field, some major progress will be made also in the context of electromagnetic telescopes, which will greatly improve the search for EM counterparts linked to GW emission and will allow expanding the redshift catalogues thanks to deeper galaxy surveys.

Appendix A

Extending the Analysis to SNR > 8 Events

In the context of this work a second analysis was made by considering all 90 events with SNR > 8. The aim of this second analysis was to investigate the impact of a larger but less robust sample on the mass function definition and construction. For this reason, the analysis was repeated analogously as described in Chapter 4 for the SNR > 12 case.

Before moving on, a crucial observation has to be made regarding the lower SNR value. In particular as already mentioned, the SNR is strictly related to the FAR of the detection: the lower the SNR threshold is set the higher FAR will be, thus including into the analysis false events leading to an incorrect (and biased) result [10]. For this, it is critical to include those events in the analysis and therefore the SNR > 8 case was studied only for completeness reasons.

A.1 Analysis at Fixed Cosmology

In this section, the main results obtained in the population analysis (astrophysical parameters are free to vary, while the cosmology is fixed) will be presented. Due to the similarity of the analysis between the SNR > 12 and the SNR > 8 cases, to not burden further the discussion with unnecessary details.

Therefore, once all the mass functions were defined, a complete Bayesian analysis considering the 90 events with SNR > 8 was made for each mass distribution using the same flat priors of the SNR > 12 case (see Table 4.1 and Table 4.8). As before, the aim of the analysis was to obtain the best values for all parameters and determine the best mass function model for the given data set.

The parameter estimation allowed us to obtain the mass function models for the BBH mass population by considering all the 90 events, which are presented in Figure A.1. One main observation that can be made is the broadness of the 90% confidence intervals with respect to the SNR > 12 case, which can be easily explained by the fact that in the SNR > 8 case more events are available for the analysis, thus having more data to constrain all the

parameters needed to define the mass models.

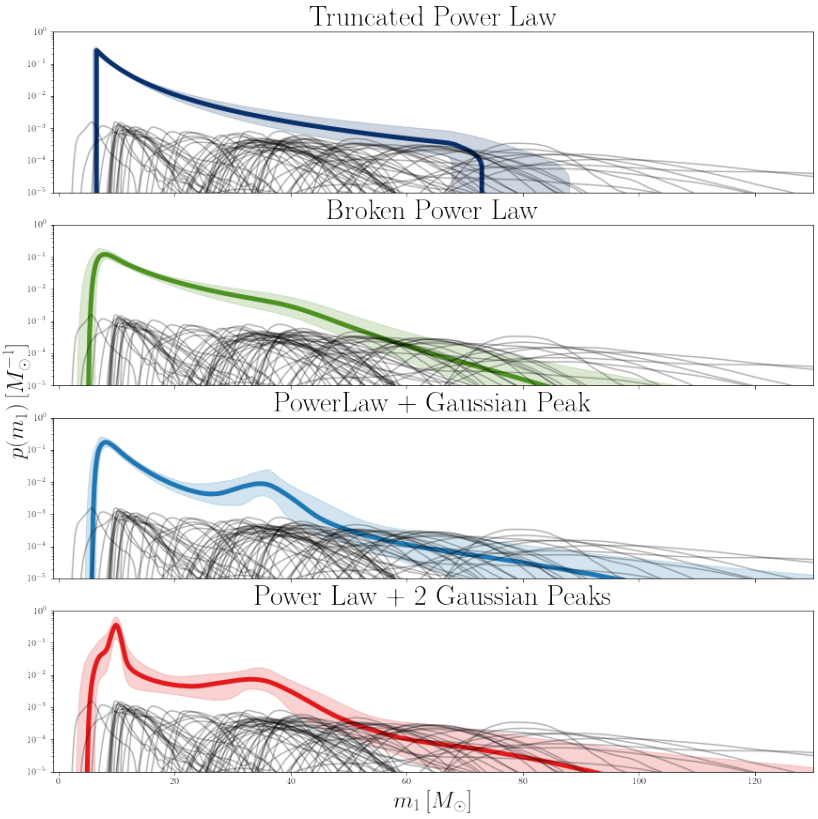

Figure A.1: Mass Functions obtained with parameters presented in this section using BBH SNR > 8 events: single mass function (solid coloured lines) with considered events (grey).

Once all the mass distributions have been constructed, it is possible to compare in a more complete and systematic way the obtained results by looking at the same common parameters as before, reported in Table A.1 with the corresponding corner plot in Figure A.3a. In addition to this, a superimposition of the mass functions with all the events considered is presented in Figure A.2.

As done previously, in order to evaluate the constraining power on each parameter, the corresponding "Gaussianized" percentage errors are compared. Therefore, to get a better insight in Table A.2 the obtained percentage errors of each parameter are reported.

It can be observed that `PowerLawPeak` seems to be the most constraining model based on the fact that it has the smallest error in two cases ($m_{5\%}$ and $m_{95\%}$), the second smallest on R_0, and the third largest only once (γ), and never the largest (i. e. the worst). In contrast with the SNR > 12 case, no further particular mass function ranking can be

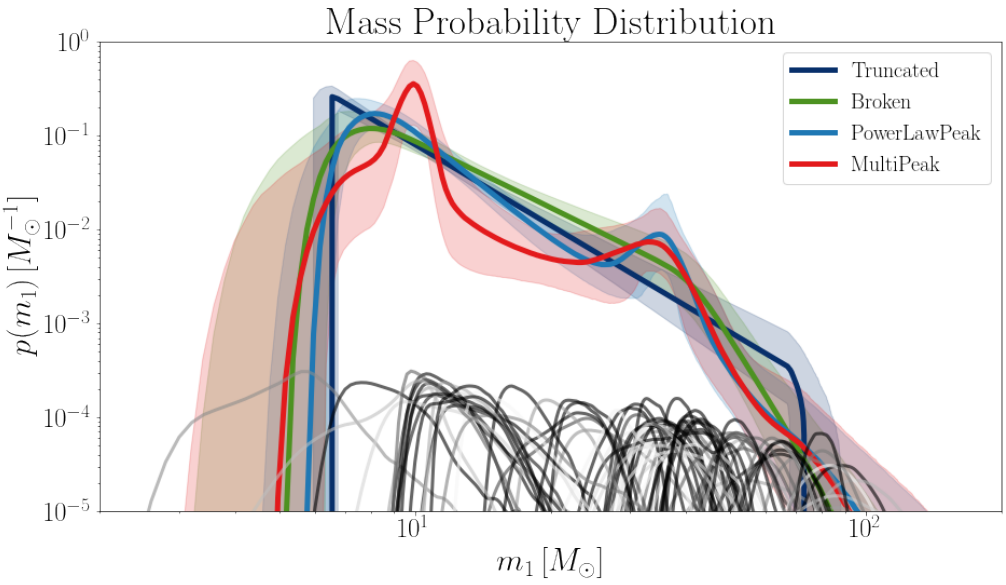

Figure A.2: Superimposition of the mass functions obtained with parameters presented in this section using SNR > 8 BBH events. The different colours represent the different models as described in the legend, with the solid line indicating the median, the shaded area the 95% confidence interval, and orange lines on the bottom are the selected BBH events for SNR > 8.

SNR > 8	R_0 [1/Gpc^3/yr]	γ	m_l [$M_\odot$]	m_h [$M_\odot$]	$m_{5\%}$ [$M_\odot$]	$m_{95\%}$ [$M_\odot$]
`Truncated`	$15.72^{+4.77}_{-3.88}$	$2.28^{+1.31}_{-1.14}$	$6.37^{+0.16}_{-0.24}$	$73.02^{+6.91}_{-3.93}$	$6.56^{+0.40}_{-0.40}$	$28.76^{+5.35}_{-4.56}$
`Broken`	$10.74^{+3.50}_{-2.87}$	$2.68^{+1.18}_{-1.14}$	$4.77^{+0.91}_{-1.32}$	$119.46^{+49.64}_{-33.03}$	$6.56^{+0.59}_{-0.79}$	$32.90^{+3.57}_{-3.96}$
`PowerLawPeak`	$12.08^{+4.06}_{-3.12}$	$2.41^{+1.12}_{-1.13}$	$5.41^{+0.53}_{-0.74}$	$121.12^{+51.32}_{-33.58}$	$6.95^{+0.37}_{-0.40}$	$35.10^{+1.98}_{-2.77}$
`Multipeak`	$12.95^{+4.34}_{-3.44}$	$2.46^{+1.15}_{-1.09}$	$4.42^{+1.09}_{-1.28}$	$109.33^{+56.64}_{-27.29}$	$7.35^{+0.99}_{-0.99}$	$34.10^{+2.58}_{-3.09}$

Table A.1: Common astrophysical parameters obtained in the population analysis for SNR > 8 BBH events.

established based on the constraining power of the parameters, due to the fact that the other models are similarly good/bad in providing a value for the parameters. Nevertheless, if a ranking must be defined, the second best model would be `Broken`, which is the most constraining in one case (γ), the second best in regard to R_0 and the third best in $m_{5\%}$ and $m_{95\%}$. In contrast, `Truncated` and `Multipeak` appear to be similarly bad in relation to their constraining power, as `Truncated` provides the best estimates in two case (R_0 and

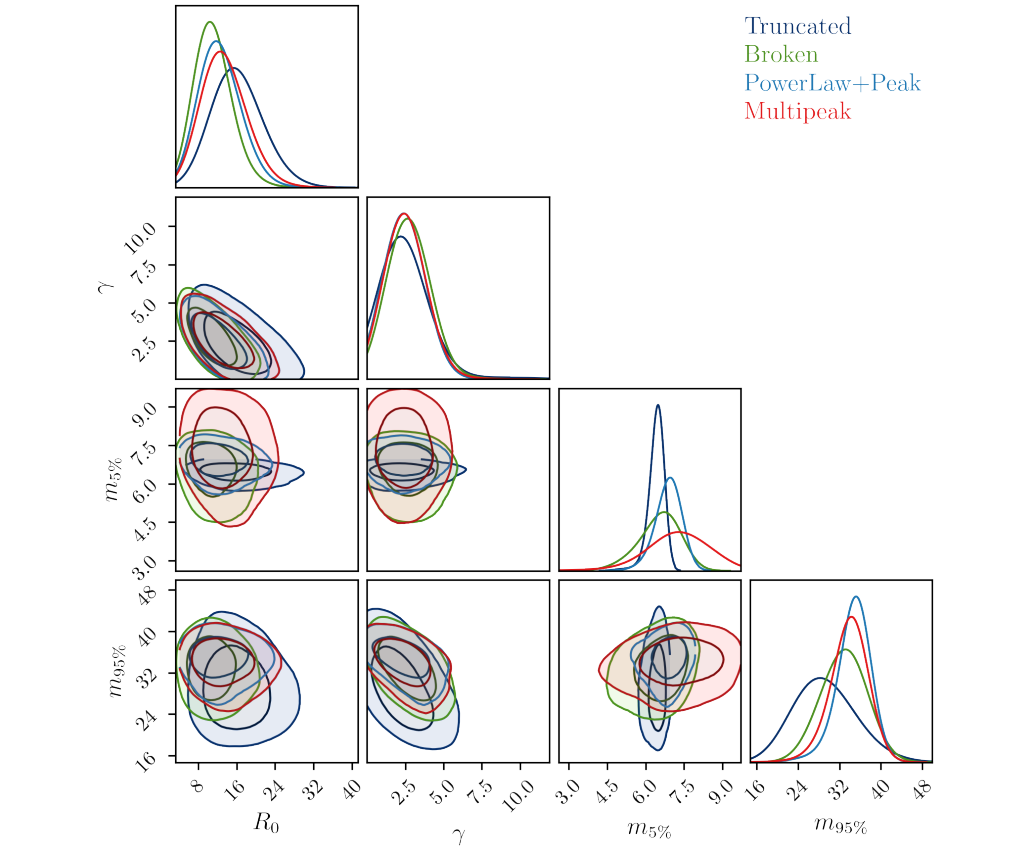

(a)

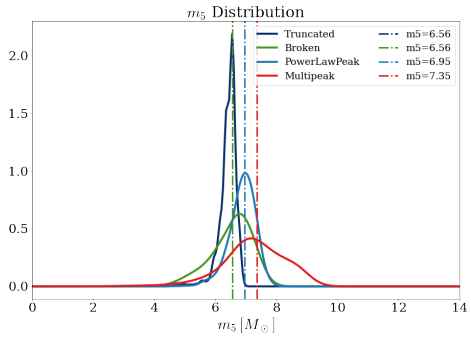

(b)

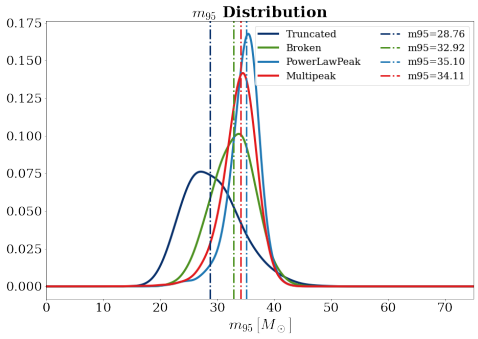

(c)

Figure A.3: (a) Corner plot for the common parameters for the different mass functions obtained by using SNR > 8 BBH events. A zoomed look of $m_{5\%}$ and $m_{95\%}$ distributions is presented in (b) and (c) respectively.

$m_{5\%}$), but is the worst model for the other two parameters; while `Multipeak` is never the best model but it provides three times with the second best estimate (R_0, γ, $m_{95\%}$) and only once the worst ($m_{5\%}$).

SNR > 8	ΔR_0	$\Delta\gamma$	Δm_l	Δm_h	$\Delta m_{5\%}$	$\Delta m_{95\%}$
`Truncated`	0.28	0.54	0.03	0.07	0.06	0.17
`Broken`	0.30	0.43	0.23	0.35	0.11	0.11
`PowerLawPeak`	0.30	0.47	0.12	0.35	0.06	0.07
`Multipeak`	0.30	0.46	0.27	0.38	0.13	0.08

Table A.2: Percentage errors of the parameters obtained in the population analysis for SNR > 8 BBH events.

Such a result can be evaluated by taking into account the number of parameters that define each mass model. As described in Section 3, the truncated power law and the broken power law have the least number of parameters: 10 and 13, respectively, thus corresponding to the least number of degrees of freedom. As a result of this, the degeneracy between the different parameters is lower and thus must lead to smaller errors. Taking this consideration into account it becomes clear why `Truncated` is not the favoured model, because, despite having the least parameters, it has the same constraining power as `Multipeak`, which has 17 parameters. Following the same logic, it is evident that from this preliminary analysis `PowerLawPeak` appears to be the best model to reproduce the data, based on the fact that it is the most constraining and has a total of 15 parameters: more than `Truncated` and `Broken`. Furthermore, by comparing `Multipeak` and `Broken` it can be inferred that these two models are similarly good in reproducing the mass population, because `Broken` is slightly more constraining but has four parameters less than `Multipeak`.

Therefore, the constraining powers of the parameters seem to suggest the following ranking: `PowerLawPeak`, `Broken` and `Multipeak`, and lastly `Truncated`, which will probably be discarded as a model since it has the least parameters but the worst constraining power.

A.2 Exploring the Cosmological Constraints

Moving on, the complete Bayesian analysis is repeated in the SNR > 8 for each mass distribution by evaluating the 90 events and using flat priors as in Table 4.8. Again, the entire analysis is omitted in order to focus only on the main results.

The parameter estimation allowed us to obtain the mass function models for the BBH mass population by considering all the 90 events, which are presented in Figure A.4. One main observation that can be made is the broadness of the 90% confidence intervals with respect to the SNR > 12 case, which can be easily explained by the fact that in the SNR > 8 case more events are available for the analysis, thus having more data to constrain all the parameters needed to define the mass models.

As before, it is now possible to compare in a more complete way the obtained results by looking at the common parameters, reported in Table A.3 with the corresponding corner plot in Figure A.6a. In addition to this, a superimposition of the mass functions with all

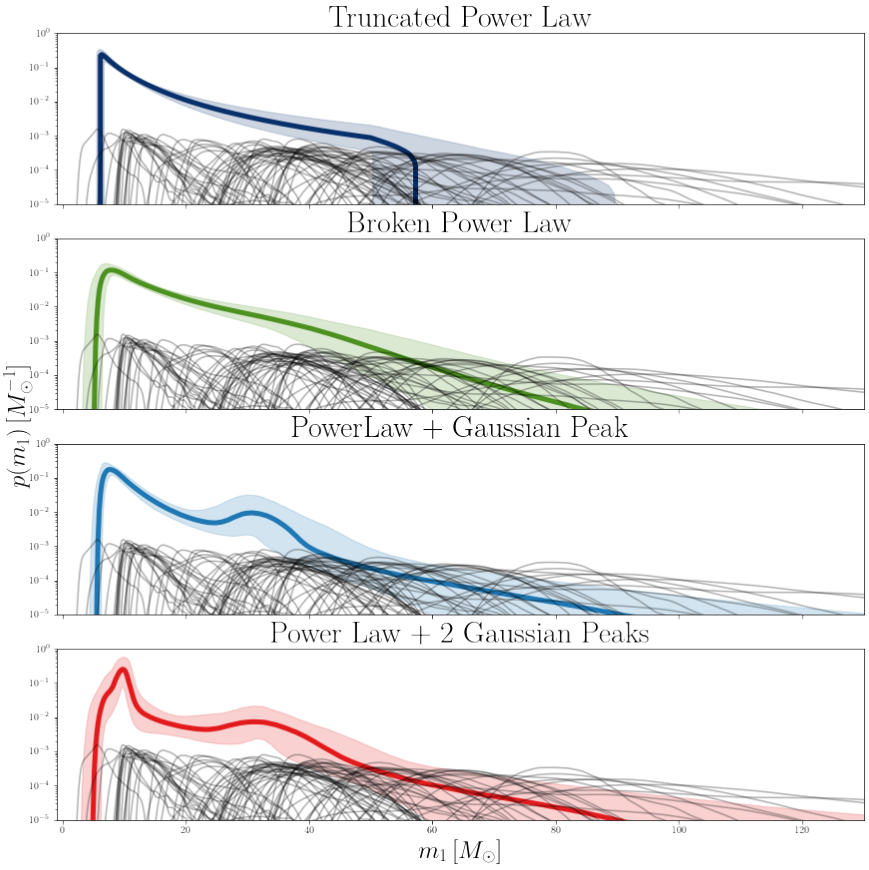

Figure A.4: Mass Functions obtained with parameters presented in this section using SNR > 8 BBH events: single mass function (solid coloured lines) with considered events (grey).

the events considered is presented in Figure A.5.

As done previously, in order to evaluate the constraining power on each parameter, the corresponding "Gaussianized" percentage errors will be compared. Therefore, to get a better insight the obtained percentage errors of each parameter are reported in Table A.4.

Differently from the fixed cosmology case, this time it is possible to infer a clear ranking based on the constraining power of the parameters. In fact, `Truncated` is by far the best model as it is the most constraining in four out of five parameters and being the worst only in regard to $m_{95\%}$, which is in accordance with the fact that this model has the least number of free parameters, and is, therefore, the mass distribution that suffers the least from the parameters' degeneracy. The second and third best models are `PowerLawPeak`

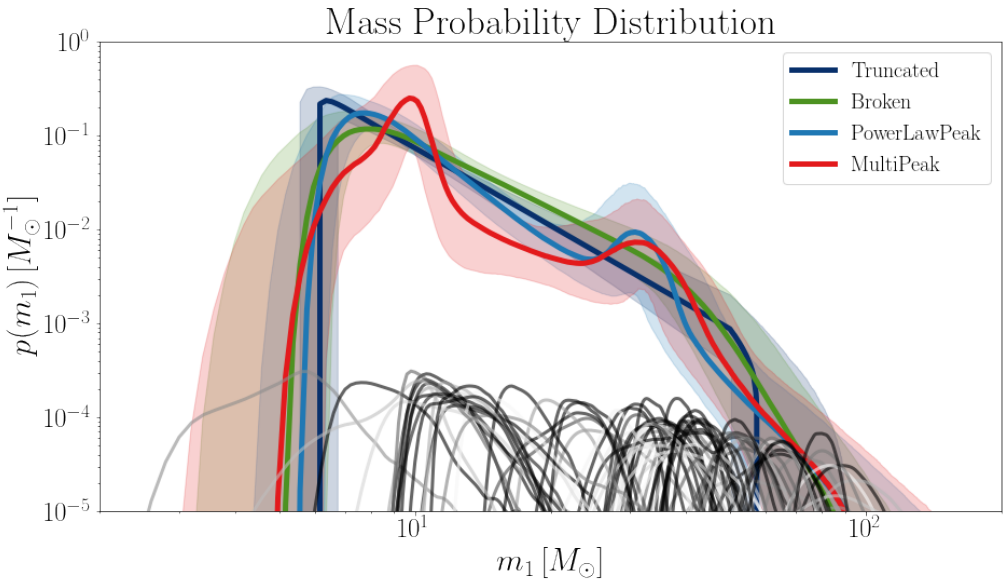

Figure A.5: Superimposition of the mass functions obtained with parameters presented in this section using SNR > 8 BBH events. The different colours represent the different models as described in the legend, with the solid line indicating the median, the shaded area the 95% confidence interval, and orange lines on the bottom are the selected GW events for SNR > 8.

SNR > 8	H_0 [km/s/Mpc]	R_0 [1/Gpc^3/yr]	γ	m_l [$M_\odot$]	m_h [$M_\odot$]	$m_{5\%}$ [$M_\odot$]	$m_{95\%}$ [$M_\odot$]
`Truncated`	$108.94^{+39.56}_{-36.76}$	$17.42^{+6.45}_{-4.79}$	$2.37^{+1.04}_{-0.92}$	$6.08^{+0.32}_{-0.34}$	$57.43^{+13.64}_{-5.55}$	$6.16^{+0.40}_{-0.40}$	$27.86^{+5.05}_{-4.26}$
`Broken`	$65.12^{+60.82}_{-38.24}$	$10.87^{+5.19}_{-3.17}$	$2.77^{+1.62}_{-1.11}$	$4.77^{+0.94}_{-1.27}$	$123.08^{+47.95}_{-39.95}$	$6.56^{+0.79}_{-0.79}$	$32.13^{+4.56}_{-4.36}$
`PowerLawPeak`	$94.59^{+42.99}_{-30.92}$	$14.18^{+6.22}_{-4.13}$	$2.23^{+1.06}_{-0.89}$	$5.23^{+0.53}_{-0.72}$	$116.45^{+56.21}_{-38.37}$	$6.56^{+0.59}_{-0.40}$	$32.13^{+3.17}_{-2.97}$
`Multipeak`	$73.45^{+35.45}_{-25.72}$	$13.74^{+5.27}_{-3.88}$	$2.36^{+1.15}_{-1.01}$	$4.46^{+1.04}_{-1.33}$	$110.80^{+57.97}_{-33.15}$	$7.15^{+0.99}_{-0.99}$	$32.92^{+3.57}_{-3.17}$

Table A.3: Common cosmological and astrophysical parameters for SNR > 8 BBH events obtained by freeing the cosmological parameters.

SNR > 8	ΔH_0	ΔR_0	$\Delta\gamma$	Δm_l	Δm_h	$\Delta m_{5\%}$	$\Delta m_{95\%}$
`Truncated`	0.35	0.32	0.41	0.05	0.17	0.07	0.17
`Broken`	0.76	0.34	0.49	0.23	0.36	0.12	0.14
`PowerLawPeak`	0.39	0.36	0.44	0.12	0.41	0.08	0.10
`Multipeak`	0.42	0.33	0.46	0.27	0.41	0.14	0.10

Table A.4: Percentage errors of the parameters obtained for SNR > 8 BBH events by freeing the cosmological parameters.

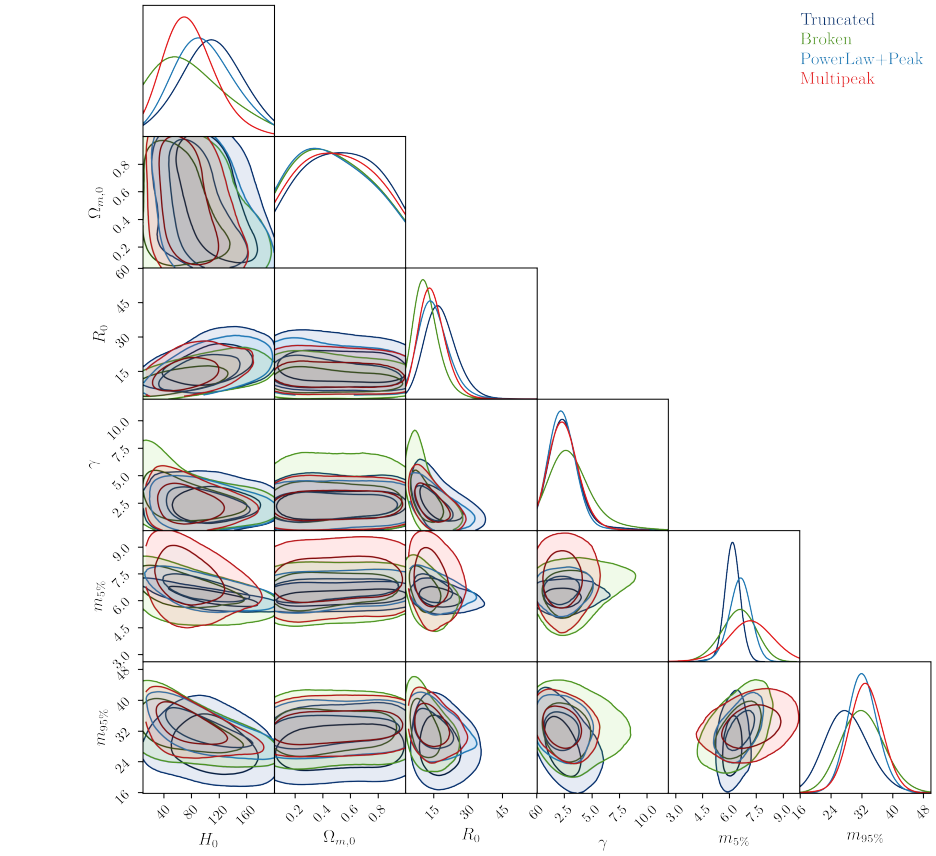

(a)

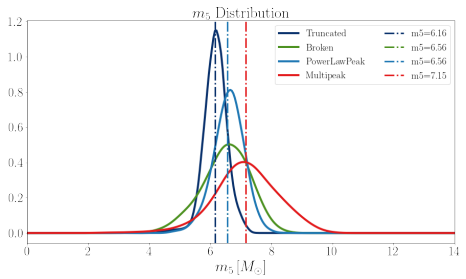

(b)

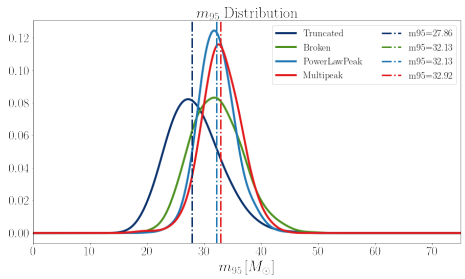

(c)

Figure A.6: (a) Corner plot for the common parameters for the different mass functions obtained by using SNR > 8 BBH events. A zoomed look of $m_{5\%}$ and $m_{95\%}$ distributions is presented in (b) and (c) respectively.

and `Multipeak`, respectively. This is not surprising given the similarity of the two mass functions and the fact that the multipeak mass function has two additional parameters with respect to the single peak model. Lastly, `Broken` is the worst model since it cannot provide a constraining power better than the third-best value with respect to the other mass function.

Therefore, the constraining powers of the parameters seem to suggest the following ranking: `Truncated`, `PowerLawPeak`, `Multipeak`, and lastly `Broken`, which will probably be discarded as a valid mass function since it has the worst constraining power but is not the model defined by the most parameters.

This result is extremely different from the one obtained in the population analysis. It appears that the addition of the two cosmological parameters, H_0 and $\Omega_{0,m}$, tends to penalize the more complex mass functions with worse constraining power, which again is opposite to the conclusion found in the $SNR > 12$ case, where the results suggested that eventually, more complex models are better for reproducing the population of events. This disagreement between the results obtained for the two SNR regimes could be interpreted as proof of the fact that a wider set of data does not directly mean that the analysis improves.

A.2.1 Hubble Constant Distribution

Another strong evidence of the goodness of fit of each model can be given by the produced H_0 distributions shown in Figure A.7. In Figure A.7a, it is again possible to observe how the broadness of the distribution follows the same trend as in the $SNR > 12$ case, thus leading to the same conclusion that `Multipeak` is the best model to reproduce the mass population given the selected data. In particular, the badness of `Truncated` is made evident, as its distribution peaks at $H_0 \sim 109\,\mathrm{km/s/Mpc}$ far away from the Planck value at $H_0 = 67\,\mathrm{km/s/Mpc}$. So, in contrast to the $SNR > 12$ case, it seems that the Hubble constant distribution clearly rules the truncated mass function out as a valid model for the BBH population.

Despite the fact that as before `Multipeak` is followed by `PowerLawPeak` in regards to the reproduction of the H_0 distribution, it appears that the single peak model is not as good as in the $SNR > 12$ case, since the resulting distribution is much broader. The same observation can be made for `Broken` which is again the third best model, but its distribution is much worse than in the $SNR > 12$ case based on the width of the distribution.

Moreover, it is possible to compare the results for H_0 obtained in this work in the context of the Hubble tension by observing Figure A.8.

An observation that can be made is the fact that the $SNR > 8$ case tends to provide higher values for H_0 than the corresponding values of $SNR > 12$ case, since only `Broken` has a lower H_0 estimate in the first case rather than in the ladder: $H_0^{SNR>8} = 109\,\mathrm{km/s/Mpc}$ vs. $H_0^{SNR>12} = 65\,\mathrm{km/s/Mpc}$. Nevertheless, it is evident that all mass functions studied in this work are not able to provide a competitive constrain on the Hubble constant as the percentage errors are typically of order $\sim 50\%$, which is extremely wider than the results obtained in literature [4, 5] as shown in Figure A.8.

A.3 Comparison of the Results at Different SNR

Now that all the mass distributions have been presented for both SNR regimes, in this section a comparison between the constructed models in the two different cases will be made,

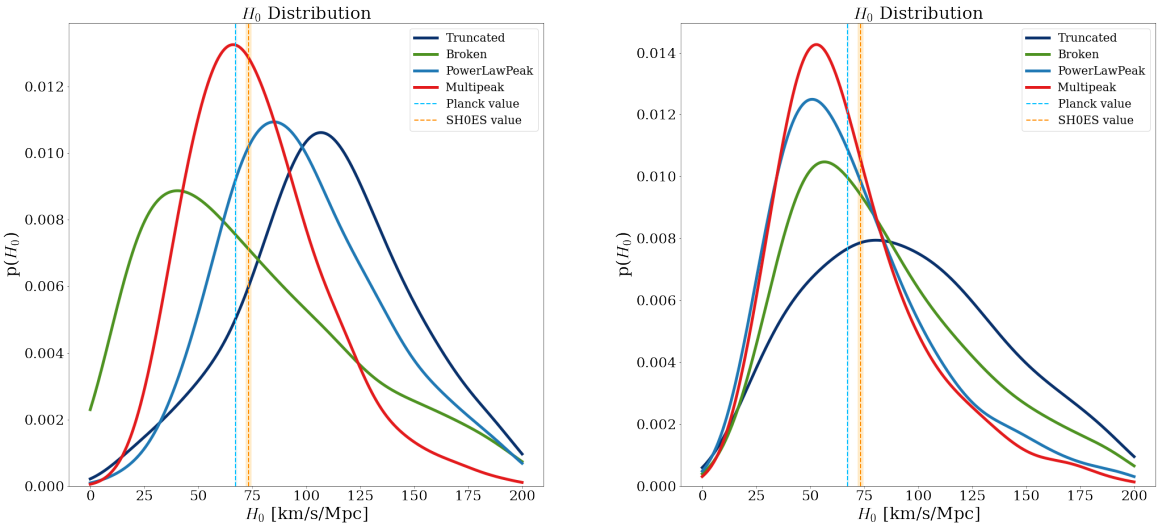

(a) (b)

Figure A.7: H_0 distribution obtained by using: (a) SNR > 8 BBH events, (b) SNR > 12 BBH events.

thus allowing us to study how the amount of data influences the results. In particular, since the effects on the mass model construction are similar, the discussion will be made jointly for both the population and the cosmology analysis, eventually outlining the few differences between the two cases. Therefore we compare Figure A.2 with Figure 4.8, and Figure A.3a with Figure 4.7a for the population analysis; while we compare Figure A.5 with Figure 4.16, and Figure A.6a with Figure 4.15a for the cosmology analysis.

As already pointed out the main difference between the mass functions in the two SNR cases that can be spotted is the broadness of the confidence intervals. In fact, in the SNR > 8 case the confidence intervals are always narrower than in the SNR > 12 case, which can be linked to the fact that in the first case more events are available for the analysis, thus having more data to constrain all the model defining parameters.

Another effect of a greater constraining power that can be noticed by observing the mentioned Figures is the shape of the first Gaussian peak (at $M \sim 12\,M_\odot$) in `Multipeak`. The peak in case SNR > 8 is visible, outstanding the general power law trend. Whereas in the second case, the Gaussian peak disappears in the power law trend causing a broadening of the initial peak of the model. The Gaussian behaviour is only detectable thanks to the presence of a spike at $M \sim 12\,M_\odot$ in the 95% C.I. of the multipeak mass model.

Furthermore, by looking more into the respective corner plots and by comparing the values and the width of the $1\,\sigma$ interval of the parameters for the different models reported in corresponding Tables, it is possible to get a better insight into the differences between the two SNR cases.

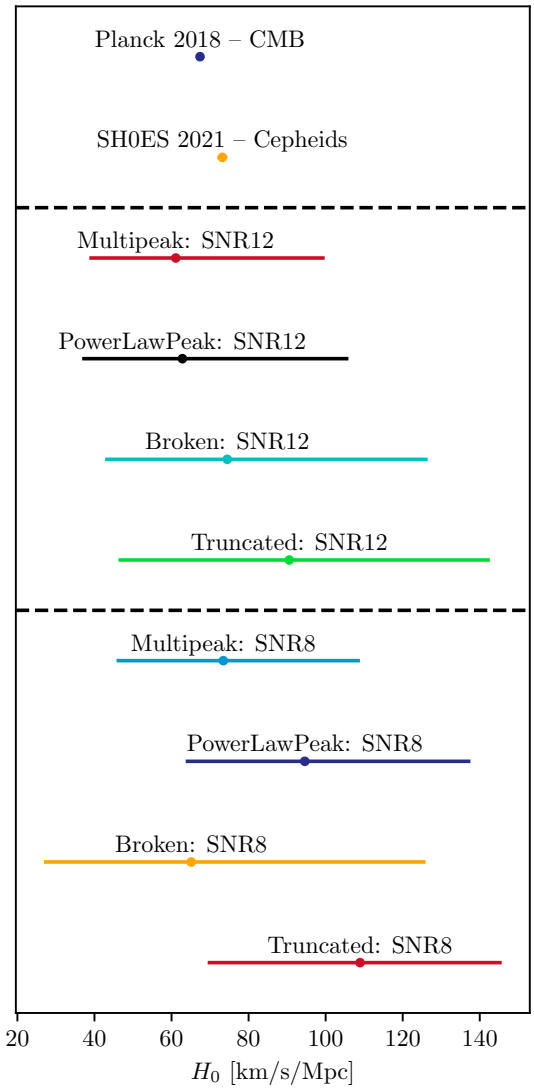

Figure A.8: Comparison between the H_0 value obtained for the different SNR cases and the values currently accepted by the scientific community in the context of the Hubble tension.

In general, it can be evinced that the effect of considering a lower SNR level is a shift to higher values for most of the considered parameters: H_0, $m_{5\%}$ and $m_{95\%}$. However, this shift is not particularly large so the estimates of the parameter are consistent between the two SNR regimes. Moreover, it can be observed that the estimate for R_0 has mostly similar values in the two SNR cases, but its distributions are much narrower in the SNR > 8 case than in the SNR > 12 one, suggesting that having more available data for the analysis in the SNR > 8 case allows obtaining better constrain for this particular parameter. The

last relevant parameter to evaluate is γ: the constant describing the slope of the merger rate. It is evident that lowering the SNR level drastically lowers the estimate for this parameter from $\gamma_{SNR>12} \sim 8$ to $\gamma_{SNR>8} \sim 2$, thus suggesting that some inconsistency in the interpretation of this parameter is found by evaluating the available data.

A.4 Model Selection

At last, the same model selection analysis was made on the mass function obtained in SNR > 8 regime. Again, only the main results and a brief discussion will be given in order to avoid burdening further the description of this work.

A.4.1 Deviance Information Criterion

The first used selection method was the DIC, of which the obtained results are displayed in Table A.5.

SNR > 8	Fixed Cosmology	Free Cosmology
`Truncated`	-31.86	-23.77
`Broken`	-17.58	-13.92
`PowerLawPeak`	-3.87	-2.42
`Multipeak`	0.00	0.00

Table A.5: Model selection results: DIC for SNR > 8 BBH events.

It can be seen that the `Multipeak` is the preferred model, with all values being zero. Furthermore, as already observed for the SNR > 12 case, the truncated mass function is the most disfavoured model, which is proven by DIC $\gtrsim 24$, indicating that such distribution cannot be the correct one to describe the BBH population. Other relevant comments can be made depending on the parameter choice (Population or Cosmology), for example:

- `PowerLawPeak` is the second best model after `Multipeak` in both analysis cases. In contrast with the SNR > 12 case, the model is not as good as before if the population analysis is considered, since $\mathrm{DIC}_{SNR>8} \approx 4$ vs. $\mathrm{DIC}_{SNR>12} \approx 0.5$. Thus, this model results to be disfavoured, despite not being ruled out;

- again `Broken` is always disfavoured with respect to `Multipeak`, but in the SNR > 8 case this model is *strongly* disfavoured as DIC $\gtrsim 14$ in both population and cosmology analysis.

A.4.2 Posterior Predictive Check

Finally, the PPD were calculated to compare the different distribution as a model selection method. Results obtained for SNR > 8 are shown in Figures A.9 and Figure A.10, for the population analysis and cosmology analysis respectively.

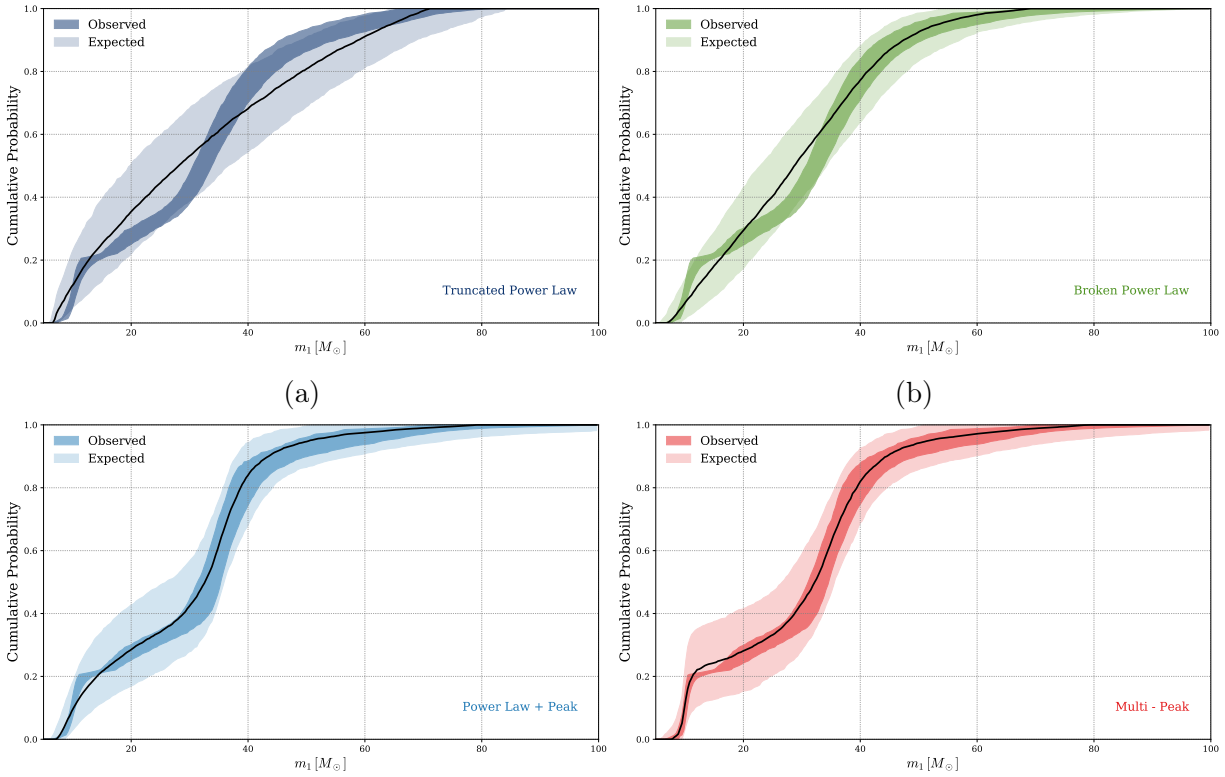

Figure A.9: PPD check in the SNR > 8 population analysis, with the different implemented mass functions: (a) Truncated Power Law; (b) Broken Power; (c) Law Power Law + Peak; (d) Multipeak Power Law. In each plot the solid line represents the median of the expected cumulative distribution function.

In general, the results found for the SNR > 8 (Figure A.9) population analysis are very similar to the ones obtained in the SNR > 12 case (Figure 4.18), with the small difference that the expected distributions are narrower, thus making it easier to exceed the borders. This behaviour could be explained by the fact that in the SNR > 8 case a much wider event sample is considered with respect to the only 35 events of the SNR > 12 case, thus making it possible to constrain the parameters and models in a better way (as proven in Section A.1), leading to narrower expected regions.

So, for the different mass functions, it is obtained that:

- **Truncated Power Law:** the observed data do not follow the general median trend and cross the borders of the expected distribution at two different mass scales:

$M \approx 30\,M_\odot$ and $M \gtrsim 40\,M_\odot$;

- **Broken Power Law:** even though the observed data do not follow the median trend, they can fit the median in a better way than the truncated model, as a confirmation that this model does only cross the limit of the expected distribution at $M \approx 30\,M_\odot$, while remaining within the allowed region for $M \gtrsim 40\,M_\odot$;

- **Power Law + Peak and Multipeak:** the observed data follow in a good way the median trend of the expected cumulative distribution function without crossing its borders. The main difference between the two models is the inability of `PowerLawPeak` to reproduce the low mass end of the distribution in a similar good way as `Multipeak`.

Therefore, it appears that the already established ranking from the SNR > 12 case is confirmed by its PPD test: `Multipeak` is the best model, just followed by `PowerLawPeak` which in comparison is not as good as `Multipeak` in fitting the low mass end of the PPD; the third mass function is `Broken`, which despite being clearly disfavoured (exceed the distribution borders) cannot be ruled out completely as the excess is small; and the worst model is `Truncated`, which due to the exceeding at $M \approx 30\,M_\odot$ and $M \gtrsim 40\,M_\odot$, can be discarded as a valid model.

The same behaviour can be observed also in the cosmology analysis. In fact, it is possible to do a similar discussion also for Figure A.10:

- **Truncated Power Law:** the observed data do not follow the general median trend and cross the borders of the expected distribution at $M \approx 30\,M_\odot$ and $M \gtrsim 40\,M_\odot$;

- **Broken Power Law:** even though the observed data do not follow the median trend, they completely include it within their range. As in the population case, due to the broadening of the distribution, the model does slightly cross the limit of the expected distribution at $M \approx 35\,M_\odot$;

- **Power Law + Peak and Multipeak:** despite the general broadening of the distributions, the observed data follow in a good way the median trend of the expected cumulative distribution function without crossing the borders. Nevertheless, for `PowerLawPeak` from $M \approx 30\,M_\odot$ to $M \approx 45\,M_\odot$ the observed distribution is just on the borders of the expected distribution, thus providing a small proof of the fact that `Multipeak` is the preferred model.

Therefore, also in this second cosmology case, the already established ranking of the different models is confirmed by the PPD test: `Multipeak` is the best one, which is followed by `PowerLawPeak` which in comparison is not as good as the previous model in fitting the PPD at $M \sim 10\,M_\odot$; the third mass function is `Broken`, which despite being clearly disfavoured due to its border crossing cannot be ruled out completely, based on the small dimensions of the excess; and the worst model is `Truncated`, which again exceeds the expected distribution at $M \gtrsim 35\,M_\odot$, and can therefore be discarded as a valid model.

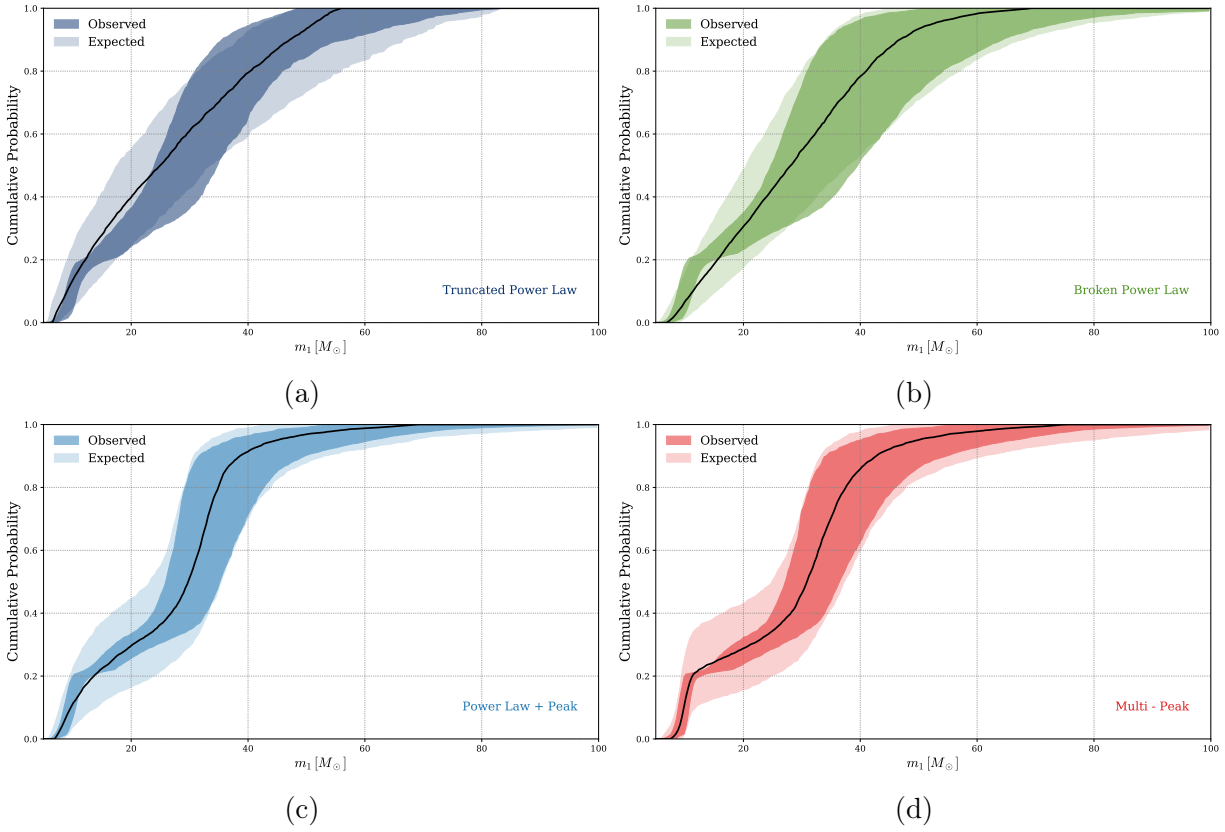

Figure A.10: PPD check in the SNR > 12 H_0 analysis, with the different implemented mass functions: (a) Truncated Power Law; (b) Broken Power Law; (c) Power Law + Peak; (d) Multipeak Power Law. In each plot, the solid line represents the median of the expected cumulative distribution function.

Therefore, it is evident that all model selection methods point to confirming the ranking of the mass function suggested qualitatively by their form and by their features.

More importantly, it stands out that the choice of a lower SNR value does not greatly impact on the mass function estimation for the BBH population. In fact, from the SNR > 12 analysis emerged that `Multipeak` is the best model to reproduce the BBH population soon followed by `PowerLawPeak`, which is only weakly disfavored, whereas the level of disfavour of `Broken` is greater and depends on the parameter choice, lastly `Truncated` is always rejected as a possible BBH population model. Despite their larger uncertainties, by taking into account the events with SNR > 8 the same result of SNR > 12 is found with a general increase of the level of disfavour for all mass functions, hence indicating in an even stronger way than `Multipeak` is the best one to reproduce the BBH population.

Appendix B

Corner Plots

In the following chapter, all the corner plots produced within the context of this work are reported. In particular, for each analysis type (population and cosmology), the plots for the SNR > 8 case will be presented first, then followed by the SNR > 12 plots.

B.1 Results at Fixed Cosmological Model

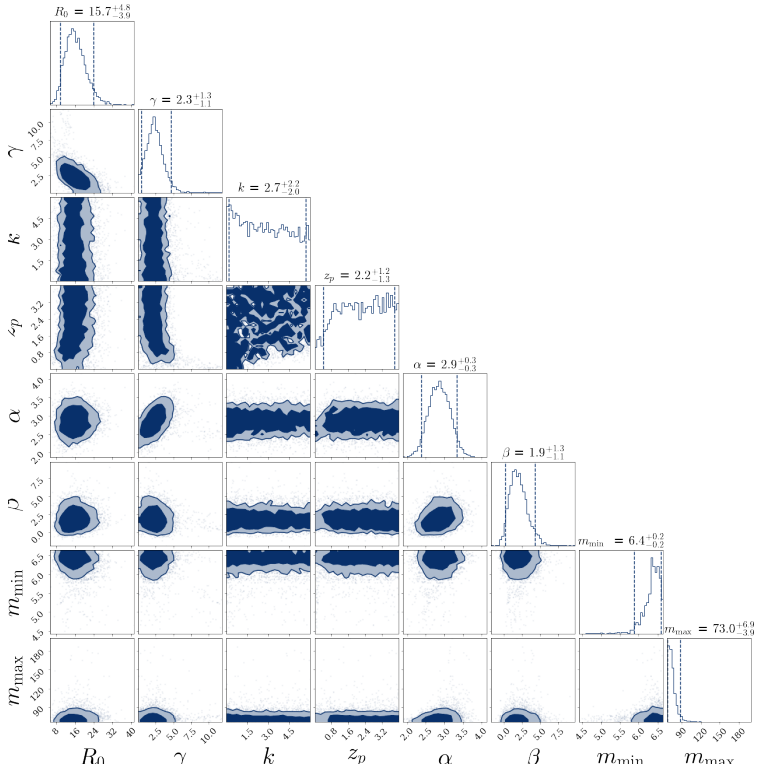

Figure B.1: Corner plot for the truncated power law parameters obtained from the Bayesian analysis by using events with SNR > 8.

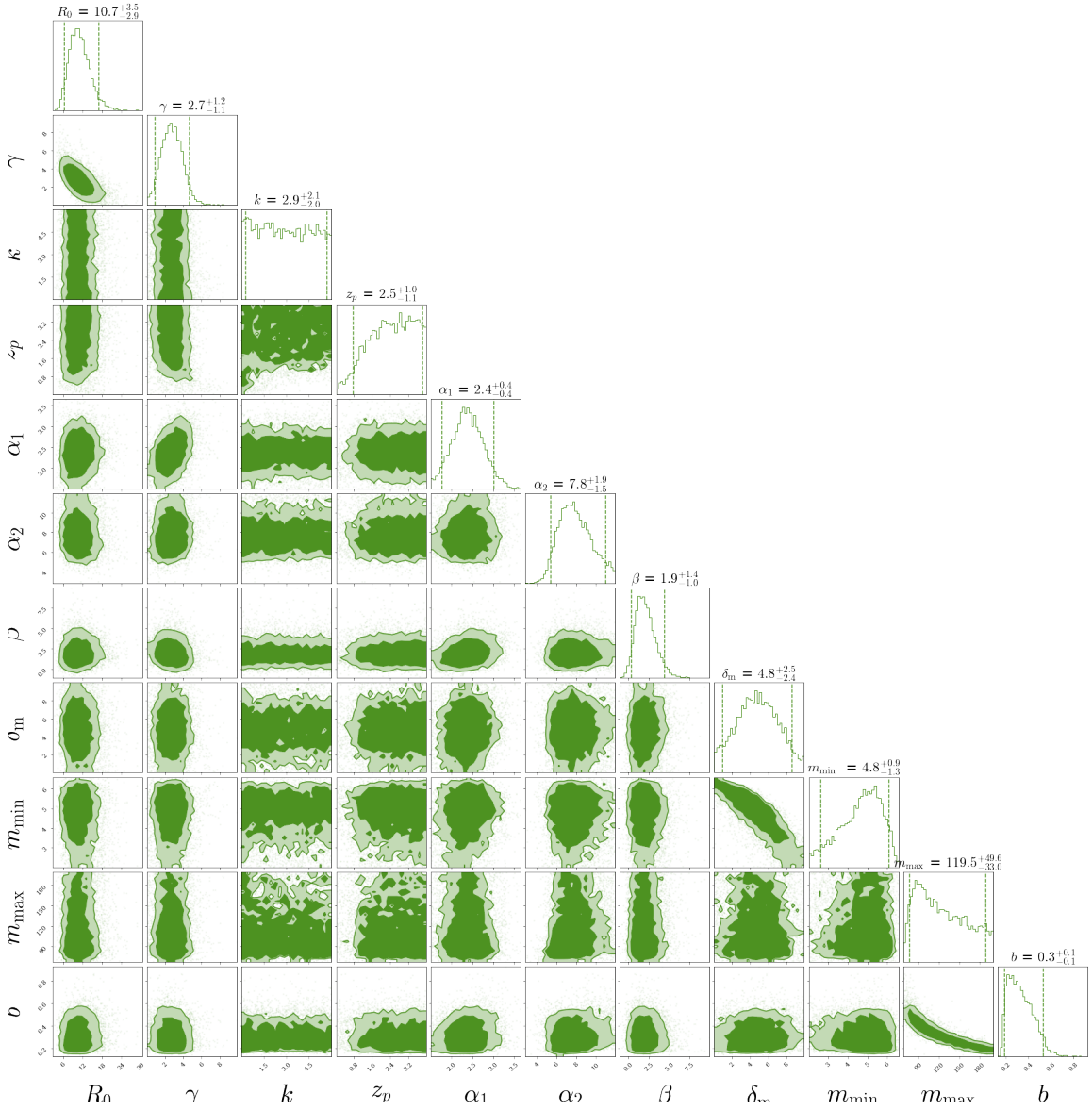

Figure B.2: Corner plot for the broken power law parameters obtained from the Bayesian analysis by using events with SNR > 8.

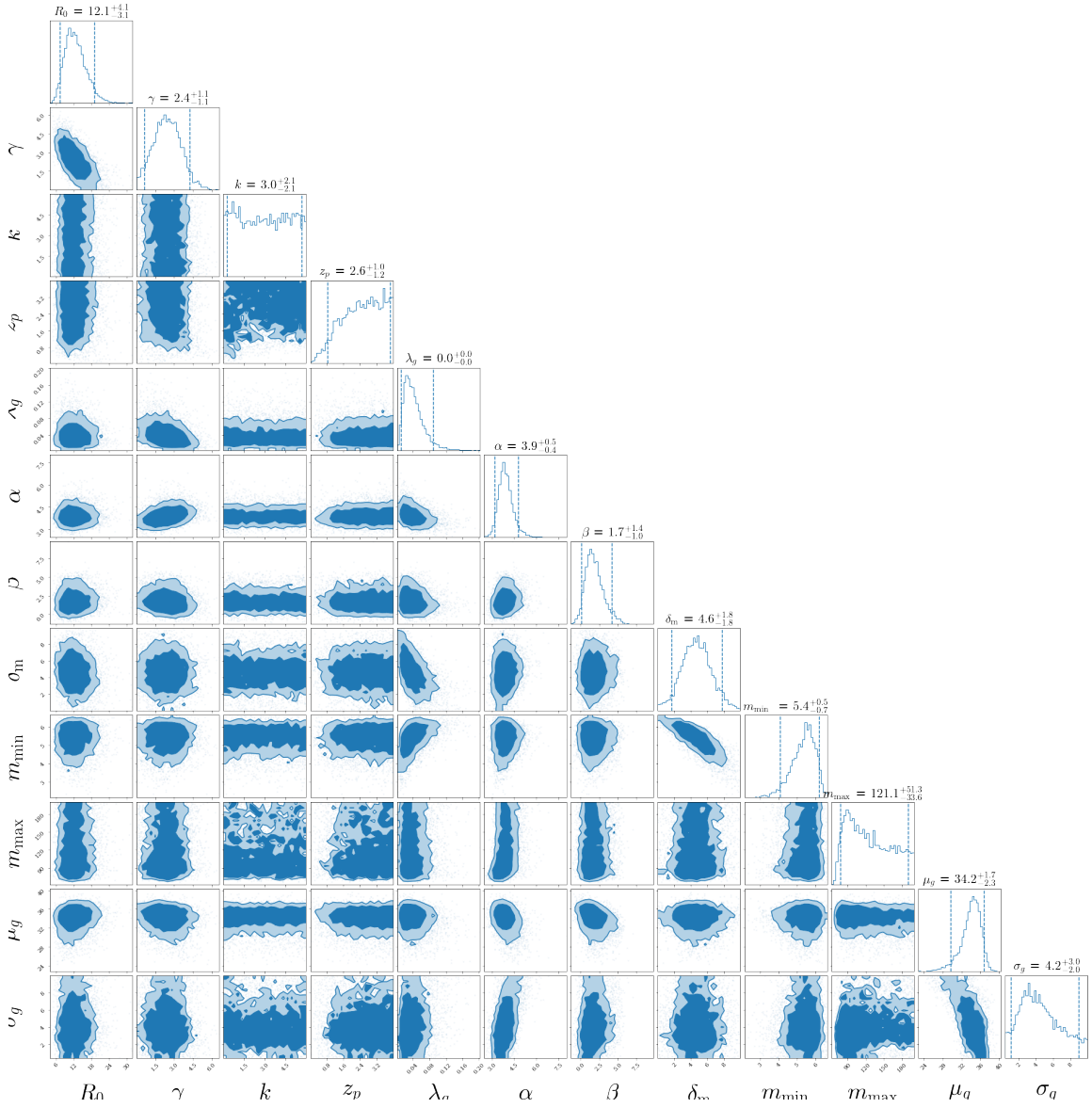

Figure B.3: Corner plot for the power law + peak parameters obtained from the Bayesian analysis by using events with SNR > 8.

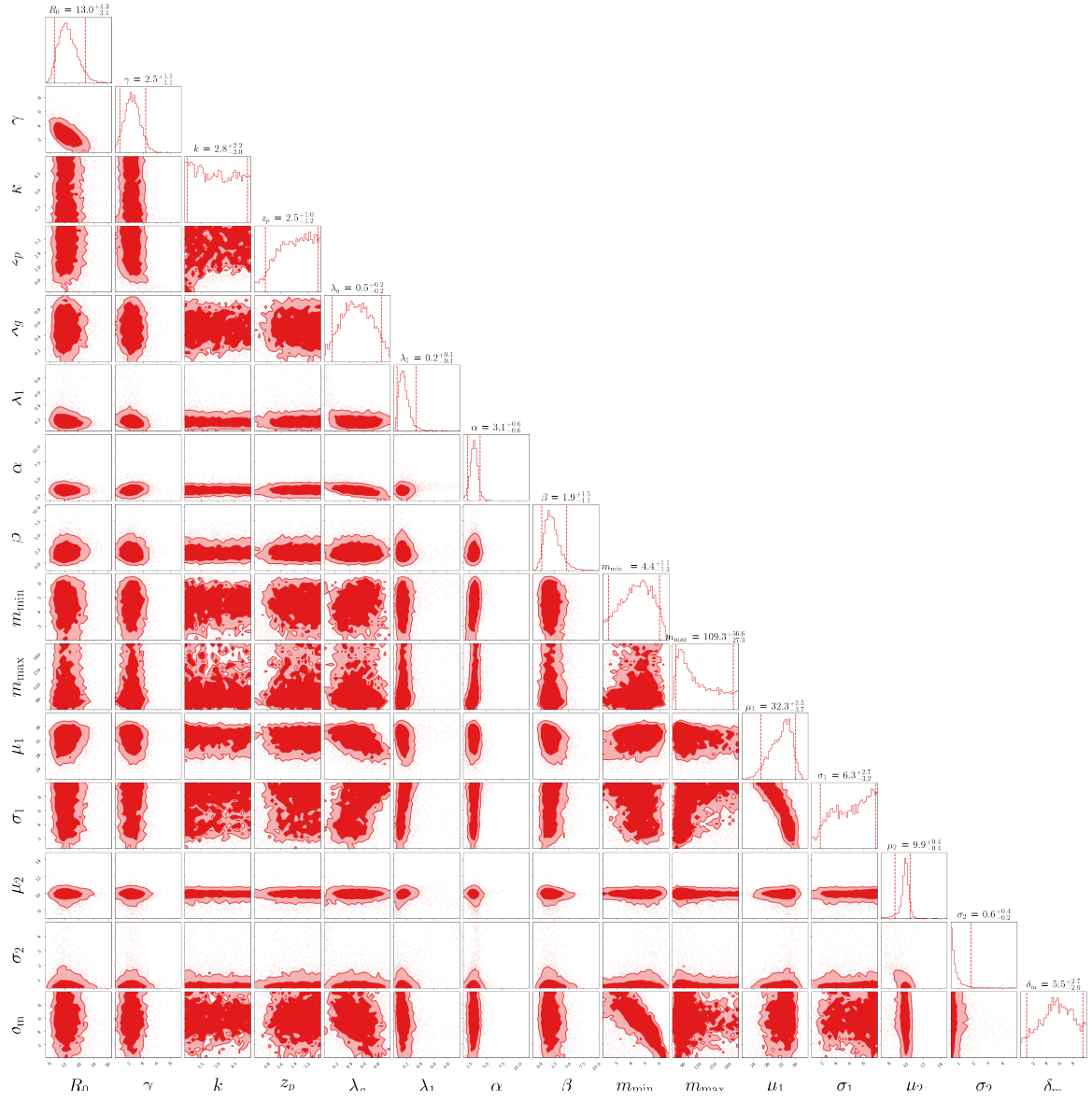

Figure B.4: Corner plot for the power law + 2 peaks parameters obtained from the Bayesian analysis by using events with SNR > 8.

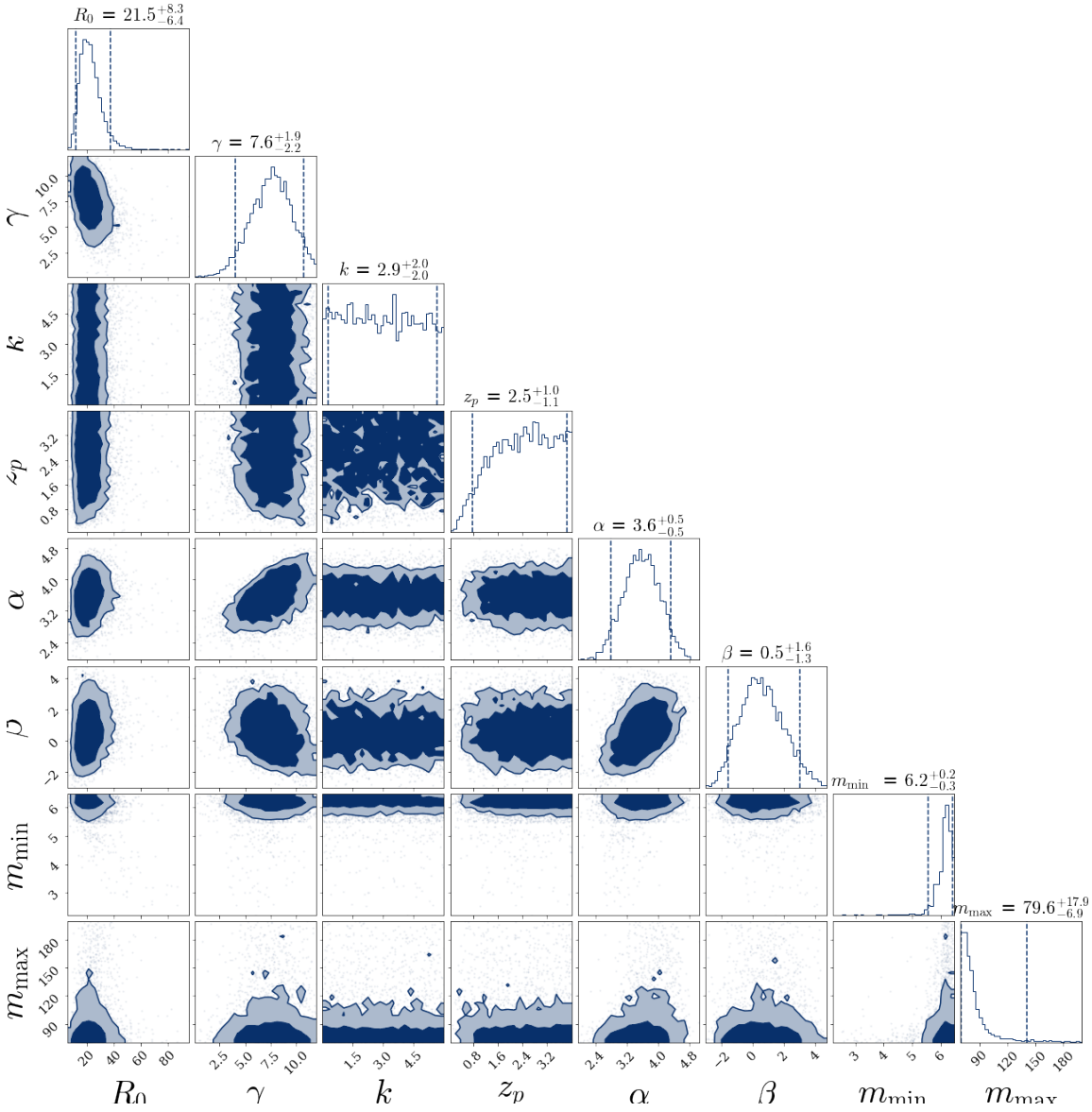

Figure B.5: Corner plot for the truncated power law parameters obtained from the Bayesian analysis by using events with SNR > 12.

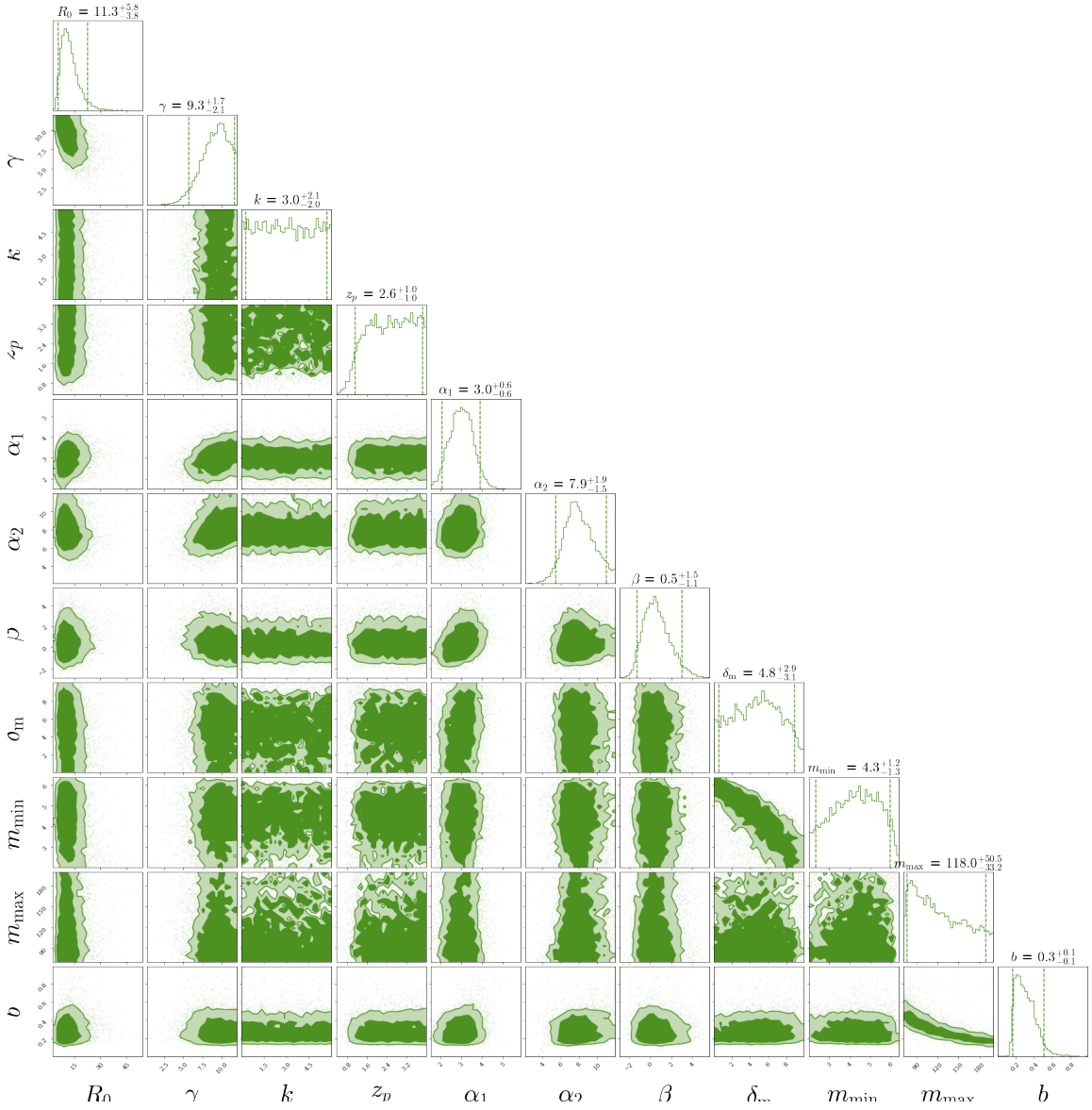

Figure B.6: Corner plot for the broken power law parameters obtained from the Bayesian analysis by using events with SNR > 12.

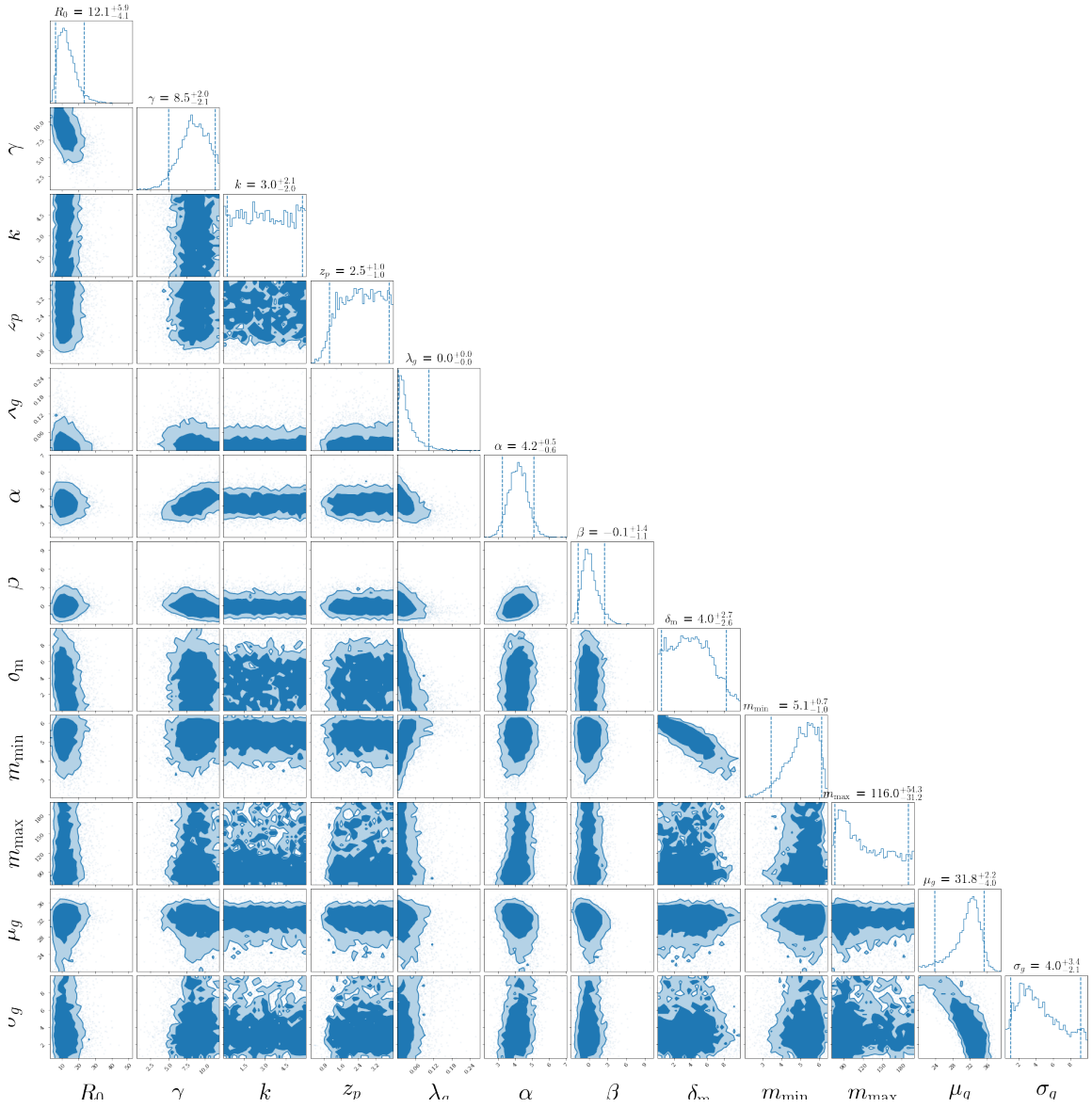

Figure B.7: Corner plot for the power law + peak parameters obtained from the Bayesian analysis by using events with SNR > 12.

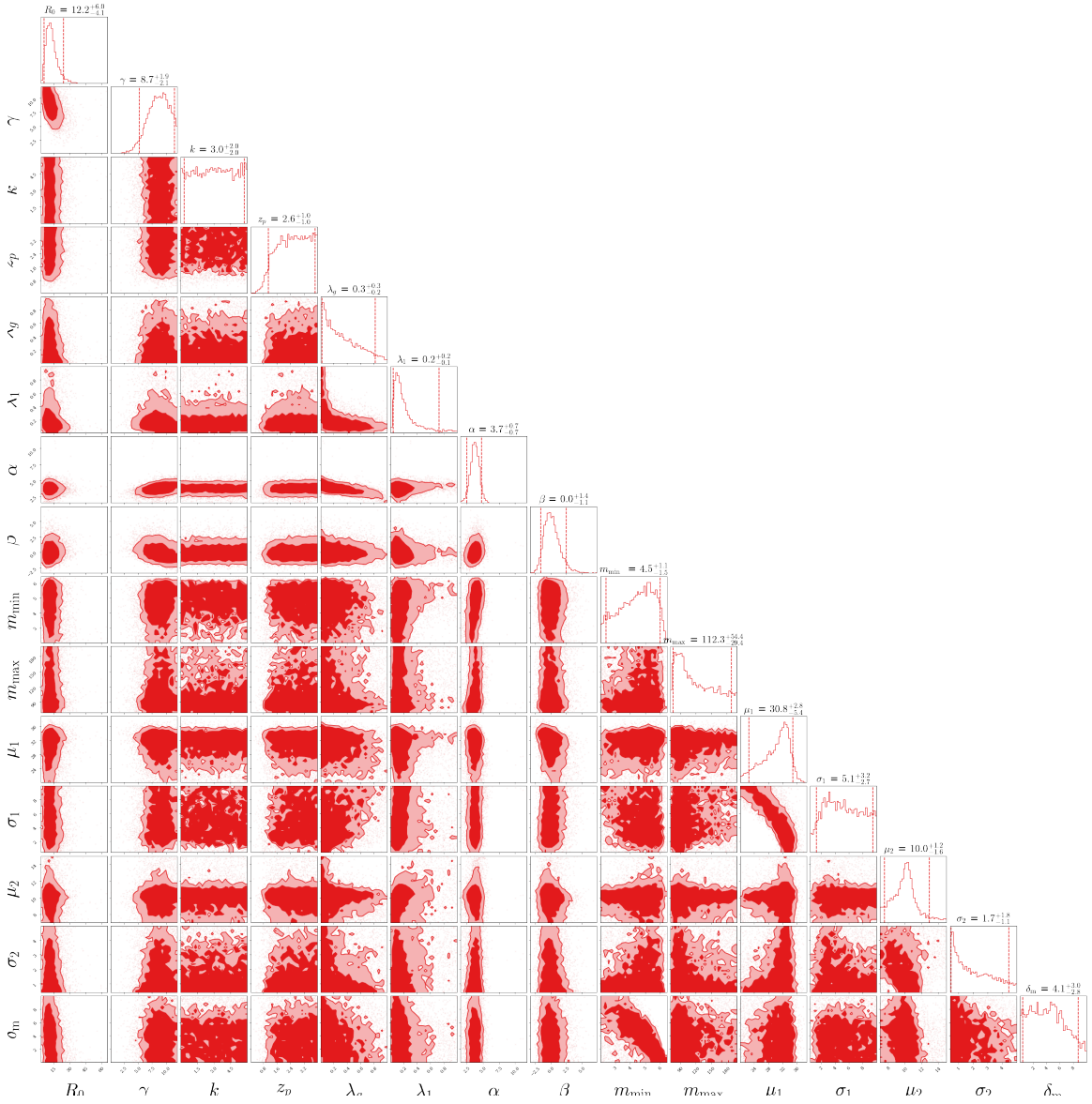

Figure B.8: Corner plot for the power law + 2 peaks parameters obtained from the Bayesian analysis by using events with SNR > 12.

B.2 Results at Free Cosmological model

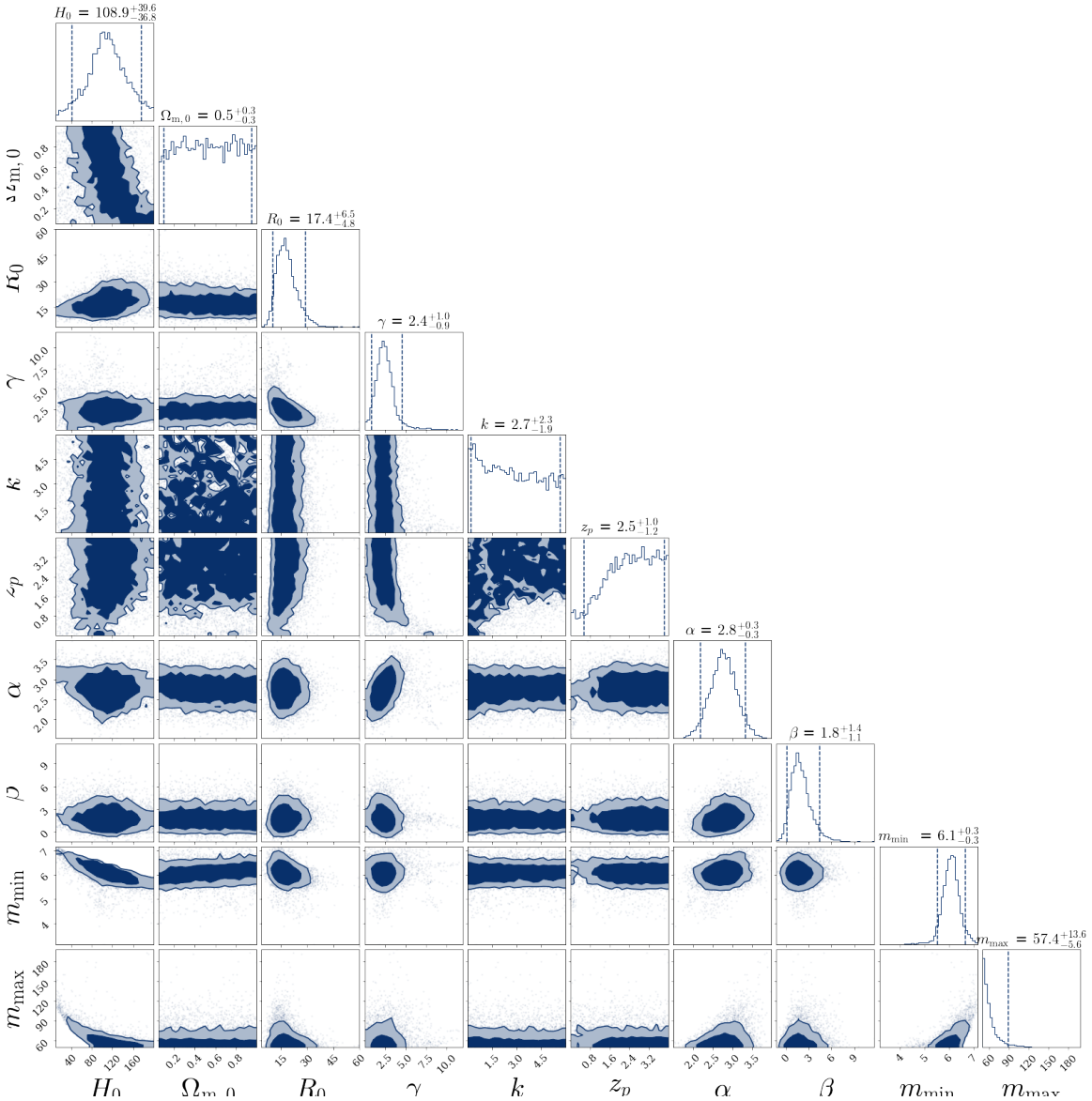

Figure B.9: Corner plot for the truncated power law parameters obtained from the Bayesian analysis by using events with SNR > 8.

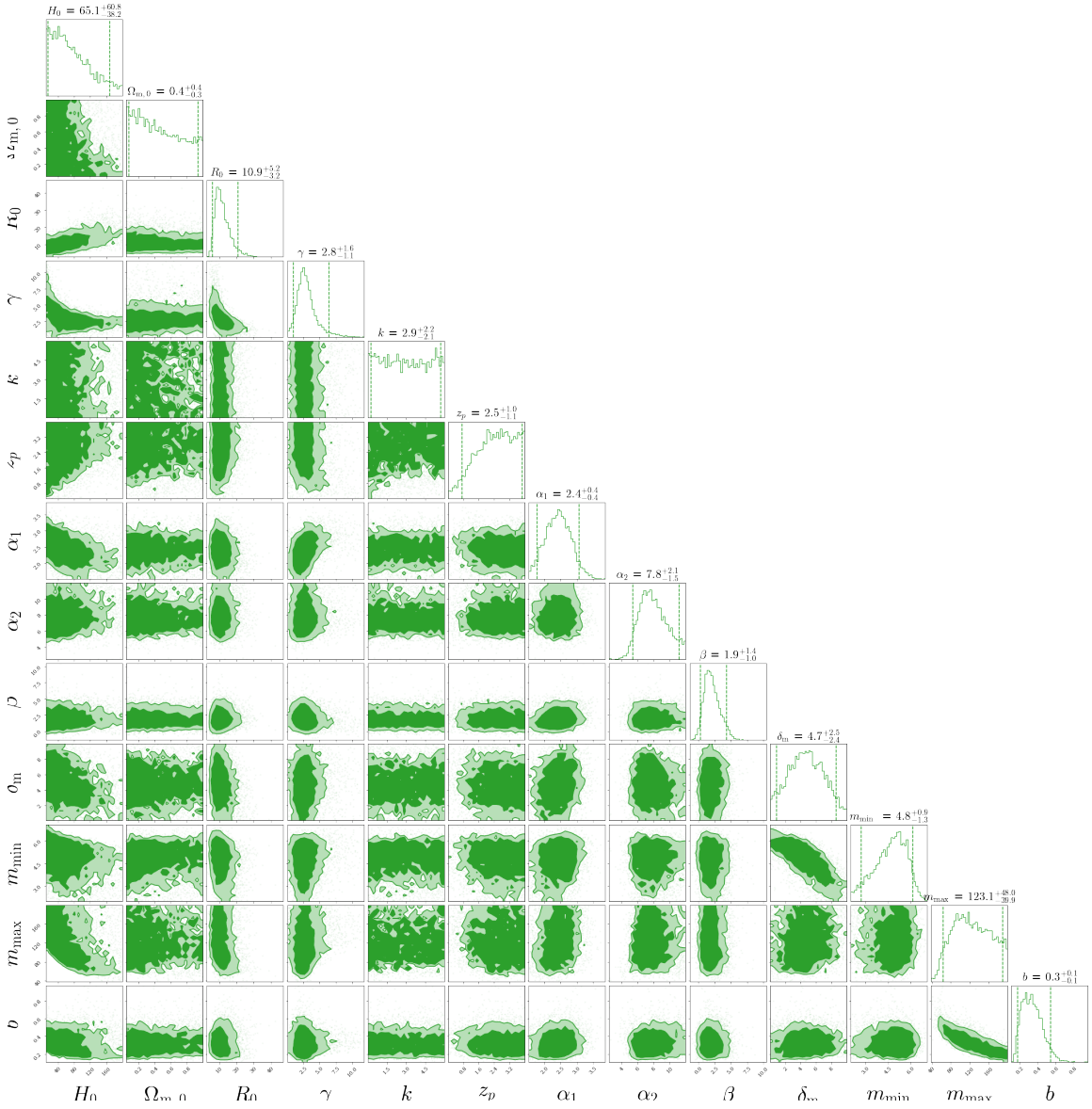

Figure B.10: Corner plot for the broken power law parameters obtained from the Bayesian analysis by using events with SNR > 8.

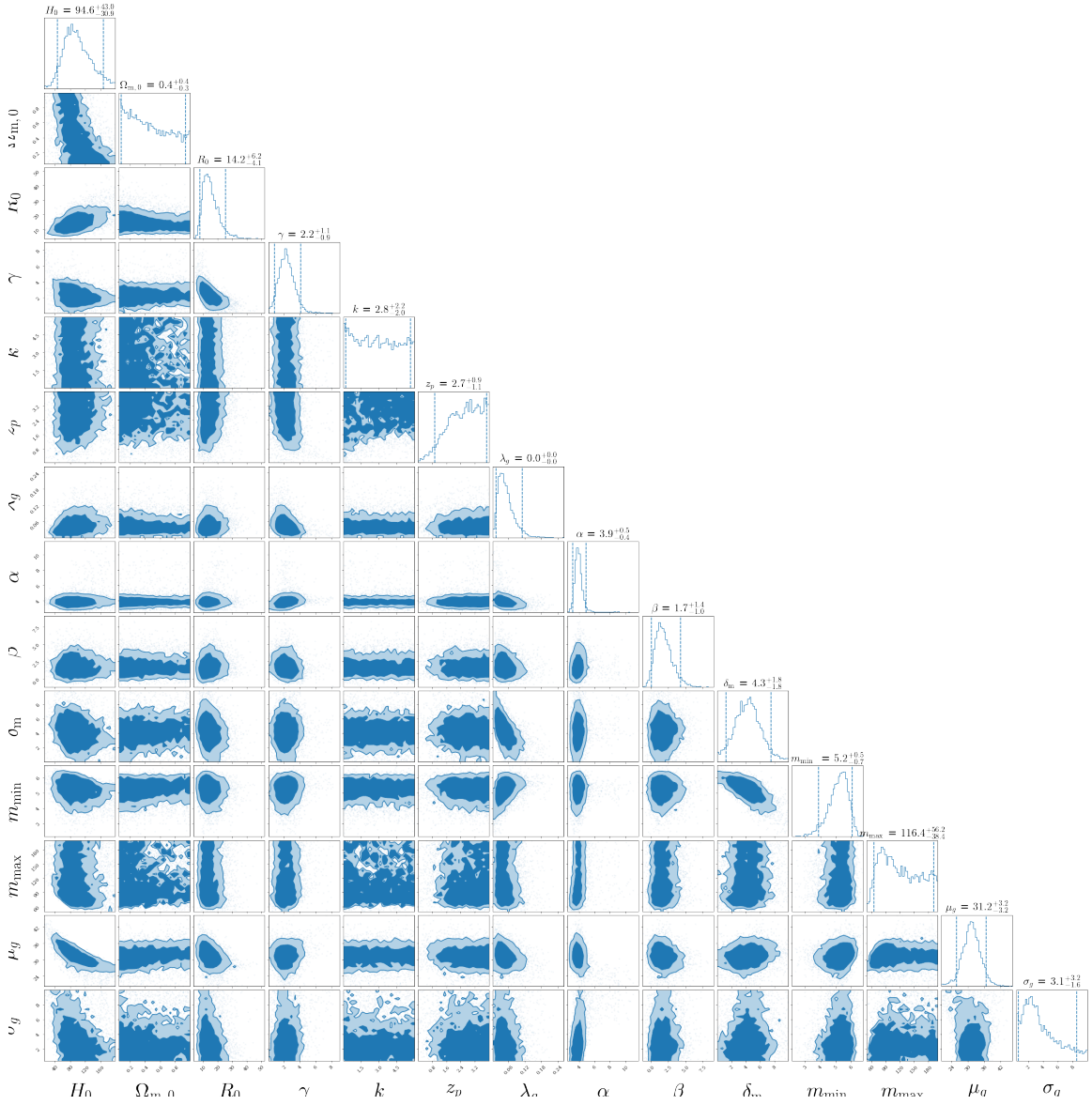

Figure B.11: Corner plot for the power law + peak parameters obtained from the Bayesian analysis by using events with SNR > 8.

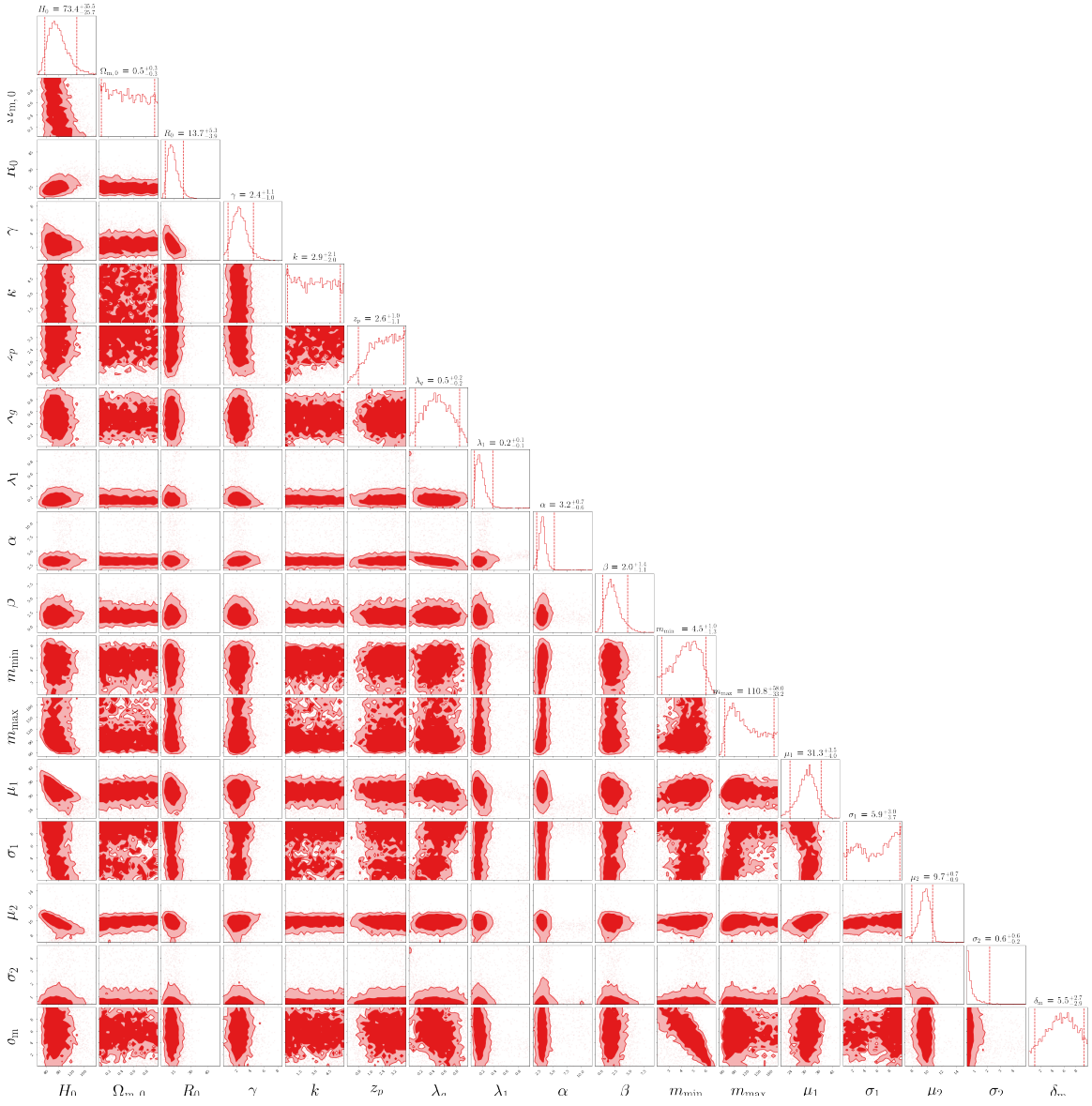

Figure B.12: Corner plot for the power law + 2 peaks parameters obtained from the Bayesian analysis by using events with SNR > 8.

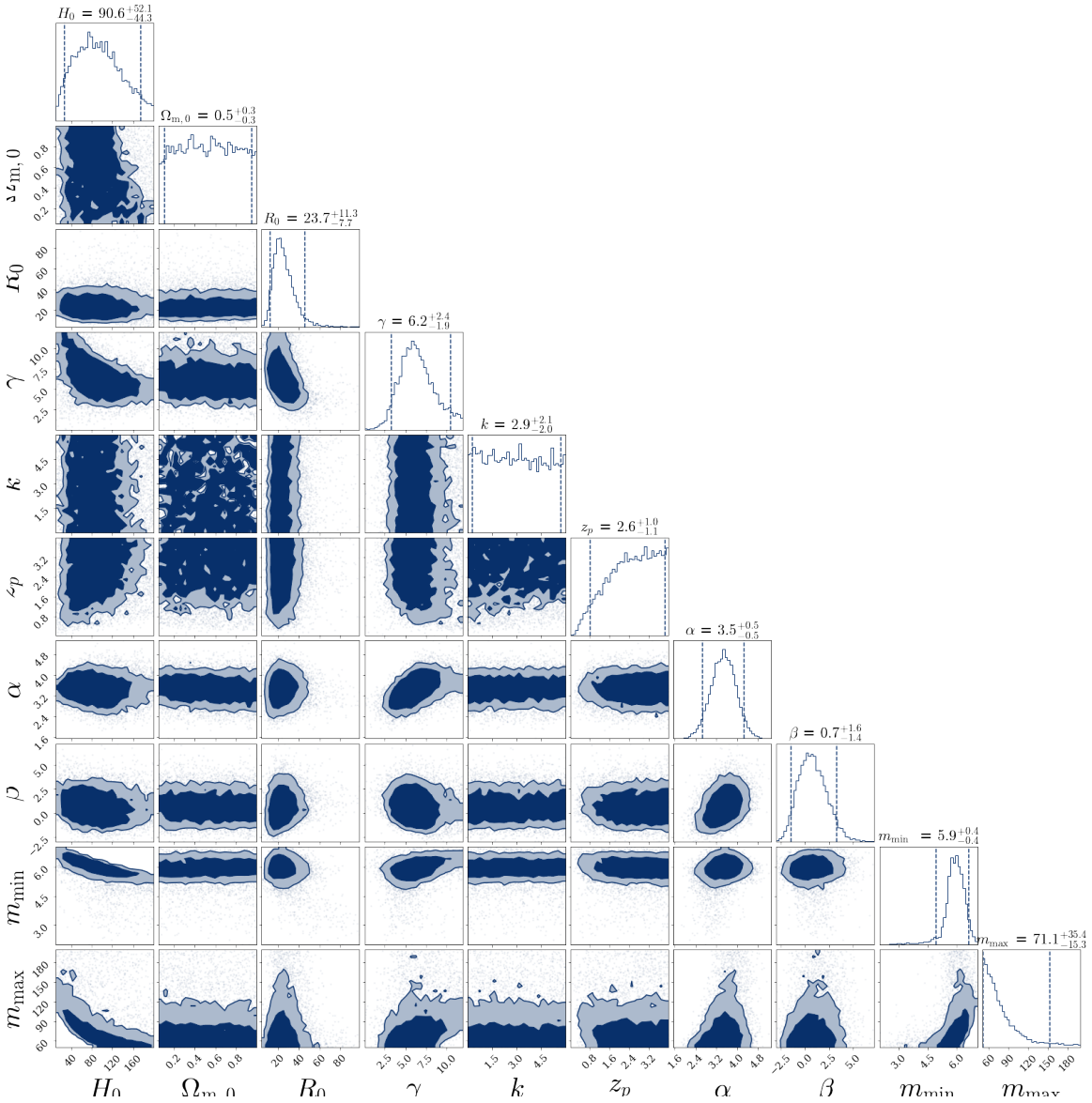

Figure B.13: Corner plot for the truncated power law parameters obtained from the Bayesian analysis by using events with SNR > 12.

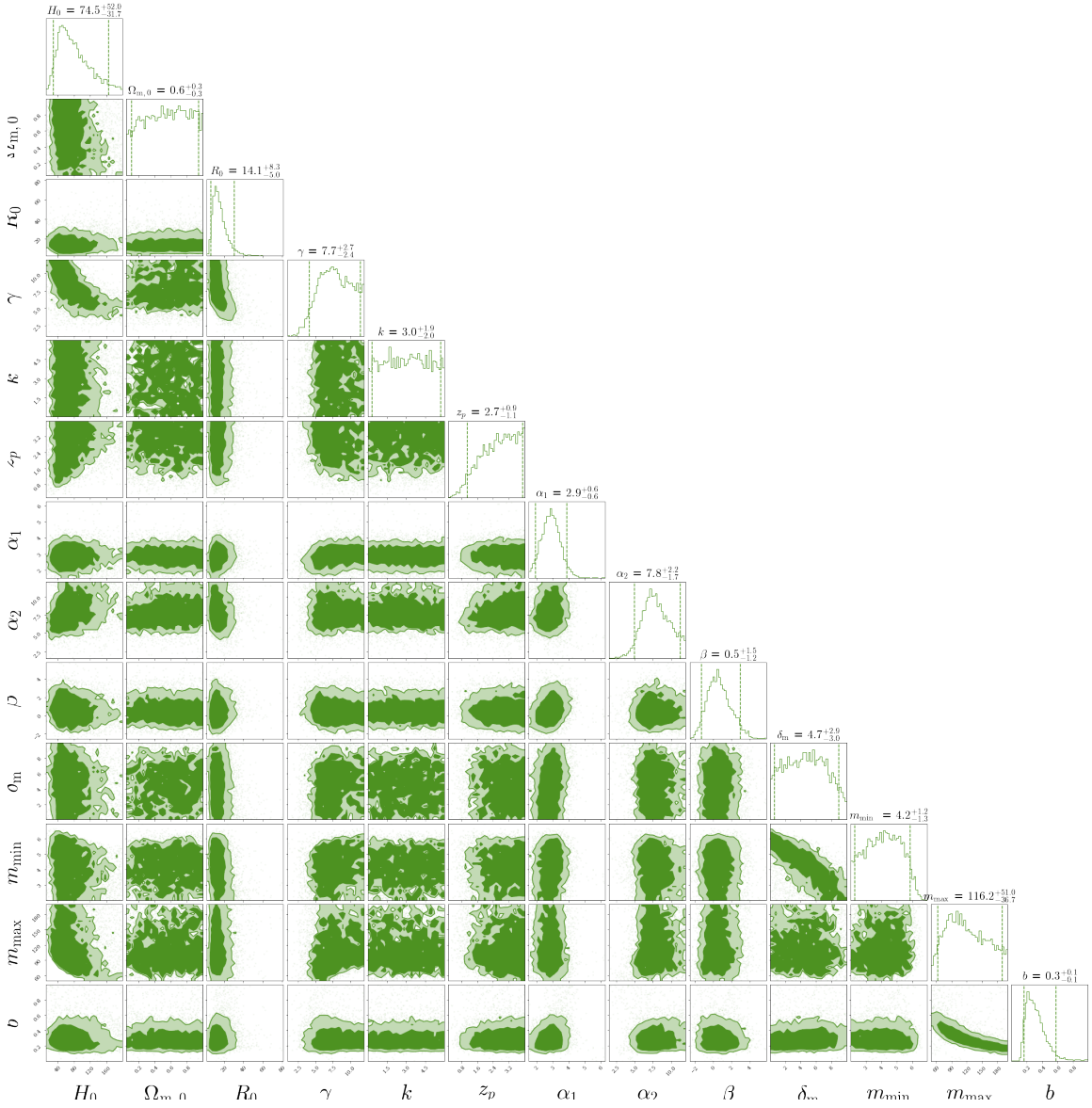

Figure B.14: Corner plot for the broken power law parameters obtained from the Bayesian analysis by using events with SNR > 12.

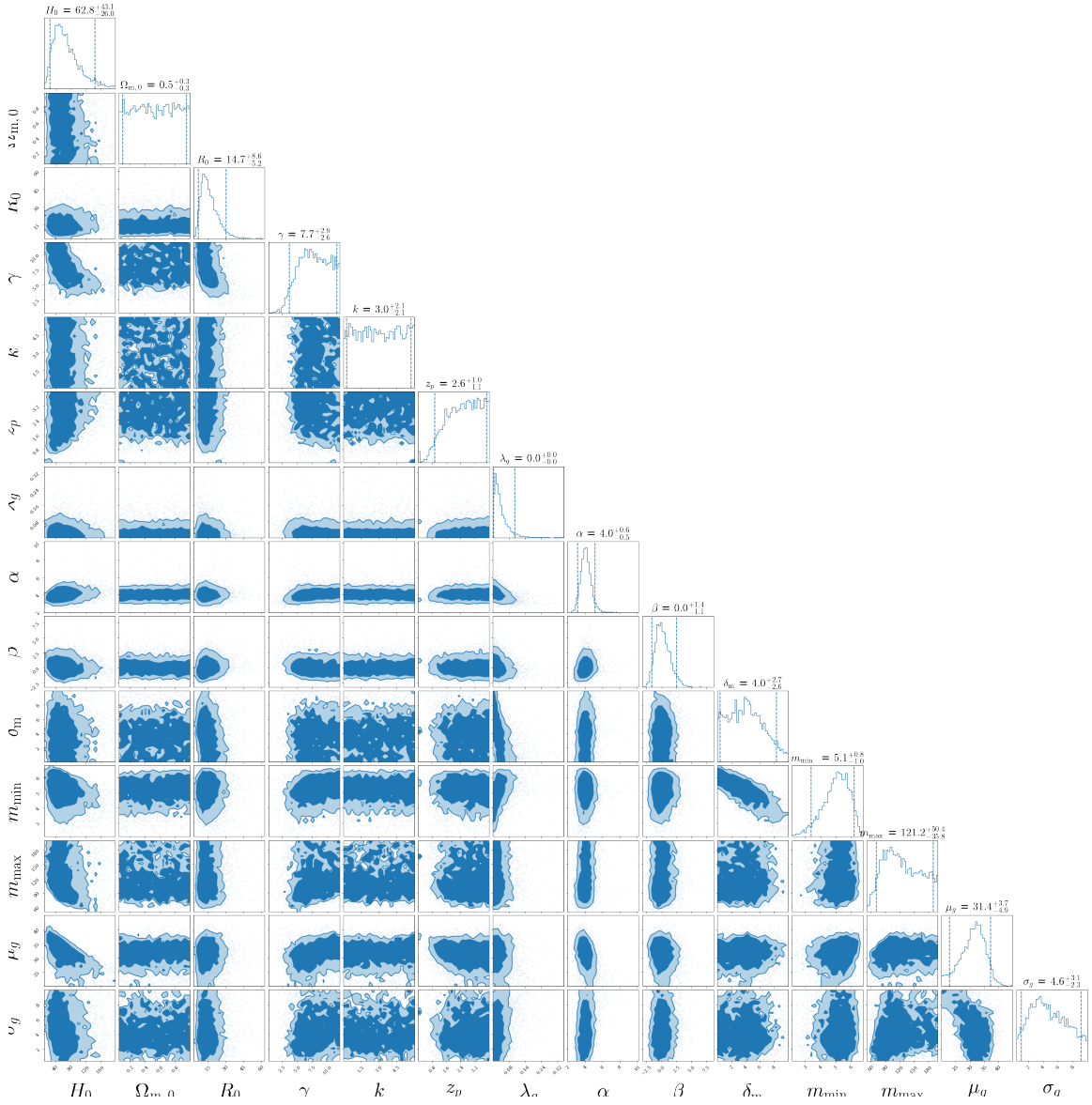

Figure B.15: Corner plot for the power law + peak parameters obtained from the Bayesian analysis by using events with SNR > 12.

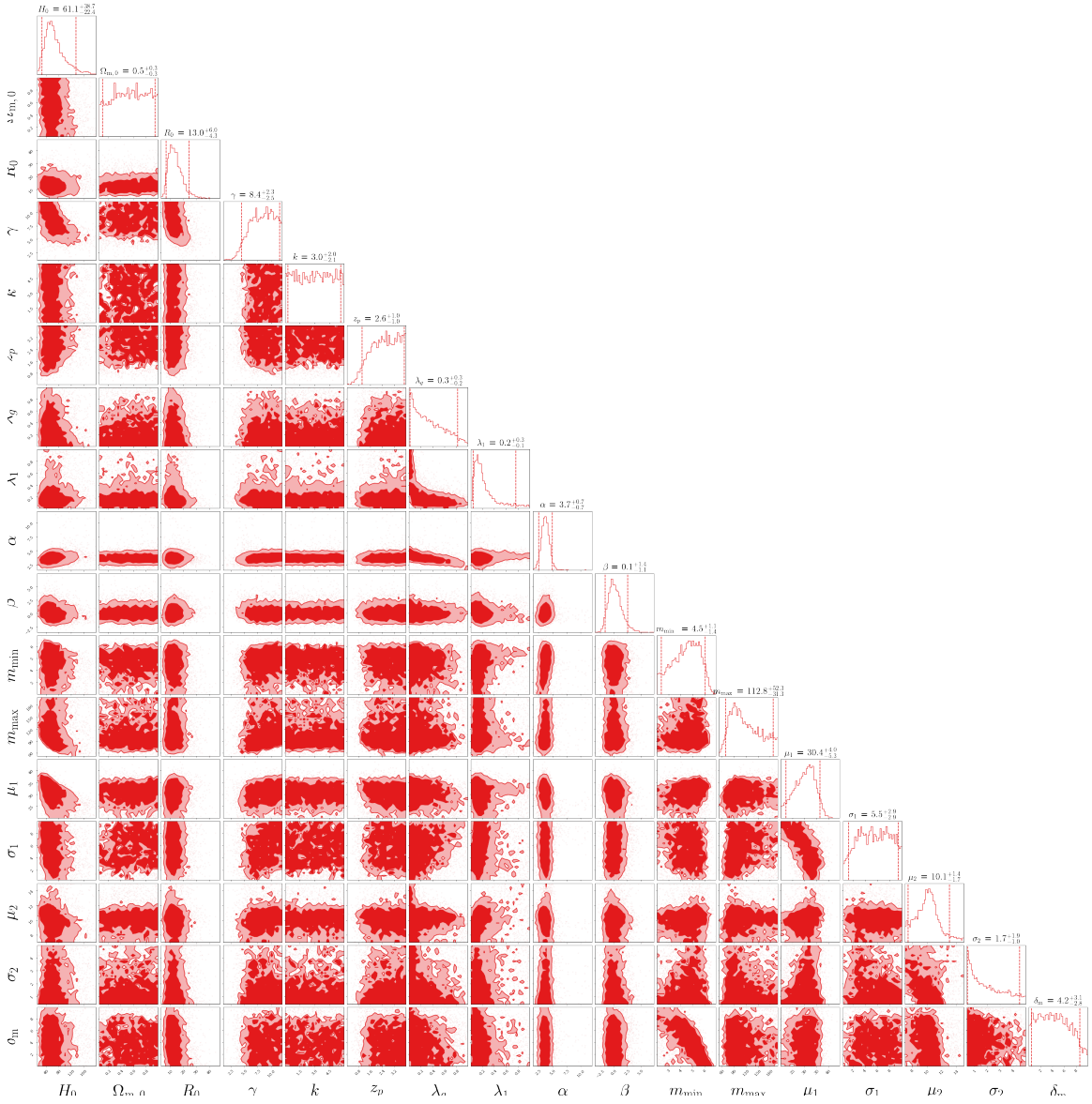

Figure B.16: Corner plot for the power law + 2 peaks parameters obtained from the Bayesian analysis by using events with SNR > 12.

Bibliography

[1] Michele Mancarella, Nicola Borghi, Stefano Foffa, Edwin Genoud-Prachex, Francesco Iacovelli, Michele Maggiore, Michele Moresco, and Matteo Schulz. Gravitational-wave cosmology with dark sirens: state of the art and perspectives for 3G detectors. In *Proceedings of 41st International Conference on High Energy physics — PoS(ICHEP2022)*. Sissa Medialab, nov 2022.

[2] A. G. Riess *et al.* Observational Evidence from Supernovae for an Accelerating Universe and a Cosmological Constant. *AJ*, 116(3):1009–1038, September 1998.

[3] S. Perlmutter *et al.*; The Supernova Cosmology Project. Measurements of Ω and Λ from 42 High-Redshift Supernovae. *ApJ*, 517(2):565–586, June 1999.

[4] N. Aghanim *et al.* (Planck Collaboration). Planck 2018 results. VI. Cosmological parameters. *Astronomy & Astrophysics*, 641:A6, sep 2020.

[5] Adam G. Riess, Stefano Casertano, Wenlong Yuan, J. Bradley Bowers, Lucas Macri, Joel C. Zinn, and Dan Scolnic. Cosmic Distances Calibrated to 1% Precision with Gaia EDR3 Parallaxes and Hubble Space Telescope Photometry of 75 Milky Way Cepheids Confirm Tension with ΛCDM. *ApJ*, 908(1):L6, February 2021.

[6] A. Font-Ribera *et al.* Quasar-lyman α forest cross-correlation from BOSS DR11: Baryon acoustic oscillations. *Journal of Cosmology and Astroparticle Physics*, 2014(05):027–027, may 2014.

[7] Licia Verde, Tommaso Treu, and Adam G. Riess. Tensions between the early and late Universe. *Nature Astronomy*, 3:891–895, September 2019.

[8] B. F. Schutz. Determining the hubble constant from gravitational wave observations. *Nature*, 323(310–311), sep 1986.

[9] M. Moresco *et al.* Unveiling the universe with emerging cosmological probes, 2022.

[10] Michele Mancarella, Edwin Genoud-Prachex, and Michele Maggiore. Cosmology and modified gravitational wave propagation from binary black hole population models. *Physical Review D*, 105(6), mar 2022.

[11] R. Abbott *et al.* (The LIGO Scientific Collaboration; The Virgo Collaboration). Population properties of compact objects from the second LIGO–virgo gravitational-wave transient catalog. *The Astrophysical Journal Letters*, 913(1):L7, may 2021.

[12] D. Foreman-Mackey, D. W. Hogg, D. Lang, and J. Goodman. emcee: The MCMC Hammer. *PASP*, 125(925):306, March 2013.

[13] R. Abbott *et al.* (LIGO Scientific Collaboration; Virgo Collaboration). GWTC-3: Compact binary coalescences observed by LIGO and Virgo during the second part of the third observing run, 2021.

[14] B. F. Schutz. *A First Course in General Relativity.* Cambridge University Press, 1985.

[15] Steven Weinberg. *Gravitation and Cosmology: Principles and Applications of the General Theory of Relativity.* John Wiley & Sons, Inc., 1972.

[16] K. Riles. Gravitational waves: Sources, detectors and searches. *Progress in Particle and Nuclear Physics*, 68:1–54, jan 2013.

[17] A. Einstein. Die grundlage der allgemeinen relativitätstheorie. *Annalen der Physik*, 354(7):769–822, 1916.

[18] D. J. Fixsen. The temperature of the cosmic microwave background. *The Astrophysical Journal*, 707(2):916–920, nov 2009.

[19] D. E. Holz, S. A. Hughes, and B. F. Schutz. Measuring cosmic distances with standard sirens. *Physics Today*, 71(12):34–40, December 2018.

[20] A. Einstein. *Näherungsweise Integration der Feldgleichungen der Gravitation.* Sitzungsberichte der Königlich Preußischen Akademie der Wissenschaften, jan 1916.

[21] J. M. Weisberg, J. H. Taylor, and L. A. Fowler. Gravitational waves from an orbiting pulsar. *Scientific American*, 245:74–82, October 1981.

[22] B. P. Abbott *et al.* (LIGO Scientific Collaboration; Virgo Collaboration). Observation of gravitational waves from a binary black hole merger. *Phys. Rev. Lett.*, 116:061102, Feb 2016.

[23] Lee Samuel Finn and David F. Chernoff. Observing binary inspiral in gravitational radiation: One interferometer. *Physical Review D*, 47(6):2198–2219, mar 1993.

[24] D. E. Holz and S. A. Hughes. Using gravitational-wave standard sirens. *The Astrophysical Journal*, 629(1):15–22, aug 2005.

[25] B. P. Abbott *et al.* (LIGO Scientific Collaboration; Virgo Collaboration). GW170817: Observation of Gravitational Waves from a Binary Neutron Star Inspiral. *Phys. Rev. Lett.*, 119(16):161101, October 2017.

[26] B. P. Abbott *et al.* (LIGO Scientific Collaboration; Virgo Collaboration). GWTC-1: A gravitational-wave transient catalog of compact binary mergers observed by LIGO and virgo during the first and second observing runs. *Physical Review X*, 9(3), sep 2019.

[27] B. P. Abbott *et al.* Prospects for observing and localizing gravitational-wave transients with advanced ligo, advanced virgo and kagra. *Living Reviews in Relativity*, 21(3), apr 2018.

[28] W. Del Pozzo. Inference of cosmological parameters from gravitational waves: Applications to second generation interferometers. *Physical Review D*, 86(4), aug 2012.

[29] C. L. MacLeod and C. J. Hogan. Precision of hubble constant derived using black hole binary absolute distances and statistical redshift information. *Physical Review D*, 77(4), feb 2008.

[30] Masamune Oguri. Measuring the distance-redshift relation with the cross-correlation of gravitational wave standard sirens and galaxies. *Physical Review D*, 93(8), apr 2016.

[31] Suvodip Mukherjee, Benjamin D Wandelt, and Joseph Silk. Probing the theory of gravity with gravitational lensing of gravitational waves and galaxy surveys. *Monthly Notices of the Royal Astronomical Society*, 494(2):1956–1970, mar 2020.

[32] S. Mukherjee, B. D. Wandelt, S. M. Nissanke, and A. Silvestri. Accurate precision cosmology with redshift unknown gravitational wave sources. *Physical Review D*, 103(4), feb 2021.

[33] X. Ding *et al.* Cosmological inference from standard sirens without redshift measurements. *Journal of Cosmology and Astroparticle Physics*, 2019(04):033–033, apr 2019.

[34] Christine Ye and Maya Fishbach. Cosmology with standard sirens at cosmic noon. *Physical Review D*, 104(4), aug 2021.

[35] Hebertt Leandro, Valerio Marra, and Riccardo Sturani. Measuring the hubble constant with black sirens. *Physical Review D*, 105(2), jan 2022.

[36] W. M. Farr, M. Fishbach, J. Ye, and D. E. Holz. A future percent-level measurement of the hubble expansion at redshift 0.8 with advanced LIGO. *The Astrophysical Journal*, 883(2):L42, oct 2019.

[37] The Virgo Collaboration R. Abbott *et al.* (The LIGO Scientific Collaboration and The KAGRA Collaboration). Constraints on the cosmic expansion history from GWTC-3, 2021.

[38] C J Moore, R H Cole, and C P L Berry. Gravitational-wave sensitivity curves. *Classical and Quantum Gravity*, 32(1):015014, dec 2014.

[39] KAGRA COLLABORATION LIGO SCIENTIFIC COLLABORATION, Virgo COLLABORATION. The LSC-Virgo-KAGRA observational science white paper (summer 2021 edition), 2021.

[40] C. D. Ott *et al.* Gravitational Waves from Axisymmetric, Rotating Stellar Core Collapse. *ApJ*, 600(2):834–864, January 2004.

[41] A. Corsi and B. J. Owen. Maximum gravitational-wave energy emissible in magnetar flares. *Phys. Rev. D*, 83(10):104014, May 2011.

[42] B. S. Sathyaprakash and B. F. Schutz. Physics, astrophysics and cosmology with gravitational waves. *Living Reviews in Relativity*, 12(1):2, dec 2009.

[43] M. Maggiore. *Gravitational Waves, Volume 2: Astrophysics and Cosmology*, volume 2. Oxford University Press, 2018.

[44] J. Abadie *et al.* (LIGO Scientific Collaboration and Virgo Collaboration). TOPICAL REVIEW: Predictions for the rates of compact binary coalescences observable by ground-based gravitational-wave detectors. *Classical and Quantum Gravity*, 27(17):173001, September 2010.

[45] J. B. Hartle. *Gravity : an introduction to Einstein's general relativity.* Addison Wesley, 2003.

[46] V. R.Pandharipande, D. Pines, and R. A. Smith. Neutron star structure: theory, observation, and speculation. *ApJ*, 208:550–566, September 1976.

[47] N. Andersson. A New Class of Unstable Modes of Rotating Relativistic Stars. *ApJ*, 502(2):708–713, August 1998.

[48] Andrew G. Lyne and Francis Graham-Smith. *Pulsar Astronomy.* Cambridge University Press, 2006.

[49] E. S. Phinney. The Rate of Neutron Star Binary Mergers in the Universe: Minimal Predictions for Gravity Wave Detectors. *ApJ*, 380:L17, October 1991.

[50] L. P. Grishchuk. Amplification of gravitational waves in an isotropic universe. *Zhurnal Eksperimentalnoi i Teoreticheskoi Fiziki*, 67:825–838, January 1974.

[51] K. S. Thorne. Gravitational radiation. In *Three Hundred Years of Gravitation*, pages 330–458. Cambridge University Press, 1987.

[52] B. Abbott *et al.* Analysis of first LIGO science data for stochastic gravitational waves. *Phys. Rev. D*, 69(12):122004, June 2004.

[53] Jens Hjorth, Andrew J. Levan, Nial R. Tanvir, Joe D. Lyman, Radosław Wojtak, Sophie L. Schrøder, Ilya Mandel, Christa Gall, and Sofie H. Bruun. The distance to NGC 4993: The host galaxy of the gravitational-wave event GW170817. *The Astrophysical Journal*, 848(2):L31, oct 2017.

[54] B. P. Abbott *et al.* (LIGO Scientific Collaboration; Virgo Collaboration). A gravitational-wave standard siren measurement of the hubble constant. *Nature*, 551(7678):85–88, nov 2017.

[55] Dougal Dobie, David L. Kaplan, Tara Murphy, Emil Lenc, Kunal P. Mooley, Christene Lynch, Alessandra Corsi, Dale Frail, Mansi Kasliwal, and Gregg Hallinan. A Turnover in the Radio Light Curve of GW170817. *ApJ*, 858(2):L15, May 2018.

[56] L. Resmi *et al.* Low-frequency View of GW170817/GRB 170817A with the Giant Metrewave Radio Telescope. *ApJ*, 867(1):57, November 2018.

[57] E. *et al.* Pian. Spectroscopic identification of r-process nucleosynthesis in a double neutron-star merger. *Nature*, 551(7678):67–70, November 2017.

[58] P. D'Avanzo *et al.* The evolution of the X-ray afterglow emission of GW 170817/ GRB 170817A in XMM-Newton observations. *A&A*, 613:L1, May 2018.

[59] K. D. Alexander, R. Margutti, P. K. Blanchard, W. Fong, E. Berger, A. Hajela, T. Eftekhari, R. Chornock, P. S. Cowperthwaite, D. Giannios, C. Guidorzi, A. Kathirgamaraju, A. MacFadyen, B. D. Metzger, M. Nicholl, L. Sironi, V. A. Villar, P. K. G. Williams, X. Xie, and J. Zrake. A Decline in the X-Ray through Radio Emission from GW170817 Continues to Support an Off-axis Structured Jet. *ApJ*, 863(2):L18, August 2018.

[60] Yiyang Wu and Andrew MacFadyen. GW170817 afterglow reveals that short gamma-ray bursts are neutron star mergers. *The Astrophysical Journal*, 880(2):L23, jul 2019.

[61] Chris L. Fryer. Mass Limits For Black Hole Formation. *ApJ*, 522(1):413–418, September 1999.

[62] Chris L. Fryer and Vassiliki Kalogera. Theoretical Black Hole Mass Distributions. *ApJ*, 554(1):548–560, June 2001.

[63] Michela Mapelli. Formation channels of single and binary stellar-mass black holes. In *Handbook of Gravitational Wave Astronomy*, pages 1–65. Springer Singapore, 2021.

[64] Chris L. Fryer, Krzysztof Belczynski, Grzegorz Wiktorowicz, Michal Dominik, Vicky Kalogera, and Daniel E. Holz. Compact Remnant Mass Function: Dependence on the Explosion Mechanism and Metallicity. *ApJ*, 749(1):91, April 2012.

[65] G. Gamow. *My world line: An informal autobiography.* Viking Press, 1970.

[66] Paweł Haensel. Urca processes in dense matter and neutron star cooling. *Space Science Reviews*, 74(3):427–436, nov 1995.

[67] William A. Fowler and F. Hoyle. Neutrino Processes and Pair Formation in Massive Stars and Supernovae. *ApJS*, 9:201, December 1964.

[68] Z. Barkat, G. Rakavy, and N. Sack. Dynamics of Supernova Explosion Resulting from Pair Formation. *Phys. Rev. Lett.*, 18(10):379–381, March 1967.

[69] G. Rakavy and G. Shaviv. Instabilities in Highly Evolved Stellar Models. *ApJ*, 148:803, June 1967.

[70] S. E. Woosley. Pulsational pair-instability supernovae. *The Astrophysical Journal*, 836(2):244, feb 2017.

[71] Michela Mapelli, Mario Spera, Enrico Montanari, Marco Limongi, Alessandro Chieffi, Nicola Giacobbo, Alessandro Bressan, and Yann Bouffanais. Impact of the Rotation and Compactness of Progenitors on the Mass of Black Holes. *ApJ*, 888(2):76, January 2020.

[72] Guglielmo Costa, Alessandro Bressan, Michela Mapelli, Paola Marigo, Giuliano Iorio, and Mario Spera. Formation of GW190521 from stellar evolution: the impact of the hydrogen-rich envelope, dredge-up, and $^{12}C(\alpha, \gamma)^{16}O$ rate on the pair-instability black hole mass gap. *MNRAS*, 501(3):4514–4533, March 2021.

[73] Krzysztof Belczynski, Daniel E. Holz, Tomasz Bulik, and Richard O'Shaughnessy. The first gravitational-wave source from the isolated evolution of two stars in the 40-100 solar mass range. *Nature*, 534(7608):512–515, June 2016.

[74] Piero Madau and Mark Dickinson. Cosmic star-formation history. *Annual Review of Astronomy and Astrophysics*, 52(1):415–486, 2014.

[75] R. C. Kennicutt and N. J. Evans. Star Formation in the Milky Way and Nearby Galaxies. *ARA&A*, 50:531–608, September 2012.

[76] R. Abbott (The LIGO Scientific Collaboration, The Virgo Collaboration, and The KAGRA Collaboration). The population of merging compact binaries inferred using gravitational waves through GWTC-3, 2021.

[77] M. Mapelli, N. Giacobbo, F. Santoliquido, and M. C. Artale. The properties of merging black holes and neutron stars across cosmic time. *Monthly Notices of the Royal Astronomical Society*, 487(1):2–13, apr 2019.

[78] B. P. Abbott *et al.* (LIGO Scientific Collaboration; Virgo Collaboration). GWTC-1: A gravitational-wave transient catalog of compact binary mergers observed by LIGO and virgo during the first and second observing runs. *Physical Review X*, 9(3), sep 2019.

[79] B. P. Abbott *et al.* (The LIGO Scientific Collaboration; The Virgo Collaboration). Binary black hole population properties inferred from the first and second observing runs of advanced LIGO and advanced Virgo. *The Astrophysical Journal*, 882(2):L24, sep 2019.

[80] B. P. Abbott *et al.* (The LIGO Scientific Collaboration; The Virgo Collaboration). GW190425: Observation of a compact binary coalescence with total mass ~ 3.4 $M_\odot$. *The Astrophysical Journal Letters*, 892(1):L3, mar 2020.

[81] B. P. Abbott *et al.* Observing gravitational-wave transient GW150914 with minimal assumptions. *Physical Review D*, 93(12), jun 2016.

[82] R. W. P. Drever. *The Detection of Gravitational Waves, edited by D. G. Blair.* Cambridge University Press, 1991.

[83] R. W. P. Drever *et al. Quantum Optics, Experimental Gravity, and Measurement Theory, edited by P. Meystre and M. O. Scully.* Springer New York, 1983.

[84] J. Mizuno *et al.* Resonant sideband extraction: a new configuration for interferometric gravitational wave detectors. *Physics Letters A*, 175(5):273–276, 1993.

[85] Brian J. Meers. Recycling in laser-interferometric gravitational-wave detectors. *Phys. Rev. D*, 38:2317–2326, Oct 1988.

[86] P. Kwee, C. Bogan, K. Danzmann, M. Frede, H. Kim, P. King, J. Pöld, O. Puncken, R. L. Savage, F. Seifert, P. Wessels, L. Winkelmann, and B. Willke. Stabilized high-power laser system for the gravitational wave detector advanced LIGO. *Opt. Express*, 20(10):10617–10634, May 2012.

[87] Chris L. Mueller, Muzammil A. Arain, Giacomo Ciani, Ryan. T. DeRosa, Anamaria Effler, David Feldbaum, Valery V. Frolov, Paul Fulda, Joseph Gleason, Matthew Heintze, Keita Kawabe, Eleanor J. King, Keiko Kokeyama, William Z. Korth, Rodica M. Martin, Adam Mullavey, Jan Peold, Volker Quetschke, David H. Reitze, David B. Tanner, Cheryl Vorvick, Luke F. Williams, and Guido Mueller. The advanced ligo input optics. *Review of Scientific Instruments*, 87(1):014502, 2016.

[88] F Acernese *et al.* (Virgo Collaboration). Advanced Virgo: a second-generation interferometric gravitational wave detector. *Classical and Quantum Gravity*, 32(2):024001, dec 2014.

[89] T. Akutsu *et al.* Overview of KAGRA: Calibration, detector characterization, physical environmental monitors, and the geophysics interferometer. *Progress of Theoretical and Experimental Physics*, 2021(5), 02 2021. 05A102.

[90] J. Aasi *et al.* (LIGO Scientific Collaboration). Advanced LIGO. *Classical and Quantum Gravity*, 32(7):074001, mar 2015.

[91] S. M. Aston *et al.* Update on quadruple suspension design for advanced LIGO. *Classical and Quantum Gravity*, 29(23):235004, oct 2012.

[92] F Matichard *et al.* Seismic isolation of advanced LIGO: Review of strategy, instrumentation and performance. *Classical and Quantum Gravity*, 32(18):185003, aug 2015.

[93] A. Effler, R. M. S. Schofield, V. V. Frolov, G. González, K. Kawabe, J. R. Smith, J. Birch, and R. McCarthy. Environmental influences on the LIGO gravitational wave detectors during the 6th science run. *Classical and Quantum Gravity*, 32(3):035017, jan 2015.

[94] E Goetz, R L Savage, J Garofoli, G Gonzalez, E Hirose, P Kalmus, K Kawabe, J Kissel, M Landry, B O'Reilly, X Siemens, A Stuver, and M Sung. Accurate calibration of test mass displacement in the LIGO interferometers. *Classical and Quantum Gravity*, 27(8):084024, apr 2010.

[95] Bruce Allen, Warren G. Anderson, Patrick R. Brady, Duncan A. Brown, and Jolien D. E. Creighton. FINDCHIRP: An algorithm for detection of gravitational waves from inspiraling compact binaries. *Physical Review D*, 85(12), jun 2012.

[96] Hsin-Yu Chen, Daniel E Holz, John Miller, Matthew Evans, Salvatore Vitale, and Jolien Creighton. Distance measures in gravitational-wave astrophysics and cosmology. *Classical and Quantum Gravity*, 38(5):055010, jan 2021.

[97] Kentaro Somiya. Detector configuration of KAGRA–the japanese cryogenic gravitational-wave detector. *Classical and Quantum Gravity*, 29(12):124007, jun 2012.

[98] Yoichi Aso, Yuta Michimura, Kentaro Somiya, Masaki Ando, Osamu Miyakawa, Takanori Sekiguchi, Daisuke Tatsumi, and Hiroaki Yamamoto. Interferometer design of the KAGRA gravitational wave detector. *Phys. Rev. D*, 88:043007, Aug 2013.

[99] D. V. Martynov *et al.* Sensitivity of the advanced LIGO detectors at the beginning of gravitational wave astronomy. *Physical Review D*, 93(11), jun 2016.

[100] B. P. Abbott *et al.* (LIGO Scientific Collaboration; Virgo Collaboration). Binary black hole mergers in the first advanced LIGO observing run. *Physical Review X*, 6(4), oct 2016.

[101] B. P. Abbott *et al.* (LIGO Scientific Collaboration; Virgo Collaboration). GW151226: Observation of gravitational waves from a 22-solar-mass binary black hole coalescence. *Phys. Rev. Lett.*, 116:241103, Jun 2016.

[102] H. Abe *et al.* (KAGRA Collaboration). Performance of the KAGRA detector during the first joint observation with GEO 600 (O3GK), jun 2022.

[103] K. L. Dooley *et al.* GEO 600 and the GEO-HF upgrade program: successes and challenges. *Classical and Quantum Gravity*, 33(7):075009, apr 2016.

[104] R. Abbott *et al.* (LIGO Scientific Collaboration; Virgo Collaboration). GWTC-2.1: Deep extended catalog of compact binary coalescences observed by ligo and virgo during the first half of the third observing run, 2021.

[105] K. Kawabe. Ph.d. thesis, 1998.

[106] M Rakhmanov, J D Romano, and J T Whelan. High-frequency corrections to the detector response and their effect on searches for gravitational waves. *Classical and Quantum Gravity*, 25(18):184017, sep 2008.

[107] L. Carbone *et al.* Sensors and actuators for the advanced LIGO mirror suspensions. *Classical and Quantum Gravity*, 29(11):115005, may 2012.

[108] C. Biwer *et al.* Validating gravitational-wave detections: The advanced LIGO hardware injection system. *Physical Review D*, 95(6), mar 2017.

[109] S. Karki *et al.* The advanced LIGO photon calibrators. *Review of Scientific Instruments*, 87(11):114503, nov 2016.

[110] D. Estevez, P. Lagabbe, A. Masserot, L. Rolland, M. Seglar-Arroyo, and D. Verkindt. The advanced Virgo photon calibrators. *Classical and Quantum Gravity*, 38(7):075007, feb 2021.

[111] F Acernese *et al.* (The Virgo Collaboration). Calibration of advanced virgo and reconstruction of the detector strain h(t) during the observing run o3. *Classical and Quantum Gravity*, 39(4):045006, jan 2022.

[112] D. Estevez, B. Mours, and T. Pradier. Newtonian calibrator tests during the Virgo o3 data taking. *Classical and Quantum Gravity*, 38(7):075012, mar 2021.

[113] M. Maggiore. Stochastic backgrounds of gravitational waves, 2000.

[114] J. Aasi *et al.* (LIGO Scientific). Gravitational waves from known pulsar: results from the initial detector era. *The Astrophysical Journal*, 785(2):119, apr 2014.

[115] J. Abadie *et al.* Publisher's note: All-sky search for gravitational-wave bursts in the first joint LIGO-GEO-Virgo run [phys. rev. d 81, 102001 (2010)]. *Phys. Rev. D*, 85:089905, Apr 2012.

[116] J. Abadie *et al.* All-sky search for gravitational-wave bursts in the second joint LIGO-virgo run. *Physical Review D*, 85(12), jun 2012.

[117] K. Cannon, A. Chapman, C. Hanna, D. Keppel, A. C. Searle, and A. J. Weinstein. Singular value decomposition applied to compact binary coalescence gravitational-wave signals. *Phys. Rev. D*, 82:044025, Aug 2010.

[118] R. Abbott *et al.* (LIGO Scientific Collaboration; Virgo Collaboration). GWTC-2: Compact binary coalescences observed by LIGO and virgo during the first half of the third observing run. *Physical Review X*, 11(2), jun 2021.

[119] C. Cutler and É. E. Flanagan. Gravitational waves from merging compact binaries: How accurately can one extract the binary's parameters from the inspiral waveform? *Physical Review D*, 49(6):2658–2697, mar 1994.

[120] B. P. Abbott *et al.* (LIGO Scientific Collaboration; Virgo Collaboration). A guide to LIGO–virgo detector noise and extraction of transient gravitational-wave signals. *Classical and Quantum Gravity*, 37(5):055002, feb 2020.

[121] P. C. Peters. Gravitational radiation and the motion of two point masses. *Phys. Rev.*, 136:B1224–B1232, Nov 1964.

[122] Luc Blanchet, Thibault Damour, Bala R. Iyer, Clifford M. Will, and Alan G. Wiseman. Gravitational-radiation damping of compact binary systems to second post-newtonian order. *Physical Review Letters*, 74(18):3515–3518, may 1995.

[123] P. Ajith, M. Hannam, S. Husa, Y. Chen, B. Brügmann, N. Dorband, D. Müller, F. Ohme, D. Pollney, C. Reisswig, L. Santamarí a, and J. Seiler. Inspiral-merger-ringdown waveforms for black-hole binaries with nonprecessing spins. *Physical Review Letters*, 106(24), jun 2011.

[124] L. Santamaria, F. Ohme, P. Ajith, B. Brügmann, N. Dorband, M. Hannam, S. Husa, P. Mösta, D. Pollney, C. Reisswig, E. L. Robinson, J. Seiler, and B. Krishnan. Matching post-newtonian and numerical relativity waveforms: Systematic errors and a new phenomenological model for nonprecessing black hole binaries. *Physical Review D*, 82(6), sep 2010.

[125] Thomas J. Loredo. Accounting for source uncertainties in analyses of astronomical survey data. In *AIP Conference Proceedings*. AIP, 2004.

[126] I. Mandel, W. M. Farr, and J. R. Gair. Extracting distribution parameters from multiple uncertain observations with selection biases. *Monthly Notices of the Royal Astronomical Society*, 486(1):1086–1093, mar 2019.

[127] Eric Thrane and Colm Talbot. An introduction to Bayesian inference in gravitational-wave astronomy: Parameter estimation, model selection, and hierarchical models. *PASA*, 36:e010, March 2019.

[128] Salvatore Vitale, Davide Gerosa, Will M. Farr, and Stephen R. Taylor. Inferring the properties of a population of compact binaries in presence of selection effects. In *Handbook of Gravitational Wave Astronomy*, pages 1–60. Springer Singapore, 2021.

[129] D. W. Hogg. Distance measures in cosmology, 1999.

[130] M. Fishbach and D. E. Holz. Where are LIGO's big black holes? *The Astrophysical Journal*, 851(2):L25, dec 2017.

[131] A. Heger and S. E. Woosley. The nucleosynthetic signature of population III. *The Astrophysical Journal*, 567(1):532–543, mar 2002.

[132] R. Trotta. Bayes in the sky: Bayesian inference and model selection in cosmology. *Contemporary Physics*, 49(2):71–104, mar 2008.

[133] Will Handley. Next generation cosmological analysis with nested sampling, aug 2022.

[134] Jonathan Goodman and Jonathan Weare. Ensemble samplers with affine invariance. *Communications in Applied Mathematics and Computational Science*, 5(1):65–80, January 2010.

[135] W. K. Hastings. Monte Carlo Sampling Methods using Markov Chains and their Applications. *Biometrika*, 57(1):97–109, April 1970.

[136] John Skilling. Nested Sampling. In Rainer Fischer, Roland Preuss, and Udo Von Toussaint, editors, *Bayesian Inference and Maximum Entropy Methods in Science and Engineering: 24th International Workshop on Bayesian Inference and Maximum Entropy Methods in Science and Engineering*, volume 735 of *American Institute of Physics Conference Series*, pages 395–405, November 2004.

[137] Greg Ashton, Noam Bernstein, Johannes Buchner, Xi Chen, Gábor Csányi, Andrew Fowlie, Farhan Feroz, Matthew Griffiths, Will Handley, Michael Habeck, Edward Higson, Michael Hobson, Anthony Lasenby, David Parkinson, Livia B. Pártay, Matthew Pitkin, Doris Schneider, Joshua S. Speagle, Leah South, John Veitch, Philipp Wacker, David J. Wales, and David Yallup. Nested sampling for physical scientists. *Nature Reviews Methods Primers*, 2(1), may 2022.

[138] Piero Madau and Tassos Fragos. Radiation Backgrounds at Cosmic Dawn: X-Rays from Compact Binaries. *ApJ*, 840(1):39, May 2017.

[139] Gregory Ashton, Moritz Hübner, Paul D. Lasky, Colm Talbot, Kendall Ackley, Sylvia Biscoveanu, Qi Chu, Atul Divakarla, Paul J. Easter, Boris Goncharov, Francisco Hernandez Vivanco, Jan Harms, Marcus E. Lower, Grant D. Meadors, Denyz Melchor, Ethan Payne, Matthew D. Pitkin, Jade Powell, Nikhil Sarin, Rory J. E. Smith, and Eric Thrane. Bilby: A user-friendly bayesian inference library for gravitational-wave astronomy. *The Astrophysical Journal Supplement Series*, 241(2):27, apr 2019.

[140] Joshua S Speagle. dynesty: a dynamic nested sampling package for estimating bayesian posteriors and evidences. *Monthly Notices of the Royal Astronomical Society*, 493(3):3132–3158, feb 2020.

[141] Sergey Koposov, Josh Speagle, Kyle Barbary, Gregory Ashton, Ed Bennett, Johannes Buchner, Carl Scheffler, Ben Cook, Colm Talbot, James Guillochon, Patricio Cubillos, Andrés Asensio Ramos, Ben Johnson, Dustin Lang, Ilya, Matthieu Dartiailh, Alex Nitz, Andrew McCluskey, Anne Archibald, Christoph Deil, Dan Foreman-Mackey, Danny Goldstein, Erik Tollerud, Joel Leja, Matthew Kirk, Matt Pitkin, Patrick Sheehan, Phillip Cargile, ruskin23, and Ruth Angus. joshspeagle/dynesty: v2.0.2, November 2022.

[142] D. J. C. MacKay. *Information Theory, Inference and Learning Algorithms*. Cambridge University Press, Oct 2003.

[143] K. Leyde, S. Mastrogiovanni, D.A. Steer, E. Chassande-Mottin, and C. Karathanasis. Current and future constraints on cosmology and modified gravitational wave friction from binary black holes. *Journal of Cosmology and Astroparticle Physics*, 2022(09):012, sep 2022.

[144] B. P. Abbott *et al.* (The LIGO Scientific Collaboration; The Virgo Collaboration). Properties of the binary neutron star merger GW170817. *Physical Review X*, 9(1), jan 2019.

[145] A. Palmese *et al.* (DES Collaboration). A Statistical Standard Siren Measurement of the Hubble Constant from the LIGO/Virgo Gravitational Wave Compact Object Merger GW190814 and Dark Energy Survey Galaxies. *ApJ*, 900(2):L33, September 2020.

[146] Michele Mancarella, Joe Kennedy, Benjamin Bose, and Lucas Lombriser. Seeking New Physics in Cosmology with Bayesian Neural Networks: Dark Energy and Modified Gravity. *arXiv e-prints*, page arXiv:2012.03992, December 2020.

[147] Francesco Iacovelli, Michele Mancarella, Stefano Foffa, and Michele Maggiore. Forecasting the detection capabilities of third-generation gravitational-wave detectors using `GWFAST`, 2022.

[148] Edwin Hubble. A relation between distance and radial velocity among extra-galactic nebulae. *Proceedings of the National Academy of Sciences*, 15(3):168–173, 1929.

[149] Alan Heavens, Yabebal Fantaye, Arrykrishna Mootoovaloo, Hans Eggers, Zafiirah Hosenie, Steve Kroon, and Elena Sellentin. Marginal likelihoods from monte carlo markov chains, 2017.

[150] B. Edelman, Z. Doctor, J. Godfrey, and B. Farr. Ain't No Mountain High Enough: Semiparametric Modeling of LIGO-Virgo's Binary Black Hole Mass Distribution. *ApJ*, 924(2):101, January 2022.

[151] B. S. Sathyaprakash and Matthew Evans. Gravitational-Wave Astronomy Still in Its Infancy. *Physics Online Journal*, 13:113, September 2020.

[152] D. Reitze *et al.* Cosmic Explorer: the U.S. contribution to gravitational-wave astronomy beyond LIGO. *Bulletin of the American Astronomical Society*, 2019.

[153] M. Punturo *et al.* The einstein telescope: a third-generation gravitational wave observatory. *Classical and Quantum Gravity*, 27(19):194002, sep 2010.